

國立臺灣大學電機資訊學院電信工程學研究所

博士論文

Graduate Institute of Communication Engineering

College of Electrical Engineering and Computer Science

National Taiwan University

Doctoral Dissertation

低延遲虛擬細胞車用通信網路下行鏈路

多用戶檢測技術之研究

Downlink Multiuser Detection in the Ultra-Low Latency  
Virtual Cell-Based Vehicular Networks

曾智修

Chih-Hsiu Zeng

指導教授：陳光禎 博士

Advisor: Kwang-Cheng Chen, Ph.D.

中華民國 108 年 7 月

July 2019





## 誌謝

在軍旅生涯任官服役12年之際，我選擇退伍，返回學校攻讀博士。說起來這是一個大膽又有點不負責任的決定，畢竟我不是年輕小伙子。感謝父、母親理解、支持我任性的選擇。

念博士感覺好像是一段自我修練、成長的過程。感謝指導教授陳光禎博士的訓練。他通常不會很具體地告訴我要做什麼，只是給一個方向、建議，引導我思考問題，實際上研究怎麼做、要做什麼，他都是讓我自己想，並說服他為什麼要做這個或這麼做。念博士的前1、2年，跟老師開會討論其實壓力挺大的，他喜歡挑戰學生的觀點、想法，他會說：「你講的東西是claim、是信仰，不是theorem、真理！」我想他真正想告訴學生的是「任何結論、陳述，都應該要提供證據」。我最喜歡老師的一句話是，當我們怕犯(說)錯，而不敢提出自己的觀點時，他會說：「如果你不敢犯錯，那你永遠不會做對！」我很慶幸我博士班的老闆是KC，如果重來一次，我仍會選KC當我指導教授，雖然他很“硬”。

感謝瑞昱半導體柳德政處長，在每次計畫報告時給我的建議，他會很細心地審視我的模擬結果、並挑出報告中的typo。謝謝電信所所辦趙姐、康小姐行政上、經費結報的幫助。謝謝曾志成學長，在我做Clustering Coefficient的研究時，耐心聽我報告並給予建議。謝謝口試委員給我的建議及肯定，特別要感謝闕志達教授，在正式口試前給我的寶貴意見。

很慶(榮)幸能夠結識實驗的學長(弟、妹)們。奕志真的幫我很多，尤其是博班第1、2年;謝謝人豪在口試及上海 ICC 的幫助; 謝謝Eisaku在美國的時候煮飯給我吃，讓我不至於天天吃垃圾食物; 也很謝謝羅恩臨，在美國時的照顧、帶我們出去玩; 謝謝紹洲、徐祥、奕丞在我當“MTK計畫”Coordinator時的鼎力幫助，跟你們討論讓我獲益良多。最後謝謝林茂昭教授實驗室的“大學長”蔡華龍博士，感謝你的關心及建議。



## 中文摘要

為普及未來自動駕駛車之應用，須建構可靠、低延遲的無線網路通信系統。近期研究成果指出，引進霧或邊緣運算(Fog or Edge Computing)有利對自動駕駛之即時管理與控制。進而整合虛擬細胞(Virtual Cell)概念、開路通訊(Open-loop Communications)、主動式網路鏈結(Proactive Network Association)，可將通信延遲時間降低至1毫秒(ms)，但鄰近細胞間(Virtual Cells)間的相互干擾卻難以避免。在開路通訊(Open-loop Communications)中，為提升頻寬使用效率，通道資訊(Channel State Information, CSI)不會反饋至傳送端，傳統波束賦形(Beamforming)或干擾對齊(Interference Alignment)將無法使用，故下行鏈路的干擾須由接收端運用多用戶檢測(Multiuser Detection, MUD)予以處理。

我們發現當使用最大似然多用戶檢測(Maximum-likelihood MUD, ML-MUD)時，位元錯誤率(Bit Error Rate, BER)對干擾源的調變技術(Modulation)非常敏感。若干擾源使用低階調變(Low-Order Modulation)，接收信號之位元錯誤率(Bit Error Rate, BER)仍可接近理論上之理想值。但是，當干擾源採用高階調變(High-Order Modulation)時，位元錯誤率則明顯地變差，我們的研究發現運用多天線技術可降低錯誤率對干擾源調變技術的敏感程度。我們也提出兩個方法降低多用戶檢測運算複雜度。第一個方法係利用下行鏈路的特性縮小所有可能解的信號空間(Solution Space)，稱為低運算最大似然多用戶檢測(Reduced-Computation ML-MUD, R-ML-MUD)。第二個方法是一新型投影接收機(Projection Receiver)，稱為一般化線性最小均方誤差等化法(Generalized Linear Minimum Mean Square Error Equalizer, GLMMSE)，其與傳統投影接收機(Projection Receiver)，相比，明顯有較佳的訊噪比(Signal-to-Noise Ratio, SNR)。

來自不同接取點(Access Points, APs)振盪器有著不相同的載波頻率偏移(Carrier Frequency Offset, CFO)，導致嚴重的子載波相互干擾(Inter-Carrier Interference, ICI)，訊號干擾的情況更為糟糕。運用非同步多用戶檢測(Asynchronous MUD)及子載波干擾白化技術(ICI Whitening)可獲得良好系統效能，然而白化技術需要干擾信號之共變異矩陣，對下行鏈路接收機而言，此項資訊實際上難以獲得或估測。鑑於此，我們發展一套兩階段干擾訊號抑制方法。第一階段為虛擬子載波干擾白化技術



(Pseudo-ICI-Whitening, P-ICI-W), 該技術不須估測子載波干擾信號之共變異矩陣, 故適用於下行鏈路接收機。第二階段即為一般化線性最小均方誤差等化法(GLMMSE), 對子載波干擾做更進一步的處理。此外我們將所發展的技術運用於時空編碼信號的干擾處理, 其中所考慮的時空編碼技術為Alamouti編碼和複雜交織正交設計(Complex Interleaved Orthogonal Design), 比較兩種編碼經由我們發展的信號處理後的效能。

最後, 我們假設虛擬細胞的存取點(APs)運用合作式頻域編碼服務自駕車。即使子載波干擾(ICI)可完美消除, 載波頻率偏移(CFO)所仍會造成嚴重效能損失, 我們提出一簡單的存取點索引原則(AP Indexing Principle)解決此問題。我們也改善原本的編碼技術, 使得存取點(APs)在任意索引方式下, 位元錯誤率(Bit Error Rate, BER)均不會明顯提升, 更有效地對抗頻率偏移(CFO)問題。

關鍵字：多用戶檢測、干擾抑制、開路通訊、車用網路、虛擬細胞、超可靠和低延遲通信、第五代移動通信技術

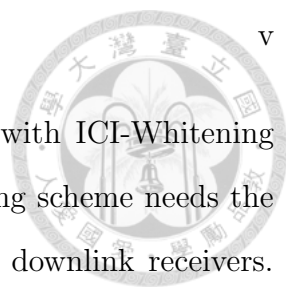


# Abstract

To achieve ultra-low latency mobile networking, recent efforts to integrate virtual cell with open-loop communications and proactive network association suggest the facilitation of new technological paradigm, but the interference from different co-locating virtual cells is hard to handle. Open-loop transmissions make beam-forming/interference alignment (IA) infeasible due to the need of channel state information (CSI) feedback. Multiuser detection (MUD) is therefore employed to address downlink interference.

We note that the bit error rate (BER) of maximum-likelihood MUD (ML-MUD) is sensitive to the modulation of interference. As the interferer uses low-order modulation, the BER of desired signal can approach the ideal case without interference. But if the interferer adopts high-order modulation, the resultant BER is significantly degraded. Our study shows that such modulation sensitivity can be eased by multi-antenna technique. We also propose two methods to reduce the notorious computational complexity of MUD, particularly involving higher-order modulations. The first scheme is termed reduced-computation ML-MUD (R-ML-MUD) that exploits the characteristic of downlink to shrink the ML solution space, consequently leading to lower detection complexity. The second scheme is a new projection receiver, called generalized linear minimum mean square error equalizer (GLMMSE) resulting in notable signal-to-noise ratio (SNR) gain over the conventional projection method.

Nevertheless, losing perfect synchronization creates difficulty in tackling multiple access interference (MAI). Multiple carrier frequency offsets (CFOs) due to different oscillators at different access points (APs) incur serious inter-carrier interfer-



ence (ICI) to complicate downlink MAI. Asynchronous MUD with ICI-Whitening was shown leading to satisfactory performance, but the whitening scheme needs the covariance matrix of ICI that is practically hard to obtain for downlink receivers. We therefore develop a two-stage ICI suppression method to resolve this challenge. The first-stage processing is Pseudo-ICI-Whitening (P-ICI-W), which does not rely on the estimation of ICI covariance and is suitable for asynchronous downlink. In terms of post-processing signal-to-interference-plus-noise ratio (SINR) and BER, our proposed mechanism can approach ICI-Whitening. The second-stage processing is based on GLMMSE to further cancel some ICI terms. We also apply our scheme to space-time-block-coded signals, considering Alamouti coding and Complex Interleaved Orthogonal Design.

Finally, we assume that APs can coordinately allocate radio resource for the served vehicles and enforce frequency-domain cooperative data encoding. Our analysis shows that CFOs will still noticeably worsen the BER, even if ICI is well-addressed. Such problem can be resolved by indexing APs according to the order of CFOs. Furthermore, we propose a robust encoding scheme that achieves satisfactory performance and allows random AP indexing, thus CFO feedback can be avoided.

**Keyword:** Multiuser detection, interference suppression, open-loop communications, vehicular networks, virtual cell, uRLLC, 5G



# Contents

Acknowledgements	i
Abstract in Chinese	ii
Abstract	iv
Contents	viii
List of Figures	xvi
List of Tables	xvii
<b>1 Introduction</b>	<b>1</b>
1.1 Ultra-Low Latency Vehicular Networking . . . . .	1
1.2 Signal Detection Schemes . . . . .	4
1.2.1 Single-User Detection . . . . .	5
1.2.2 Multiuser Detection . . . . .	6
1.2.3 ZF/LMMSE Detection . . . . .	8
1.2.4 Projection Receiver . . . . .	10
1.3 Joint Detection to Address Interference in the Virtual Cell: Feasibility and Possible Issues . . . . .	11
1.4 OFDMA-Based Virtual Cell Networks . . . . .	13
1.4.1 Signal Model in Perfect Synchronization . . . . .	14
1.4.2 CFO-Induced ICI . . . . .	16



1.4.3	Challenges in Asynchronous Downlink . . . . .	18
1.5	Organization and Contributions of Dissertation . . . . .	21
<b>2</b>	<b>Modulation Sensitivity in Multiuser Detection</b>	<b>25</b>
2.1	Signal Model and Preliminaries . . . . .	26
2.2	The Impact of Modulation of Interference on BER . . . . .	28
2.3	Comparison with LMMSE . . . . .	33
2.4	Simulation Results . . . . .	34
2.5	Summary . . . . .	37
<b>3</b>	<b>Low-Complexity Multiuser Detection</b>	<b>39</b>
3.1	Comparison between SUD and ML-MUD . . . . .	39
3.2	Reduced-Computation ML-MUD . . . . .	43
3.3	Generalized LMMSE . . . . .	49
3.4	Case Study by Simulations . . . . .	55
3.5	Summary . . . . .	59
<b>4</b>	<b>Two-Stage Inter-Carrier Interference Suppression</b>	<b>63</b>
4.1	Asynchronous Modelling . . . . .	64
4.1.1	Probabilistic Analysis of TDOA-Induced ISI . . . . .	65
4.1.2	Signal Model for Multi-CFO Issue . . . . .	68
4.2	First-Stage Processing . . . . .	71
4.2.1	Pseudo Whitening . . . . .	72
4.2.2	Joint Detection . . . . .	78
4.3	Second-Stage Processing . . . . .	81
4.3.1	ICI Suppression by Projection Method . . . . .	81
4.3.2	Compare Different ICI-Suppression Alternatives by Simulations	82
4.4	Generalization to the Case with STBC . . . . .	90
4.4.1	Complex Interleaved Orthogonal Design . . . . .	90



CONTENTS

viii

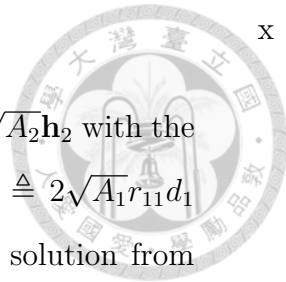


4.4.2 Alamouti Coding . . . . .	92
4.4.3 Performance Comparison . . . . .	94
4.5 Summary . . . . .	98
<b>5 Cooperative Coding in Frequency Domain</b>	<b>99</b>
5.1 Cooperative Encoding and MRC . . . . .	100
5.2 Benchmark Analysis: Asynchronous MRC . . . . .	106
5.3 AP Indexing Principle . . . . .	111
5.4 Robust Cooperative Encoding Against CFO . . . . .	116
5.5 Summary . . . . .	118
<b>6 Conclusion</b>	<b>119</b>
6.1 Dissertation Summary . . . . .	119
6.2 Future Work . . . . .	120
<b>Bibliography</b>	<b>123</b>
<b>Appendix A Proof of (2.23)</b>	<b>133</b>
<b>Appendix B Proof of (2.32)</b>	<b>135</b>
<b>Appendix C Proof of (4.66)</b>	<b>137</b>
<b>Appendix D Proof of (5.26)</b>	<b>139</b>
<b>Appendix E Proof of (5.29)</b>	<b>141</b>



# List of Figures

1.1	(Left) Each vehicle is served by multiple APs to form a virtual cell. Without central optimization of radio resource allocation, each AP may randomly select RRUs to provide downlink services, incurring co-channel interference. Even worse, such interference could also be from a HPN. (Right) Co-channel MAI in channel-1. . . . .	3
1.2	Downlink MAI scenario. Without loss of generality, we look at the channel where AP- $N$ relays the desired data of uRLLC applications from the AN to the AV, and AP-1~AP-( $N - 1$ ) are interferers. . . .	5
1.3	(Left) Each AP in the virtual cell allocates a RRU to serve a vehicle. (Right) Co-channel MAI in RRU-1. . . . .	14
1.4	The signals from different APs reach the vehicle with various delays, and $\Delta t_n$ represents the discrete timing offset for AP- $n$ 's signal relative to the first-arriving signal from some AP, say AP-1. (a) If $N_{\text{ch}} < N_{\text{cp}} - \Delta t_n$ , there is no ISI. (b) If $N_{\text{ch}} \geq N_{\text{cp}} - \Delta t_n$ , ISI and ICI occur.	16
1.5	CFOs cause ICI. At the receiver's $q$ th FFT output, the desired data symbol from the $q$ th subcarrier of AP-1 are coupled with the signals from all the subcarriers of APs-1~3. . . . .	19
1.6	Organization and contributions of dissertation. . . . .	24



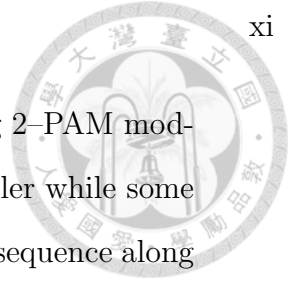
2.1 (a)  $\mathcal{M}_1$  and  $\mathcal{M}_2$  are rotated and scaled by  $\sqrt{A_1}\mathbf{h}_1$  and  $\sqrt{A_2}\mathbf{h}_2$  with the spacings of adjacent constellation points becoming  $\Delta_1 \triangleq 2\sqrt{A_1}r_{11}d_1$  and  $2\sqrt{A_2}\|\mathbf{h}_2\|_2 d_2$ . (b) The receiver searches the ML solution from a composite constellation under 2-PAM (Left) / 4-PAM (Right) interference. When  $\mathbf{x}$  is the transmitted sequence, the most likely error is decoding  $\mathbf{x}$  as  $\tilde{\mathbf{x}}$ , and the distance between them is  $D_{\text{ML}}$ . The constellation points of AP-1 act like quantization levels to quantize  $2\sqrt{A_2}r_{12}d_2\mathbf{q}_1$ . . . . . 29

2.2 (Left)  $N_{\text{rx}} = 2$ . (Right)  $N_{\text{rx}} = 3$ . AP-2 uses QPSK to transmit the desired data while  $\frac{A_2}{A_1} = 0$  dB. The average BERs under different modulated interference are plotted. . . . . 35

2.3 (Left)  $N_{\text{rx}} = 2$ . (Right)  $N_{\text{rx}} = 3$ . AP-2 uses QPSK to transmit the desired data being interfered by AP-1's 16-QAM modulated signal. The average BERs are plotted for  $\frac{A_2}{A_1} = \pm 3$  dB. . . . . 36

3.1  $\mathcal{M}_1$  and  $\mathcal{M}_2$  are rotated and scaled by channel gains, becoming  $\tilde{\mathcal{M}}_1$  and  $\tilde{\mathcal{M}}_2$  with the spacings of adjacent constellation points,  $\tilde{\Delta}_1 \triangleq 2\sqrt{A_1}\|\mathbf{h}_1\|_2 d_1$  and  $2\sqrt{A_2}\|\mathbf{h}_2\|_2 d_2$ . MRC projects interference to  $\text{span}(\mathbf{h}_2)$ , deviating the transmitted symbol from its original position.  $D_{\text{SUD}} = 2\sqrt{A_2}\|\mathbf{h}_2\|_2 d_2 - (I_1 - 1)\tilde{\Delta}_1$ , and  $I_1 = 4$ . . . . . 40

3.2 The receiver searches the ML solution from a composite constellation  $\mathcal{M}$ . When  $\mathbf{x}$  is the transmitted sequence, the most likely error is decoding  $\mathbf{x}$  as  $\tilde{\mathbf{x}}$ , and the distance between them is  $D_{\text{ML}}$ .  $D_{\text{SUD}} = 2\sqrt{A_2}\|\mathbf{h}_2\|_2 d_2 - (I_1 - 1)\tilde{\Delta}_1$  and  $D_{\text{ZF}} = 2\sqrt{A_2}r_{22}d_2$  account for the detection performance of SUD and ZF. . . . . 42



3.3 (a) The receiver treats the 4-PAM interference as being 2-PAM modulated. (b) The composite constellation space gets smaller while some extra interference is introduced to shift the transmitted sequence along  $\pm \mathbf{q}_1$ .  $D_{\text{RML}}$  and  $e_{\text{R,qua}}$  are defined similarly. The extra interference makes the transmitted sequence  $(-2d_1, d_2)$  closer to or further away from the dashed purple/green line. . . . . 44

3.4 AP-3 uses BPSK to transmit the desired signal. The average BERs of R-ML-MUD with different detection complexity are plotted. The 64-QAM interference from AP-1 is ignored or treated as being 16-QAM/QPSK modulated.  $N_{\text{rx}} = 3$ ,  $\frac{A_3}{A_2} = -5$  dB, and  $\frac{A_3}{A_1} = 5$  dB. . . . 46

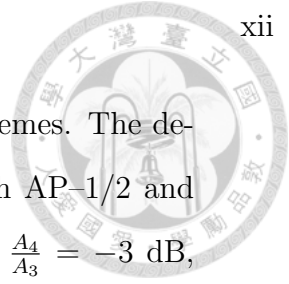
3.5 AP-3 uses BPSK to transmit the desired signal. The average BERs of R-ML-MUD with different detection complexity are plotted. The 16-QAM interference from AP-1 is ignored or treated as being QPSK modulated.  $N_{\text{rx}} = 3$ ,  $\frac{A_3}{A_2} = -5$  dB, and  $\frac{A_3}{A_1} = 5$  dB. . . . . 48

3.6 The average BERs are plotted for PR and GLMMSE. The desired signal from AP-5 is QPSK-modulated while APs-1~4 use BPSK.  $N_{\text{rx}} = 6$ , and  $\frac{A_5}{A_4} = \frac{A_5}{A_3} = \frac{A_5}{A_2} = \frac{A_5}{A_1} = 0$  dB. . . . . 52

3.7 The average BERs are plotted for PR and GLMMSE. The desired signal from AP-5 is QPSK-modulated while APs-1~4 use BPSK.  $N_{\text{rx}} = 6$ , and  $\frac{A_5}{A_4} = \frac{A_5}{A_3} = \frac{A_5}{A_2} = \frac{A_5}{A_1} = 5$  dB. . . . . 53

3.8 The average BERs are plotted for PR and GLMMSE. The desired signal from AP-5 is QPSK-modulated while APs-1~4 use BPSK.  $N_{\text{rx}} = 6$ , and  $\frac{A_5}{A_4} = 0$  dB, and  $\frac{A_5}{A_3} = \frac{A_5}{A_2} = \frac{A_5}{A_1} = 0, 3, 6$  dB. . . . . 54

3.9 The average BERs are plotted for different detection schemes. The desired signal from AP-3 is QPSK modulated while both AP-1 and AP-2 use 16-QAM.  $N_{\text{rx}} = 3$ ,  $\frac{A_3}{A_2} = -5$  dB, and  $\frac{A_3}{A_1} = 5$  dB. . . . . 55



3.10 The average BERs is plotted for different detection schemes. The desired signal from AP-4 is QPSK modulated while both AP-1/2 and AP-3 use 64-QAM and BPSK, respectively.  $N_{\text{rx}} = 4$ ,  $\frac{A_4}{A_3} = -3$  dB,  $\frac{A_4}{A_2} = 3$  dB, and  $\frac{A_4}{A_1} = 6$  dB. . . . . 56

3.11 The average BERs are plotted for different detection schemes. The desired signal from AP-4 is QPSK modulated while both AP-1/2 and AP-3 use 64-QAM and BPSK, respectively.  $N_{\text{rx}} = 4$ ,  $\frac{A_4}{A_3} = 3$  dB,  $\frac{A_4}{A_2} = -3$  dB, and  $\frac{A_4}{A_1} = 6$  dB. . . . . 57

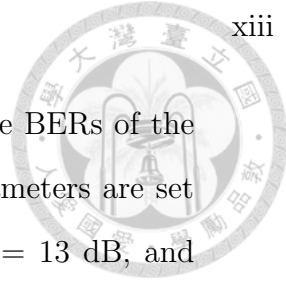
3.12 The average BERs are plotted for different detection schemes. The desired signal from AP-5 is QPSK modulated while both APs-1~2 and APs-3~4 adopt BPSK and 64-QAM, respectively.  $N_{\text{rx}} = 4$ ,  $\frac{A_5}{A_4} = \frac{A_5}{A_3} = 0$  dB,  $\frac{A_5}{A_2} = 6$  dB, and  $\frac{A_5}{A_1} = 8$  dB. . . . . 58

3.13 The average BERs are plotted for different detection schemes. The desired signal from AP-5 is QPSK modulated while both APs-1~2 and APs-3~4 adopt BPSK and 64-QAM, respectively.  $N_{\text{rx}} = 4$ ,  $\frac{A_5}{A_4} = \frac{A_5}{A_3} = 0$  dB,  $\frac{A_5}{A_2} = 6$  dB, and  $\frac{A_5}{A_1} = 8$  dB. . . . . 59

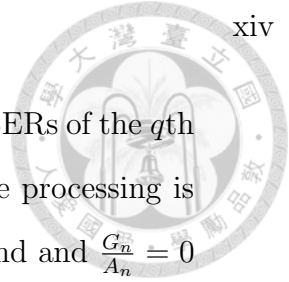
4.1 (Left)  $t_{\text{cp}} = 0.59\mu\text{s}$ . (Right)  $t_{\text{cp}} = 1.19\mu\text{s}$ . The probability of  $U_{(N)} - U_{(1)} > \Delta d$  is plotted for different  $N$  and  $\lambda_{\text{ap}}$ . We set that  $t_{\text{ch}} = \frac{t_{\text{cp}}}{2}$ . . . . . 67

4.2 (Left)  $\beta = 1$ . (Right)  $\beta = 2$ . The average SINR loss of ICI-W and P-ICI-W versus CFO difference  $\Delta\varepsilon$  is plotted. The parameters are set as  $\frac{A_2}{\sigma_V^2} = \frac{A_1}{\sigma_V^2} = 10$  dB, and  $\frac{G_n}{A_n} = 0, \pm 2, \pm 5$  dB for  $n = 1, 2$ . . . . . 75

4.3 (Left)  $\beta = 1$ . (Right)  $\beta = 2$ . In 2-AP case, the average BERs of the  $q$ th subcarrier of AP-2 are plotted w.r.t  $\Delta\varepsilon$ . The parameters are set as  $\varepsilon_2 = 0$ ,  $\Delta\varepsilon = \varepsilon_1 - \varepsilon_2$ ,  $q = 20$ ,  $N_{\text{rx}} = 2$ ,  $\frac{A_2}{\sigma_V^2} = \frac{A_1}{\sigma_V^2} = 13$  dB, and  $\frac{G_n}{A_n} = 0$  dB for  $n = 1, 2$ . . . . . 79



- 4.4 (Left)  $\alpha = 2$ . (Right)  $\alpha = 6$ . In 2-AP case, the average BERs of the  $q$ th subcarrier of AP-2 are plotted w.r.t  $\Delta\varepsilon$ . The parameters are set as  $\varepsilon_2 = 0$ ,  $\Delta\varepsilon = \varepsilon_1 - \varepsilon_2$ ,  $q = 20$ ,  $N_{\text{rx}} = 2$ ,  $\frac{A_2}{\sigma_V^2} = \frac{A_1}{\sigma_V^2} = 13$  dB, and  $\frac{G_n}{A_n} = 0, \pm 5$  dB for  $n = 1, 2$ . . . . . 80
- 4.5 In 3-AP case, the average BERs of the  $q$ th subcarrier of AP-2 are plotted w.r.t  $\Delta\varepsilon$ . The parameters are set as  $\alpha = 10$ ,  $N_{\text{rx}} = 3$ ,  $\varepsilon_2 = 0$ ,  $\Delta\varepsilon = \varepsilon_1 - \varepsilon_2 = \varepsilon_2 - \varepsilon_3$ ,  $\frac{A_n}{\sigma_V^2} = 10$  dB, and  $\frac{G_n}{A_n} = 0$  dB for  $n = 1, 2, 3$ . The two-stage processing is implemented as PT-ICI-W + GLMMSE/PR. 84
- 4.6 (Upper)  $\beta = 2$ . (Lower)  $\beta = 3$ . In 3-AP case, the average BERs of the  $q$ th subcarrier of AP-2 are plotted w.r.t  $\Delta\varepsilon$ . The parameters are set as  $\alpha = 10$ ,  $N_{\text{rx}} = 3$ ,  $\varepsilon_2 = 0$ ,  $\Delta\varepsilon = \varepsilon_1 - \varepsilon_2 = \varepsilon_2 - \varepsilon_3$ ,  $\frac{A_n}{\sigma_V^2} = 10$  dB, and  $\frac{G_n}{A_n} = 0, \pm 5$  dB for  $n = 1, 2, 3$ . One stage-processing is based on PT-ICI-W, and two-stage processing is implemented as PT-ICI-W + GLMMSE. . . . . 85
- 4.7 In 3-AP case, the average BERs of the  $q$ th subcarrier of AP-2 are plotted w.r.t  $\Delta\varepsilon$ . The parameters are set as  $\alpha = 10$ ,  $N_{\text{rx}} = 3$ ,  $\varepsilon_2 = 0$ ,  $\Delta\varepsilon = \varepsilon_1 - \varepsilon_2 = \varepsilon_2 - \varepsilon_3$ ,  $\frac{A_n}{\sigma_V^2} = 10$  dB, and  $\frac{G_n}{A_n} = 0$  dB for  $n = 1, 2, 3$ . The two-stage processing is implemented as PT-ICI-W + GLMMSE. 86
- 4.8 In 3-AP case, the average BERs of the  $q$ th subcarrier of AP-2 are plotted w.r.t  $\Delta\varepsilon$ . The parameters are set as  $\alpha = 10$ ,  $N_{\text{rx}} = 3$ ,  $\varepsilon_2 = 0$ ,  $\Delta\varepsilon = \varepsilon_1 - \varepsilon_2 = \varepsilon_2 - \varepsilon_3$ ,  $\frac{A_n}{\sigma_V^2} = 10$  dB, and  $\frac{G_n}{A_n} = 0$  dB for  $n = 1, 2, 3$ . The two-stage processing is implemented as PT-ICI-W + PR. . . . . 87
- 4.9 (Upper)  $\beta = 2$ . (Lower)  $\beta = 3$ . In 3-AP case, the average BERs of the  $q$ th subcarrier of AP-2 are plotted w.r.t  $\Delta\varepsilon$ . The parameters are set as  $\alpha = 10$ ,  $N_{\text{rx}} = 3$ ,  $\varepsilon_2 = 0$ ,  $\Delta\varepsilon = \varepsilon_1 - \varepsilon_2 = \varepsilon_2 - \varepsilon_3$ ,  $\frac{A_n}{\sigma_V^2} = 10$  dB, and  $\frac{G_n}{A_n} = 0, \pm 5$  dB for  $n = 1, 2, 3$ . The two-stage processing is implemented as PT-ICI-W + GLMMSE with Alternative-2. . . . . 88



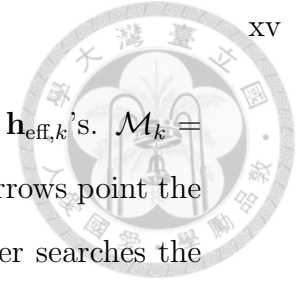
4.10 (Left)  $\beta = 2$ . (Right)  $\beta = 3$ . In 4-AP case, the average BERs of the  $q$ th subcarrier of AP-2 are plotted w.r.t  $\Delta\varepsilon$ . The two-stage processing is implemented as PT-ICI-W + GLMMSE with  $\alpha = 10$  and  $\frac{G_n}{A_n} = 0$  dB for  $n = 1, 2, 3, 4$ . The parameters are set as ,  $N_{\text{rx}} = 4$ ,  $\varepsilon_2 = 0.35$ ,  $\varepsilon_1 = 0.45$ ,  $\varepsilon_3 = \varepsilon_2 - \Delta\varepsilon$ ,  $\varepsilon_4 = \varepsilon_2 - \Delta\varepsilon - 0.02$ ,  $\frac{A_2}{\sigma_V^2} = 7$  dB,  $\frac{A_1}{A_2} = 3$  dB,  $\frac{A_3}{A_2} = -3$  dB,  $\frac{A_4}{A_2} = -5$  dB. Alternative-5 means suppressing neighboring, far- and self-adjacent ICI. . . . . 89

4.11 (Left) Alternative-5. (Right) Alternative-6. In 2-AP case, the average BERs of the  $q$ th subcarrier of AP-2 are plotted w.r.t  $\Delta\varepsilon$ . The two-stage processing is implemented as PT-ICI-W ( $\alpha = 8$ ,  $\beta = 2$ , and  $\frac{G_n}{A_n} = 0$ dB for  $n = 1, 2$ ) + GLMMSE. Other parameters are  $\varepsilon_2 = 0$ ,  $\Delta\varepsilon = \varepsilon_1 - \varepsilon_2 \in [0, 0.5]$ ,  $N_{\text{rx}} = 2$ ,  $\frac{A_2}{\sigma_V^2} = 13$  dB, and  $\frac{A_1}{A_2} = -3$  dB. . . . 95

4.12 (Upper-Left)  $\Delta\varepsilon = 0$ . (Upper-Right)  $\Delta\varepsilon = 0.2$ . (Lower-Left)  $\Delta\varepsilon = 0.3$ . (Lower-Right)  $\Delta\varepsilon = 0.5$ . In 2-AP case, the average BERs of Alternative-6 versus SNR  $\frac{A_2}{\sigma_V^2}$  are plotted. The two-stage processing is implemented as PT-ICI-W ( $\alpha = 8$ ,  $\beta = 2$ , and  $\frac{G_n}{A_n} = 0$  dB for  $n = 1, 2$ ) + GLMMSE. Other parameters are  $\varepsilon_2 = 0$ ,  $\Delta\varepsilon = \varepsilon_1 - \varepsilon_2$ ,  $N_{\text{rx}} = 2$ , and  $\frac{A_1}{A_2} = -3$  dB. . . . . 97

5.1 The serving APs in virtual cell are coordinated by the AN to allocate the same RRU for the green car and enforce cooperative transmissions. The blanks between different RRUs are intended for guard bands or pilots. Due to CFO issue, the ICI from other RRUs will interfere with green car's data receiving from RRU-1. . . . . 100

5.2 Illustration of frequency domain cooperative encoding. . . . . 101



5.3 (a) The constellations  $\mathcal{M}_k$ 's are rotated and scaled by  $\mathbf{h}_{\text{eff},k}$ 's.  $\mathcal{M}_k = \{\pm 1\}$  for  $k = q, q + 1, q + 2$ . The green, red, and blue arrows point the directions of  $\mathbf{h}_{\text{eff},q}$ ,  $\mathbf{h}_{\text{eff},q+1}$ , and  $\mathbf{h}_{\text{eff},q+2}$ . (b) The receiver searches the ML solution from the composite constellation  $\mathcal{M}_{q,\eta}$ . . . . . 102

5.4 APs-1  $\sim N$  respectively use only the  $q$ th  $\sim (q + N - 1)$ th subcarriers to transmit  $\bar{X}_q^z$ . At the receiver, MRC is performed. . . . . 103

5.5 (Left)  $N_{\text{rx}} = 1$ . (Right)  $N_{\text{rx}} = 2$ . The average BER of ideal MRC and encoding scheme are plotted.  $A_1 = A_2$ ,  $\eta = 3$ , and BPSK is adopted. 105

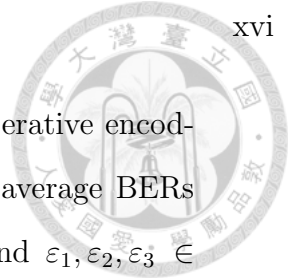
5.6 (Left)  $N_{\text{rx}} = 1$ . (Right)  $N_{\text{rx}} = 2$ . The average BER of ideal MRC and encoding scheme are plotted.  $A_1 = A_2$ ,  $\eta = 3$ , and QPSK is adopted. 106

5.7 (Upper) For asynchronous MRC of 2-AP case, the approximated and simulated values of average BERs are plotted w.r.t  $\Delta\varepsilon = \varepsilon_2 - \varepsilon_1$ . The parameters are  $\frac{A_1}{\sigma_V^2} = \frac{A_2}{\sigma_V^2} = 5$  dB,  $N_{\text{rx}} = 2$ . (Lower) The correlation between  $\mathbf{c}_q(\varepsilon_1)$  and  $\mathbf{c}_{q+1}(\varepsilon_2)$  is plotted w.r.t  $\Delta\varepsilon$ . . . . . 109

5.8 The approximated and simulated values of average BERs are plotted for different CFO orders. The values of CFOs are all different, and  $\varepsilon_1, \varepsilon_2, \varepsilon_3 \in \{-0.3, 0.1, 0.45\}$ , and other parameters are  $N_{\text{rx}} = 1$ ,  $\frac{A_1}{A_2} = 2$  dB,  $\frac{A_3}{A_2} = -3$  dB. . . . . 110

5.9 (Upper) For the cooperative encoding of 2-AP case with  $\eta = 3$ , the simulated values of average BERs are plotted w.r.t  $\Delta\varepsilon = \varepsilon_2 - \varepsilon_1$ . BPSK is adopted, and the parameters are  $\frac{A_1}{\sigma_V^2} = \frac{A_2}{\sigma_V^2} = 5$  dB,  $N_{\text{rx}} = 2$ . (Lower) The correlations respectively between  $\mathbf{c}_q(\varepsilon_1)$  and  $\mathbf{c}_{q+1}(\varepsilon_2)$ ,  $\mathbf{c}_{q+1}(\varepsilon_1)$  and  $\mathbf{c}_{q+2}(\varepsilon_2)$ ,  $\mathbf{c}_{q+2}(\varepsilon_1)$  and  $\mathbf{c}_q(\varepsilon_2)$  are plotted w.r.t  $\Delta\varepsilon$  . . . . . 111





- 5.10 (Left)  $\bar{X}_q^z$ . (Middle)  $\bar{X}_{q+1}^z$ . (Right)  $\bar{X}_{q+2}^z$ . For the cooperative encoding of 3-AP case with  $\eta = 3$ , the simulated values of average BERs are plotted. The values of CFOs are all different, and  $\varepsilon_1, \varepsilon_2, \varepsilon_3 \in \{-0.3, 0.1, 0.45\}$ . BPSK is adopted, and the parameters are  $\frac{A_1}{A_2} = 2$  dB,  $\frac{A_3}{A_2} = -3$  dB,  $N_{\text{rx}} = 1$ . . . . . 112
- 5.11 Illustration of frequency domain cooperative encoding. The scheme in (a) requires proper AP indexing such that  $\varepsilon_1 < \varepsilon_2 < \varepsilon_3$ . The coding schemes in (b) and (c) are robust in the sense that the AN can index APs randomly. . . . . 114
- 5.12 (Upper-Left)  $\bar{X}_q^z$ . (Upper-Right)  $\bar{X}_{q+1}^z$ . (Lower-Left)  $\bar{X}_{q+2}^z$ . (Lower-Right)  $\bar{X}_{q+3}^z$ . For the cooperative encoding of 3-AP case with  $\eta = 4$ , the simulated values of average BERs are plotted. The values of CFOs are all different, and  $\varepsilon_1, \varepsilon_2, \varepsilon_3 \in \{-0.3, 0.1, 0.45\}$ . BPSK is adopted, and the parameters are  $\frac{A_1}{A_2} = 2$  dB,  $\frac{A_3}{A_2} = -3$  dB,  $N_{\text{rx}} = 1$ . . . . . 115
- 5.13 (Left) 2-AP case cooperative encoding with  $\eta = 3$ . (Right) 2-AP case robust encoding with  $\eta = 4$ . the average BERs of different  $\bar{X}_k^z$ 's are collectively evaluated. the CFOs are different with  $\varepsilon_1, \varepsilon_2 \in \{\pm 0.35\}$ . BPSK is adopted, and the parameters are  $A_1 = A_2$ ,  $N_{\text{rx}} = 2$ . . . . . 116
- 5.14 (Left) 3-AP case cooperative encoding with  $\eta = 4$ . (Right) 2-AP case robust encoding with  $\eta = 6$ . the average BERs of different  $\bar{X}_k^z$ 's are collectively evaluated. The values of CFOs are all different, and  $\varepsilon_1, \varepsilon_2, \varepsilon_3 \in \{-0.3, 0.1, 0.45\}$ . BPSK is adopted, and the parameters are  $\frac{A_1}{A_2} = 2$  dB,  $\frac{A_3}{A_2} = -3$  dB,  $N_{\text{rx}} = 1$ . . . . . 117



# List of Tables

1.1	The Maximum absolute value of CFO normalized w.r.t subcarrier spacing for $\pm 20$ ppm oscillator frequency mismatch . . . . .	17
3.1	The reduced-order constellation of 16-QAM and 64-QAM . . . . .	47
4.1	Parameters/Notations . . . . .	75



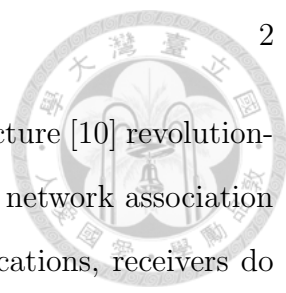
# Chapter 1

## Introduction

5G networks contain three major components [1]: enhanced mobile broadband (eMBB), massive machine-type communication (mMTC), and ultra-reliable low-latency communication (uRLLC). eMBB aims at high data rates, and mMTC accommodates connectivity of massive devices to enable the Internet of Things (IoT); meanwhile uRLLC is expected to support a wide range of new services from industrial automation to augmented reality, which require both low latency and high reliability [2, 3]. Undoubtedly, due to safety concerns, vehicular networking is one of uRLLC applications with the most stringent latency and reliability restriction.

### 1.1 Ultra-Low Latency Vehicular Networking

To widely deploy autonomous vehicles (AVs), the common agreement of target end-to-end networking latency should be at the order of 1 *ms* [4, 5], far below the latency of 100 *ms* in 4G systems. Due to the high mobility of AVs, the required technologies can be even more challenging than Tactile Internet [6]. According to [7–10], such kind of uRLLC can be promisingly realized by introducing fog/edge computing in a heterogeneous network architecture, consisting of low-power access points (APs) to enhance spectrum efficiency and high-power nodes (HPNs) to ensure ubiquitous services. A group of APs are governed by an anchor node (AN) serving fog/edge computing to warrant real-time management and control of AVs.



To greatly curtail latency in radio access, the network architecture [10] revolutionarily utilizes open-loop communications together with proactive network association and anticipatory mobility management. In open-loop communications, receivers do not provide transmitters with CSI and acknowledgment messages for physical layer (PHY) transmissions to forward packets to higher layer as fast as possible [8]. For better reliability, AVs communicate with the AN through multiple APs (multiple paths). In the uplink, each AV proactively associates with appropriate APs to access and proceed transmissions [9] while the grant-free transmissions [11, 12] are carried out. The reliability can be guaranteed given that at least one of the multi-path transmissions succeeds. On the other hand, the AN with fog/edge computing can execute anticipatory mobility management to predict the APs with which each vehicle is going to associate [13]. Consequently, the downlink packets can be sent from the AN to appropriate APs and subsequently relayed to the vehicle in time.

The packet size is typically small in uRLLC [14]. Regarding short-packet transmissions, the achievable capacity has been derived in [15], and [16] gives a review of recent information-theoretic works in communication with short packets. In [17], the blocklength design to minimize the decoding error probability is proposed to support uRLLC-enabled unmanned aerial vehicle (UAV) system. As to the candidate channel coding schemes including polar code, low density parity check (LDPC) code, convolutional code, etc., the comparative investigations can be found in [14, 18, 19].

In traditional wireless networks, each mobile node (a vehicle in our context) is served by one AP or base station (BS) with complicated closed-loop control signaling, and handover is performed when nodes move across the coverage boundaries of APs or BSs. Differently, in the discussed uRLLC vehicular network, each AV is served by multiple APs, which virtually form a large cell, in addition, the conventional time-consuming handover process is greatly simplified through proactive network association and anticipatory mobility management. That is, in this vehicle-

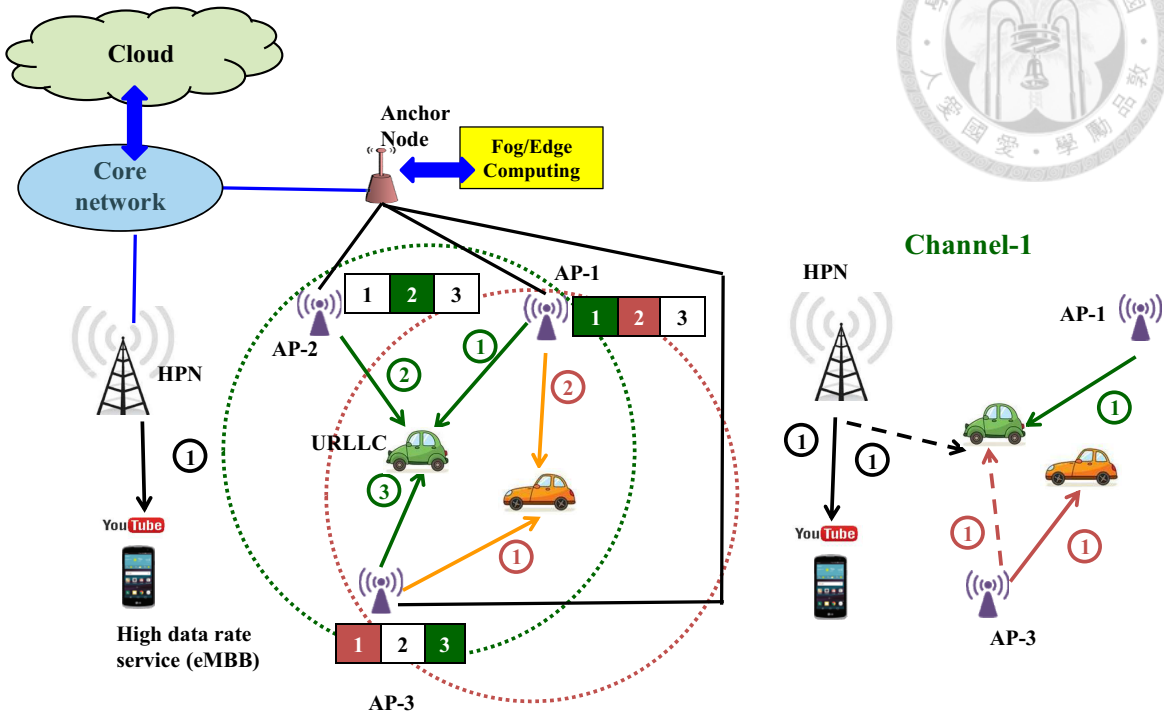
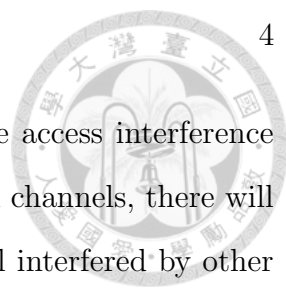


Figure 1.1: (Left) Each vehicle is served by multiple APs to form a virtual cell. Without central optimization of radio resource allocation, each AP may randomly select RRUs to provide downlink services, incurring co-channel interference. Even worse, such interference could also be from a HPN. (Right) Co-channel MAI in channel-1.

centric networking, there is only one AV in each virtual cell, and multiple APs serve this mobile node. Each AP is designated as a network and radio slice [20, 21] to this virtual cell, and simultaneously serves multiple virtual cells using other radio slices. In order to facilitate this concept, APs and subsequently the AN must run network virtualization in software defined networking (SDN) [7].

However, the holistic design of resource management remains technically challenging in uRLLC [22]. Due to the broadcast nature of wireless medium to incur interference, it seems that radio resource allocation should be globally optimized across APs and HPNs, requiring information from AVs and other user equipments (UEs). Nevertheless, the overall processing time for global optimization plus collecting information from different network entities could be too long to satisfy the dynamic vehicle network. To ultimately save overhead and latency, each AP may just randomly se-



lect radio resource units (RRUs) to serve AVs, making multiple access interference (MAI) inevitable. From the receiver's angle, in each of downlink channels, there will be only one AP in the virtual cell to transmit the desired signal interfered by other APs' transmissions. Even worse, such MAI could be also from a HPN, as an inherent challenge in heterogeneous networks [23,24]. For example, in the left part of Fig. 1.1, there are two virtual cells centered at different colored cars. APs-1~3 respectively allocate channels-1~3 to the green car, while these APs and the HPN serve other vehicles/UEs via different RRUs to interfere with the green car's packets receiving in channel-1, as shown in the right part of Fig. 1.1. Although beam-forming [25,26] and interference alignment (IA) [24,27] are known to suppress inter-cell interference, such schemes do not fit open-loop communications due to the need of CSI at transmitters.

## 1.2 Signal Detection Schemes

As just indicated, MAI is hard to manage/suppress from network/transmitter side because the required processing time may violate the latency constraint. Thus MAI is supposed to be handled at the receiver side, and a more sophisticated receiver is desirable. In this section, some well-known detection schemes against MAI are introduced. To enhance receiving performance, the diversity technique shall be adopted. Here we assume spatial diversity by multiple receiving antennas.

Suppose that the vehicle associates with  $N \geq 2$  APs to form a virtual cell. Using multi-path transmissions, the AN sends the packets to the vehicle through the  $N$  APs, which may randomly select radio channels to serve the vehicle. In the worst case, the vehicle receives the packets from different APs and different channels. Like the situation mentioned at Section 1.1 (Fig. 1.1), in each channel, only one AP sends the desired signal, and other APs cause co-channel interference (CCI). Without loss of generality, we look at the channel where AP- $N$  relays the desired data of uRLLC applications from the AN to the AV, and AP-1~AP- $(N - 1)$  are interferers (refer

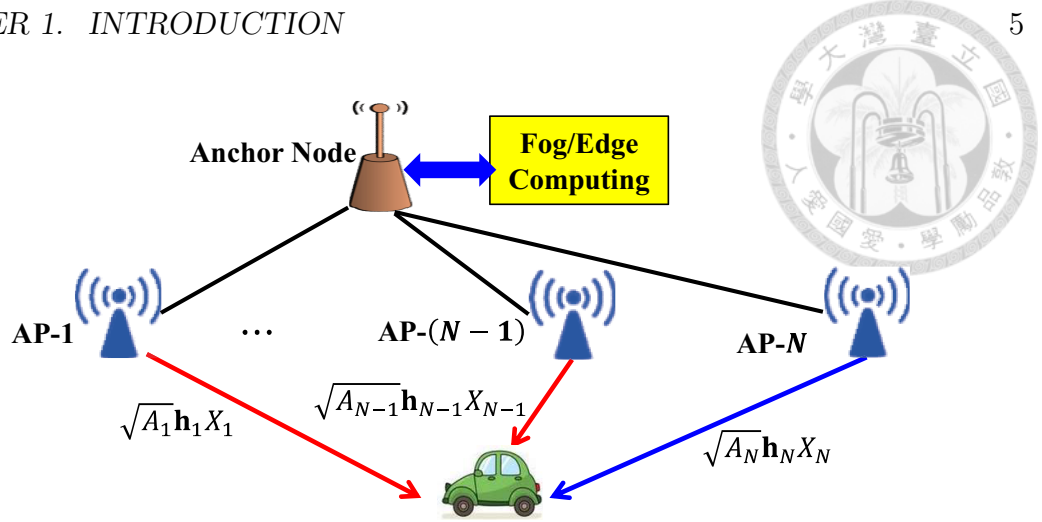


Figure 1.2: Downlink MAI scenario. Without loss of generality, we look at the channel where AP- $N$  relays the desired data of uRLLC applications from the AN to the AV, and AP- $1 \sim$  AP- $(N-1)$  are interferers.

to Fig. 1.2). For  $n = 1, \dots, N$ ,  $X_n$  and  $\mathcal{M}_n$  represent the transmitted symbol and signal constellation of AP- $n$ , and  $E[|X_n|^2] = 1$ . Assume that each AP is equipped with a single antenna, and the vehicle is equipped with  $N_{\text{rx}}$  antennas for  $N_{\text{rx}} \geq N$ , then the received signal  $\mathbf{y}$  is

$$\mathbf{y} = \sum_{n=1}^N \sqrt{A_n} \mathbf{h}_n X_n + \mathbf{v}. \quad (1.1)$$

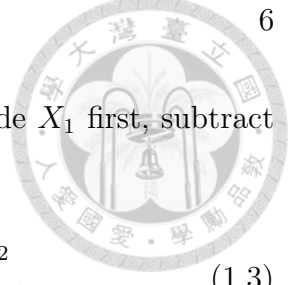
$A_n$  is AP- $n$ 's mean signal power received at the vehicle,  $\mathbf{h}_n = [H_{1n} \dots H_{N_{\text{rx}}n}]^T$  is the fading gain from AP- $n$  to the vehicle, and  $\mathbf{v} = [V_1 \dots V_{N_{\text{rx}}}]^T$  is the white noise at the receiving antennas with  $\mathbf{v} \sim CN(0, \sigma_V^2 \mathbf{I}_{N_{\text{rx}}})$ . Next, we give a brief summary of conventional detection schemes in the following subsections.

### 1.2.1 Single-User Detection

A single-user detection for  $X_N$  treats the interference term  $\sum_{n=1}^{N-1} \sqrt{A_n} \mathbf{h}_n X_n$  in (1.1) as noise, and estimate  $X_N$  according to

$$\hat{X}_N = \arg \min_{x_N \in \mathcal{M}_N} \left\| \mathbf{y} - \sqrt{A_N} \mathbf{h}_N x_N \right\|_2^2. \quad (1.2)$$

The detection works well only when the interfering signals from other APs are much weaker than the desired signal from AP- $N$ . If the interference from some AP, say



AP-1, is stronger than the desired signal, the receiver can decode  $X_1$  first, subtract  $\sqrt{A_1}\mathbf{h}_1\hat{X}_1$  from  $\mathbf{y}$ , and then decode  $X_N$  by

$$\hat{X}_N = \arg \min_{x_N \in \mathcal{M}_N} \left\| \mathbf{y} - \sqrt{A_1}\mathbf{h}_1\hat{X}_1 - \sqrt{A_N}\mathbf{h}_N x_N \right\|_2^2, \quad (1.3)$$

$$\hat{X}_1 = \arg \min_{x_1 \in \mathcal{M}_1} \left\| \mathbf{y} - \sqrt{A_1}\mathbf{h}_1 x_1 \right\|_2^2. \quad (1.4)$$

Without losing generality, we assume that the interference from APs-1~ $K$  is weaker than AP- $N$ 's signal, can be estimated according to the descending signal power order  $A_1 > A_2 > \dots > A_K$  by (1.4) and (1.5).

$$\hat{X}_n = \arg \min_{x_n \in \mathcal{M}_n} \left\| \mathbf{y} - \sum_{g=1}^{n-1} \sqrt{A_g}\mathbf{h}_g\hat{X}_g - \sqrt{A_n}\mathbf{h}_n x_n \right\|_2^2 \quad \text{for } n = 2, \dots, K. \quad (1.5)$$

Then the estimate of  $X_N$  is obtained via

$$\hat{X}_N = \arg \min_{x_N \in \mathcal{M}_N} \left\| \mathbf{y} - \sum_{n=1}^K \sqrt{A_n}\mathbf{h}_n\hat{X}_n - \sqrt{A_N}\mathbf{h}_N x_N \right\|_2^2. \quad (1.6)$$

The method described in (1.4)~(1.6) is called successive interference cancellation (SIC), its effectiveness heavily depends on the significant differences in signal strengths.

## 1.2.2 Multiuser Detection

In MUD, the receiver may adopt individually optimum or jointly optimum strategies [28]. The individually optimum decision is made according to maximum a posterior (MAP) rule given in (1.7) to minimize the error probability  $\Pr \{ \hat{X}_N \neq X_N \}$ .

$$\hat{X}_N = \arg \min_{x_N \in \mathcal{M}_N} \sum_{(x_1, \dots, x_{N-1}) \in \prod_{n=1}^{N-1} \mathcal{M}_n} \Pr \{ X_1 = x_1, \dots, X_N = x_N \} \exp \left( \frac{- \left\| \mathbf{y} - \sum_{n=1}^N \sqrt{A_n}\mathbf{h}_n x_n \right\|_2^2}{\sigma_V^2} \right) \quad (1.7)$$

$$= \arg \min_{x_N \in \mathcal{M}_N} \sum_{(x_1, \dots, x_{N-1}) \in \prod_{n=1}^{N-1} \mathcal{M}_n} \exp \left( \frac{- \left\| \mathbf{y} - \sum_{n=1}^N \sqrt{A_n}\mathbf{h}_n x_n \right\|_2^2}{\sigma_V^2} \right). \quad (1.8)$$



The equality in (1.8) holds when the constellation points  $x_n$  in  $\mathcal{M}_n$  are equiprobable for any  $n$ .

On the other hand, the jointly optimum decisions are the maximum-likelihood (ML) decisions  $(\hat{X}_1, \dots, \hat{X}_N)$  obtained by

$$(\hat{X}_1, \dots, \hat{X}_N) = \arg \min_{(x_1, \dots, x_N) \in \prod_{n=1}^N \mathcal{M}_n} \left\| \mathbf{y} - \sum_{n=1}^N \sqrt{A_n} \mathbf{h}_n x_n \right\|_2^2. \quad (1.9)$$

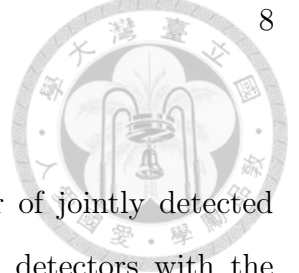
The operation of (1.9) is also called maximum likelihood sequence estimation (MLSE) or ML-MUD.

In (1.8), if the SNR is not extremely low, the sum is dominated by the largest term, the following approximation can be used [29, 30].

$$\begin{aligned} & \sum_{(x_1, \dots, x_{N-1}) \in \prod_{n=1}^{N-1} \mathcal{M}_n} \exp \left( \frac{- \left\| \mathbf{y} - \sum_{n=1}^N \sqrt{A_n} \mathbf{h}_n x_n \right\|_2^2}{\sigma_V^2} \right) \\ & \approx \max_{(x_1, \dots, x_{N-1}) \in \prod_{n=1}^{N-1} \mathcal{M}_n} \exp \left( \frac{- \left\| \mathbf{y} - \sum_{n=1}^N \sqrt{A_n} \mathbf{h}_n x_n \right\|_2^2}{\sigma_V^2} \right), \end{aligned} \quad (1.10)$$

whereby (1.8) is simplified as (1.9), both type of decisions will agree with very high probability [28], and the difference between their performance is small, particularly at high SNR [29].

SIC and MUD require the knowledge of modulation format of interferers and interfering channel gains. The modulation information is usually encoded in the preamble, so it can be decodable at the receiver even though the signals from APs- $1 \sim (N-1)$  are not intended for the vehicle in the discussed scenario (Fig. 1.2), and the channel estimation is made possible by appropriate placement of pilots.



### 1.2.3 ZF/LMMSE Detection

The complexity of MUD grows exponentially with the number of jointly detected symbols  $N$ . In this subsection, we introduce two suboptimal detectors with the complexity that grows linearly with  $N$ , and the method of SIC derived from them.

#### 1) Zero-forcing (ZF) detection

Let  $\mathbf{H}_A = [\sqrt{A_1}\mathbf{h}_1 \cdots \sqrt{A_n}\mathbf{h}_N]$  and  $\mathbf{x} = [X_1 \cdots X_N]^T$ . The received signal  $\mathbf{y}$  in (1.1) is rewritten as

$$\mathbf{y} = \mathbf{H}_A \mathbf{x} + \mathbf{v}. \quad (1.11)$$

Using ZF [31, 32] to entirely eliminate MAI, the received signal is pre-multiplying by the Moore-Penrose pseudo inverse of the channel matrix  $\mathbf{H}_A$ , leading to

$$\tilde{\mathbf{y}} = (\mathbf{H}_A^H \mathbf{H}_A)^{-1} \mathbf{H}_A^H \mathbf{y} = \mathbf{x} + (\mathbf{H}_A^H \mathbf{H}_A)^{-1} \mathbf{H}_A^H \mathbf{v}. \quad (1.12)$$

Denote the  $N$ th component of  $\tilde{\mathbf{y}}$  by  $\tilde{Y}_N$ , the desired data symbol is detected via

$$\hat{X}_N = \arg \min_{X_N \in \mathcal{M}_N} |\tilde{Y}_N - X_N|^2, \quad (1.13)$$

where

$$\tilde{Y}_N = \mathbf{e}_N^H \tilde{\mathbf{y}} = \mathbf{w}_{\text{ZF}}^H \mathbf{y} \quad (1.14)$$

$$\mathbf{w}_{\text{ZF}} = \mathbf{H}_A \mathbf{C}^{-1} \mathbf{e}_N, \quad (1.15)$$

$$\mathbf{C} = \mathbf{H}_A^H \mathbf{H}_A. \quad (1.16)$$

In the above equations,  $\mathbf{e}_N$  is a  $N \times 1$  vector with the  $N$ th entry replaced with one.

#### 2) Linear minimum mean square error (LMMSE) detection

The LMMSE detection [31–33] is to estimate the desired signal by linearly combining the weighted versions of received signals. The weighting vector is derived based

on mean square error minimization (1.17) or SINR maximization (1.18) criterion.

$$\mathbf{w}_{\text{MMSE}} = \arg \min_{\mathbf{w}} \text{E} \left[ |\mathbf{w}^H \mathbf{y} - X_N|^2 \right] = \sqrt{A_N} \mathbf{C}_y^{-1} \mathbf{h}_N, \quad (1.17)$$

$$\mathbf{w}_{\text{MaxSINR}} \arg \max_{\mathbf{w}} \frac{A_N |\mathbf{w}^H \mathbf{h}_N|^2}{\text{E} \left[ \left| \mathbf{w}^H \left( \sum_{n=1}^{N-1} \sqrt{A_n} \mathbf{h}_n X_n + \mathbf{v} \right) \right|^2 \right]} = \sqrt{A_N} \mathbf{C}_I^{-1} \mathbf{h}_N. \quad (1.18)$$

where

$$\mathbf{C}_y = \text{E} [\mathbf{y} \mathbf{y}^H] = \mathbf{C}_I + A_N \mathbf{h}_N \mathbf{h}_N^H, \quad (1.19)$$

$$\mathbf{C}_I = \sum_{n=1}^{N-1} A_n \mathbf{h}_n \mathbf{h}_n^H + \sigma_V^2 \mathbf{I}_{N_{\text{rx}}} \quad (1.20)$$

Using the matrix inversion lemma [28],

$$\begin{aligned} \mathbf{w}_{\text{MMSE}} &= \sqrt{A_N} (\mathbf{C}_I + A_N \mathbf{h}_N \mathbf{h}_N^H)^{-1} \mathbf{h}_N \\ &= \sqrt{A_N} \left( \mathbf{C}_I^{-1} - \frac{\mathbf{C}_I^{-1} \mathbf{h}_N \mathbf{h}_N^H \mathbf{C}_I^{-1}}{A_N^{-1} + \mathbf{h}_N^H \mathbf{C}_I^{-1} \mathbf{h}_N} \right) \mathbf{h}_N \\ &= \sqrt{A_N} \left( \mathbf{C}_I^{-1} \mathbf{h}_N - \frac{\mathbf{C}_I^{-1} \mathbf{h}_N \mathbf{h}_N^H \mathbf{C}_I^{-1} \mathbf{h}_N}{A_N^{-1} + \mathbf{h}_N^H \mathbf{C}_I^{-1} \mathbf{h}_N} \right) \\ &= \sqrt{A_N} \left( \frac{A_N^{-1}}{A_N^{-1} + \mathbf{h}_N^H \mathbf{C}_I^{-1} \mathbf{h}_N} \right) \mathbf{C}_I^{-1} \mathbf{h}_N \\ &= \left( \frac{A_N^{-1}}{A_N^{-1} + \mathbf{h}_N^H \mathbf{C}_I^{-1} \mathbf{h}_N} \right) \mathbf{w}_{\text{MaxSINR}}, \end{aligned} \quad (1.21)$$

which shows that  $\mathbf{w}_{\text{MMSE}}$  and  $\mathbf{w}_{\text{MaxSINR}}$  are proportional to each other. Since multiplicative constants in weighting vectors do not change the resultant SINR, the two criteria are equivalent. Thus, the LMMSE detection is to execute

$$\hat{X}_N = \arg \min_{x_N \in \mathcal{M}_N} \left| \mathbf{w}_{\text{MMSE}}^H \left( \mathbf{y} - \sqrt{A_N} \mathbf{h}_N x_N \right) \right|^2. \quad (1.22)$$

### 3) LMMSE/ZF-Successive interference cancellation (LMMSE/ZF-SIC)

The receiver applies successive interference cancellation to recover the streams (interfering signals or desired signals) one by one. At each step, the receiver estimates one stream according ZF or LMMSE detection, then subtracts the estimated component from the received signal. For example, after  $\ell$  steps, the received signal is

$$\hat{\mathbf{y}}_\ell = \mathbf{y} - \sum_{s=1}^{\ell} \sqrt{A_{n_s}} \mathbf{h}_{n_s} \hat{X}_{n_s}, \quad (1.23)$$

where  $n_s$  is the index of cancelled signal at the  $s$ th step. In other words, this type of detector tries to generate an identical copy of MAI by ZF/LMMSE-estimate of  $X_n$ 's from interfering APs and cancel the associated interference successively until the desired symbol is detected.

### 1.2.4 Projection Receiver

Multuser projection receiver (PR) [35, 36] partially eliminates MAI, then jointly detects the remaining interference and desired signal in the following manner.

$$\left(\hat{X}_{K+1}, \dots, \hat{X}_N\right) = \arg \min_{(x_{K+1}, \dots, x_N) \in \prod_{n=K+1}^N \mathcal{M}_n} \left\| \mathbf{P} \left( \mathbf{y} - \sum_{n=K+1}^N \sqrt{A_n} \mathbf{h}_n x_n \right) \right\|_2^2, \quad (1.24)$$

where

$$\mathbf{P} = \mathbf{I}_{N_{\text{rx}}} - \mathbf{H}_I (\mathbf{H}_I^H \mathbf{H}_I)^{-1} \mathbf{H}_I^H, \quad (1.25)$$

$$\mathbf{H}_I = \left[ \sqrt{A_1} \mathbf{h}_1 \cdots \sqrt{A_K} \mathbf{h}_K \right]. \quad (1.26)$$

The operation of (1.24) means that the receiver jointly decodes  $X_{K+1}, \dots, X_N$  after cancelling the interfering signals from APs-1  $\sim K$ .

When  $K = N - 1$  in (1.26), we have

$$\mathbf{w}_{\text{ZF}} = \left[ \mathbf{H}_I \quad \sqrt{A_N} \mathbf{h}_N \right] \mathbf{C}^{-1} \mathbf{e}_N = \left[ \mathbf{H}_I \quad \sqrt{A_N} \mathbf{h}_N \right] \left[ (\mathbf{C}^{-1})_{1N} \cdots (\mathbf{C}^{-1})_{NN} \right]^T, \quad (1.27)$$

$$\mathbf{H}_I = \left[ \sqrt{A_1} \mathbf{h}_1 \cdots \sqrt{A_K} \mathbf{h}_{N-1} \right], \quad (1.28)$$

$$\mathbf{C} = \mathbf{H}_A^H \mathbf{H}_A = \begin{bmatrix} \mathbf{H}_I^H \mathbf{H}_I & \sqrt{A_N} \mathbf{H}_I^H \mathbf{h}_N \\ \sqrt{A_N} \mathbf{h}_N^H \mathbf{H}_I & A_N \mathbf{h}_N^H \mathbf{h}_N \end{bmatrix}. \quad (1.29)$$

By the block-wise matrix inversion formula [34],

$$\left[ (\mathbf{C}^{-1})_{1N} \cdots (\mathbf{C}^{-1})_{(N-1)N} \right]^T = -\sqrt{A_N} (\mathbf{H}_I^H \mathbf{H}_I)^{-1} \mathbf{H}_I^H \mathbf{h}_N (\mathbf{C}^{-1})_{NN}. \quad (1.30)$$

Substituting (1.30) into (1.27) leads to

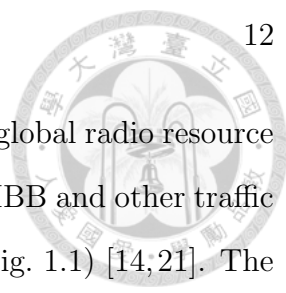
$$\mathbf{w}_{\text{ZF}} = (\mathbf{C}^{-1})_{NN} \left( \mathbf{I}_{N_{\text{rx}}} - \mathbf{H}_I (\mathbf{H}_I^H \mathbf{H}_I)^{-1} \mathbf{H}_I^H \right) \left( \sqrt{A_N} \mathbf{h}_N \right). \quad (1.31)$$

From (1.31) and (1.25), ZF equalizer can be deemed as a special case of PR.

### 1.3 Joint Detection to Address Interference in the Virtual Cell: Feasibility and Possible Issues

Please recall that ultra-low latency is achieved mainly by system architecture innovation, networking protocols simplification, etc. As a matter of fact, the significant gain in end-to-end networking latency does not come from signal detection in PHY; however, proactive and open-loop communication contributes such latency deduction but also creates a new technology challenge to reliably detect and demodulate signals [10]. In other words, the concern “how to receive the low-latency data transmissions reliably?” naturally arises in this innovative cross-layer system design, where we adopt MUD to achieve the best possible BER performance that is closely related to “reliability”.

MUD, the joint detection of multiple simultaneous transmissions, has been long investigated in code division multiple access (CDMA) [28, 30] and multiple-input multiple-output (MIMO) communications [32]. In CDMA, ML-MUD can effectively overcome the near-far problem [37], in which a near user causes excess interference to a far user. But the detection complexity grows exponentially as the number of involved users increases, as a major obstacle to practical implementation. Likewise, MIMO receivers suffer from high detection complexity for high-order modulation. However, in our scenario, the number of neighboring APs is limited. In addition, high-order modulation might not be necessary since the ultimate goal of our system design is to achieve ultra-low latency rather than pursuing high data rate [14]. In other words, we care about uRLLC traffic instead of eMBB traffic in this research. High instantaneous data rate does not necessarily imply good uRLLC throughput if the time for running networking protocols is considered. A great amount of latency can be saved in layer-1 and layer-2 via proactive open-loop communications, the average throughput can possibly meet the requirement of uRLLC by low-order modulation, say BPSK or QPSK.



Unfortunately, owing to lacking sufficient processing time for global radio resource allocation, some high-order modulated signals generated from eMBB and other traffic can still interfere with uRLLC in the PHY of air interface (see Fig. 1.1) [14;21]. The threat from MAI particularly of high-order modulation is twofold: degrading BER performance more and increasing detection complexity. By ML-MUD, it is possible to approach the ideal detection performance as if no interferer was present, but the BER is very sensitive to the modulation schemes of interferers. It is well-known that ML-MUD in CDMA and general multiuser communication scenarios is “asymptotically” near-far resistant and thus insensitive to interference power [37]. Nonetheless, in our context that is not possible to enjoy the asymptotic behavior, ML-MUD is found still suffering from the sensitivity to the modulations of interfering signals that is seldom discussed in the traditional MUD literatures. Interferers using high-order modulations obviously further deteriorate the joint detection especially for comparable received power of desired signal and interference at the receiver. Luckily, we discover that such sensitivity can be easily relieved by multi-antenna technique [38, 39].

When the interfering signal with high-order modulation has weaker received power than the desired signal (due to path loss and/or shadowing), the receiver may just ignore it, but the BER will be poor if the interference is not weaker enough. ML-MUD suffers from high-complexity concern, and ignoring the interference may lead to bad performance. This dilemma suggests something in-between. Different from typical uplink MUD, the purpose of downlink MUD is to counter MAI, not to correctly decode all the received signals from designated transmitter and interferers. Instead of disregarding interference, we exploit this downlink distinction to propose a unique realization of MUD, R-ML-MUD, treating high-order modulated interfering signal as being lower-order modulated (which is equivalent to partially ignoring weak interference), whereby the ML solution space shrinks substantially [38, 40]. The resulting BER can be acceptable even when LMMSE does not ideally function. Although the

complexity still grows exponentially with the increased number of interfering sources, R-ML-MUD can practically lower the computation load down to a reasonable level because of the limited number of neighboring APs, particularly if smart arrangement of RRUs in use.

To entirely avoid the high complexity of ML-MUD, using ZF/LMMSE to cancel all the interference is common, but leads to diversity loss [31,41]. Conventional projection receiver (PR) [35,36] to cancel just a portion of interference serves a compromise between complexity and performance. The received signal is projected towards the orthogonal complement of subspace spanned by some portion of interfering signals, which can be totally removed. Nonetheless, the energy of desired signal could be lost a lot after projection. Towards mitigating the drawback, we propose a generalization of LMMSE (GLMMSE) [38] as a new type of projection detection structure to find a subspace where there is some residue of suppressed interference after projection, but more amount of energy will be retained in the desired signal. Compared to the conventional PR, GLMMSE has noticeable SNR gain for multiple weaker interfering signals being suppressed.

## 1.4 OFDMA-Based Virtual Cell Networks

Our research is conducted based on Orthogonal Frequency Division Multiple Access (OFDMA), which has been widely used in many applications such as wireless local area Networks (WLAN), *The Third Generation Partnership Project Long-Term-Evolution (3GPP-LTE)*. In OFDMA-based virtual cell networks, the scenario in Fig. 1.1 can be depicted as Fig. 1.3, where each AP allocates a RRU composed of several resource elements (REs) for the served vehicle, and each RE is 1 subcarrier  $\times$  1 OFDM symbol. In this section, we introduce the signal model of OFDM [42,43], and account for the challenge in asynchronous downlink.

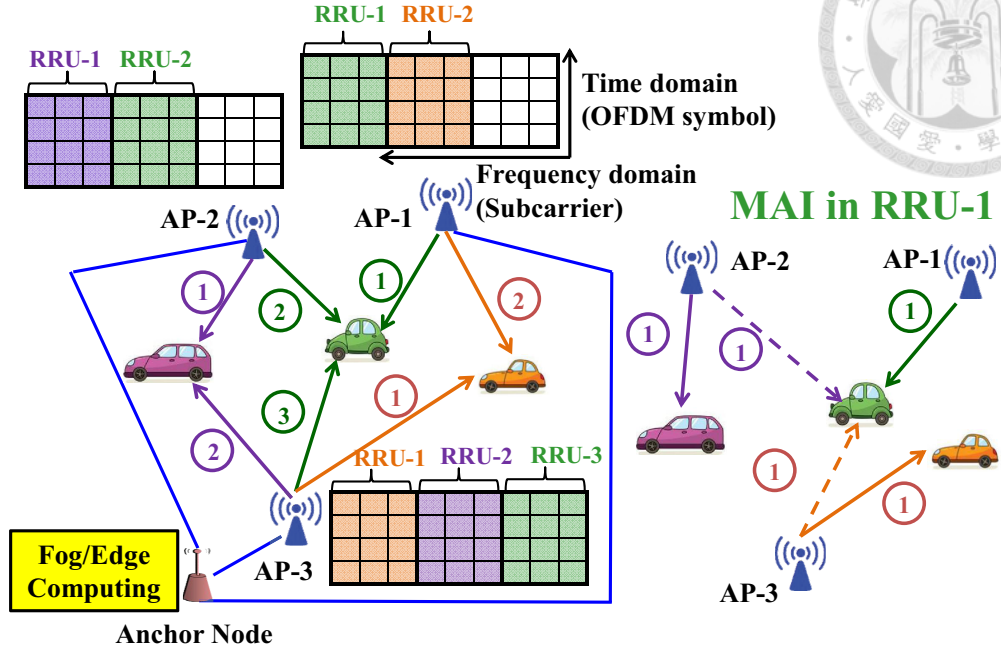


Figure 1.3: (Left) Each AP in the virtual cell allocates a RRU to serve a vehicle. (Right) Co-channel MAI in RRU-1.

### 1.4.1 Signal Model in Perfect Synchronization

The discrete time-domain transmitted signal from AP- $n$  during the  $z$ th OFDM symbol duration is

$$x_{n,\ell}^z = \frac{1}{N_{\text{fft}}} \sum_{k=0}^{N_{\text{fft}}-1} X_{n,k}^z e^{\frac{j2\pi k(\ell - N_{\text{cp}} - (z-1)(N_{\text{fft}} + N_{\text{cp}}))}{N_{\text{fft}}}}, \quad (z-1)(N_{\text{fft}} + N_{\text{cp}}) \leq \ell \leq z(N_{\text{fft}} + N_{\text{cp}}), \quad (1.32)$$

where  $\ell$  is the sample index of time-domain signal,  $X_{n,k}^z$  is the  $k$ th subcarrier data symbol of AP- $n$ ,  $N_{\text{fft}}$  and  $N_{\text{cp}}$  are the size of fast Fourier transform (FFT) and cyclic prefix (CP) length. CP is a copy of the last  $N_{\text{cp}}$  samples appended in front of each OFDM symbol. The channel impulse response (CIR) between AP- $n$  and the vehicle's  $m$ th antenna is denoted by  $h_{n,\tau}^m$ , which is assumed to be time-invariant over several OFDM symbol periods in uRLLC, where the latency requirement is typically shorter than the channel coherence time [22, 44]. In addition, the CIR length  $N_{\text{ch}}$  is smaller than CP length, i.e.  $N_{\text{ch}} < N_{\text{cp}}$ .

The signals from different APs reach the vehicle with different propagation delays,



and  $\Delta t_n$  represents the discrete timing offset from AP- $n$ 's signal relative to the first arriving signal from some AP, say AP-1. For any  $n$ , suppose that  $N_{\text{ch}} < N_{\text{cp}} - \Delta t_n$  and the receiver's FFT window is precisely aligned with AP-1's OFDM symbols, as shown in Fig. 1.4(a). At the  $q$ th FFT output, AP- $n$ 's signal received at the vehicle's  $m$ th antenna is

$$\begin{aligned}
Y_{z,n,q}^m &= \sum_{\ell=0}^{N_{\text{fft}}-1} \left[ \sum_{\tau=0}^{N_{\text{ch}}-1} h_{n,\tau}^m x_{n,\ell-\tau-\Delta t_n}^z \right] e^{-\frac{j2\pi q\ell}{N_{\text{fft}}}} \\
&= \sum_{\ell=0}^{N_{\text{fft}}-1} \left[ \sum_{\tau=0}^{N_{\text{ch}}-1} h_{n,\tau}^m \left( \frac{1}{N_{\text{fft}}} \sum_{k=0}^{N_{\text{fft}}-1} X_{n,k}^z e^{\frac{j2\pi k(\ell-\tau-\Delta t_n)}{N_{\text{fft}}}} \right) \right] e^{-\frac{j2\pi q\ell}{N_{\text{fft}}}} \\
&= \sum_{k=0}^{N_{\text{fft}}-1} \left[ X_{n,k}^z e^{-\frac{j2\pi k\Delta t_n}{N_{\text{fft}}}} \left( \sum_{\tau=0}^{N_{\text{ch}}-1} h_{n,\tau}^m e^{-\frac{j2\pi k\tau}{N_{\text{fft}}}} \right) \frac{1}{N_{\text{fft}}} \sum_{\ell=0}^{N_{\text{fft}}-1} e^{\frac{j2\pi(k-q)\ell}{N_{\text{fft}}}} \right] \\
&= \sum_{k=0}^{N_{\text{fft}}-1} H_{n,k}^m X_{n,k}^z \left( \frac{1}{N_{\text{fft}}} \sum_{\ell=0}^{N_{\text{fft}}-1} e^{\frac{j2\pi(k-q)\ell}{N_{\text{fft}}}} \right) = H_{n,q}^m X_{n,q}^z, \tag{1.33}
\end{aligned}$$

where

$$H_{n,k}^m = e^{-\frac{j2\pi k\Delta t_n}{N_{\text{fft}}}} \sum_{\tau=0}^{N_{\text{ch}}-1} h_{n,\tau}^m e^{-\frac{j2\pi k\tau}{N_{\text{fft}}}}. \tag{1.34}$$

Taking the mean received signal power  $A_n$  into account, the  $q$ th FFT outputs across different receiving antennas can be expressed as

$$\mathbf{y}_{z,q} = \sum_{n=1}^N \sqrt{A_n} \mathbf{h}_{n,q} X_{n,q}^z + \mathbf{v}_q, \tag{1.35}$$

where  $\mathbf{h}_{n,q} = [H_{n,q}^1 \cdots H_{n,q}^{N_{\text{rx}}}]^T$  and  $\mathbf{v}_q$  is the noise term. Without loss of generality, we can consider only one OFDM symbol and one FFT output. Dropping the indices  $z, q$  in (1.35) and letting  $H_{n,q}^m = H_{mn}$ , we obtain the signal model in (1.1).

However, if the time differences of arrival (TDOA) is not small enough such that  $N_{\text{ch}} \geq N_{\text{cp}} - \Delta t_n$  (see Fig. 1.4(b)) to cause inter-symbol interference (ISI) and inter-carrier interference (ICI) [45], the signal model of (1.33) and (1.35) will not be applicable. Whether such propagation delay-induced ISI/ICI occurs depends on the virtual cell size (the number of serving AP in a virtual cell), AP density, and the CP length. Using the well-known stochastic geometry modeling [46], we conduct a probabilistic

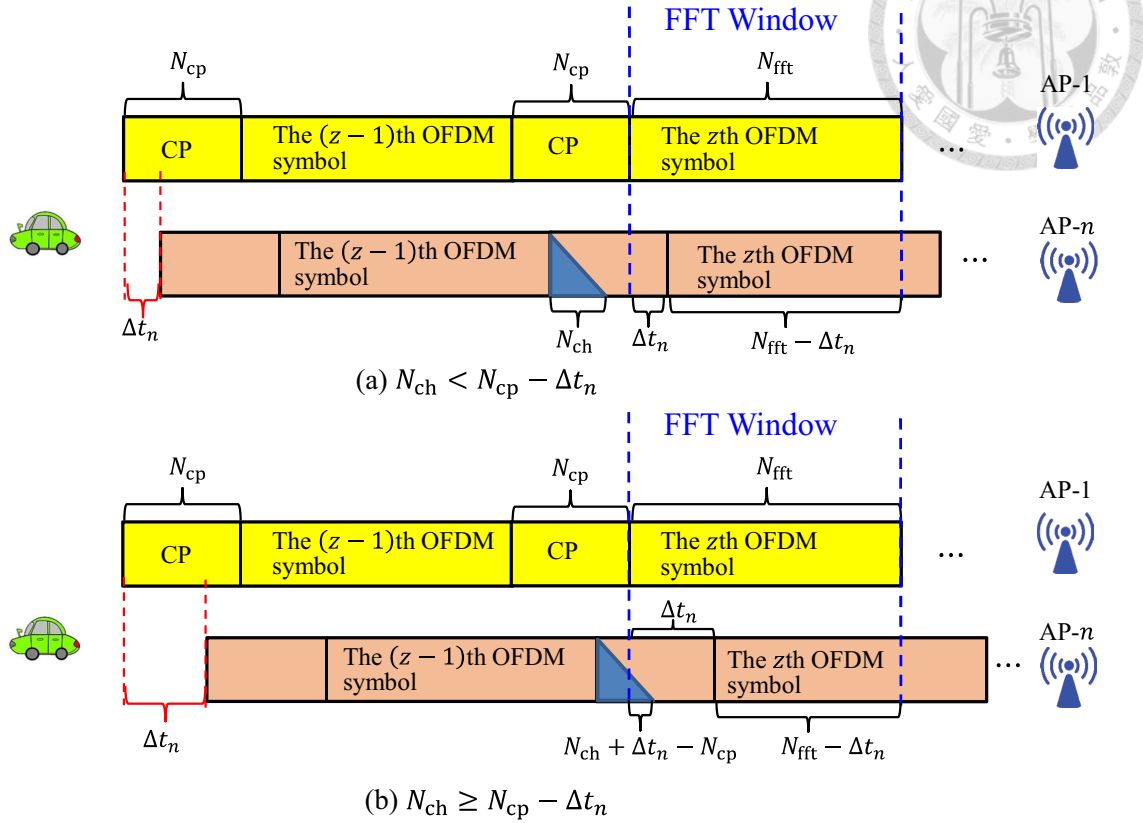


Figure 1.4: The signals from different APs reach the vehicle with various delays, and  $\Delta t_n$  represents the discrete timing offset for AP- $n$ 's signal relative to the first-arriving signal from some AP, say AP-1. (a) If  $N_{ch} < N_{cp} - \Delta t_n$ , there is no ISI. (b) If  $N_{ch} \geq N_{cp} - \Delta t_n$ , ISI and ICI occur.

analysis in Section 4.1.1, showing that the occurrence probability of TDOA-related ISI/ICI can be little in small cell deployment if the CP length and the size of virtual cell are properly designed.

### 1.4.2 CFO-Induced ICI

Refer to Fig. 1.4(a) and consider carrier frequency offset (CFO) resulting from oscillator mismatch to incur ICI. Let  $\varepsilon_n$  stand for the normalized CFO (w.r.t the subcarrier spacing) between the vehicle and AP- $n$ . If the oscillator precision tolerance is specified to be less than  $\pm 20$  ppm, the CFO ranges between  $-40$  ppm and  $+40$  ppm. For different subcarrier spacings and carrier frequencies, the maximum absolute values of normalized CFO  $|\varepsilon_n|$  are listed in Table 1.1. ICI is caused by the fractional part of

Table 1.1: The Maximum absolute value of CFO normalized w.r.t subcarrier spacing for  $\pm 20$  ppm oscillator frequency mismatch

Sucarrier spacing	15 kHz	30 kHz	60 kHz	120 kHz
Carrier frequency 1.9 GHz	5.0667	2.5333	1.2667	0.6333
Carrier frequency 2.4 GHz	6.4	3.2	1.6	0.8
Carrier frequency 5.9 GHz	15.7333	7.8667	3.9333	1.9667

CFO, thus we simply assume that  $|\varepsilon_n| \leq 0.5$ , and derive the expression of  $Y_{z,n,q}^m$  in the following.

$$\begin{aligned}
Y_{z,n,q}^m &= \sqrt{A_n} \sum_{\ell=0}^{N_{\text{fft}}-1} \left[ \left( \sum_{\tau=0}^{N_{\text{ch}}-1} h_{n,\tau}^m x_{n,\ell-\tau-\Delta t_n}^z \right) e^{\frac{j2\pi\varepsilon_n[(z-1)(N_{\text{fft}}+N_{\text{cp}})+N_{\text{cp}}+\ell]}{N_{\text{fft}}}} \right] e^{-\frac{j2\pi q\ell}{N_{\text{fft}}}} \\
&= e^{j((z-1)\phi_n+\rho_n)} \sqrt{A_n} \sum_{\ell=0}^{N_{\text{fft}}-1} \left[ \sum_{\tau=0}^{N_{\text{ch}}-1} h_{n,\tau}^m \left( \frac{1}{N_{\text{fft}}} \sum_{k=0}^{N_{\text{fft}}-1} X_{n,k}^z e^{\frac{j2\pi k(\ell-\tau-\Delta t_n)}{N_{\text{fft}}}} \right) e^{\frac{j2\pi\varepsilon_n\ell}{N_{\text{fft}}}} \right] e^{-\frac{j2\pi q\ell}{N_{\text{fft}}}} \\
&= e^{j((z-1)\phi_n+\rho_n)} \sqrt{A_n} \sum_{k=0}^{N_{\text{fft}}-1} \left[ X_{n,k}^z e^{-j\gamma_{n,k}} \left( \sum_{\tau=0}^{N_{\text{ch}}-1} h_{n,\tau}^m e^{-\frac{j2\pi k\tau}{N_{\text{fft}}}} \right) \frac{1}{N_{\text{fft}}} \sum_{\ell=0}^{N_{\text{fft}}-1} e^{\frac{j2\pi(k-q+\varepsilon_n)\ell}{N_{\text{fft}}}} \right] \\
&= e^{j(z-1)\phi_n} \sum_{k=0}^{N_{\text{fft}}-1} \sqrt{A_n} H_{n,k}^m X_{n,k}^z \left( \frac{1}{N_{\text{fft}}} \sum_{\ell=0}^{N_{\text{fft}}-1} e^{\frac{j2\pi(k-q+\varepsilon_n)\ell}{N_{\text{fft}}}} \right) \quad (1.36) \\
&= e^{j(z-1)\phi_n} e^{\frac{j\pi\varepsilon_n(N_{\text{fft}}-1)}{N_{\text{fft}}}} \frac{\sin(\pi\varepsilon_n)}{N_{\text{fft}} \sin\left(\frac{\pi\varepsilon_n}{N_{\text{fft}}}\right)} \sqrt{A_n} H_{n,q}^m X_{n,q}^z
\end{aligned}$$

$$+ e^{j(z-1)\phi_n} \sum_{k \neq q} e^{\frac{j\pi(k-q+\varepsilon_n)(N_{\text{fft}}-1)}{N_{\text{fft}}}} \frac{\sin(\pi(k-q+\varepsilon_n))}{N_{\text{fft}} \sin\left(\frac{\pi(k-q+\varepsilon_n)}{N_{\text{fft}}}\right)} \sqrt{A_n} H_{n,k}^m X_{n,k}^z \quad (1.37)$$

with  $\phi_n = \frac{2\pi(N_{\text{fft}}+N_{\text{cp}})\varepsilon_n}{N_{\text{fft}}}$ ,  $\rho_n = \frac{2\pi N_{\text{cp}}\varepsilon_n}{N_{\text{fft}}}$ ,  $\gamma_{n,k} = \frac{2\pi k\Delta t_n}{N_{\text{fft}}}$ , and

$$H_{n,k}^m = e^{j(\rho_n-\gamma_{n,k})} \sum_{\tau=0}^{N_{\text{ch}}-1} h_{n,\tau}^m e^{-\frac{j2\pi k\tau}{N_{\text{fft}}}}.$$

The second term of (1.37) denotes the ICI, namely the signals from other subcarriers. From the first term of (1.37), we also see that another effect of CFO is to cause attenuation in magnitude, phase shift of the signal conveyed by the  $q$ th subcarrier.

Define the CFO matrix as

$$\mathbf{C}(\varepsilon_n) = \mathbf{F}\mathbf{D}(\varepsilon_n)\mathbf{F}^H \quad (1.38)$$

where  $\mathbf{D}(\varepsilon_n) = \text{diag}\left(1, e^{j\frac{2\pi}{N_{\text{fft}}}\varepsilon_n}, \dots, e^{j\frac{2\pi}{N_{\text{fft}}}(N_{\text{fft}}-1)\varepsilon_n}\right)$ , and  $\mathbf{F}$  is the  $N_{\text{fft}} \times N_{\text{fft}}$  unitary DFT matrix with  $(\mathbf{F})_{ql} = \frac{1}{\sqrt{N_{\text{fft}}}} e^{-j\frac{2\pi ql}{N_{\text{fft}}}}$ . For the matrices  $\mathbf{C}(\varepsilon_n)$ ,  $\mathbf{F}$ , and  $\mathbf{D}(\varepsilon_n)$ , the row/column/entry indices begin with zero. The  $(q, k)$  entry of  $\mathbf{C}(\varepsilon_n)$  is

$$\begin{aligned} (\mathbf{C}(\varepsilon_n))_{qk} &= \sum_{s=0}^{N_{\text{fft}}-1} (\mathbf{F})_{qs} [\mathbf{D}(\varepsilon_n) \mathbf{F}^H]_{sk} = \sum_{s=0}^{N_{\text{fft}}-1} (\mathbf{F})_{qs} \sum_{l=0}^{N_{\text{fft}}-1} (\mathbf{D}(\varepsilon_n))_{sl} (\mathbf{F}^H)_{lk} \\ &= \frac{1}{N_{\text{fft}}} \sum_{s=0}^{N_{\text{fft}}-1} e^{-j\frac{2\pi qs}{N_{\text{fft}}}} e^{j\frac{2\pi \varepsilon_n s}{N_{\text{fft}}}} e^{j\frac{2\pi ks}{N_{\text{fft}}}} = \frac{1}{N_{\text{fft}}} \sum_{\ell=0}^{N_{\text{fft}}-1} e^{j\frac{2\pi(k-q+\varepsilon_n)\ell}{N_{\text{fft}}}}. \end{aligned} \quad (1.39)$$

By (1.36) and (1.39), AP- $n$ 's frequency-domain signal received from the vehicle's  $m$ th antenna can be expressed as

$$[Y_{z,n,0}^m \cdots Y_{z,n,N_{\text{fft}}-1}^m]^T = e^{j(z-1)\phi_n} \sum_{k=0}^{N_{\text{fft}}-1} \sqrt{A_n} H_{n,k}^m X_{n,k}^z \mathbf{c}_k(\varepsilon_n). \quad (1.40)$$

In (1.40),  $\mathbf{c}_k(\varepsilon_n)$  is the  $k$ th column of  $\mathbf{C}(\varepsilon_n)$ , which is also known as the signature waveform of AP- $n$ 's  $k$ th subcarrier. Therefore, the overall frequency-domain received signal can be written as

$$\mathbf{y}_{z,\mathbf{F}}^m = \sum_{n=1}^N \sum_{k=0}^{N_{\text{fft}}-1} e^{j(z-1)\phi_n} \sqrt{A_n} H_{n,k}^m X_{n,k}^z \mathbf{c}_k(\varepsilon_n) + \mathbf{v}_{z,\mathbf{F}}^m. \quad (1.41)$$

Here  $\mathbf{v}_{z,\mathbf{F}}^m$  is the noise term.

### 1.4.3 Challenges in Asynchronous Downlink

Go back to Fig. 1.3, and let  $q$  denote the index of subcarrier on which the desired data is transmitted from AP-1 to the green car. If synchronization is ideally achieved, at the  $q$ th output of receiver's FFT module, only the signals from different APs'  $q$ th subcarriers are superimposed without any interference from other subcarriers. The receiver only needs to deal with co-channel interference (CCI) by performing MUD or other interference cancellation schemes individually on each subcarrier.

Unfortunately, ICI rising from CFO makes the downlink MAI in Fig. 1.3 more disastrous, as portrayed in Fig. 1.5, where we depict the superimposition of CCI and ICI on the desired signal at the receiver's  $q$ th FFT output. Different APs have different

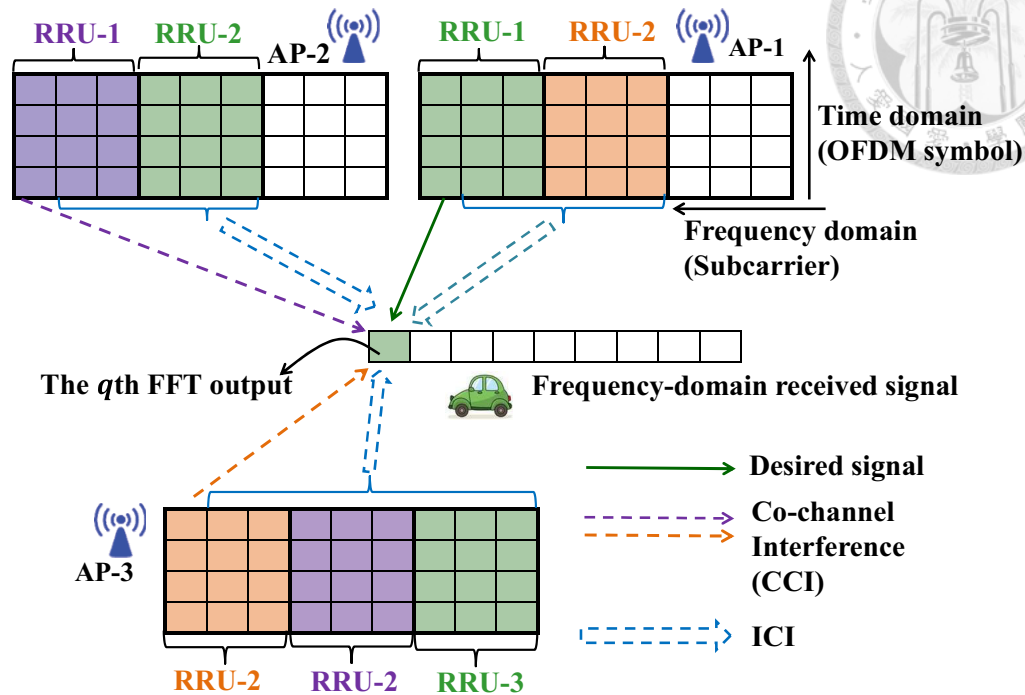
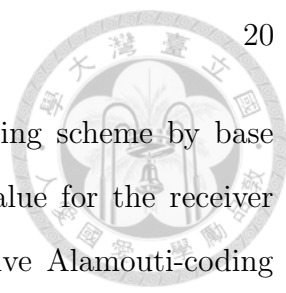


Figure 1.5: CFOs cause ICI. At the receiver's  $q$ th FFT output, the desired data symbol from the  $q$ th subcarrier of AP-1 are coupled with the signals from all the subcarriers of APs-1~3.

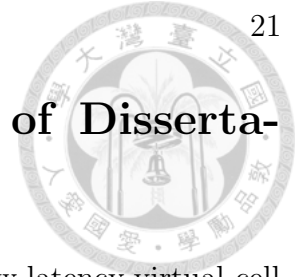
oscillators, resulting in various CFOs that may not be simultaneously compensable at the vehicle even though their estimates are available by the schemes in [47–49] and the references therein. Resolving this issue at transmitter sides, i.e. APs might be infeasible because each AP probably belongs to multiple virtual cells, it is hard to find a frequency offset value to pre-compensate that is universally suitable for all vehicles in service.

Multi-CFO problem inherently exists in OFDMA uplink [50–55] and cooperative communications [45, 56–61] with a brief summary of recent works given in the following. Reference [51] formulates a tri-linear signal model, whereby a subspace nulling approach is invented to address CFO-induced MAI in uplink MIMO-OFDM systems. For massive MIMO uplink, [54] proposes an angle-domain adaptive filtering scheme, in which the beamformers for each user are constructed to enable separate CFO estimation and data detection. In a downlink coordinated multi-point (CoMP) trans-



mission scenario, [56] proposes a frequency-domain data-encoding scheme by base stations (BSs), and derive a suboptimal CFO compensation value for the receiver to improve SINR. In a relay network, [58] designs a cooperative Alamouti-coding scheme, which nearly achieves full diversity under the consideration of oscillator frequency offsets and Doppler shifts. In spatial modulation OFDM system with multiple CFOs, a symbol-by-symbol-aided iterative detector and a LMMSE-based detector are developed in [62] and [63].

In terms of BER, the optimal countermeasure against ICI is to jointly detect the signals on all the subcarriers, but the complexity will be extremely high, not practical to implement. A reasonable compromise for the detection should include only the dominant ICI terms that are the signals on several nearest neighboring subcarriers from the one conveying the desired data. However, there will be an irreducible error floor incurred by the far (or residual) ICI, which is supposed to be whitened before signal detection to improve the performance [64]. Like general LMMSE equalization schemes [45, 55, 57, 59–61, 63], ICI-Whitening (ICI-W) must rely on the knowledge of ICI covariance matrix whose estimate is based on the channel conditions of the subcarriers, from which the residual ICI originates. In proactive uplink, it is normal for the receiver to perform channel estimation on all the subcarriers, the whitening scheme is practical. Nonetheless, in proactive open-loop downlink communications, it may be unreasonable and very difficult to estimate channel gains on all the subcarriers that do not belong to the radio slices allocated for the receiver, making ICI-W infeasible. Such a problem unique to downlink receiver implementation about network/resource slicing remains unknown in the existing literatures.



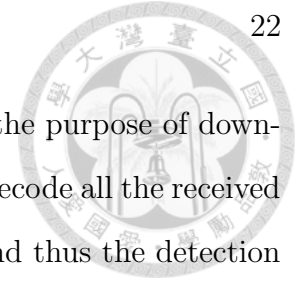
## 1.5 Organization and Contributions of Dissertation

Our objective is to investigate the transceiver design for ultra-low latency virtual-cell network, and the research is conducted in the following steps:

- 1) Starting with the perfect synchronization assumption (i.e. no ISI/ICI), where the serving APs allocate the RRUs randomly, and the vehicle decodes the desired data from different paths (APs) separately (refer to Fig. 1.1 and Fig. 1.2), we look at how high-order modulated interference affects MUD performance, which is relevant to the coexistence of uRLLC and eMBB services. Two methods of lowering the MUD complexity in this scenario are also proposed.
- 2) After that, a more complicated situation with multi-CFO problem (Fig. 1.5) is considered. We investigate how to practically address ICI and perform MUD in downlink.
- 3) Finally, we discuss the design of APs' cooperative transmissions that is made possible by the AN's coordination, and the multi-CFO problem is still taken into consideration.

The organization and contributions of this dissertation are sketched below (and also summarized in Fig. 1.6).

- Chapter 2: The modulation sensitivity problem of MUD is analyzed under the scenario of Fig. 1.2. We discover that the BER performance of ML-MUD is very sensitive to the modulations of interfering signals, and such sensitivity can be lessened by increasing antennas of receiver. The comparison of ML-MUD and LMMSE/ZE detection is also given. In addition to mathematical derivation and simulation study, we provide an easily understandable way to view the distinction between different detection schemes.
- Chapter 3: This chapter proposes two new detection schemes based on the



model of Chapter 2. Different than typical uplink MUD, the purpose of downlink MUD is to combat against MAI, but not necessary to decode all the received signals from the designated transmitter and interferers, and thus the detection performance of packets from interfering APs is not worth attention. We therefore utilize this feature of downlink transmissions to propose a unique realization of MUD, R-ML-MUD to reduce the complexity of detection, which is different from traditional sphere decoding [65, 66] and deemed as a method scheme to “partially ignore weak interference”. Furthermore, we note the drawback of conventional multiuser projection receiver [35, 36] to propose GLMMSE as a new type of projection detection structure that partially suppresses interference. After that, we strike flexible trade-off between complexity and performance by combining the two proposed methods.

- Chapter 4: Taking multi-CFO problem into account, we construct a two-stage ICI suppression method that is more practical to downlink receiver in the scenario described in Fig. 1.5. The first-stage processing is Pseudo-ICI-Whitening (P-ICI-W) [67], which does not rely on the estimation of ICI covariance and is thus suitable for asynchronous downlink. The proposed mechanism is shown to approach ICI-Whitening in terms of post-processing SINR and BER. The second-stage processing is to further cancel some ICI terms by GLMMSE developed in Chapter 3. Moreover, our proposed scheme is compatible with space-time-block-coded signals, namely Alamouti [68] coding and Complex Interleaved Orthogonal Design (CIOD) [69] to yield more reliable proactive wireless communications.
- Chapter 5: We shift our focus onto transmission design according to the asynchronous signal model used in Chapter 4. Under the coordination of AN, the serving APs of virtual cell are assumed to be able to cooperatively encode trans-



mitted data symbols across space-frequency domain. Our analysis reveals that the multi-CFO issue will still result in serious performance loss, even though ICI is perfectly addressed or does not exist. Such issue can be easily resolved by our AP indexing principle. Moreover, we propose a robust encoding scheme against CFOs that not only achieve better performance but also allow AN to index APs randomly, eliminating the necessity of CFO feedback.

- Chapter 6: This chapter is devoted to the concluding remark. Additionally, some future works towards developing virtual-cell networks are also suggested.

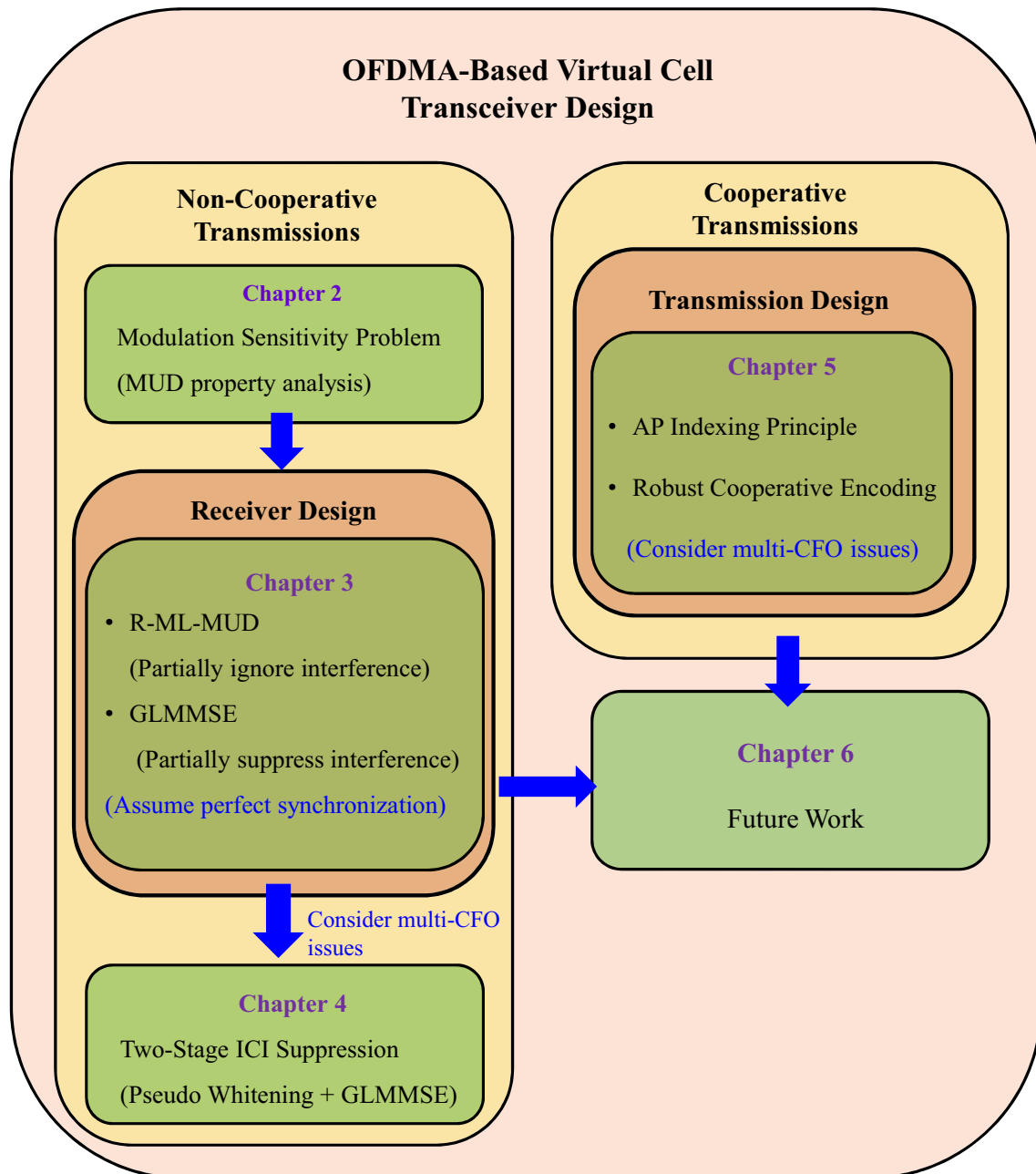


Figure 1.6: Organization and contributions of dissertation.



## Chapter 2

# Modulation Sensitivity in Multiuser Detection

In this chapter, we discuss how MUD works in our virtual cell-based vehicular networks. The analysis is conducted based on the situation of Fig. 1.2 with perfect synchronization. For better readability, the scenario is re-stated. The vehicle associates with  $N \geq 2$  APs to form a virtual cell. In multi-path transmissions, the AN sends the packets to the vehicle through the  $N$  APs, which randomly choose radio channels to serve the vehicle. In the worst case, the vehicle receives the packets from different APs and different channels. Without loss of generality, we look at the channel (or subcarrier ) where AP- $N$  relays the desired data from the AN to the AV, and AP- $1 \sim AP-(N - 1)$  are interferers. As a MAI countermeasure, we analyze the effectiveness of ML-MUD in terms of uncoded BER, comparing it with ZF/LMMSE.

In traditional MIMO systems where the spatial streams are usually assumed to convey the data symbols with the same modulation format, and the detection performance is evaluated across the data symbols from all the transmit antennas. However, in our downlink scenario of Fig. 1.2, only the detection performance of AP- $N$ 's signal is the receiver's concern. Lacking global resource allocation and precise power control, the signals from different APs may originate from different services, and are perhaps differently modulated. Due to this particularity, it is necessary to figure out how the characteristics of interfering signals such as modulation and power affect the BER of

desired data, as the starting point of our research.

It is common sense that BER strongly depends on modulation schemes. We note that in MUD higher modulation order of interference also adversely affect the desired signal's BER, although the interfering signals are not intended for the considered receiver. This is what we call "modulation sensitivity" that gives rise to a serious concern in our innovative system design especially when uRLLC coexists with eMBB and other applications using high-order modulation. Fortunately, this modulation sensitivity can be eased by increasing receiving antennas, as shown in this chapter.

## 2.1 Signal Model and Preliminaries

To facilitate the explanation of our idea, the signal model and ML-MUD are described again, however, in more detail. For  $n = 1, \dots, N$ ,  $X_n$  stands for the transmitted symbol from AP- $n$ , and  $E[|X_n|^2] = 1$ . Assume that each AP has a single antenna, and the vehicle is equipped with  $N_{\text{rx}}$  antennas for  $N_{\text{rx}} \geq N$ , then the received signal  $\mathbf{y}$  is

$$\mathbf{y} = \sum_{n=1}^N \sqrt{A_n} \mathbf{h}_n X_n + \mathbf{v}. \quad (2.1)$$

$A_n$  is AP- $n$ 's mean signal power received at the vehicle,  $\mathbf{h}_n = [H_{1n} \dots H_{N_{\text{rx}}n}]^T$  is the fading gain from AP- $n$  to the vehicle, and  $\mathbf{v} = [V_1 \dots V_{N_{\text{rx}}}]^T$  is the noise at the receiving antennas. The fading coefficients and the noise are zero-mean complex Gaussian random variables with variances 1 and  $\sigma_v^2$ , i.e.,  $H_{mn} \sim CN(0, 1)$  and  $V_m \sim CN(0, \sigma_v^2)$  for  $m = 1, \dots, N_{\text{rx}}$ .  $A_n$  is the composite of transmission power, path loss, and shadowing, which changes very slowly compared to the fading, thus being treated as a constant. In small cell deployment, the received power of desired and interfering signals may be comparable. The signal from a closer AP does not imply stronger received power due to shadowing. Furthermore, in some downlink channels, interfering signals are stronger than the desired signal at the receiver. Hence, we have  $A_n \geq A_N$  or  $A_N < A_n$  for  $n = 1, \dots, N - 1$ .

By ML-MUD, the receiver jointly decodes the desired signal and interference according to

$$\left(\widehat{\mathbf{x}}_{-N}, \widehat{X}_N\right) = \arg \min_{(\mathbf{x}_{-N}, X_N) \in \prod_{n=1}^N \mathcal{M}_n} \left\| \mathbf{y} - \sum_{n=1}^N \sqrt{A_n} \mathbf{h}_n X_n \right\|_2^2, \quad (2.2)$$

where  $\mathcal{M}_n$  is the signal constellation of AP- $n$ . For  $I_n$ -ary PAM,

$$\mathcal{M}_n = \{\pm d_n, \pm 3d_n, \dots, \pm (I_n - 1) d_n\}, \quad (2.3)$$

$$d_n = \sqrt{3/(I_n^2 - 1)}. \quad (2.4)$$

For  $J_n$ -ary QAM,

$$\mathcal{M}_n = \{s_R + j s_I\}, \quad (2.5)$$

$$s_R, s_I \in \{\pm d_n, \pm 3d_n, \dots, \pm (\sqrt{J_n} - 1) d_n\}, \quad (2.6)$$

$$d_n = \sqrt{3/2 (J_n - 1)}. \quad (2.7)$$

Here  $\mathbf{x}_{-N} = (X_1, \dots, X_{N-1})$ , and  $\widehat{\mathbf{x}}_{-N}$  is defined similarly. In order to perform (2.2), the vehicle has to spend extra effort to estimate  $\sqrt{A_n} \mathbf{h}_n$  for  $n = 1, \dots, N - 1$  that is also the inherent cost of beam-forming and IA, but does not need to feedback CSI. The information regarding  $\mathcal{M}_1, \dots, \mathcal{M}_N$  is supposed to be provided by the AN through control channels or to be encoded in the preambles of data packets. Please note that the vehicle only cares about the correctness of  $\widehat{X}_N$  despite  $X_N$  and  $\mathbf{x}_{-N}$  being jointly decoded. We focus on how the interference  $\sum_{n=1}^{N-1} \sqrt{A_n} \mathbf{h}_n X_n$  affects the detection of  $X_N$  and take the performance of ideal single-user detection (SUD) (simply called the ideal detection) as the benchmark.

Lemmas 1 ~ 3 are re-stated respectively from [70], [31, 71], giving deep insight to our research.

**Lemma 1.** Let  $\mathbf{H} = [\mathbf{h}_1 \cdots \mathbf{h}_N]$  and denote its QR-decomposition by  $\mathbf{H} = \mathbf{Q}\mathbf{R}$ . The entries of  $\mathbf{R}$  are independent, the square of diagonal entries follow Gamma distribution, i.e.,  $R_{nn}^2 \sim \text{Gamma}(N_{\text{rx}} - n + 1, 1)$  for  $n = 1, \dots, N$ , and the off-diagonal entry

$R_{ji}$  for  $i > j$  is a zero-mean complex Gaussian random variable with unit variance, that is,  $R_{ji} \sim CN(0, 1)$ .

**Lemma 2.** The output SNR of the desired signal at ZF equalizer is

$$\text{SNR}_{\text{ZF}} = \frac{A_N}{\sigma_V^2} R_{NN}^2. \quad (2.8)$$

**Lemma 3.** The output signal-to-interference-plus-noise ratio (SINR) of the desired signal at LMMSE equalizer is

$$\text{SINR}_{\text{LMMSE}} = \frac{A_N}{\sigma_V^2} \tilde{R}_{NN}^2 - 1. \quad (2.9)$$

Here  $\tilde{R}_{NN}$  is the  $(N, N)$ -th entry of  $\tilde{\mathbf{R}}$  obtained by QR-decomposition

$$\tilde{\mathbf{H}} = [\tilde{\mathbf{h}}_1 \cdots \tilde{\mathbf{h}}_N] = \begin{bmatrix} \mathbf{H} \\ \mathbf{D} \end{bmatrix} = \tilde{\mathbf{Q}}\tilde{\mathbf{R}}, \quad (2.10)$$

where

$$\mathbf{D} = \text{diag} \left( \sqrt{\frac{\sigma^2}{A_1}}, \dots, \sqrt{\frac{\sigma^2}{A_N}} \right). \quad (2.11)$$

## 2.2 The Impact of Modulation of Interference on BER

For clear depiction, we initially examine the 2-AP case that AP-1 and AP-2 use 2-PAM/4-PAM and 2-PAM, respectively. Express  $\mathbf{h}_1$  and  $\mathbf{h}_2$  as  $\mathbf{h}_1 = R_{11}\mathbf{q}_1$  and  $\mathbf{h}_2 = R_{12}\mathbf{q}_1 + R_{22}\mathbf{q}_2$ , where  $\mathbf{q}_n$  is the  $n$ th column of  $\mathbf{Q}$  in Lemma 1. Taking  $A_1$ ,  $A_2$ ,  $\mathbf{h}_1$ , and  $\mathbf{h}_2$  into account, the composite constellation of AP-1 and AP-2 is

$$\mathcal{M} = \left\{ \sqrt{A_1}R_{11}X_1\mathbf{q}_1 + \sqrt{A_2}X_2\mathbf{h}_2 \mid X_1 \in \mathcal{M}_1, X_2 \in \mathcal{M}_2 \right\}. \quad (2.12)$$

Conditioning on some realization of fading that  $R_{11} = r_{11}$ ,  $R_{12} = r_{12}$ , and  $R_{22} = r_{22}$ , the constellations  $\mathcal{M}_1$  and  $\mathcal{M}_2$  are scaled and rotated by  $\sqrt{A_1}\mathbf{h}_1$  and  $\sqrt{A_2}\mathbf{h}_2$ , as shown in Fig. 2.1(a), where the red and blue arrows point the direction of  $\mathbf{h}_1$  and  $\mathbf{h}_2$ , and the spacings of adjacent constellation points of AP-1 and AP-2 become  $\Delta_1 \triangleq 2\sqrt{A_1}r_{11}d_1$  and  $2\sqrt{A_2}\|\mathbf{h}_2\|_2 d_2$  while the resultant  $\mathcal{M}$ , defined in (2.12), is shown in Fig. 2.1(b).

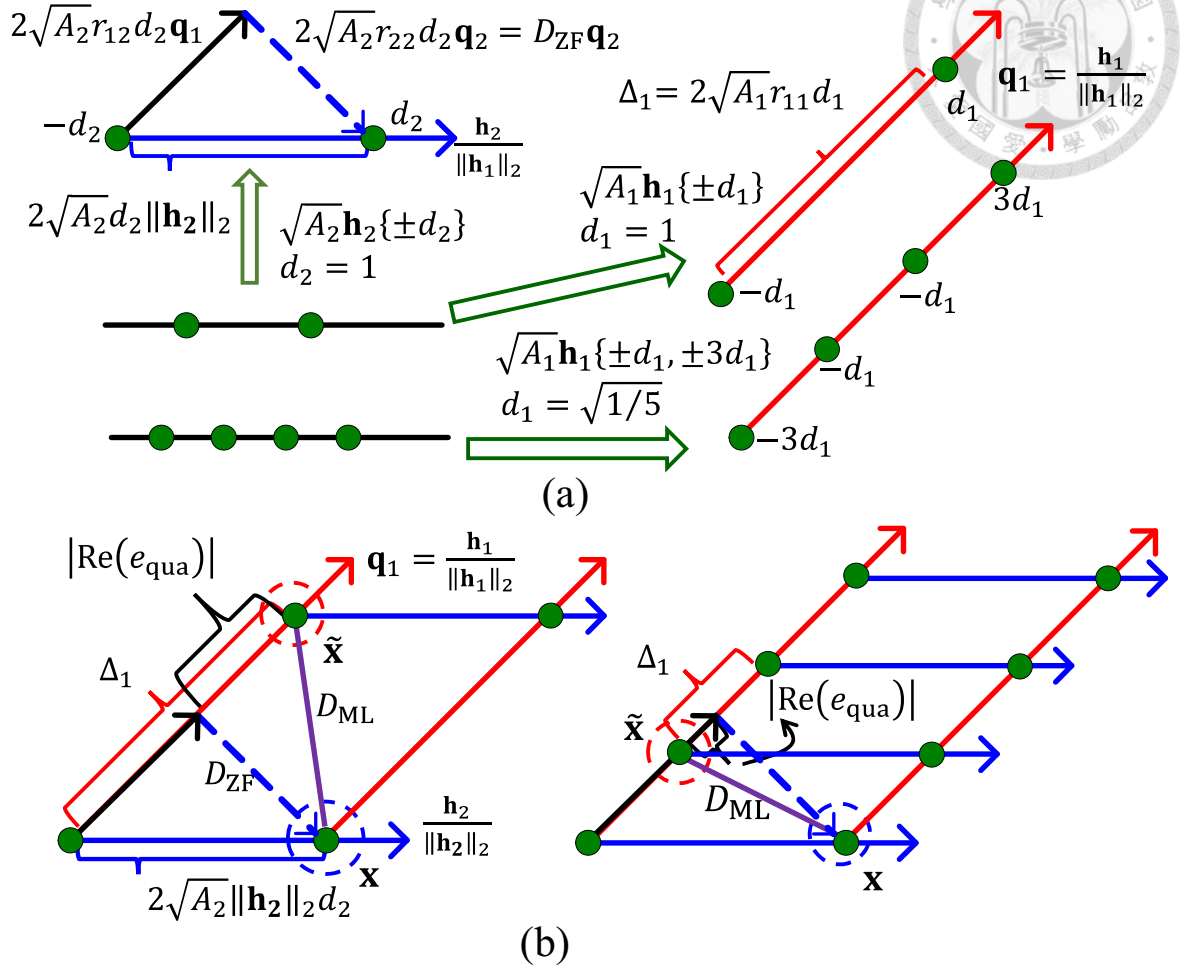
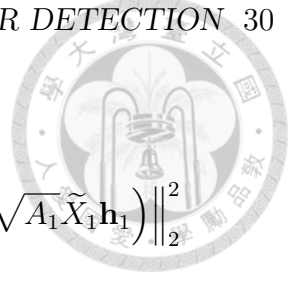


Figure 2.1: (a)  $\mathcal{M}_1$  and  $\mathcal{M}_2$  are rotated and scaled by  $\sqrt{A_1}\mathbf{h}_1$  and  $\sqrt{A_2}\mathbf{h}_2$  with the spacings of adjacent constellation points becoming  $\Delta_1 \triangleq 2\sqrt{A_1}r_{11}d_1$  and  $2\sqrt{A_2}\|\mathbf{h}_2\|_2 d_2$ . (b) The receiver searches the ML solution from a composite constellation under 2-PAM (Left) / 4-PAM (Right) interference. When  $\mathbf{x}$  is the transmitted sequence, the most likely error is decoding  $\mathbf{x}$  as  $\tilde{\mathbf{x}}$ , and the distance between them is  $D_{ML}$ . The constellation points of AP-1 act like quantization levels to quantize  $2\sqrt{A_2}r_{12}d_2\mathbf{q}_1$ .

The bit error event corresponds to the pairwise error between the transmitted sequence  $\mathbf{x} = (X_1, X_2)$  and some other sequence  $\tilde{\mathbf{x}} = (\tilde{X}_1, \tilde{X}_2)$  for  $X_2 \neq \tilde{X}_2$ . Let's first consider the situation in the left part of Fig. 2.1(b), in which  $\mathbf{x} = (-d_1, d_2)$  is enclosed by the dashed blue circle. The most likely error is that  $\mathbf{x}$  is decoded as  $\tilde{\mathbf{x}}$



with  $\tilde{X}_2 = -d_2$ , whose squared distance to  $\mathbf{x}$  is

$$\begin{aligned}
 D_{\text{ML}}^2 &= \min_{\tilde{X}_1 \in \mathcal{M}_1} \left\| \left( \sqrt{A_2} X_2 \mathbf{h}_2 + \sqrt{A_1} X_1 \mathbf{h}_1 \right) - \left( \sqrt{A_2} \tilde{X}_2 \mathbf{h}_2 + \sqrt{A_1} \tilde{X}_1 \mathbf{h}_1 \right) \right\|_2^2 \\
 &= \min_{\tilde{X}_1 \in \mathcal{M}_1} \left\| \sqrt{A_2} (X_2 - \tilde{X}_2) \mathbf{h}_2 + \sqrt{A_1} (X_1 - \tilde{X}_1) \mathbf{h}_1 \right\|_2^2 \\
 &= \min_{\tilde{X}_1 \in \mathcal{M}_1} \left\| 2\sqrt{A_2} d_2 (r_{12} \mathbf{q}_1 + r_{22} \mathbf{q}_2) - 2\sqrt{A_1} r_{11} d_1 \frac{\tilde{X}_1 - X_1}{2d_1} \mathbf{q}_1 \right\|_2^2 \\
 &= \left( 2\sqrt{A_2} d_2 r_{22} \right)^2 + \min_{\tilde{X}_1 \in \mathcal{M}_1} \left\| \left( 2\sqrt{A_2} r_{12} d_2 - \Delta_1 \frac{\tilde{X}_1 - X_1}{2d_1} \right) \mathbf{q}_1 \right\|_2^2, \quad (2.13)
 \end{aligned}$$

where the last equality follows from  $\Delta_1 = 2\sqrt{A_1} r_{11} d_1$  as well as the orthogonality between  $\mathbf{q}_1$  and  $\mathbf{q}_2$ . We define  $D_{\text{ZF}} \triangleq 2\sqrt{A_2} r_{22} d_2$  (the length of dashed blue arrow in Fig. 2.1) as the spacing between adjacent constellation points of AP-2 when ZF is applied (see Lemma 2). In the second term of (2.13), we may view  $L_{X_1} = \left\{ \Delta_1 \frac{\tilde{X}_1 - X_1}{2d_1} \mathbf{q}_1 \mid \tilde{X}_1 \in \mathcal{M}_1 \right\}$  as the quantization levels with quantization interval  $\Delta_1$  to quantize  $2\sqrt{A_1} r_{12} d_2 \mathbf{q}_1$ . Let  $\mathcal{Q}_{L_{X_1}}[\cdot]$  denote the quantization operation, and

$$\mathcal{Q}_{L_{X_1}} \left[ 2\sqrt{A_2} r_{12} d_2 \mathbf{q}_1 \right] = \Delta_1 \frac{\hat{X}_1 - X_1}{2d_1} \mathbf{q}_1, \quad (2.14)$$

$$\hat{X}_1 = \arg \min_{\tilde{X}_1 \in \mathcal{M}_1} \left\| \left( 2\sqrt{A_2} r_{12} d_2 - \Delta_1 \frac{\tilde{X}_1 - X_1}{2d_1} \right) \mathbf{q}_1 \right\|_2^2. \quad (2.15)$$

Then the second term of (2.13) is the square of quantization error, and  $D_{\text{ML}}^2$  can be expressed as

$$D_{\text{ML}}^2 = D_{\text{ZF}}^2 + \|\mathbf{e}_{\text{qua}}\|_2^2, \quad (2.16)$$

where

$$\mathbf{e}_{\text{qua}} = 2\sqrt{A_2} r_{12} d_2 \mathbf{q}_1 - \mathcal{Q}_{L_{X_1}} \left[ 2\sqrt{A_2} r_{12} d_2 \mathbf{q}_1 \right] = e_{\text{qua}} \mathbf{q}_1. \quad (2.17)$$

Specifically, in our discussed case,

$$e_{\text{qua}} = \text{Re}(e_{\text{qua}}) + j2\sqrt{A_2} \text{Im}(r_{12}) d_2, \quad (2.18)$$

$$|\text{Re}(e_{\text{qua}})| = \min_{\tilde{X}_1 \in \mathcal{M}_1} \left| 2\sqrt{A_2} \text{Re}(r_{12}) d_2 - \Delta_1 \frac{\tilde{X}_1 - X_1}{2d_1} \right|, \quad (2.19)$$



where  $\text{Re}(\cdot)$  and  $\text{Im}(\cdot)$  stand for the real and imaginary parts. The squared distance between  $(X_1, d_2)$  and  $(\tilde{X}_1, -d_2)$  with  $X_1 = \tilde{X}_1$  is  $4A_2 \|\mathbf{h}_2\|_2^2 d_2^2 = D_{\text{ZF}}^2 + 4A_2 |r_{12}|^2 d_2^2$ , whose component in  $\text{span}(\mathbf{h}_1)$  is totally removed by the ZF equalizer. However, in ML-MUD, some “distance gain” can be obtained from  $\text{span}(\mathbf{h}_1)$  that is the quantization error  $\|\mathbf{e}_{\text{qua}}\|_2$ , as seen from (2.16). Finer quantization levels generally lead to smaller quantization error, consequently smaller  $D_{\text{ML}}^2$ , which manifests that high-order modulated interference results in worse BER because  $\Delta_1$  is proportional to  $2d_1$ , the spacing of constellation points of interference (see the right part of Fig. 2.1(b)). Additionally,  $\Delta_1$  is also in proportion to  $\sqrt{A_1}$ , then ML-MUD generally has better performance under stronger interference.

When  $\Delta_1$  is large enough such that

$$\left| 2\sqrt{A_2} \text{Re}(r_{12}) d_2 \right| < \frac{1}{2} \Delta_1, \quad (2.20)$$

$2\sqrt{A_2} r_{12} d_2 \mathbf{q}_1$  will be quantized as zero. Accordingly, the pairwise error probability (PEP) is

$$p_{\text{ML}} \{\mathbf{x} \rightarrow \tilde{\mathbf{x}}\} = Q \left( \sqrt{\frac{D_{\text{ML}}^2}{2\sigma_V^2}} \right) = Q \left( \sqrt{\frac{2A_2 \|\mathbf{h}_2\|_2^2 d_2^2}{\sigma_V^2}} \right), \quad (2.21)$$

which is the BER of ideal detection. Hence the more likely that (2.20) holds, the closer the average BER of ML-MUD (averaged over fading gain) approaches to the ideal detection performance. The condition for (2.21) can be written as

$$\frac{|\text{Re}(R_{12})|}{R_{11}} < \frac{1}{2} \sqrt{\frac{A_1}{A_2}} \frac{d_1}{d_2}. \quad (2.22)$$

By Lemma 1,  $R_{11}^2 \sim \text{Gamma}(N_{\text{rx}}, 1)$ . As the number of receiving antennas increases from  $N_{\text{rx}}$  to  $N_{\text{rx}} + 1$ ,  $R_{11}^2 \sim \text{Gamma}(N_{\text{rx}} + 1, 1)$ , but it remains that  $R_{12} \sim \text{CN}(0, 1)$ . Then  $|\text{Re}(R_{12})|/R_{11}$  will be statistically smaller, making (2.22) hold with higher probability. Hence increasing receiving antennas bridges the performance gap between ML-MUD and ideal detection in terms of average BER. However, the gap always exists when ZF is applied because the potential gain from  $\text{span}(\mathbf{h}_1)$  is lost.

Now we generalize the preceding analysis for  $N > 2$ . Denote the transmitted sequence by  $\mathbf{x} = (\mathbf{x}_{-N}, X_N)$ . In the bit/symbol error event  $X_N \neq \tilde{X}_N$ , the most likely situation is that  $\mathbf{x}$  is decoded as  $\tilde{\mathbf{x}} = (\tilde{\mathbf{x}}_{-N}, \tilde{X}_N)$ , whose squared distance to  $\mathbf{x}$  is expressed as

$$\begin{aligned} D_{\text{ML}}^2 &= \min_{\tilde{\mathbf{x}}_{-N} \in \prod_{n=1}^{N-1} \mathcal{M}_n} \left\| \sqrt{A_N} (X_N - \tilde{X}_N) \mathbf{h}_N + \sum_{n=1}^{N-1} \sqrt{A_n} (X_n - \tilde{X}_n) \mathbf{h}_n \right\|_2^2 \\ &= D_{\text{ZF}}^2 + \|\mathbf{e}_{\text{qua}}\|_2^2, \end{aligned} \quad (2.23)$$

where

$$D_{\text{ZF}}^2 = A_N R_{NN}^2 |X_N - \tilde{X}_N|^2, \quad (2.24)$$

$$\|\mathbf{e}_{\text{qua}}\|_2^2 = \min_{\tilde{\mathbf{x}}_{-N} \in \prod_{n=1}^{N-1} \mathcal{M}_n} \left\| \sum_{n=1}^{N-1} \frac{\left( \sqrt{A_N} (X_N - \tilde{X}_N) R'_{nN} - \frac{\Delta_n (\tilde{X}_n - X_n)}{2d_n} \right) \mathbf{h}_n}{\|\mathbf{h}_n\|_2} \right\|_2^2, \quad (2.25)$$

$$R'_{nN} = \left( R_{nN} + \frac{\sum_{m=n+1}^{N-1} \text{cof}(\mathbf{R}_{IS})_{mn} R_{mN}}{\prod_{i \neq n} R_{ii}} \right) \left( \sum_{k=1}^n \frac{|R_{kn}|^2}{R_{nn}^2} \right)^{\frac{1}{2}}. \quad (2.26)$$

The proof of (2.23) is given in Appendix A. In (2.26),  $\mathbf{R}_{IS}$  is the  $(N-1) \times (N-1)$  matrix obtained from  $\mathbf{R}$  by deleting its  $N$ th row and  $N$ th column, and  $\text{cof}(\mathbf{R}_{IS})_{mn}$  is the  $(m, n)$ -th cofactor of  $\mathbf{R}_{IS}$ . In (2.25),  $\sum_{n=1}^{N-1} \sqrt{A_n} (X_N - \tilde{X}_N) R'_{nN} \frac{\mathbf{h}_n}{\|\mathbf{h}_n\|_2}$  is the orthogonal projection of  $\sqrt{A_N} (X_N - \tilde{X}_N) \mathbf{h}_N$  to  $\text{span}(\mathbf{h}_1, \dots, \mathbf{h}_{N-1})$  (see Appendix A), and

$$L_{\mathbf{x}_{-N}} = \left\{ \sum_{n=1}^{N-1} \frac{\Delta_n (\tilde{X}_n - X_n)}{2d_n} \frac{\mathbf{h}_n}{\|\mathbf{h}_n\|_2} \mid \tilde{\mathbf{x}}_{-N} \in \prod_{n=1}^{N-1} \mathcal{M}_n \right\}$$

are the quantization levels with  $\Delta_n = 2\sqrt{A_n} \|\mathbf{h}_n\|_2 d_n$ , which is proportional to  $\sqrt{A_n}$  and  $d_n$ , implying that (i) for fixed  $\sqrt{A_n}$ , higher-order modulated interference, which makes quantization levels finer and leads to smaller quantization error, is more harmful to the BER performance; (ii) for the same modulation order, stronger interference, resulting in coarse quantization levels, is generally less detrimental. Additionally, by

Lemma 1, as the number of antennas increases,  $R'_{nN}$  is closer to  $R_{nN}$  in average,  $\Delta_n$  is statistically larger, thus  $\sum_{n=1}^{N-1} \sqrt{A_N} \left( X_N - \tilde{X}_N \right) R'_{nN} \frac{\mathbf{h}_n}{\|\mathbf{h}_n\|_2}$  is quantized as zero with higher probability, meaning that the gap of average BER between ML-MUD and ideal detection will be bridged.

## 2.3 Comparison with LMMSE

Now we make a comparison with LMMSE. Likewise, our analysis begins with the case of  $N = 2$ . By Lemmas 2~3,

$$\eta_{\text{SNR}} \triangleq \text{SINR}_{\text{LMMSE}} - \text{SNR}_{\text{ZF}} = \frac{A_2}{\sigma_V^2} \tilde{R}_{22}^2 - 1 - \frac{A_2}{\sigma_V^2} R_{22}^2. \quad (2.27)$$

From (2.10), the (2, 2)-th entry of  $\tilde{\mathbf{R}}$  can be expressed as

$$\tilde{R}_{22}^2 \stackrel{(c)}{=} \|\mathbf{h}_2\|_2^2 + \frac{\sigma_V^2}{A_2} - \left| \tilde{R}_{12} \right|^2 \stackrel{(d)}{=} |R_{12}|^2 + R_{22}^2 + \frac{\sigma_V^2}{A_2} - \left| \tilde{R}_{12} \right|^2. \quad (2.28)$$

The norm of second column of  $\tilde{\mathbf{H}}$  (or  $\mathbf{H}$ ) is equal to that of  $\tilde{\mathbf{R}}$  (or  $\mathbf{R}$ ), thus (c) and (d) in (2.28) hold. Besides,

$$\left| \tilde{R}_{12} \right|^2 = \frac{\left| \tilde{\mathbf{h}}_1^H \tilde{\mathbf{h}}_2 \right|^2}{\left\| \tilde{\mathbf{h}}_1 \right\|_2^2} = \frac{\left| \mathbf{h}_1^H \mathbf{h}_2 \right|^2}{\left\| \mathbf{h}_1 \right\|_2^2 + \frac{\sigma_V^2}{A_1}} = \frac{|R_{12}|^2 R_{11}^2}{R_{11}^2 + \frac{\sigma_V^2}{A_1}}. \quad (2.29)$$

By (2.27)~(2.29), we obtain

$$\begin{aligned} \eta_{\text{SNR}} &= \frac{A_2}{\sigma_V^2} \left( |R_{12}|^2 + R_{22}^2 + \frac{\sigma_V^2}{A_2} - \left| \tilde{R}_{12} \right|^2 \right) - 1 - \frac{A_2}{\sigma_V^2} R_{22}^2 \\ &= \frac{A_2}{\sigma_V^2} \left( |R_{12}|^2 - \left| \tilde{R}_{12} \right|^2 \right) = \frac{A_2}{\sigma_V^2} |R_{12}|^2 \left( 1 - \frac{R_{11}^2}{R_{11}^2 + \frac{\sigma_V^2}{A_1}} \right) \\ &= \frac{|R_{12}|^2}{\frac{A_1}{A_2} R_{11}^2 + \frac{\sigma_V^2}{A_2}}. \end{aligned} \quad (2.30)$$

Approximating the sum of interference and noise as being Gaussian [31], the BER of LMMSE is approximated as

$$p_{\text{LMMSE}} \left\{ X_2 \rightarrow \tilde{X}_2 \right\} \approx Q \left( \sqrt{2 (\text{SNR}_{\text{ZF}} + \eta_{\text{SNR}}) d_2^2} \right). \quad (2.31)$$

Like ML-MUD, LMMSE can obtain some equivalent “distance gain” from  $\text{span}(\mathbf{h}_1)$ , as shown in (2.30). However,  $\eta_{\text{SNR}}$  is smaller for larger  $A_1$ , that is, the distance gain will diminish as the interference power becomes stronger and stronger, being opposite to ML-MUD. On the other hand, by the same reasoning to explain the performance gap reduction between ML-MUD and ideal detection, increasing the receiving antennas makes  $\eta_{\text{SNR}}$  smaller in average, then the performance of LMMSE and ZF will be closer to each other.

Generalizing the analysis to the case of  $N > 2$ , it can be shown that

$$\lim_{\frac{A_N}{\sigma_V^2} \rightarrow \infty} \eta_{\text{SNR}} = \left\| R_{NN} \mathbf{\Gamma}_N \mathbf{r}_{NS}^- \right\|_2^2, \quad (2.32)$$

where

$$\mathbf{\Gamma}_N = \text{diag} \left( \sqrt{\frac{A_N}{A_1}}, \dots, \sqrt{\frac{A_N}{A_{N-1}}} \right), \quad (2.33)$$

$$\mathbf{r}_{NS}^- = \left[ (\mathbf{R}^{-1})_{1N}, \dots, (\mathbf{R}^{-1})_{(N-1)N} \right]^T. \quad (2.34)$$

From (2.32) (proven in Appendix B), it is easy to draw the conclusion that (i) stronger interference yields smaller  $\eta_{\text{SNR}}$ ; (ii) more antennas makes  $\text{SINR}_{\text{LMMSE}}$  closer to  $\text{SNR}_{\text{ZF}}$  averagely.

## 2.4 Simulation Results

We carry out simulations in 2-AP case, where AP-2 uses QPSK to transmit the desired data being interfered by AP-1’s signal. In the left part of Fig. 2.2, we show the simulation results for  $N_{\text{rx}} = 2$ . As the interference is BPSK modulated, the average BER of ML-MUD is very close to that of the ideal detection, achieving  $10^{-3}$  when  $\frac{A_2}{\sigma_V^2}$  is approximately 14 dB. However, if the interference is 16-QAM or 64-QAM modulated,  $\frac{A_2}{\sigma_V^2}$  needs to be about 18 dB or higher to achieve the same average BER. In the right part of Fig. 2.2, the results with  $N_{\text{rx}} = 3$  are reported. For identical average BER, the values of  $\frac{A_2}{\sigma_V^2}$  for the ideal detection and ML-MUD with BPSK interference

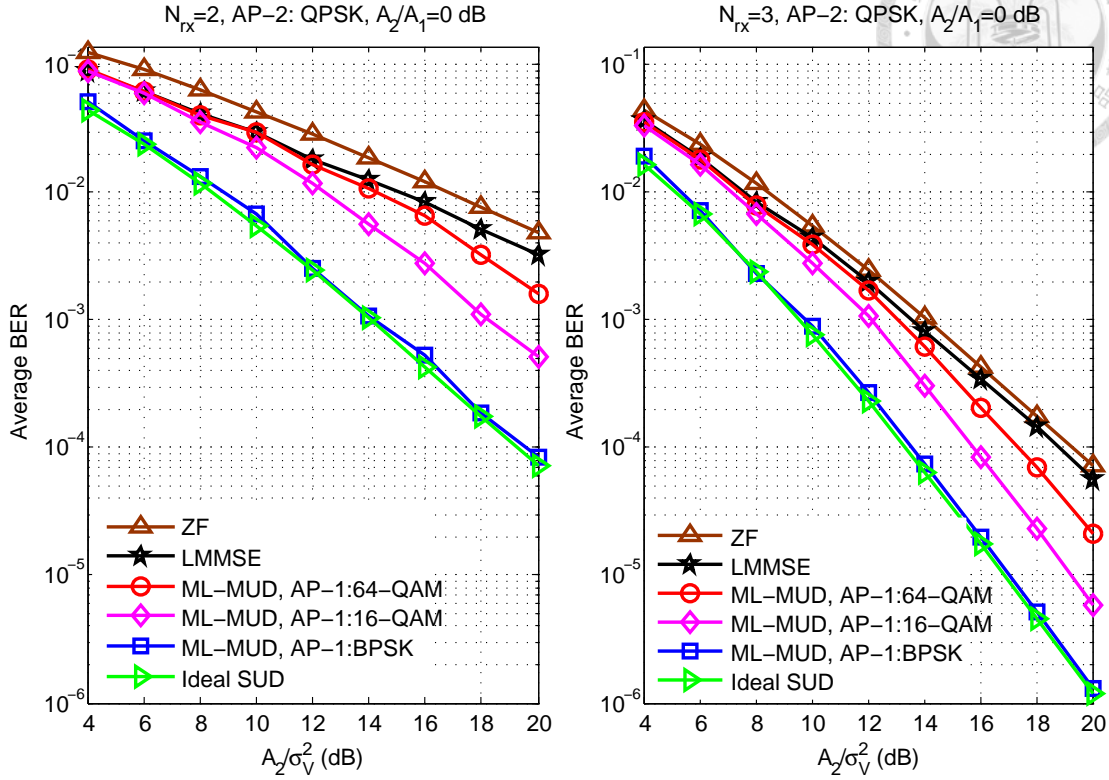


Figure 2.2: (Left)  $N_{rx} = 2$ . (Right)  $N_{rx} = 3$ . AP-2 uses QPSK to transmit the desired data while  $\frac{A_2}{A_1} = 0$  dB. The average BERs under different modulated interference are plotted.

are close to each other. At average BER  $10^{-3}$  or  $10^{-4}$ , the difference of  $\frac{A_2}{\sigma_v^2}$  between the ideal detection and ML-MUD with 16-QAM (or 64-QAM) interference is about 2 (or 3.5) dB. Hence, ML-MUD is possible to approach the ideal detection, but its performance is very sensitive to the modulation of interference, and increasing the number of antennas can relieve such sensitivity. The above observation is consistent with the analysis in Section 2.2. In a lower SNR regime, the constellation points of high order modulation are closely situated in the subspace  $\text{span}(\mathbf{h}_1)$ , leading to very small quantization error, which is only a little more than the “distance gain” of LMMSE (refer to (2.27)). We therefore can see that ML-MUD with 64-QAM interference is close to LMMSE for SNR smaller than 14 dB in Fig. 2.2.

For 16-QAM interference and signal-to-interference ratio (SIR)  $\frac{A_2}{A_1} = \pm 3$  dB, the average BERs of desired data are plotted in Fig. 2.3. In the left part of Fig. 2.3 with

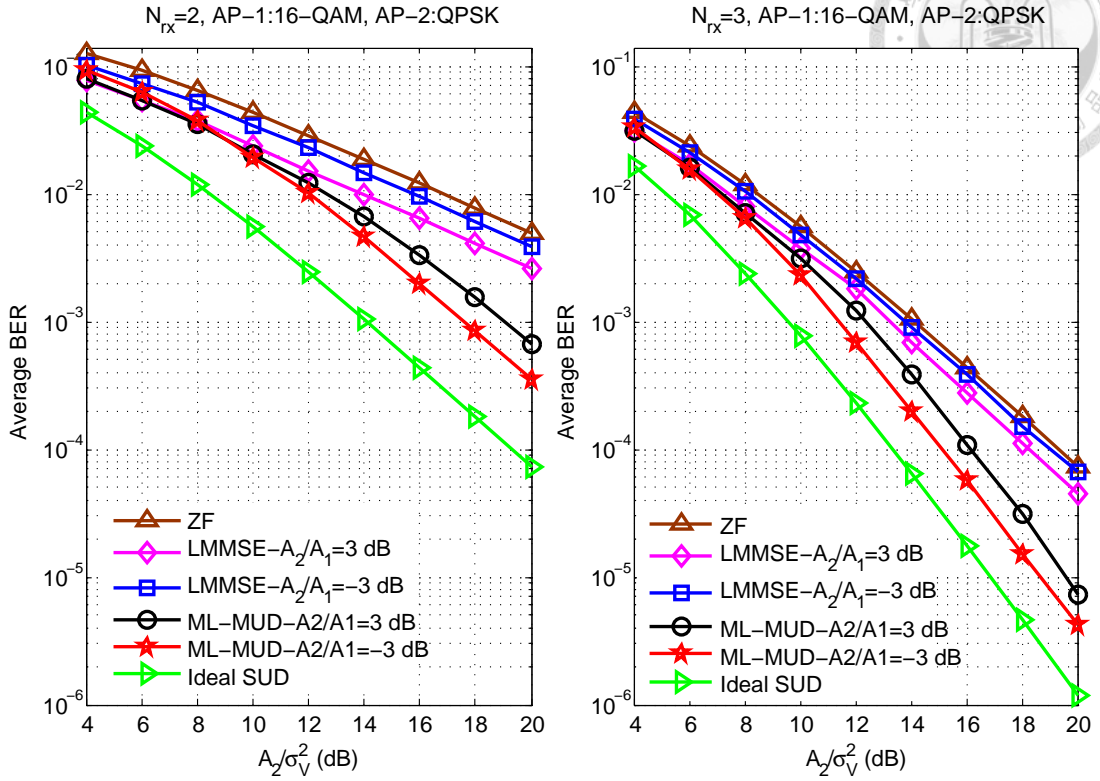


Figure 2.3: (Left)  $N_{\text{rx}} = 2$ . (Right)  $N_{\text{rx}} = 3$ . AP-2 uses QPSK to transmit the desired data being interfered by AP-1's 16-QAM modulated signal. The average BERs are plotted for  $\frac{A_2}{A_1} = \pm 3$  dB.

$N_{\text{rx}} = 2$ , LMMSE and ZF are closer to each other under stronger interference. At average BER  $10^{-3}$ , the value of  $\frac{A_2}{\sigma_v^2}$  for ML-MUD is around 18 dB when  $\frac{A_2}{A_1} = -3$  dB. As  $\frac{A_2}{A_1} = 3$  dB, ML-MUD requires  $\frac{A_2}{\sigma_v^2}$  to be about 19 dB for the same performance. This result indicates that stronger interference is less detrimental to ML-MUD. In right part of Fig. 2.3 with  $N_{\text{rx}} = 3$ , the analogous observation is obtained. Moreover, from Fig. 2.2 and Fig. 2.3, we also observe that increasing antennas reduces the performance gap between ZF and LMMSE, corresponding with the analysis in Section 2.3. The average BERs of 3-AP case with respect to different modulated interference and SIRs can be found in [39] that shows similar results.

## 2.5 Summary

Traditional beam-forming and IA are not suitable for ultra-low latency vehicular networking. Open-loop communication and proactive network association suggest the necessity of MUD to deal with downlink inference at receivers. We find that the performance of ML-MUD is very sensitivity to the modulations of interferers, and such sensitivity is shown to be relieved by multi-antenna technique. Another interesting observation is that the performance of LMMSE is closer to ZF under stronger interference, which is generally in favor of ML-MUD implementation. This discovery also gives us insight regarding which interfering signals to cancel when we introduce GLMMSE in Chapter 3.







## Chapter 3

# Low-Complexity Multiuser Detection

On the basis of the system model in Chapter 2, we propose two methods to reduce the notorious computational complexity of MUD in this chapter. The first scheme is termed reduced-computation ML-MUD (R-ML-MUD) that exploits the characteristic of downlink to shrink the ML solution space, consequently leading to lower detection complexity. The second scheme is a new projection receiver, called generalized LMMSE (GLMMSE) that yields notable SNR gain over the conventional projection method. Besides, a comprehensive simulation study is also provided to compare different detection schemes.

### 3.1 Comparison between SUD and ML-MUD

For the sake of holistic comparison, we review the impact of interference on SUD in our 2-AP case, where AP-1 and AP-2 use 4-PAM and 2-PAM. This review also help readers better understand the idea behind our proposed scheme.

Assume that the interference from AP-1 has weaker received power than the desired signal from AP-2. The receiver disregards the interference and performs maximal ratio combining (MRC), then the received signal becomes

$$\tilde{Y}_{\text{mrc}} = \frac{\mathbf{h}_2^H}{\|\mathbf{h}_2\|_2} \mathbf{y} = \sqrt{A_2} \|\mathbf{h}_2\|_2 X_2 + \sqrt{A_1} \frac{\mathbf{h}_2^H \mathbf{h}_1}{\|\mathbf{h}_2\|_2} X_1 + \frac{\mathbf{h}_2^H \mathbf{v}}{\|\mathbf{h}_2\|_2}. \quad (3.1)$$

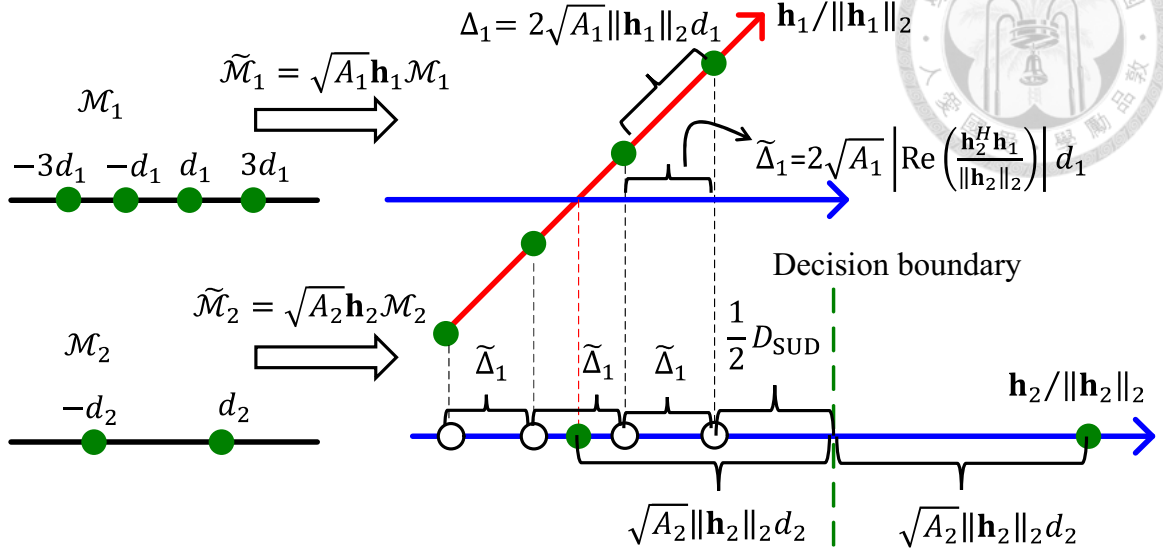


Figure 3.1:  $\mathcal{M}_1$  and  $\mathcal{M}_2$  are rotated and scaled by channel gains, becoming  $\tilde{\mathcal{M}}_1$  and  $\tilde{\mathcal{M}}_2$  with the spacings of adjacent constellation points,  $\Delta_1 \triangleq 2\sqrt{A_1} \|\mathbf{h}_1\|_2 d_1$  and  $2\sqrt{A_2} \|\mathbf{h}_2\|_2 d_2$ . MRC projects interference to  $\text{span}(\mathbf{h}_2)$ , deviating the transmitted symbol from its original position.  $D_{\text{SUD}} = 2\sqrt{A_2} \|\mathbf{h}_2\|_2 d_2 - (I_1 - 1) \tilde{\Delta}_1$ , and  $I_1 = 4$ .

Referring to Fig. 3.1, from the second term of (3.1), MRC projects interference to  $\text{span}(\mathbf{h}_2)$  such that the transmitted symbol is displaced to be closer to or further away from the decision boundary of SUD (the green dashed line in the right part of Fig. 3.1). If  $X_2 = -d_2$  and  $\text{Re}\left(\frac{\mathbf{h}_2^H \mathbf{h}_1}{\|\mathbf{h}_2\|_2}\right) > 0$ , then (3.1) can be written as

$$\tilde{Y}_{\text{mrc}} = -\sqrt{A_2} \|\mathbf{h}_2\|_2 d_2 + \frac{X_1}{2d_1} \tilde{\Delta}_1 + j\sqrt{A_1} \text{Im}\left(\frac{\mathbf{h}_2^H \mathbf{h}_1}{\|\mathbf{h}_2\|_2}\right) X_1 + \frac{\mathbf{h}_2^H \mathbf{v}}{\|\mathbf{h}_2\|_2}, \quad (3.2)$$

where  $\tilde{\Delta}_1 \triangleq 2\sqrt{A_1} \left| \text{Re}\left(\frac{\mathbf{h}_2^H \mathbf{h}_1}{\|\mathbf{h}_2\|_2}\right) \right| d_1$ , and  $-\sqrt{A_2} \|\mathbf{h}_2\|_2 d_2 + \frac{X_1}{2d_1} \tilde{\Delta}_1$  is the position of transmitted symbol shifted by interference. For instance,  $X_1 = \pm 3d_1$  corresponds to the rightmost/leftmost white point in Fig. 3.1. Then the BER is

$$\begin{aligned} \text{BER}_{\text{SUD}} &= \frac{1}{I_1} \sum_{k=0}^{I_1-1} p \left\{ \text{Re}\left(\frac{\mathbf{h}_2^H \mathbf{v}}{\|\mathbf{h}_2\|_2}\right) > \frac{1}{2} D_{\text{SUD}} + k \tilde{\Delta}_1 \right\} \\ &= \frac{1}{I_1} \sum_{k=0}^{I_1-1} Q \left( \sqrt{\frac{\left( D_{\text{SUD}} + 2k \tilde{\Delta}_1 \right)^2}{2\sigma_v^2}} \right), \end{aligned} \quad (3.3)$$

where  $I_1 = 4$ , and  $\frac{1}{2} D_{\text{SUD}} = \sqrt{A_2} \|\mathbf{h}_2\|_2 d_2 - (I_1 - 1) \frac{\tilde{\Delta}_1}{2}$  is the distance between the decision boundary and the white point closest to it. The Q-function can be bounded

by  $Q(x) < \frac{1}{\sqrt{2\pi}} \frac{1}{x} e^{-\frac{x^2}{2}}$ , which is tight as  $x > 1.5$  [28]. At high SNR, we therefore approximate  $\text{BER}_{\text{SUD}}$  as follows.

$$\begin{aligned}
\text{BER}_{\text{SUD}} &\approx \frac{1}{I_1} \sum_{k=0}^{I_1-1} \frac{1}{\sqrt{2\pi}} \sqrt{\frac{2\sigma_V^2}{(D_{\text{SUD}} + 2k\tilde{\Delta}_1)^2}} \exp\left(-\frac{(D_{\text{SUD}} + 2k\tilde{\Delta}_1)^2}{4\sigma_V^2}\right) \\
&= \left[ \frac{1}{I_1} \sum_{k=0}^{I_1-1} \sqrt{\frac{D_{\text{SUD}}^2}{(D_{\text{SUD}} + 2k\tilde{\Delta}_1)^2}} \exp\left(\frac{D_{\text{SUD}}^2 - (D_{\text{SUD}} + 2k\tilde{\Delta}_1)^2}{4\sigma_V^2}\right) \right] \\
&\quad \frac{1}{\sqrt{2\pi}} \sqrt{\frac{2\sigma_V^2}{D_{\text{SUD}}^2}} \exp\left(\frac{-D_{\text{SUD}}^2}{4\sigma_V^2}\right) \\
&= \frac{\rho_{\text{SUD}}}{\sqrt{2\pi}} \sqrt{\frac{2\sigma_V^2}{D_{\text{SUD}}^2}} \exp\left(\frac{-D_{\text{SUD}}^2}{4\sigma_V^2}\right) \\
&\approx \rho_{\text{SUD}} Q\left(\sqrt{\frac{D_{\text{SUD}}^2}{2\sigma_V^2}}\right), \tag{3.4}
\end{aligned}$$

$$\rho_{\text{SUD}} = \frac{1}{I_1} \sum_{k=0}^{I_1-1} \frac{D_{\text{SUD}}}{D_{\text{SUD}} + 2k\tilde{\Delta}_1} \exp\left(\frac{D_{\text{SUD}}^2 - (D_{\text{SUD}} + 2k\tilde{\Delta}_1)^2}{4\sigma_V^2}\right). \tag{3.5}$$

From (3.4), the BER is dominated by  $D_{\text{SUD}}$ . Hence, SUD will work poorly if  $D_{\text{SUD}}$  is not large enough. In other words, it is not possible to achieve acceptable BER unless the interference is much weaker than the desired signal in received power.

In ML-MUD, the detection error occurs when the transmitted sequence  $\mathbf{x} = (X_1, X_2)$  is decoded as  $\tilde{\mathbf{x}} = (\tilde{X}_1, \tilde{X}_2)$  for  $X_2 \neq \tilde{X}_2$ , as shown in Fig. 3.2, where  $\mathbf{x} = (-3d_1, d_2)$ . From Fig. 3.2, it is not difficult to see that BER of ML-MUD can be bounded as follows.

$$\text{BER}_{\text{ML}} < \frac{1}{I_1} \sum_{i=0}^{I_1-1} \sum_{k=i}^{I_1-1+i} Q\left(\sqrt{\frac{D_{\text{ZF}}^2 + \Delta_{k,\text{qua}}^2 + 4A_2 |\text{Im}(r_{12}) d_2|^2}{2\sigma_V^2}}\right), \tag{3.6}$$

where  $\Delta_{k,\text{qua}} = |\text{Re}(e_{\text{qua}})| + k\Delta_1$ . By the same approximation of Q-function used in

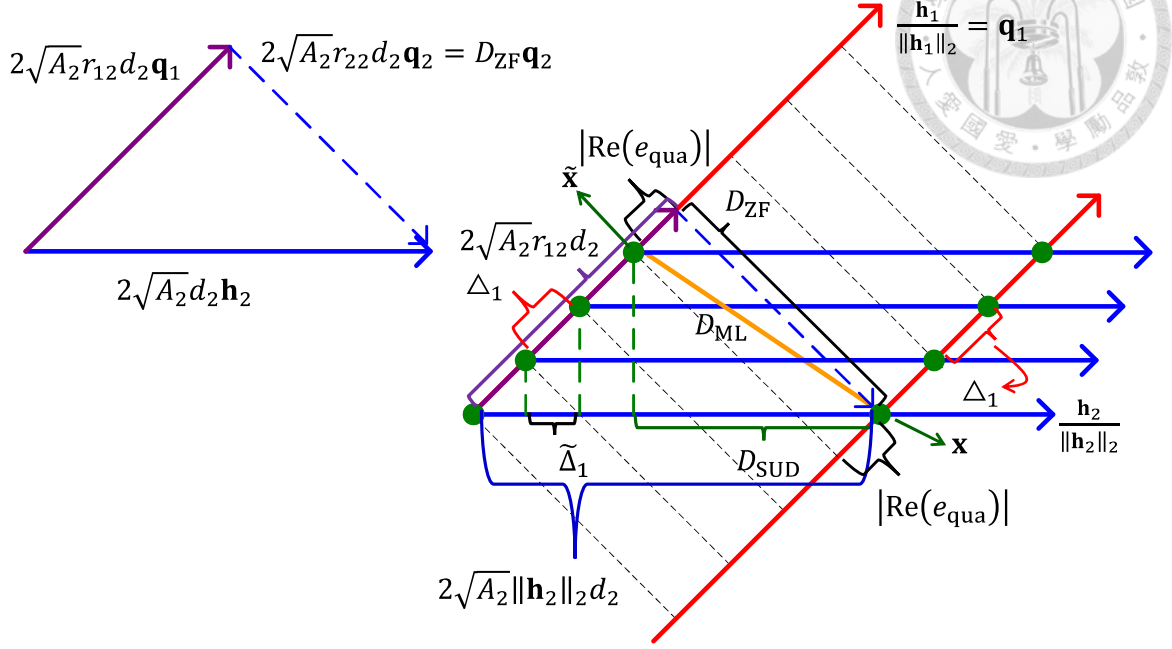


Figure 3.2: The receiver searches the ML solution from a composite constellation  $\mathcal{M}$ . When  $\mathbf{x}$  is the transmitted sequence, the most likely error is decoding  $\mathbf{x}$  as  $\tilde{\mathbf{x}}$ , and the distance between them is  $D_{\text{ML}}$ .  $D_{\text{SUD}} = 2\sqrt{A_2}\|\mathbf{h}_2\|_2 d_2 - (I_1 - 1)\tilde{\Delta}_1$  and  $D_{\text{ZF}} = 2\sqrt{A_2}r_{22}d_2$  account for the detection performance of SUD and ZF.

(3.4), as SNR is high, we obtain a similar expression for the upper bound of  $\text{BER}_{\text{ML}}$ .

$$\text{BER}_{\text{ML}} < \rho_{\text{ML}} Q \left( \sqrt{\frac{D_{\text{ML}}^2}{2\sigma_V^2}} \right), \quad (3.7)$$

$$\rho_{\text{ML}} = \frac{1}{I_1} \sum_{i=0}^{I_1-1} \sum_{k=i}^{I_1-1+i} \frac{D_{\text{ML}} \exp \left( \frac{|\text{Re}(e_{\text{qua}})|^2 - \Delta_{k,\text{qua}}^2}{4\sigma_V^2} \right)}{\sqrt{(D_{\text{ZF}}^2 + \Delta_{k,\text{qua}}^2 + 4A_2 |\text{Im}(r_{12}) d_2|^2)}}. \quad (3.8)$$

The derivation of (3.7) implicitly assumes that  $|2\sqrt{A_2}\text{Re}(r_{12})d_2| \geq (I_1 - 1)\tilde{\Delta}_1$  (see Fig. 3.2), however, for  $|2\sqrt{A_2}\text{Re}(r_{12})d_2| < (I_1 - 1)\tilde{\Delta}_1$ , we still can have the same expression for the upper bound of  $\text{BER}_{\text{ML}}$  with  $\rho_{\text{ML}}$  being defined differently, which does not change the fact that  $\text{BER}_{\text{ML}}$  is dominated by  $D_{\text{ML}}$ . In Fig. 3.2, the distances  $D_{\text{ZF}}$  and  $D_{\text{SUD}}$  are also marked, providing a clear view of the distinction between different detection schemes. From (3.4) and (3.7), as well as the observation of  $D_{\text{SUD}}$  and  $D_{\text{ML}}$  in Fig. 3.2, it is easy to see the effectiveness of ML-MUD to combat against MAI, but at the expense of higher detection complexity.

## 3.2 Reduced-Computation ML-MUD

In uplink MUD, the receiver (AP or BS) has to correctly decode the signals from all the transmitters. However, the purpose of downlink MUD is mainly to lessen the affection of interference, the detection performance of packets from interferers is actually not worth caring. Therefore, the exhaustive search of ML estimate over the constellation  $\mathcal{M}$  is not necessary anymore, suggesting a unique way to relieve practical computation load.

The receiver may treat the interference of high-order modulation as being lower-order modulated. In our example, the vehicle can presume that  $X_1$  is a 2-PAM symbol from  $\mathcal{M}_1^r = \{\pm 2d_1\}$  (as shown in Fig. 3.3(a)), to execute

$$\left(\hat{X}_1^r, \hat{X}_2\right) = \arg \min_{(X_1^r, X_2) \in \mathcal{M}_1^r \times \mathcal{M}_2} \left\| \mathbf{y} - \sqrt{A_1} \mathbf{h}_1 X_1^r - \sqrt{A_2} \mathbf{h}_2 X_2 \right\|_2^2. \quad (3.9)$$

The operation of (3.9) is call “reduced-computation ML-MUD” (R-ML-MUD), and  $\mathcal{M}_1^r$  is termed “reduced-order constellation”. Accordingly, the received signal is written as

$$\mathbf{y} = \sqrt{A_2} \mathbf{h}_2 X_2 + \sqrt{A_1} \mathbf{h}_1 X_1^r + \sqrt{A_1} \mathbf{h}_1 (X_1 - X_1^r) + \mathbf{v}. \quad (3.10)$$

Obviously, the solution space shrinks, implying less computation for detection, but bringing some extra interference that is the third term of (3.10) to shift the transmitted sequence. For instance, in Fig. 3.3(b),  $X_1 = -d_1, -3d_1$  and  $X_2 = d_2$ , the transmitted sequence in  $\mathcal{M}_1^r \times \mathcal{M}_2$  is  $(X_1^r, X_2) = (-2d_1, d_2)$ , then (3.10) becomes that

$$\mathbf{y} = \sqrt{A_2} \mathbf{h}_2 d_2 - 2\sqrt{A_1} \mathbf{h}_1 d_1 \pm \sqrt{A_1} \mathbf{h}_1 d_1 + \mathbf{v}. \quad (3.11)$$

The extra interference  $\pm\sqrt{A_1} \mathbf{h}_1 d_1$  in (3.11) displaces the transmitted sequence along the direction  $\pm \mathbf{q}_1$  by  $\Delta_1/2$ , increasing the PEP for each pair of sequences in  $\mathcal{M}_1^r \times \mathcal{M}_2$ .

We individually examine the effect of extra interference on the pairwise errors. Let’s first consider the pair of sequences  $(-2d_1, d_2)$  and  $(-2d_1, -d_2)$ . Please refer

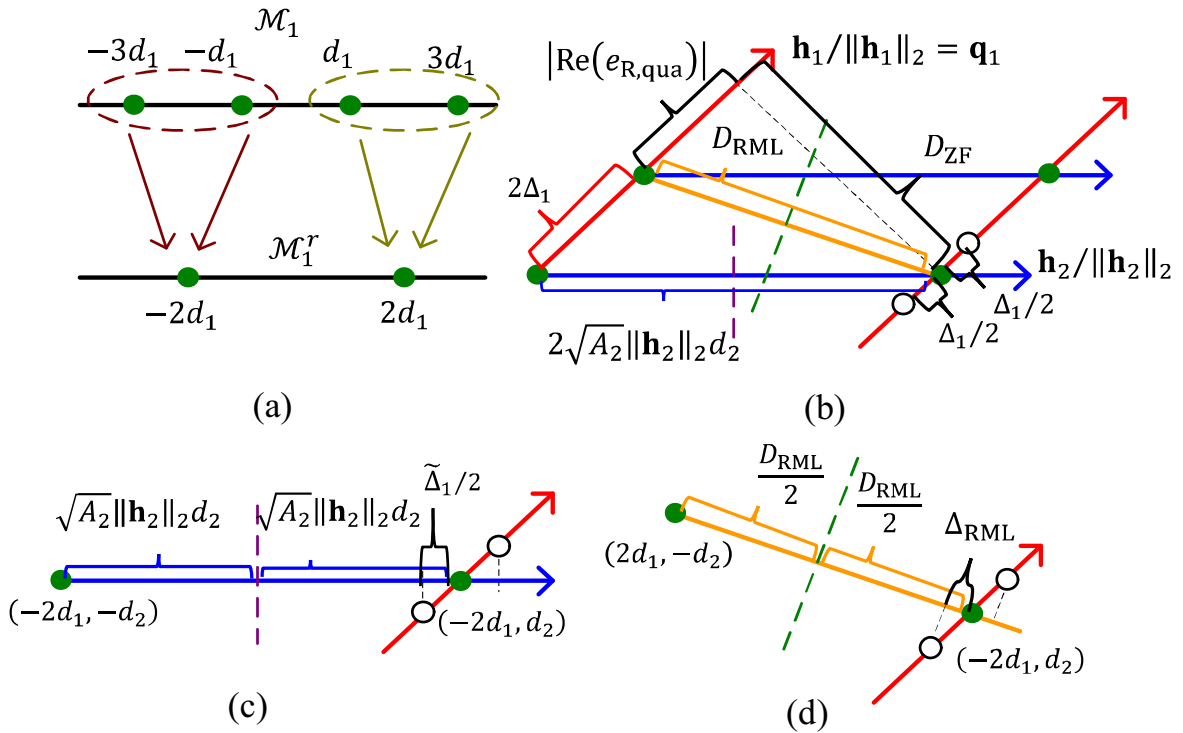


Figure 3.3: (a) The receiver treats the 4-PAM interference as being 2-PAM modulated. (b) The composite constellation space gets smaller while some extra interference is introduced to shift the transmitted sequence along  $\pm \mathbf{q}_1$ .  $D_{\text{RML}}$  and  $e_{\text{R,qua}}$  are defined similarly. The extra interference makes the transmitted sequence  $(-2d_1, d_2)$  closer to or further away from the dashed purple/green line.

to Fig. 3.3(c). The PEP is determined by the minimum distance between the green point and the dashed purple line, which plays the role similar to the decision boundary in SUD. The extra interference  $\pm\sqrt{A_1}\mathbf{h}_1d_1$  causes  $(-2d_1, d_2)$  to be closer to or further away from the purple dashed boundary only by  $\tilde{\Delta}_1/2$ , while the deviation of transmitted symbol towards the decision boundary in SUD can be up to  $3\tilde{\Delta}_1/2$  (see Fig. 3.1).

Next, we look into the pair of sequences,  $(-2d_1, d_2)$  and  $(2d_1, -d_2)$ , in Fig. 3.3(d). The vector from  $(2d_1, -d_2)$  to  $(-2d_1, d_2)$  is  $\mathbf{d}_{\text{RML}} = e_{\text{R,qua}}\mathbf{q}_1 + D_{\text{ZF}}\mathbf{q}_2$ , where  $e_{\text{R,qua}}\mathbf{q}_1$ , defined similarly, is the difference between  $2\sqrt{A_2}r_{12}d_2\mathbf{q}_1$  and the output of quantization operation by the levels stemming from  $\mathcal{M}_1^r$ . In the worst case, the extra interference makes  $(-2d_1, d_2)$  closer to the green dashed boundary by  $\Delta_{\text{RML}}$ , expressed as

$$\begin{aligned}\Delta_{\text{RML}} &= \frac{|\text{Re}(\mathbf{d}_{\text{RML}}^H (\sqrt{A_1}\mathbf{h}_1d_1))|}{\|\mathbf{d}_{\text{RML}}\|_2} \\ &= \frac{\sqrt{A_1} |\text{Re}((e_{\text{R,qua}}\mathbf{q}_1 + D_{\text{ZF}}\mathbf{q}_2)^H \mathbf{q}_1)| r_{11}d_1}{\sqrt{|e_{\text{R,qua}}|^2 + D_{\text{ZF}}^2}} \\ &= \frac{\sqrt{A_1} |\text{Re}(e_{\text{R,qua}})| r_{11}d_1}{\sqrt{|e_{\text{R,qua}}|^2 + D_{\text{ZF}}^2}}.\end{aligned}\quad (3.12)$$

Then the distance between the deviated sequence and the green dashed boundary in Fig. 3.3(d) is

$$\frac{D_{\text{RML}}}{2} - \Delta_{\text{RML}} = \frac{\sqrt{|e_{\text{R,qua}}|^2 + D_{\text{ZF}}^2}}{2} - \frac{\sqrt{A_1} |\text{Re}(e_{\text{R,qua}})| r_{11}d_1}{\sqrt{|e_{\text{R,qua}}|^2 + D_{\text{ZF}}^2}}, \quad (3.13)$$

where the definition of  $D_{\text{RML}}$  is similar to (2.13) with  $X_1$  and  $\mathcal{M}_1$  replaced by  $X_1^r$  and  $\mathcal{M}_1^r$ . The above analysis reveals that the extra interference does not affect the R-ML-MUD as much as the interference impacts on SUD. In SUD, the interference is totally disregarded, while in R-ML-MUD, the receiver partially ignores the interfering signal (which in our example is  $\sqrt{A_1}\mathbf{h}_1(X_1 - X_1^r)$ ).

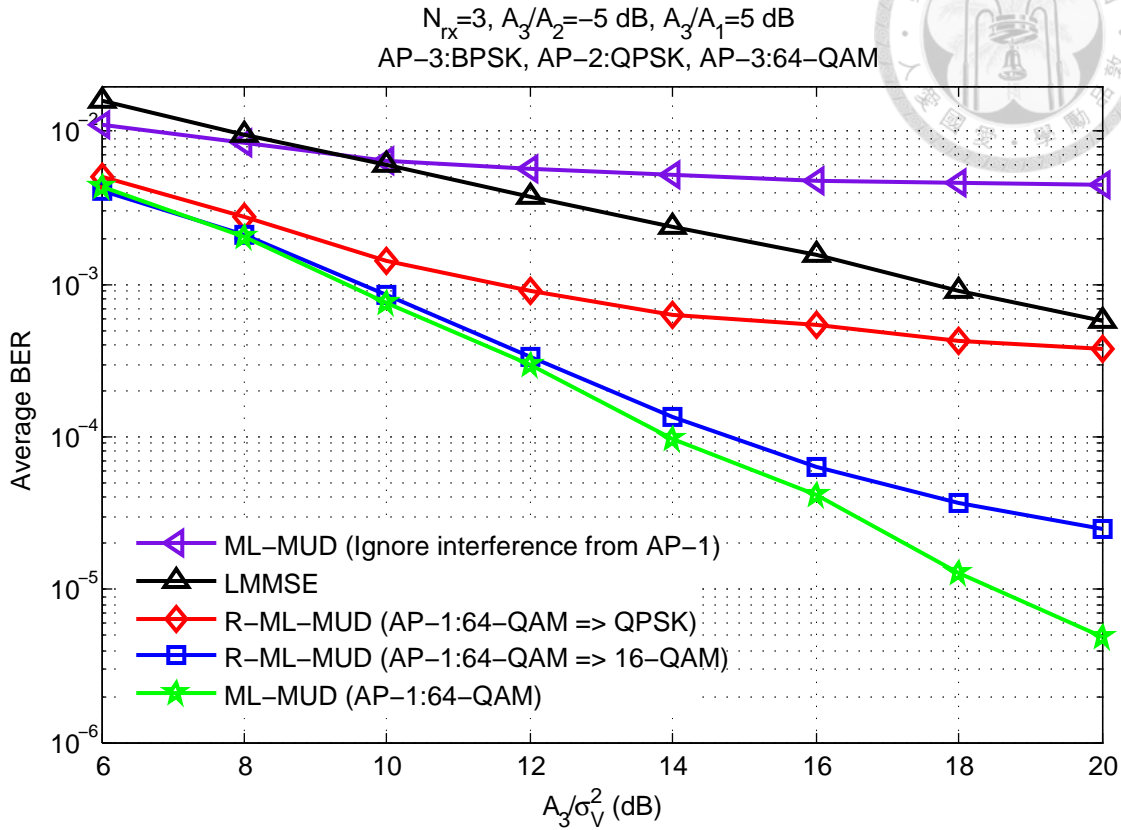


Figure 3.4: AP-3 uses BPSK to transmit the desired signal. The average BERs of R-ML-MUD with different detection complexity are plotted. The 64-QAM interference from AP-1 is ignored or treated as being 16-QAM/QPSK modulated.  $N_{rx} = 3$ ,  $\frac{A_3}{A_2} = -5 \text{ dB}$ , and  $\frac{A_3}{A_1} = 5 \text{ dB}$ .

By the same way, we are able to shrink the constellation of two-dimensional modulation such as 16-QAM shrunk to QPSK and 64-QAM shrunk to 16-QAM or QPSK, as listed in Table 3.1.

We conduct simulations in 3-AP case, in which AP-3 transmits the desired signal. AP-3, AP-2, and AP-1 use BPSK, QPSK, and 64-QAM/16-QAM, respectively. At the receiver, the interference from AP-2/AP-1 has 5 dB stronger/weaker power than the desired signal, that is,  $\frac{A_3}{A_2} = -5 \text{ dB}$  and  $\frac{A_3}{A_1} = 5 \text{ dB}$ . According to Table 3.1, the receiver shrinks the constellation of interference from AP-1. In Fig. 3.4, AP-1's signal is 64-QAM modulated. Cutting the actual computation by 75%, R-ML-MUD with  $\mathcal{M}_1^r$  of 16-QAM and ML-MUD are close to each other for  $\frac{A_3}{\sigma_v^2} < 12 \text{ dB}$ . At average



Table 3.1: The reduced-order constellation of 16-QAM and 64-QAM

Original Modulation	Reduced-order Constellation $\mathcal{M}_n^r = \{s_R^r + js_I^r\}$	$d_n$
16-QAM	QPSK: $s_R^r, s_I^r \in \{\pm 2d_n\}$	$\frac{1}{\sqrt{10}}$
64-QAM	16-QAM: $s_R^r, s_I^r \in \{\pm 2d_n, \pm 6d_n\}$ QPSK: $s_R^r, s_I^r \in \{\pm 4d_n\}$	$\frac{1}{\sqrt{42}}$

BER  $10^{-4}$ , the difference of  $\frac{A_3}{\sigma_v^2}$  between the two detection methods is merely about 1 dB. For the computational burden further reduced by a factor of 16 (i.e.  $\mathcal{M}_1^r$  of QPSK), more amount of extra interference will be introduced. R-ML-MUD is thus much worse than ML-MUD, but it is still obviously better than LMMSE in a wide range of SNR. It is also seen that the performance of ignoring AP-1's signal is very poor even though the interference is weaker than the desired signal by 5 dB at the receiver.

For AP-1's signal being 16-QAM modulated, the average BERs of different detection schemes are reported in Fig. 3.5, where R-ML-MUD shows similar behavior. For more simulation results with different parameter setting, please refer to [40].

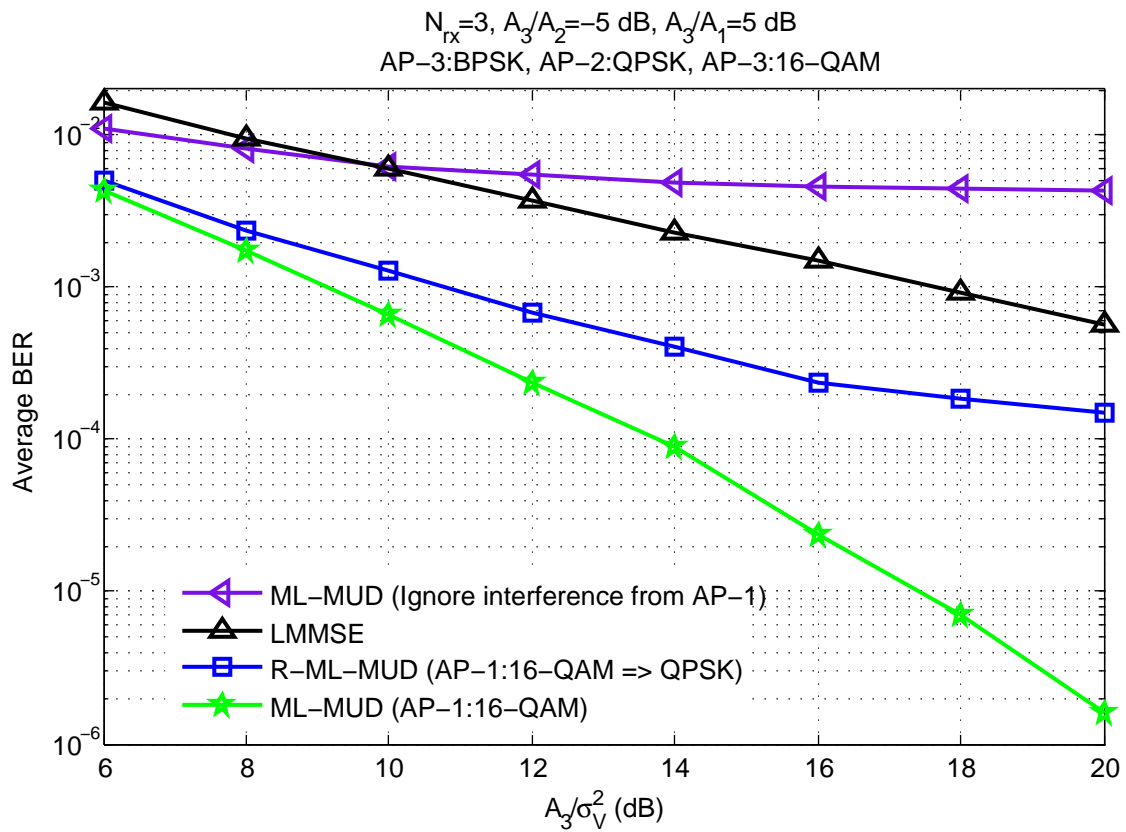


Figure 3.5: AP-3 uses BPSK to transmit the desired signal. The average BERs of R-ML-MUD with different detection complexity are plotted. The 16-QAM interference from AP-1 is ignored or treated as being QPSK modulated.  $N_{rx} = 3$ ,  $\frac{A_3}{A_2} = -5 \text{ dB}$ , and  $\frac{A_3}{A_1} = 5 \text{ dB}$ .



### 3.3 Generalized LMMSE

Alternatively, the conventional projection receiver (PR) [35, 36] can be utilized to cancel a portion of interference so as to have a smaller solution space. We rewrite (2.1) as

$$\mathbf{y} = \sum_{m=1}^K \sqrt{A_m} \mathbf{h}_m X_m + \sum_{n=K+1}^N \sqrt{A_n} \mathbf{h}_n X_n + \mathbf{v}, \quad (3.14)$$

where  $\sqrt{A_m} \mathbf{h}_m X_m$ 's for  $m = 1, \dots, K$  are the interfering signals to be cancelled. The conventional PR projects  $\mathbf{y}$  to  $\text{span}(\mathbf{h}_1, \dots, \mathbf{h}_K)^\perp$ , and then implements MUD, that is, to execute the following.

$$\left( \hat{X}_{K+1}, \dots, \hat{X}_N \right) = \arg \min_{(X_{K+1}, \dots, X_N) \in \prod_{n=K+1}^N \mathcal{M}_n} \left\| \mathbf{P} \left( \mathbf{y} - \sum_{n=K+1}^N \sqrt{A_n} \mathbf{h}_n X_n \right) \right\|_2^2, \quad (3.15)$$

where

$$\mathbf{P} = \mathbf{I}_{N_{\text{rx}}} - \mathbf{H}_I (\mathbf{H}_I^H \mathbf{H}_I)^{-1} \mathbf{H}_I^H, \quad (3.16)$$

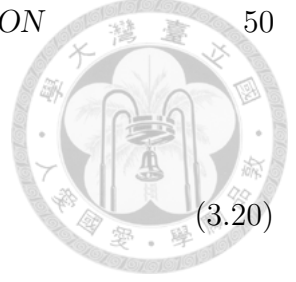
$$\mathbf{H}_I = \left[ \sqrt{A_1} \mathbf{h}_1 \cdots \sqrt{A_K} \mathbf{h}_K \right]. \quad (3.17)$$

The main drawback of conventional PR is that the desired signal's power will greatly lost when multiple interfering APs' signals are cancelled. For the signal taken into the operation of (3.15), the lost power due to projection is  $A_n \mathbf{h}_n^H (\mathbf{I}_{N_{\text{rx}}} - \mathbf{P}) \mathbf{h}_n$ , being irrelevant to  $A_m$  for  $m = 1, \dots, K$ . In other words, the amount of reduced signal power after this projection method is identical for different values of  $A_m$ 's. This is, executing (3.15) may cost a large portion of power in the desired signal even though the interfering signals to be removed are much weaker. From this observation, it seems that the traditional PR is not a reasonable approach to cancel weak interference.

Let us temporarily consider a simple scenario where there are only APs-1~K and AP-n in the virtual cell. The received signal is expressed as

$$\mathbf{y}_{K,n} = \sqrt{A_n} \mathbf{h}_n X_n + \tilde{\mathbf{v}} \quad \text{for } n = K+1, \dots, N, \quad (3.18)$$

$$\tilde{\mathbf{v}} = \sum_{m=1}^K \sqrt{A_m} \mathbf{h}_m X_m + \mathbf{v}. \quad (3.19)$$



Applying ZF on (3.18), the output SNR of the  $n$ th signal is

$$\text{SNR}_{\text{ZF},(K,n)} = \frac{A_n \mathbf{h}_n^H \mathbf{P} \mathbf{h}_n}{\sigma_V^2}, \quad (3.20)$$

which is also the resultant SNR of the  $n$ th signal after taking projection  $\mathbf{P}$  on (3.18), denoted by  $\text{SNR}_{\mathbf{P},(K,n)}$ . Thus, we write

$$\text{SNR}_{\mathbf{P},(K,n)} = \text{SNR}_{\text{ZF},(K,n)}, \quad (3.21)$$

and think of ZF as a special case of the conventional projection to cancel all interfering signals  $\sqrt{A_m} \mathbf{h}_m X_m$ 's for  $m = 1, \dots, K$ . On the other hand, we can also view LMMSE as a special case of some other projection. When LMMSE is applied to (3.18), the weighting vector  $\mathbf{w}_n$  for  $\sqrt{A_n} \mathbf{h}_n X_n$  is

$$\mathbf{w}_n = \sqrt{A_n} \mathbf{C}_{\tilde{\mathbf{v}}}^{-1} \mathbf{h}_n, \quad (3.22)$$

$$\mathbf{C}_{\tilde{\mathbf{v}}} = \mathbf{H}_I \mathbf{H}_I^H + \sigma_V^2 \mathbf{I}_{N_{\text{rx}}}. \quad (3.23)$$

After LMMSE, AP- $n$ 's signal has SINR

$$\text{SINR}_{\text{LMMSE},(K,n)} = \frac{A_n \mathbf{w}_n^H \mathbf{h}_n \mathbf{h}_n^H \mathbf{w}_n}{\mathbf{w}_n^H \mathbf{C}_{\tilde{\mathbf{v}}} \mathbf{w}_n}. \quad (3.24)$$

Define a new projection matrix  $\mathbf{G} \triangleq \mathbf{w}_n (\mathbf{w}_n^H \mathbf{w}_n)^{-1} \mathbf{w}_n^H$ . Suppressing  $\sqrt{A_m} \mathbf{h}_m X_m$ 's by  $\mathbf{G}$  leads to

$$\mathbf{G} \mathbf{y}_{K,n} = \frac{\mathbf{w}_n^H \mathbf{y}_{K,n}}{\|\mathbf{w}_n\|_2^2} \mathbf{w}_n. \quad (3.25)$$

Then the SINR of the  $n$ th signal, denoted by  $\text{SINR}_{\mathbf{G},(K,n)}$ , is

$$\text{SINR}_{\mathbf{G},(K,n)} = \frac{\text{E} \left[ \left\| \sqrt{A_n} \mathbf{G} \mathbf{h}_n X_n \right\|_2^2 \right]}{\text{E} \left[ \left\| \mathbf{G} \tilde{\mathbf{v}} \right\|_2^2 \right]} = \text{SINR}_{\text{LMMSE},(K,n)}. \quad (3.26)$$

From (3.21) and (3.26), the resultant SNR difference between the projections  $\mathbf{P}$  and  $\mathbf{G}$  is equal to the output SNR gap between ZF and LMMSE, which is larger for higher values of  $\frac{A_n}{A_m}$ 's, as indicated in Section 2.3 (refer to (2.32)).  $\mathbf{G}$  projects the received signal towards  $\text{span}(\mathbf{w}_n)$ , where there is some residue of interference from APs- $1 \sim K$ ,

but the amount of energy will be retained in AP- $n$ 's signal more. In addition, from (3.22) and (3.23), the new projection method adjusts  $\text{span}(\mathbf{w}_n)$  according to the values of  $A_1, A_2, \dots, A_K$  to yield better SINR than the conventional projection  $\mathbf{P}$  does.

Now we go back to (3.14), the situation of interest. In order to suppress  $\sum_{m=1}^K \sqrt{A_m} \mathbf{h}_m X_m$  while retaining more energy in APs- $(K+1) \sim N$ 's signals, we define

$$\mathbf{G} \triangleq \mathbf{W} (\mathbf{W}^H \mathbf{W})^{-1} \mathbf{W}^H, \quad (3.27)$$

$$\mathbf{W} = [\mathbf{w}_{K+1} \mathbf{w}_{K+2} \cdots \mathbf{w}_N], \quad (3.28)$$

where  $\mathbf{w}_n$  has already been given in (3.22). With  $\mathbf{G}$ , the receiver searches solution via

$$\left( \hat{X}_{K+1}, \dots, \hat{X}_N \right) = \arg \min_{(X_{K+1}, \dots, X_N) \in \prod_{n=K+1}^N \mathcal{M}_n} \left\| \mathbf{G} \left( \mathbf{y} - \sum_{n=K+1}^N \sqrt{A_n} \mathbf{h}_n X_n \right) \right\|_2^2. \quad (3.29)$$

From now on, the multiplication of  $\mathbf{G}$  is termed "GLMMSE" to stand for the generalization of LMMSE, and the conventional PR is called "PR" for brevity. Let  $\tilde{\mathbf{d}}$  be any unit vector in  $\text{span}(\mathbf{w}_{K+1} \mathbf{w}_{K+2} \cdots \mathbf{w}_N)$ , then  $\tilde{\mathbf{d}}$  can be expressed as  $\tilde{\mathbf{d}} = \sum_{n=K+1}^N t_n \mathbf{w}_n$  with  $\|\tilde{\mathbf{d}}\|_2 = 1$ . After GLMMSE, the interference from APs- $1 \sim K$  plus noise in the direction of any  $\tilde{\mathbf{d}}$  has power

$$\begin{aligned} \mathbb{E} \left\{ \left| \tilde{\mathbf{d}}^H \mathbf{G} \tilde{\mathbf{v}} \right|^2 \right\} &= \mathbb{E} \left\{ \tilde{\mathbf{d}}^H \tilde{\mathbf{v}} \tilde{\mathbf{v}}^H \mathbf{d} \right\} = \left( \sum_{n=K+1}^N t_n \mathbf{w}_n \right)^H \mathbf{C}_{\tilde{\mathbf{v}}} \left( \sum_{\ell=K+1}^N t_\ell \mathbf{w}_\ell \right) \\ &= \sum_{n=K+1}^N \sum_{\ell=K+1}^N t_n^* t_\ell \mathbf{w}_n^H \mathbf{C}_{\tilde{\mathbf{v}}} \mathbf{w}_\ell. \end{aligned} \quad (3.30)$$

Besides,

$$\left| \mathbf{w}_n^H \mathbf{C}_{\tilde{\mathbf{v}}} \mathbf{w}_l \right|^2 \leq \left\| \mathbf{C}_{\tilde{\mathbf{v}}}^{\frac{1}{2}} \mathbf{w}_n \right\|_2^2 \left\| \mathbf{C}_{\tilde{\mathbf{v}}}^{\frac{1}{2}} \mathbf{w}_l \right\|_2^2 = (\mathbf{w}_n^H \mathbf{C}_{\tilde{\mathbf{v}}} \mathbf{w}_n) (\mathbf{w}_l^H \mathbf{C}_{\tilde{\mathbf{v}}} \mathbf{w}_l), \quad (3.31)$$

where the inequality follows from Cauchy-Schwarz inequality. In (3.18), LMMSE selects the weighting vector  $\mathbf{w}_n$  to maximum the SINR of AP- $n$ 's signal [28, 33].

When  $\text{SINR}_{\text{LMMSE},(K,n)}$  is sufficiently high,  $\mathbf{w}_n^H \mathbf{C}_{\tilde{\mathbf{v}}} \mathbf{w}_n$  will be very small compared

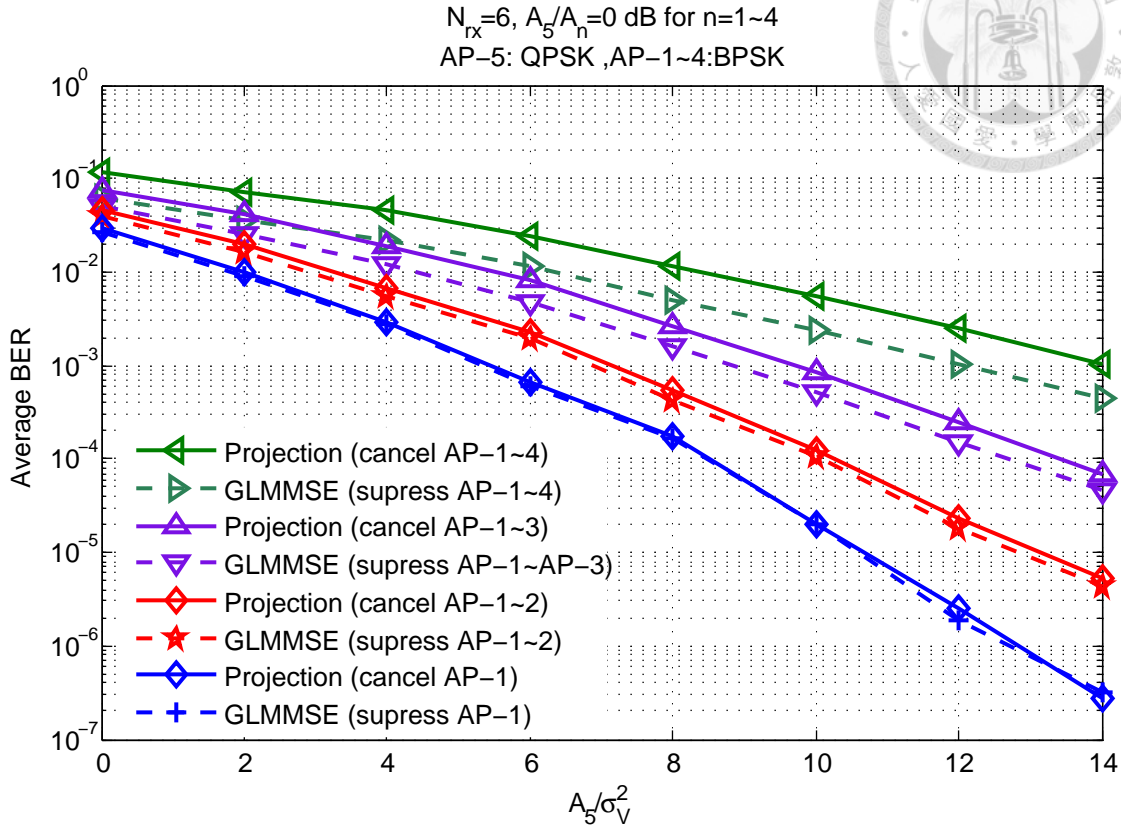


Figure 3.6: The average BERs are plotted for PR and GLMMSE. The desired signal from AP-5 is QPSK-modulated while APs-1~4 use BPSK.  $N_{rx} = 6$ , and  $\frac{A_5}{A_4} = \frac{A_5}{A_3} = \frac{A_5}{A_2} = \frac{A_5}{A_1} = 0 \text{ dB}$ .

to  $A_n \mathbf{w}_n^H \mathbf{h}_n \mathbf{h}_n^H \mathbf{w}_n$ . Therefore, from (3.31),  $E \left\{ \left| \tilde{\mathbf{d}}^H \mathbf{G} \tilde{\mathbf{v}} \right|^2 \right\}$  can be small compared to AP- $n$ 's signal power  $A_n \mathbf{h}_n^H \mathbf{G} \mathbf{h}_n$ .

Now we investigate the behavior of GLMMSE via simulations of 5-AP case. The desired signal from AP-5 is QPSK modulated while APs-1~4 adopt BPSK. We observe the performance of PR and GLMMSE that suppress different numbers of APs' signals under different values of SIRs,  $\frac{A_5}{A_1}, \dots, \frac{A_5}{A_4}$ . The average BERs with  $\frac{A_5}{A_n} = 0 \text{ dB for } n = 1 \sim 4$  are plotted in Fig. 3.6, where GLMMSE is close to PR if only the interference from AP-1 or APs-1~2 is suppressed. For the interference from APs-1~3 or APs-1~4 being suppressed, GLMMSE is clearly better than PR. If the interfering signals are weaker than the desired signal at the receiver, the performance

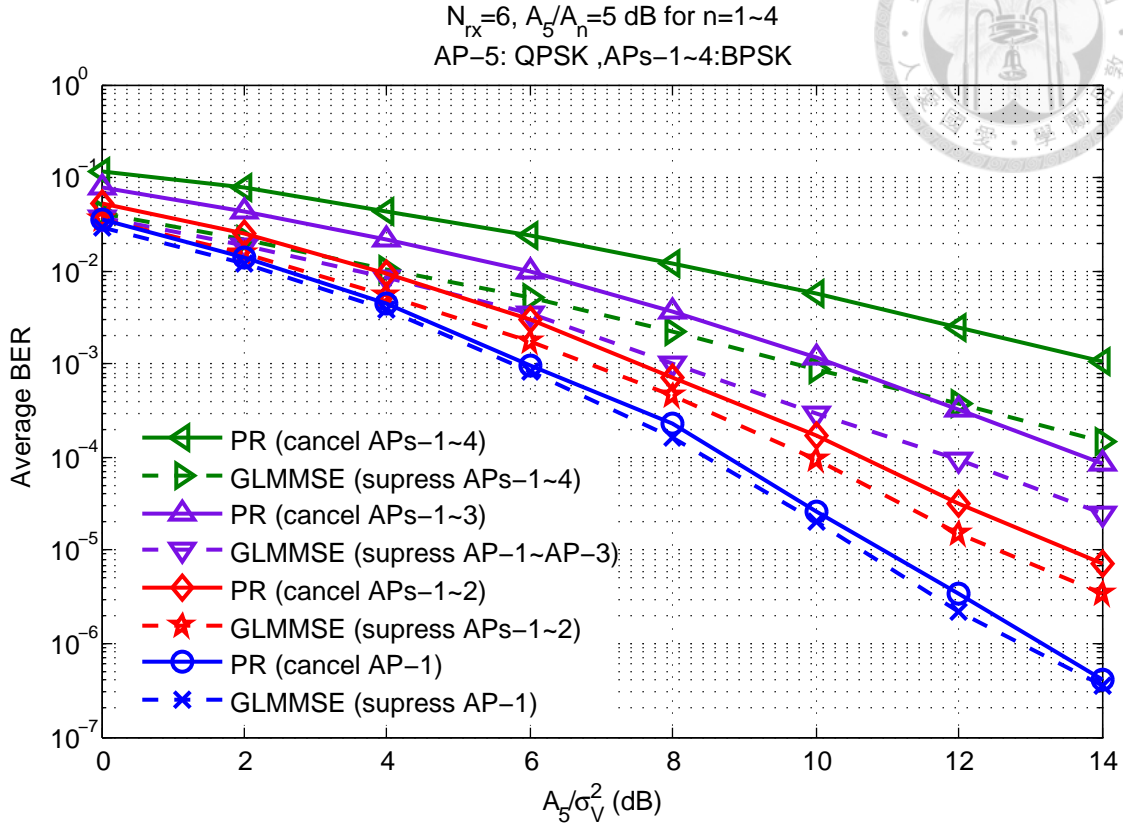
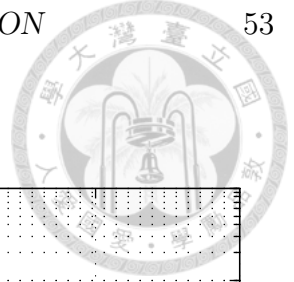


Figure 3.7: The average BERs are plotted for PR and GLMMSE. The desired signal from AP-5 is QPSK-modulated while APs-1~4 use BPSK.  $N_{rx} = 6$ , and  $\frac{A_5}{A_4} = \frac{A_5}{A_3} = \frac{A_5}{A_2} = \frac{A_5}{A_1} = 5$  dB.

gap will be more noticeable, and gets wider when suppressing more interfering APs' signals, as shown in Fig. 3.7, where  $\frac{A_5}{A_n} = 5$  dB for  $n = 1 \sim 4$ .

In the same 5-AP case with  $\frac{A_5}{A_4} = 0$  dB and  $\frac{A_5}{A_3} = \frac{A_5}{A_2} = \frac{A_5}{A_1} = 0, 3, 6$  dB, we report the results in Fig. 3.8, where the receiver cancels the interference from APs-1~3. It can be seen that the weaker the cancelled interference is, the better GLMMSE behaves. However, the performance of PR remains unchanged. This exhibits that the advantage of GLMMSE over PR is similar to the advantage of LMMSE over ZF.

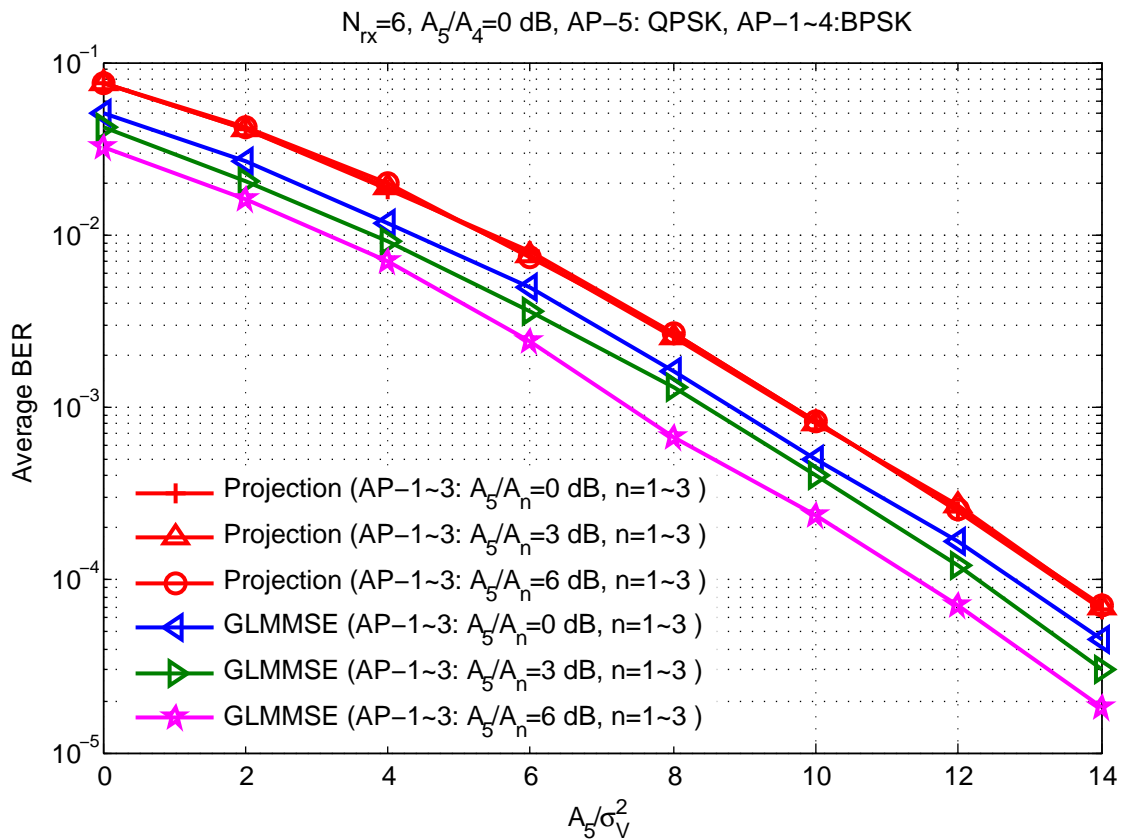
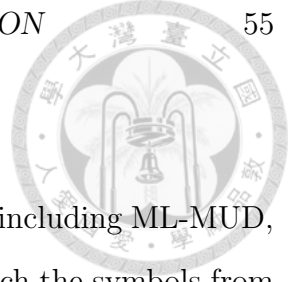


Figure 3.8: The average BERs are plotted for PR and GLMMSE. The desired signal from AP-5 is QPSK-modulated while APs-1~4 use BPSK.  $N_{rx} = 6$ , and  $\frac{A_5}{A_4} = 0$  dB, and  $\frac{A_5}{A_3} = \frac{A_5}{A_2} = \frac{A_5}{A_1} = 0, 3, 6$  dB.





### 3.4 Case Study by Simulations

Further simulations are conducted to compare different schemes, including ML-MUD, R-ML-MUD, GLMMSE, PR, LMMSE, and LMMSE-SIC, in which the symbols from interfering APs are detected and subtracted from the received signal successively in the order of decreasing received power. In 3~5-AP cases, we examine the receiving performance of QPSK signals, corresponding to the ultra-low latency transmissions of desired data.

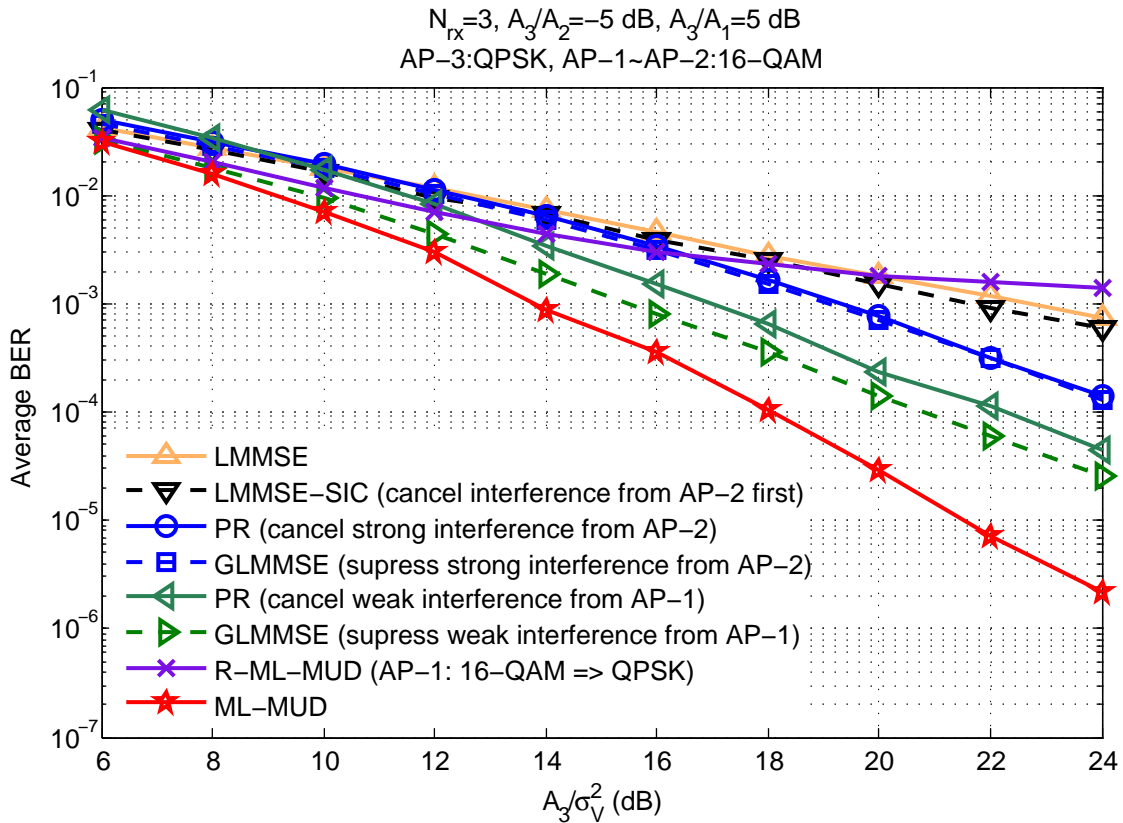


Figure 3.9: The average BERs are plotted for different detection schemes. The desired signal from AP-3 is QPSK modulated while both AP-1 and AP-2 use 16-QAM.  $N_{rx} = 3$ ,  $\frac{A_3}{A_2} = -5$  dB, and  $\frac{A_3}{A_1} = 5$  dB.

First of all, in 3-AP case, where AP-3 transmits the desired data that is interfered by 16-QAM signals from AP-1 and AP-2. Other parameters are set as  $N_{rx} = 3$ ,  $\frac{A_3}{A_2} = -5$  dB, and  $\frac{A_3}{A_1} = 5$  dB. As shown in Fig. 3.9, applying R-ML-MUD to AP-1's

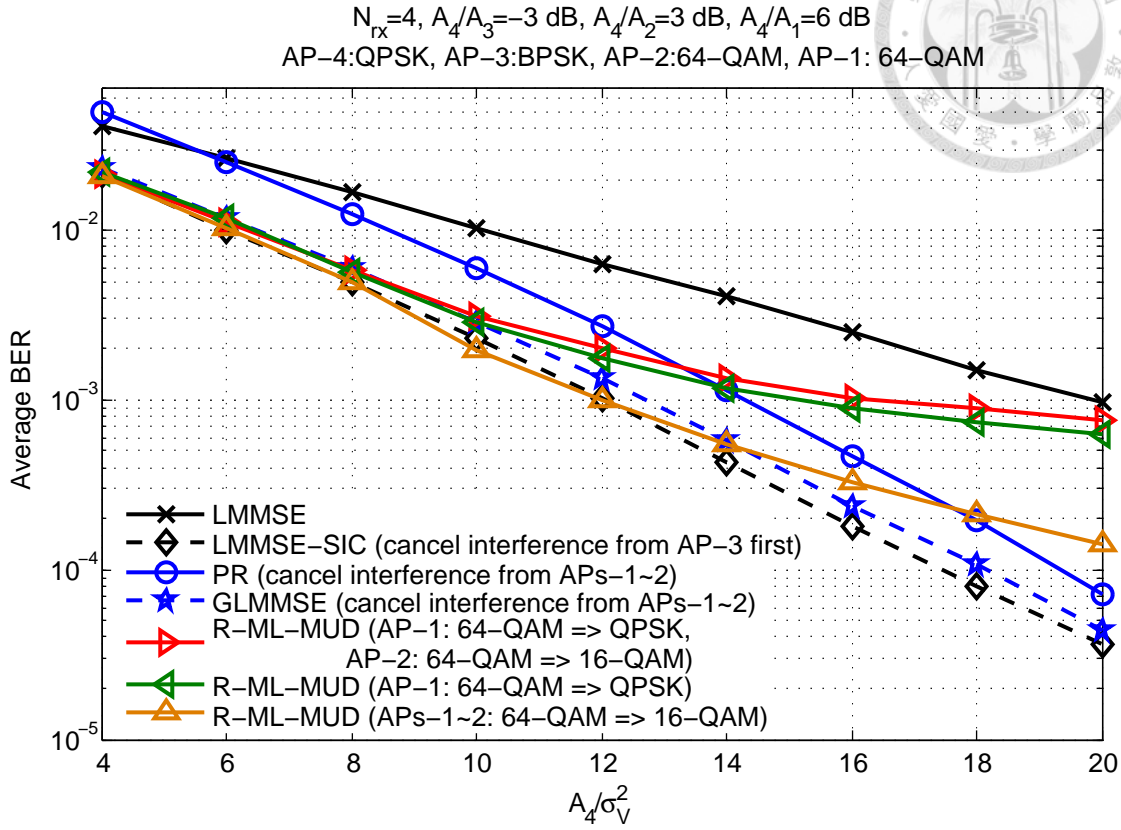


Figure 3.10: The average BERs is plotted for different detection schemes. The desired signal from AP-4 is QPSK modulated while both AP-1/2 and AP-3 use 64-QAM and BPSK, respectively.  $N_{rx} = 4$ ,  $\frac{A_4}{A_3} = -3$  dB,  $\frac{A_4}{A_2} = 3$  dB, and  $\frac{A_4}{A_1} = 6$  dB.

signal does not lead to satisfactory performance because this 16-QAM interference is not weak enough and treating it as QPSK signal brings too much extra interference. If the weak interfering signal is suppressed by GLMMSE or PR, the performance is much better. From the green curves in Fig 3.9, we can see the SNR gain of GLMMSE over PR, however, there is almost no difference between these two methods when the strong interference from AP-2 is suppressed (see the blue curves). As indicated in Section 2.2, for identical modulation, stronger interference is generally less harmful to ML-MUD, hence it is better to suppress weak interference from AP-1 rather than strong interference from AP-2, as observed from the blue and green curves in Fig 3.9.

Next, we investigate 4-AP case, where the desired signal is from AP-4. The signals from AP-1 and AP-2 are 64-QAM modulated, and weaker than the desired signal

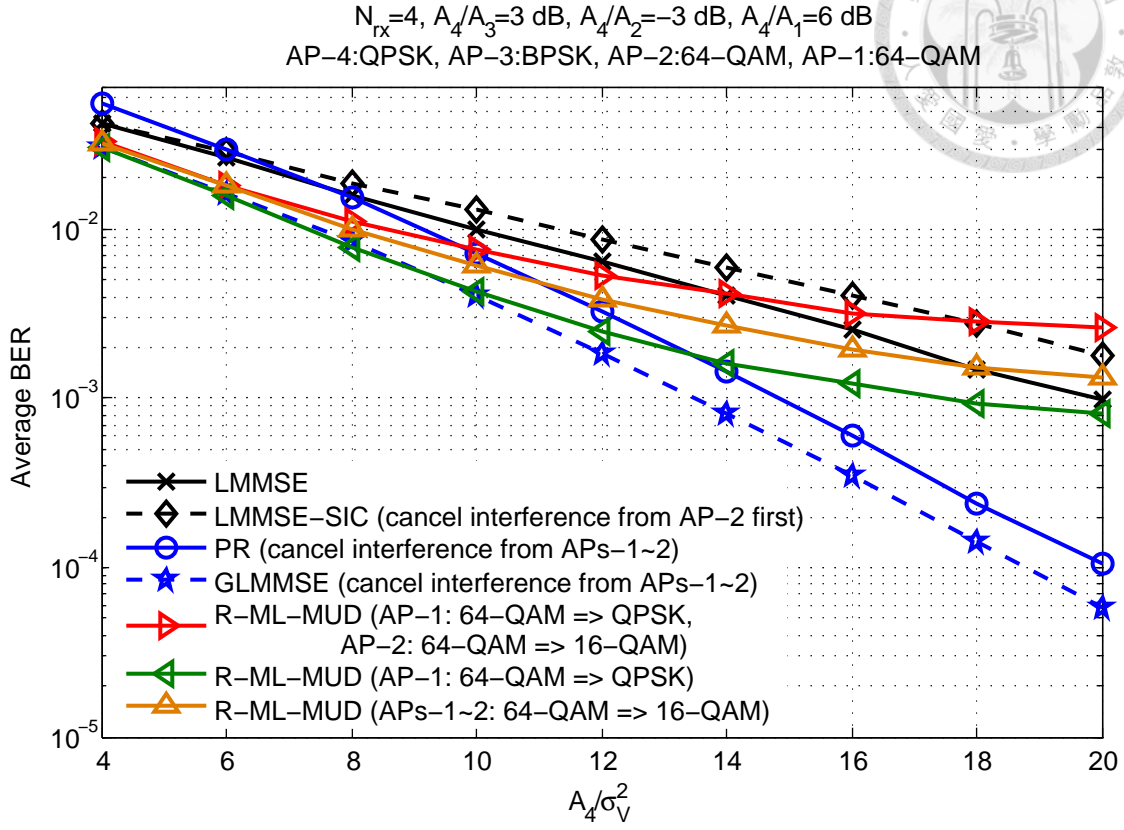


Figure 3.11: The average BERs are plotted for different detection schemes. The desired signal from AP-4 is QPSK modulated while both AP-1/2 and AP-3 use 64-QAM and BPSK, respectively.  $N_{rx} = 4$ ,  $\frac{A_4}{A_3} = 3$  dB,  $\frac{A_4}{A_2} = -3$  dB, and  $\frac{A_4}{A_1} = 6$  dB.

respectively by 6 dB and 3 dB at the receiver side, i.e.  $\frac{A_4}{A_1} = 6$  dB and  $\frac{A_4}{A_2} = 3$  dB. The BPSK signal from AP-3 is stronger than the desired signal by 3 dB, that is,  $\frac{A_4}{A_3} = -3$  dB. From Fig. 3.10, we note that LMMSE-SIC is better than our proposed methods. Nevertheless, as shown in Fig. 3.11, when the 64-QAM/BPSK interference from AP-2/AP-3 is stronger/weaker than the desired signal by 3 dB ( $\frac{A_4}{A_2} = -3$  dB and  $\frac{A_4}{A_3} = 3$  dB), LMMSE-SIC is not well-behaved and even worse than LMMSE. From Fig. 3.10 and Fig. 3.11, it is clear that LMMSE-SIC is sensitive to the modulation of stronger interference if the detection order is determined only based on the received power or SINRs, as the general LMMSE-SIC implementation.

Finally, we design a 5-AP scenario with only 4 receiving antennas, and the desired

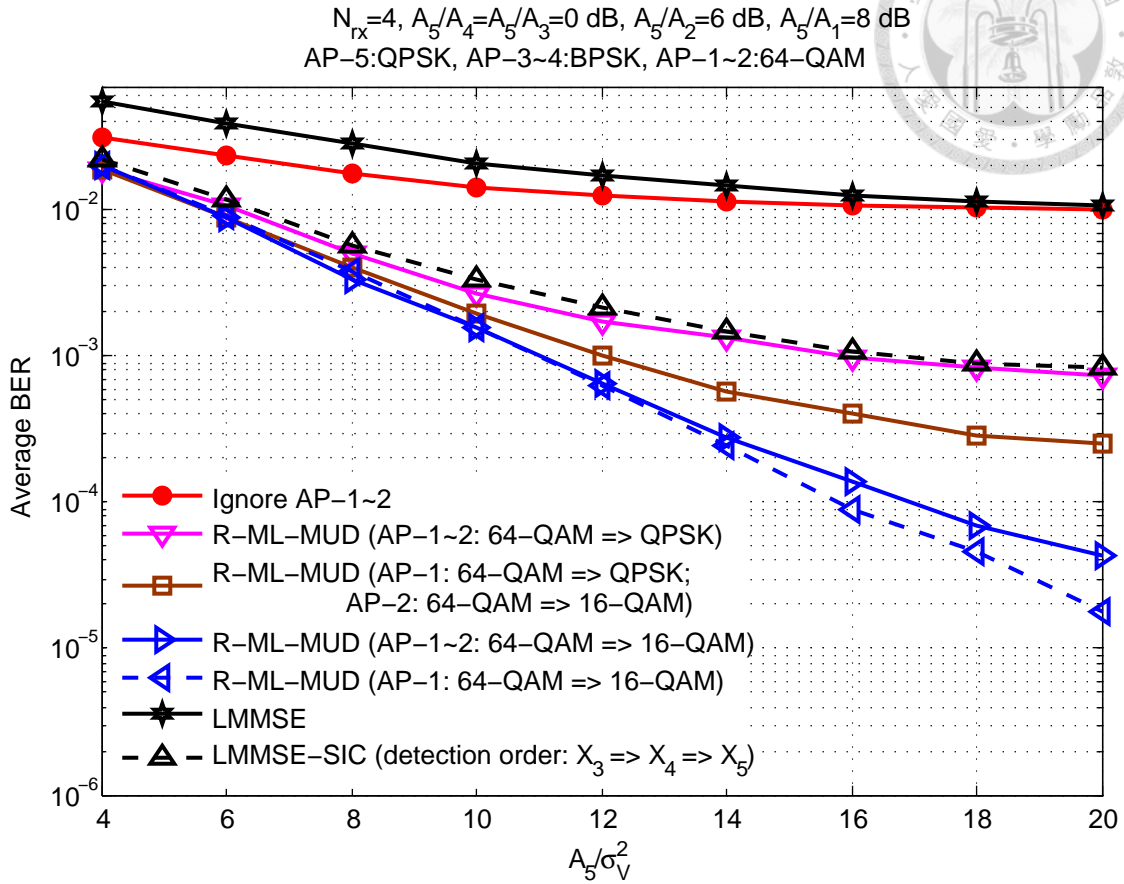


Figure 3.12: The average BERs are plotted for different detection schemes. The desired signal from AP-5 is QPSK modulated while both APs-1~2 and APs-3~4 adopt BPSK and 64-QAM, respectively.  $N_{rx} = 4$ ,  $\frac{A_5}{A_4} = \frac{A_5}{A_3} = 0 \text{ dB}$ ,  $\frac{A_5}{A_2} = 6 \text{ dB}$ , and  $\frac{A_5}{A_1} = 8 \text{ dB}$ .

signal is from AP-5. APs-1~2 and APs-3~4 adopt 64-QAM and BPSK, respectively. SIRs are set as  $\frac{A_5}{A_4} = \frac{A_5}{A_3} = 0 \text{ dB}$ ,  $\frac{A_5}{A_2} = 6 \text{ dB}$ , and  $\frac{A_5}{A_1} = 8 \text{ dB}$ . In Fig. 3.12, we report the average BERs of R-ML-MUD with different reduced-order constellations, which are all better than LMMSE-SIC. It also reveals that ignoring the interference from APs-1~2 or applying LMMSE is poor. The average BERs of GLMMSE and PR that suppress the interference from APs-1~2 are plotted in Fig. 3.13. Since the receiver has only 4 antennas,  $\mathbf{G}$  is constructed from  $\mathbf{W} = [\mathbf{w}_4 \ \mathbf{w}_5]$  to project the signal towards a subspace of dimension 2, and the advantage of GLMMSE over PR is seen again. We also show the results of the integration of GLMMSE/PR with R-ML-MUD

that cancels AP-2's signal and shrinks  $\mathcal{M}_1$  to  $\mathcal{M}_1^r$  of 16-QAM, and the performance can be closer to R-ML-MUD with the solution space shrunk merely by a factor of 16 (the blue curve in Fig. 3.13).

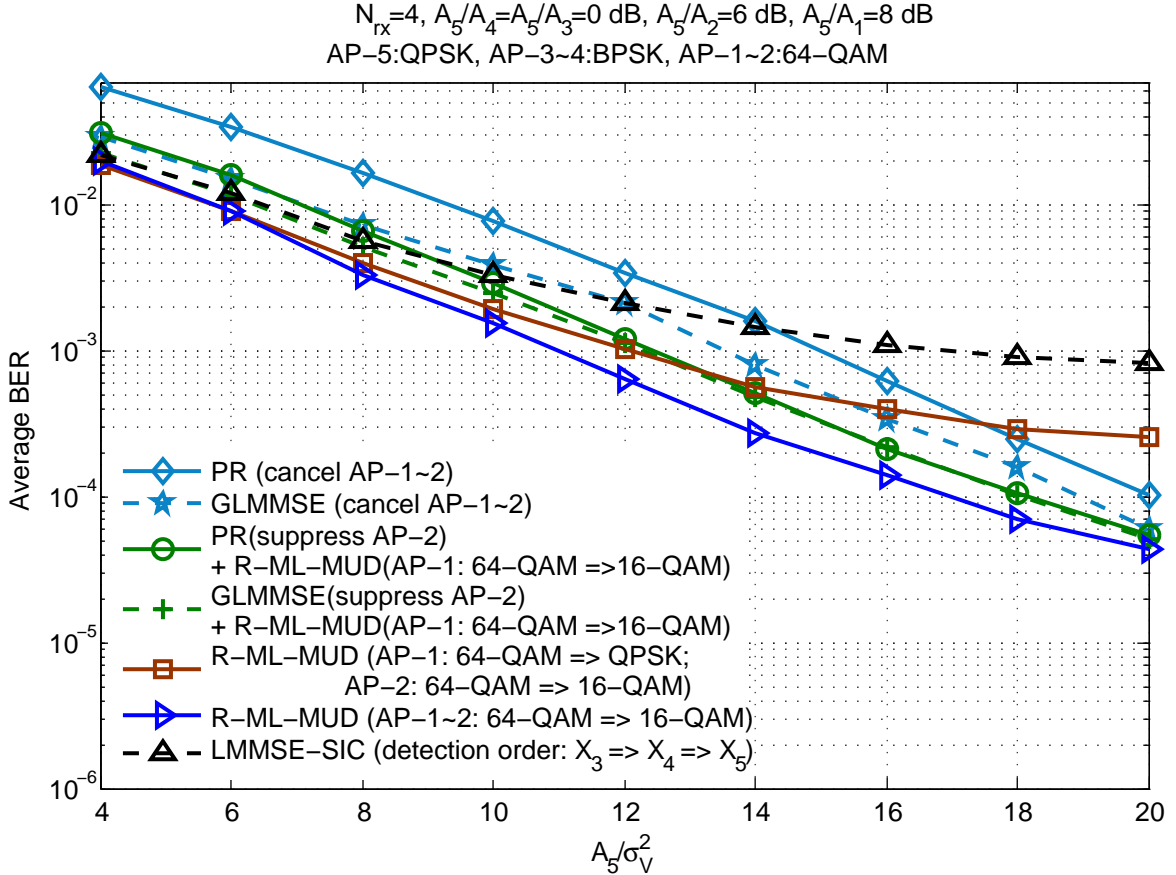


Figure 3.13: The average BERs are plotted for different detection schemes. The desired signal from AP-5 is QPSK modulated while both APs-1~2 and APs-3~4 adopt BPSK and 64-QAM, respectively.  $N_{\text{rx}} = 4$ ,  $\frac{A_5}{A_4} = \frac{A_5}{A_3} = 0 \text{ dB}$ ,  $\frac{A_5}{A_2} = 6 \text{ dB}$ , and  $\frac{A_5}{A_1} = 8 \text{ dB}$ .

### 3.5 Summary

Leveraging the feature of downlink transmissions, R-ML-MUD is proposed to reduced the complexity of MUD by partially ignoring interference. The saving in computation depends on the extent to which the interference is ignored. For instance, if a 64-QAM interfering signal is treated as being 16-QAM or QPSK, the computation burden is

decreased by a factor of 4 or 16, in other words, the actual computation is cut down by 75% or 93.75% for each desired data symbol to be estimated.

Another proposed method is GLMMSE to partially suppress interference, which has obvious SNR gain over PR. The computation saving in MUD operation is easily derived from the number and modulation orders of suppressed interfering signals. The question “Which interfering signals to cancel?” is equivalent to “Which interfering signals to jointly detect with the desired signal?”. From Chapter 2, we know that it is generally better to cancel weak interference and include strong interference in the execution of MUD.

The proposed methods and their combination provide flexible trade-off between complexity and performance, and are shown to yield satisfactory performance even when LMMSE and LMMSE-SIC can not function well. To end this chapter, we suggest several extended works in the following.

### 1) Extension from R-ML-MUD

Similar to the concept of interference-ignorant SUD or power-domain non-orthogonal multiple access (NOMA) [72], R-ML-MUD exploits the significant differences in received signal powers. To some extent, we may say that R-ML-MUD partially ignore the weak interference. Compared to SUD or power-domain NOMA, R-ML-MUD has higher detection complexity, but the strict received power ratio constraint can be relaxed. The detailed analysis of applying R-ML-MUD to 5G NOMA scenario will be interesting.

As a well-known complexity reduction method, sphere decoding [65, 66] searches ML solution from a subset of a large composite constellation space. Differently, R-ML-MUD shrinks the large solution space to a smaller one. Combing the two methods, the receiver can reduce the modulation order of interference first, then apply sphere decoding. That is, the integration of R-ML-MUD and sphere decoding searches the solution from a subset of a smaller solution space to save more detection computation

in downlink, which serves a future research.

## 2) Extension from GLMMSE

R-ML-MUD will not be applicable if the desired signal is weaker than interference, and the performance of GLMMSE to cancel strong interference may not be good enough. In this situation, we can generalize the concept of LMMSE-SIC. That is, the receiver first decodes several stronger interfering signals via GLMMSE detection, subtract their estimates from the received signal, then decode the desired signal by ML-MUD. We name this scheme GLMMSE-SIC, and further investigation is required to demonstrate its effectiveness.









## Chapter 4

# Two-Stage Inter-Carrier Interference Suppression

Our work in Chapter 2 and Chapter 3 is implicitly based on the assumption of perfect synchronization. In this chapter, we take time and frequency asynchronous issues into consideration. The signals from different APs experience different propagation delays to reach the receiver on the vehicle. The time differences of arrival (TDOA) may cause ISI and ICI [45]. By the commonly applied stochastic geometry modelling [46], we first show that the probability that TDOA-induced ISI/ICI occurs can be very small, and our probabilistic analysis also helps with the future system parameter design. Indeed, the CFO creates serious concerns. Different APs have different oscillators, leading to multiple CFOs that can not be compensated simultaneously at the vehicle, bringing serious ICI.

In downlink, it is not reasonable and difficult to infer channel conditions of sub-carriers not allocated for the receiver. Hence it is not feasible to suppress ICI by conventional LMMSE or whitening technique that needs knowing ICI covariance. The methods to address ICI terms originating inside and outside the allocated radio slices should be different. We therefore propose a two-stage ICI suppression scheme to separately deal with them.

In this chapter, we develop a method to resolve ICI challenge in a more practical way. Without the need to estimate the covariance of far ICI, we construct a pseudo

covariance matrix using CFOs estimate to replace the true ICI covariance matrix. The proposed operation is called Pseudo-ICI-W (P-ICI-W) [67] and followed by the joint detection of desired signal and several dominant ICI terms. Via simulations, we show that P-ICI-W can approach the ideal whitening technique in terms of SINR and BER. After P-ICI-W, the remaining dominant ICI terms from multiple associated APs can collectively make the joint detection very computationally demanding. Sphere decoding is capable of reducing detection complexity substantially, but the complexity of sphere decoding still grows exponentially with the number of jointly detected data symbols [73], thus further suppressing some of remaining ICI terms is desirable, and can be implemented by GLMMSE [38] or PR [35, 36]. Overall, the proposed signal processing has two stages: (i) P-ICI-W to tackle far/residual ICI (ii) GLMMSE or PR to partially suppress the dominant ICI terms that remain after pseudo-whitening.

Finally, we demonstrate the application of proposed scheme to the scenario that APs adopt space-time block codes (STBCs) to strengthen the reliability of uRLLC services. In addition to Alamouti coding [68], Complex Interleaved Orthogonal Design (CIOD) [69] suitable for asynchronous transmissions is taken into the two-stage processing and evaluated via simulations to complete downlink uRLLC design.

## 4.1 Asynchronous Modelling

Unlike the conventional cellular system where the arrival times of uplink signals can be made approximately aligned at the base station (BS) by adjusting transmit timing of each user equipment (UE). But in our downlink scenario, it seems not possible to implement a transmission-timing control across different APs that serve multiple virtual cells because the amount of transmission-timing offset for one vehicle may not applicable to another. Likewise, it is very challenging to pre-compensate CFOs from APs.

In Subsection 4.1.1, we derive the probability of TDOA-related ISI/ICI, which

can be little in small cell deployment. So we focus on CFO-induced ICI in this dissertation. Subsection 4.1.2 reviews the signal model with CFOs, based on which our technique is developed.

### 4.1.1 Probabilistic Analysis of TDOA-Induced ISI

The distances between APs and the vehicle are different, thus the signals from serving APs of virtual cell arrive with various propagation delays. If the TDOA together with the lengths of channel impulse responses (CIRs) exceed the cyclic prefix (CP) length, ISI and ICI will occur [45]. The probability of this event depends on the dimension of virtual cell (i.e. the number of APs serving in a virtual cell), AP density, and the CP length. Next we derive this probability based on the widely adopted stochastic geometry model [46].

Taking the snapshot at any time instant, assume that the vehicle's position is the origin of  $\mathbb{R}^2$ , and APs are distributed as a two-dimensional homogeneous Poisson point process (PPP) with density  $\lambda_{\text{ap}}$ . Suppose that the vehicle is served by the  $N$  nearest APs whose distances to the vehicle are  $U_1, \dots, U_N$ . Let  $U_{(1)} = \min_{1 \leq n \leq N} U_n$  and  $U_{(N)} = \max_{1 \leq n \leq N} U_n$ . ISI and ICI will happen if

$$U_{(N)} - U_{(1)} > \Delta d, \quad (4.1)$$

where  $\Delta d = c(t_{\text{cp}} - t_{\text{ch}})$ ,  $c$  is the light speed,  $t_{\text{cp}}$  and  $t_{\text{ch}}$  are the lengths of CP and CIR. The probability density function (PDF) of  $U_{(N)}$  is

$$f_{U_{(N)}}(u_{(N)}) = \frac{2}{\Gamma(N)} (\lambda_{\text{ap}} \pi)^N u_{(N)}^{2N-1} e^{-\lambda_{\text{ap}} \pi u_{(N)}^2}. \quad (4.2)$$

Let  $U$  be the distance between the vehicle and any AP, which is closer to the vehicle than the furthest serving AP. The cumulative distribution function (CDF) of  $U$  and PDF of  $U_{(1)}$  conditioned on  $U_{(N)} = u_{(N)}$  are given as follows.



$$\begin{aligned}
 F_{U|U(N)}(u|u(N)) &= \frac{u^2}{u_{(N)}^2}, \\
 f_{U(1)|U(N)}(u(1)|u(N)) &= \frac{d}{du(1)} \left[ 1 - \left( 1 - \frac{u_{(1)}^2}{u_{(N)}^2} \right)^{N-1} \right] = (N-1) \frac{2u(1)}{u_{(N)}^2} \left( 1 - \frac{u_{(1)}^2}{u_{(N)}^2} \right)^{N-2}.
 \end{aligned} \tag{4.3}$$

From (4.2) and (4.3), the joint PDF of  $U(1)$  and  $U(N)$  is

$$\begin{aligned}
 f_{U(1)U(N)}(u(1), u(N)) &= f_{U(1)|U(N)}(u(1)|u(N)) f_{U(N)}(u(N)) \\
 &= \frac{4(\lambda_{\text{ap}}\pi)^N}{\Gamma(N-1)} u(1)u(N) (u_{(N)}^2 - u_{(1)}^2)^{N-2} e^{-\lambda_{\text{ap}}\pi u_{(N)}^2}.
 \end{aligned} \tag{4.4}$$

The probability of  $U(N) - U(1) > \Delta d$  can be derived as

$$\begin{aligned}
 &p\{U(N) - U(1) > \Delta d\} \\
 &= \int_{\Delta d}^{\infty} \int_0^{u(N)-\Delta d} f_{U(1)U(N)}(u(1), u(N)) du(1)du(N) \\
 &= \frac{4(\lambda_{\text{ap}}\pi)^N}{\Gamma(N-1)} \int_{\Delta d}^{\infty} u(N) e^{-\lambda_{\text{ap}}\pi u_{(N)}^2} \int_0^{u(N)-\Delta d} u(1) (u_{(N)}^2 - u_{(1)}^2)^{N-2} du(1)du(N) \\
 &= \frac{4(\lambda_{\text{ap}}\pi)^N}{\Gamma(N-1)} \int_{\Delta d}^{\infty} u(N) e^{-\lambda_{\text{ap}}\pi u_{(N)}^2} \int_0^{u(N)-\Delta d} u(1) \left[ \sum_{k=0}^{N-2} \binom{N-2}{k} (-1)^k u_{(1)}^{2k} u_{(N)}^{2N-4-2k} \right] du(1)du(N) \\
 &= \frac{4(\lambda_{\text{ap}}\pi)^N}{\Gamma(N-1)} \sum_{k=0}^{N-2} \frac{\binom{N-2}{k} (-1)^k}{2k+2} \int_{\Delta d}^{\infty} u_{(N)}^{2N-3-2k} (u(N) - \Delta d)^{2k+2} e^{-\lambda_{\text{ap}}\pi u_{(N)}^2} du(N) \\
 &= \frac{2(\lambda_{\text{ap}}\pi)^N (\Delta d)^2}{\Gamma(N-1)} \sum_{k=0}^{N-2} \sum_{j=0}^{2k+2} \frac{\binom{N-2}{k} \binom{2k+2}{j} (-1)^{k-j} (\Delta d)^{2k-j}}{k+1} \int_{\Delta d}^{\infty} u_{(N)}^{2N-3-2k+j} e^{-\lambda_{\text{ap}}\pi u_{(N)}^2} du(N).
 \end{aligned} \tag{4.5}$$

Using the change of variable by  $z = \lambda_{\text{ap}}\pi u_{(N)}^2$ , the integral of (4.5) becomes

$$\begin{aligned}
 &\frac{1}{2} (\lambda_{\text{ap}}\pi)^{k-N+1-\frac{j}{2}} \int_{\lambda_{\text{ap}}\pi(\Delta d)^2}^{\infty} z^{N-k-2+\frac{j}{2}} e^{-z} dz \\
 &= \frac{1}{2} (\lambda_{\text{ap}}\pi)^{-N} B_{k,j} \int_{\lambda_{\text{ap}}\pi(\Delta d)^2}^{\infty} \frac{z^{(N-k-1+\frac{j}{2})-1} e^{-z}}{\Gamma(N-k-1+\frac{j}{2})} dz,
 \end{aligned} \tag{4.6}$$

where

$$B_{k,j} = (\lambda_{\text{ap}}\pi)^{k+1-\frac{j}{2}} \Gamma\left(N-k-1+\frac{j}{2}\right). \tag{4.7}$$

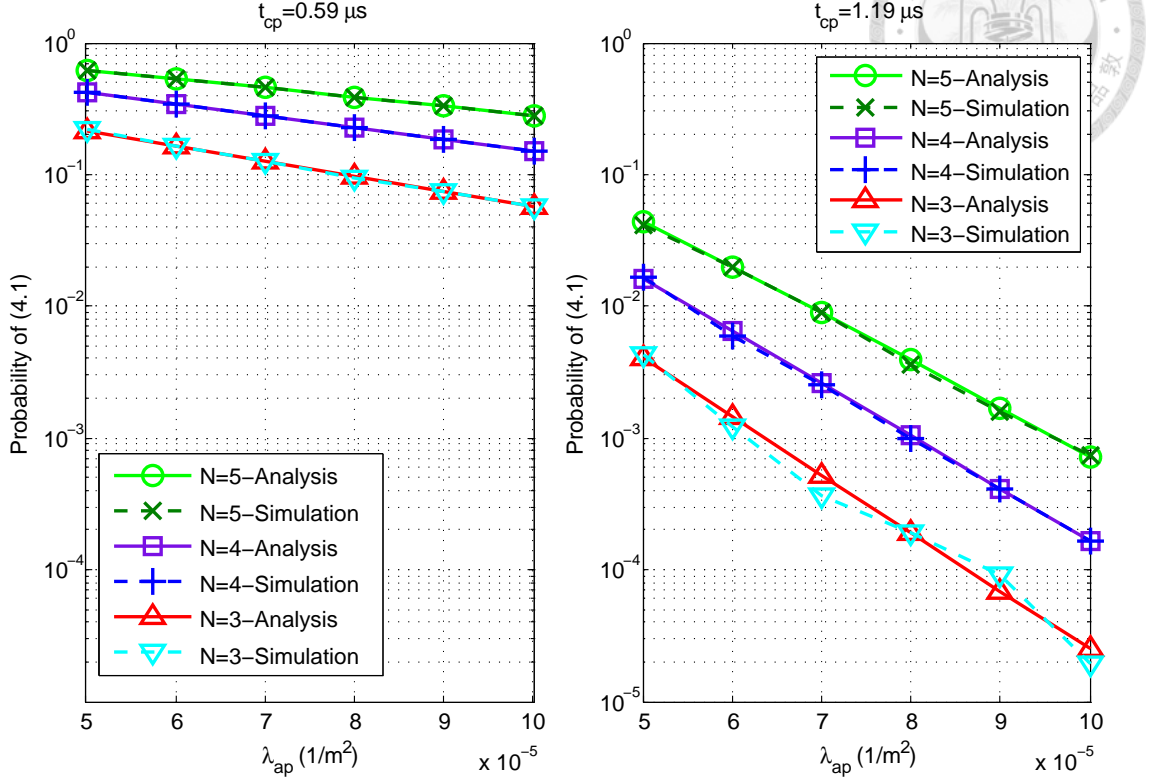


Figure 4.1: (Left)  $t_{cp} = 0.59 \mu s$ . (Right)  $t_{cp} = 1.19 \mu s$ . The probability of  $U_{(N)} - U_{(1)} > \Delta d$  is plotted for different  $N$  and  $\lambda_{ap}$ . We set that  $t_{ch} = \frac{t_{cp}}{2}$ .

The integrand in (4.6) is the PDF of Gamma random variable, thus the integration results in  $\bar{F}(\lambda_{ap}\pi(\Delta d)^2; \frac{2N-2k-2+j}{2}, 1)$ , where  $\bar{F}(\cdot; \frac{2N-2k-2+j}{2}, 1)$  is the complementary CDF (CCDF) of  $Gamma(\frac{2N-2k-2+j}{2}, 1)$ . From (4.5) and (4.6),

$$p\{U_{(N)} - U_{(1)} > \Delta d\} = \frac{(\Delta d)^2}{\Gamma(N-1)} \sum_{k=0}^{N-2} \sum_{j=0}^{2k+2} \frac{\binom{N-2}{k} \binom{2k+2}{j} (-1)^{k-j} (\Delta d)^{2k-j}}{k+1} B_{k,j} \bar{F}\left(\lambda_{ap}\pi(\Delta d)^2; \frac{2N-2k-2+j}{2}, 1\right). \quad (4.8)$$

We validate the above analysis through simulations, where we set  $t_{cp} = 0.59, 1.19 \mu s$  [44],  $t_{ch} = \frac{t_{cp}}{2}$ , and  $\lambda_{ap} = 5 \times 10^{-5} \sim 10^{-4} (1/m^2)$ . The simulation results as well as the numerical values obtained from (4.8) are plotted in Fig. 4.1, which shows that the probability of (4.1) decreases as either or both of  $\lambda_{ap}$  and  $t_{cp}$  increase. ISI and ICI due to time aynchronization rarely occurs in small cell deployment (dense deployment of APs) if the CP length and the dimension of virtual cell are carefully selected.



### 4.1.2 Signal Model for Multi-CFO Issue

For better readability, we recap the OFDM signal model considering CFO, according to which, our proposed scheme is constructed.

Suppose that the vehicle associates with  $N \geq 2$  APs forming a virtual cell. Via multi-path cooperative transmissions, the AN sends the packets to the vehicle through the  $N$  APs, which may allocate radio resources imperfectly to incur MAI. In the worst case, the vehicle receives data from different APs and different RRUs like the situation shown in Fig. 1.5. Assume that each AP is equipped with a single antenna, and the vehicle is equipped with  $N_{\text{rx}}$  antennas for  $N \geq N_{\text{rx}}$ . Let  $X_{n,k}^z$  expresses the data symbol that AP- $n$  transmits on the  $z$ th OFDM symbol's  $k$ th subcarrier. The data symbols are independent across different indices  $n, z, k$ , and  $\mathbb{E}[|X_{n,k}^z|^2] = 1$ . The FFT size and CP length are respectively  $N_{\text{fft}}$  and  $N_{\text{cp}}$ . The normalized CFO (w.r.t the subcarrier spacing) between AP- $n$  and the vehicle is  $\varepsilon_n$ . Since ICI is caused by the fractional part of CFO, we simply assume that  $|\varepsilon_n| \leq 0.5$ .

In uRLLC, the latency requirement is typically shorter than the channel coherence time [22, 44], the CIR between AP- $n$  and vehicle's  $m$ th antenna,  $h_{n,\tau}^m$ , is considered to be time-invariant over several OFDM symbol durations. Taking the discrete Fourier transform (DFT) of  $h_{n,\tau}^m$  yields  $\bar{H}_{n,k}^m = \sum_{\tau=0}^{N_{\text{ch}}-1} h_{n,\tau}^m e^{\frac{-j2\pi k\tau}{N_{\text{fft}}}}$ , where  $N_{\text{ch}}$  is the channel length and  $N_{\text{ch}} < N_{\text{cp}}$ . Moreover,  $h_{n,\tau}^m$  is a zero-mean complex Gaussian random variable with variance  $\sigma_\tau^2$ , i.e.,  $h_{n,\tau}^m \sim CN(0, \sigma_\tau^2)$ , and  $\sum_{\tau=0}^{N_{\text{ch}}-1} \sigma_\tau^2 = 1$  (The sum of variances is normalized to be one). It is also assumed that

$$\sigma_\tau^2 = \frac{1 - e^{\frac{-1}{\sigma_h}}}{1 - e^{\frac{-N_{\text{ch}}}{\sigma_h}}} e^{\frac{-\tau}{\sigma_h}} \quad \text{for } \tau = 0, 1, \dots, N_{\text{ch}} - 1, \quad (4.9)$$

$$\sigma_h = -\frac{N_{\text{ch}} - 1}{\ln(0.01)}. \quad (4.10)$$

The signals from different APs reach the vehicle with various delays, and  $\Delta t_n$  denotes the discrete timing offset for AP- $n$ 's signal relative to the first-arriving signal (from some AP). When  $\Delta t_n > N_{\text{cp}} - N_{\text{ch}}$ , inter-symbol interference (ISI) occurs. In small cell deployment, the probability that  $\Delta t_n > N_{\text{cp}} - N_{\text{ch}}$  can be small with carefully selected CP length and APs' number in the virtual cell [38], so we focus on ISI-free situation.

At the  $m$  receiving antenna, the frequency-domain signal of  $z$ th OFDM symbol is expressed as [50–52]

$$\mathbf{y}_{z,\text{F}}^m = \sum_{n=1}^N \sum_{k=0}^{N_{\text{fft}}-1} \sqrt{A_n} e^{j((z-1)\phi_n + \rho_n - \gamma_{n,k})} \bar{H}_{n,k}^m X_{n,k}^z \mathbf{c}_k(\varepsilon_n) + \mathbf{v}_{z,\text{F}}^m, \quad (4.11)$$

where  $A_n$  is AP- $n$ 's mean signal power received at the vehicle, which is the composite of transmission power, path loss, and shadowing effect;  $\phi_n = 2\pi \frac{(N_{\text{fft}} + N_{\text{cp}})}{N_{\text{fft}}} \varepsilon_n$ ,  $\rho_n = 2\pi \frac{N_{\text{cp}}}{N_{\text{fft}}} \varepsilon_n$ , and  $\gamma_{n,k} = 2\pi \frac{k\Delta t_n}{N_{\text{fft}}}$  account for the phase rotations induced by CFO and timing offset;  $\mathbf{v}_{z,\text{F}}^m = [V_{z,0}^m \cdots V_{z,N_{\text{fft}}-1}^m]^T$  is the frequency-domain white noise with  $V_{z,k}^m \sim CN(0, \sigma_V^2)$ .

Besides,  $\mathbf{c}_k(\varepsilon_n)$ , known as signature waveform, is the  $k$ th column of CFO matrix  $\mathbf{C}(\varepsilon_n) = \mathbf{F}\mathbf{D}(\varepsilon_n)\mathbf{F}^H$ , that is,  $\mathbf{c}_k(\varepsilon_n) = \mathbf{C}(\varepsilon_n)\mathbf{e}_k$ , where  $\mathbf{F}$  is the  $N_{\text{fft}} \times N_{\text{fft}}$  unitary DFT matrix,  $\mathbf{D}(\varepsilon_n) = \text{diag}\left(1, e^{j\frac{2\pi}{N_{\text{fft}}}\varepsilon_n}, \dots, e^{j\frac{2\pi}{N_{\text{fft}}}(N_{\text{fft}}-1)\varepsilon_n}\right)$ , and  $\mathbf{e}_k$  is a  $N_{\text{fft}} \times 1$  zero vector with  $k$ th entry replaced by one. In this chapter, the row/column/entry indices of matrices/vectors begin with zero.



The inner product between  $\mathbf{c}_{k_1}(\varepsilon_{n_1})$  and  $\mathbf{c}_{k_2}(\varepsilon_{n_2})$  is

$$\begin{aligned}
 \mathbf{c}_{k_1}^H(\varepsilon_{n_1}) \mathbf{c}_{k_2}(\varepsilon_{n_2}) &= \mathbf{e}_{k_1}^H \mathbf{F} \mathbf{D}^H(\varepsilon_{n_1}) \mathbf{F}^H \mathbf{F} \mathbf{D}(\varepsilon_{n_2}) \mathbf{F}^H \mathbf{e}_{k_2} = \mathbf{e}_{k_1}^H \mathbf{F} \mathbf{D}(\varepsilon_{n_2} - \varepsilon_{n_1}) \mathbf{F}^H \mathbf{e}_{k_2} \\
 &= [\mathbf{C}(\varepsilon_{n_2} - \varepsilon_{n_1})]_{k_1 k_2} = \sum_{s=0}^{N_{\text{fft}}-1} (\mathbf{F})_{k_1 s} [\mathbf{D}(\varepsilon_{n_2}) - \varepsilon_{n_1}]_{s k_2} \\
 &= \sum_{s=0}^{N_{\text{fft}}-1} (\mathbf{F})_{k_1 s} \sum_{\ell=0}^{N_{\text{fft}}-1} [\mathbf{C}(\varepsilon_{n_2} - \varepsilon_{n_1})]_{s \ell} (\mathbf{F}^H)_{\ell k_2} \\
 &= \frac{1}{N_{\text{fft}}} \sum_{s=0}^{N_{\text{fft}}-1} e^{-j \frac{2\pi k_1 s}{N_{\text{fft}}}} e^{j \frac{2\pi(\varepsilon_{n_2} - \varepsilon_{n_1}) s}{N_{\text{fft}}}} e^{j \frac{2\pi k_2 s}{N_{\text{fft}}}} \\
 &= \frac{1}{N_{\text{fft}}} \sum_{s=0}^{N_{\text{fft}}-1} e^{j \frac{2\pi(k_2 - k_1 + \varepsilon_{n_2} - \varepsilon_{n_1}) s}{N_{\text{fft}}}} = \frac{1}{N_{\text{fft}}} \frac{1 - e^{j 2\pi(k_2 - k_1 + \varepsilon_{n_2} - \varepsilon_{n_1})}}{1 - e^{j \frac{2\pi(k_2 - k_1 + \varepsilon_{n_2} - \varepsilon_{n_1})}{N_{\text{fft}}}}} \\
 &= \frac{1}{N_{\text{fft}}} e^{j \frac{\pi(N_{\text{fft}}-1)(k_2 - k_1 + \varepsilon_{n_2} - \varepsilon_{n_1})}{N_{\text{fft}}}} \frac{e^{-j\pi(k_2 - k_1 + \varepsilon_{n_2} - \varepsilon_{n_1})} - e^{j\pi(k_2 - k_1 + \varepsilon_{n_2} - \varepsilon_{n_1})}}{e^{j \frac{-\pi(k_2 - k_1 + \varepsilon_{n_2} - \varepsilon_{n_1})}{N_{\text{fft}}}} - e^{j \frac{\pi(k_2 - k_1 + \varepsilon_{n_2} - \varepsilon_{n_1})}{N_{\text{fft}}}}} \\
 &= (-1)^{k_2 - k_1} e^{j \frac{\pi(N_{\text{fft}}-1)(k_2 - k_1 + \varepsilon_{n_2} - \varepsilon_{n_1})}{N_{\text{fft}}}} \frac{\sin(\pi(\varepsilon_{n_2} - \varepsilon_{n_1}))}{N_{\text{fft}} \sin\left(\frac{\pi(k_2 - k_1 + \varepsilon_{n_2} - \varepsilon_{n_1})}{N_{\text{fft}}}\right)}, \tag{4.12}
 \end{aligned}$$

which is also the  $(k_1, k_2)$ th entry of  $\mathbf{C}(\varepsilon_{n_2} - \varepsilon_{n_1})$  and leads to the following properties that are helpful in our research.

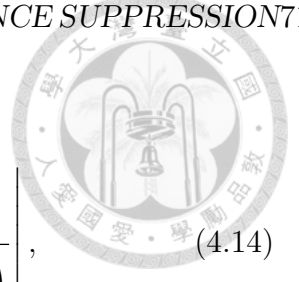
**Property 1.** For any  $k$  and  $n$ ,

$$\|\mathbf{c}_k(\varepsilon_n)\|_2^2 = \mathbf{e}_k^H \mathbf{F} \mathbf{D}^H(\varepsilon_n) \mathbf{F}^H \mathbf{F} \mathbf{D}(\varepsilon_n) \mathbf{F}^H \mathbf{e}_k = 1. \tag{4.13}$$

This property means that CFO does not decrease the received signal power, but spreads the power over frequency domain.

**Property 2.** For  $k_1 \neq k_2$ ,  $\mathbf{c}_{k_1}^H(\varepsilon_n) \mathbf{c}_{k_2}(\varepsilon_n) = 0$ , which implies the signature waveforms from the same AP are mutually orthogonal. That is to say, CFO does not destroy the orthogonality among the subcarriers of the same AP if we observe the receiver's overall FFT outputs.





**Property 3.** For  $0 < |\varepsilon_{n_2} - \varepsilon_{n_1}| < 0.5$ ,

$$|\mathbf{c}_{k_1}^H(\varepsilon_{n_1}) \mathbf{c}_{k_2}(\varepsilon_{n_2})| = \left| \frac{\sin(\pi(\varepsilon_{n_2} - \varepsilon_{n_1}))}{N_{\text{fft}} \sin\left(\frac{\pi(k_2 - k_1 + \varepsilon_{n_2} - \varepsilon_{n_1})}{N_{\text{fft}}}\right)} \right|, \quad (4.14)$$

which decreases as  $\Delta k$  increases. Here  $\Delta k = \min\{\langle \pm(k_2 - k_1) \rangle_{N_{\text{fft}}}\}$  and  $\langle \cdot \rangle_{N_{\text{fft}}}$  represents the modulo- $N_{\text{fft}}$  operation.

In general, not all of the subcarriers are utilized. Denoting the set of indices of used subcarriers by  $\mathcal{B}$  and absorbing the phase rotation  $\rho_n - \gamma_{n,k}$  into  $\bar{H}_{n,k}^m$ , (4.11) is simplified as

$$\mathbf{y}_{z,\text{F}}^m = \sum_{n=1}^N \sum_{k \in \mathcal{B}} \sqrt{A_n} H_{n,k}^m \mathbf{c}_k(\varepsilon_n) e^{j(z-1)\phi_n} X_{n,k}^z + \mathbf{v}_{z,\text{F}}^m, \quad (4.15)$$

with  $H_{n,k}^m = e^{j(\rho_n - \gamma_{n,k})} \bar{H}_{n,k}^m$ . It is straightforward to generalize the model (4.15) to the case, where APs have multiple antennas. This generalization will be given in Section 4.4, considering STBCs.

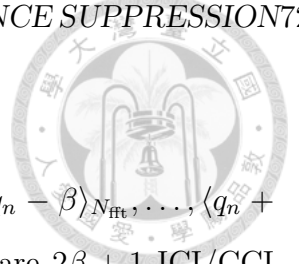
## 4.2 First-Stage Processing

Without loss of generality, we study the detection of  $X_{r,q}^z$  that is the desired data symbol conveyed on the  $z$ th OFDM symbol's  $q$ th subcarrier of AP- $r$ . Like the situation in Fig. 1.5, the desired data symbol is coupled with CCI and ICI. Let

$$q_n = \begin{cases} q & \text{if } n = r, \\ q - \text{sgn}(\varepsilon_n - \varepsilon_r) \mathbf{1}(|\varepsilon_n - \varepsilon_r| > 0.5) & \text{if } n \neq r. \end{cases} \quad (4.16)$$

$$\tilde{\varepsilon}_n = \begin{cases} \varepsilon_n - \varepsilon_r & \text{if } |\varepsilon_n - \varepsilon_r| \leq 0.5, \\ \varepsilon_n - \varepsilon_r - \text{sgn}(\varepsilon_n - \varepsilon_r) & \text{if } |\varepsilon_n - \varepsilon_r| > 0.5, \end{cases} \quad (4.17)$$

where  $\text{sgn}(\cdot)$  and  $\mathbf{1}(\cdot)$  are sign function and indicator function. The interference from  $q_n$ th subcarrier of AP- $n$  with  $n \neq r$  is the term closest to AP- $r$ 's  $q$ th subcarrier in frequency domain, and called CCI for  $X_{r,q}^z$ . The normalized frequency difference (w.r.t the subcarrier spacing) between the subcarriers of desired data and CCI is  $\tilde{\varepsilon}_n$ . The interference from any AP's  $k$ th subcarrier with  $k \neq q_n$  is defined as ICI.



### 4.2.1 Pseudo Whitening

Let  $\beta$  be an integer satisfying  $0 \leq \beta \leq \lfloor \frac{N_{\text{fft}}-1}{2} \rfloor$  and  $\Omega_{n,q} = \{\langle q_n - \beta \rangle_{N_{\text{fft}}}, \dots, \langle q_n + \beta \rangle_{N_{\text{fft}}}\}$ . For  $n \neq r$ , AP- $n$ 's subcarriers with indices from  $\Omega_{n,q}$  are  $2\beta + 1$  ICI/CCI terms closest to AP- $r$ 's  $q$ th subcarrier. To combat against CCI and ICI, the data symbols  $X_{n,k}^z$ 's for  $k \in \Omega_{n,q}$  are jointly decoded. The ICI terms that originate from the subcarriers with indices belonging to  $\mathcal{B} \setminus \Omega_{n,q}$  and  $\Omega_{n,q} \setminus q_n$  are respectively named as far ICI and dominant ICI terms. The far ICI plus noise is

$$\mathbf{v}_{z,-q}^m = \sum_{n=1}^N \sum_{k \in \mathcal{B} \setminus \Omega_{n,q}} \sqrt{A_n} H_{n,k}^m \mathbf{c}_k(\varepsilon_n) e^{j(z-1)\phi_n} X_{n,k}^z + \mathbf{v}_{z,F}^m. \quad (4.18)$$

The subscript “ $-q$ ” of  $\mathbf{v}_{z,-q}^m$  means that the term is defined from the angle of AP- $r$ 's  $q$ th subcarrier. For better performance,  $\mathbf{v}_{z,-q}^m$  is first whitened [64] via pre-multiplying  $\mathbf{y}_{z,F}^m$  by  $(\Phi_{-q}^m)^{-\frac{1}{2}}$ , where  $\Phi_{-q}^m = \mathbb{E} \left[ \mathbf{v}_{z,-q}^m (\mathbf{v}_{z,-q}^m)^H \right]$  is the covariance matrix of far ICI plus noise, and expressed as

$$\begin{aligned} \Phi_{-q}^m &= \sum_{n=1}^N \sum_{k \in \mathcal{B} \setminus \Omega_{n,q}} A_n |H_{n,k}^m|^2 \mathbf{c}_k(\varepsilon_n) \mathbf{c}_k^H(\varepsilon_n) + \sigma_V^2 \mathbf{I}_{N_{\text{fft}}} \\ &= \mathbf{C}_{-q} \mathbf{D}_{-q}^m \mathbf{C}_{-q}^H + \sigma_V^2 \mathbf{I}_{N_{\text{fft}}}. \end{aligned} \quad (4.19)$$

For  $n \in \{1, \dots, N\}$  and  $k \in \mathcal{B} \setminus \Omega_{n,q}$ ,  $\mathbf{c}_k(\varepsilon_n)$ 's constitute the columns of  $\mathbf{C}_{-q}$ , and  $\mathbf{D}_{-q}^m$  is a diagonal matrix with the diagonal entries  $A_n |H_{n,k}^m|^2$ 's at the locations corresponding to the columns of  $\mathbf{C}_{-q}$ . The pre-multiplication of  $(\Phi_{-q}^m)^{-\frac{1}{2}}$  is called ICI-Whitening (ICI-W). After ICI-W, the  $q$ th subcarrier of AP- $r$  has the whitened signature waveform  $\tilde{\mathbf{c}}_q(\varepsilon_r) = (\Phi_{-q}^m)^{-\frac{1}{2}} \mathbf{c}_q(\varepsilon_r)$ , and the component of  $(\Phi_{-q}^m)^{-\frac{1}{2}} \mathbf{v}_{z,-q}^m$  (whitened far ICI plus noise) in the direction of  $\tilde{\mathbf{c}}_q(\varepsilon_r)$  is  $\tilde{\mathbf{c}}_q^H(\varepsilon_r) (\Phi_{-q}^m)^{-\frac{1}{2}} \mathbf{v}_{z,-q}^m / \|\tilde{\mathbf{c}}_q(\varepsilon_r)\|_2$ , where  $\|\cdot\|_2$  stands for the  $\ell^2$ -norm. The post-whitening SINR is

$$\begin{aligned} \text{SINR}_{\text{W},r,q} &= \frac{A_r |H_{r,q}^m|^2 \|\tilde{\mathbf{c}}_q(\varepsilon_r)\|_2^2}{\mathbb{E} \left[ \left| \frac{\tilde{\mathbf{c}}_q^H(\varepsilon_r)}{\|\tilde{\mathbf{c}}_q(\varepsilon_r)\|_2} (\Phi_{-q}^m)^{-\frac{1}{2}} \mathbf{v}_{z,-q}^m \right|^2 \right]} = \frac{A_r |H_{r,q}^m|^2 \|\tilde{\mathbf{c}}_q(\varepsilon_r)\|_2^4}{\tilde{\mathbf{c}}_q^H(\varepsilon_r) (\Phi_{-q}^m)^{-\frac{1}{2}} \Phi_{-q}^m (\Phi_{-q}^m)^{-\frac{1}{2}} \tilde{\mathbf{c}}_q(\varepsilon_r)} \\ &= \frac{A_r |H_{r,q}^m|^2 \left( \mathbf{c}_q^H(\varepsilon_r) (\Phi_{-q}^m)^{-1} \mathbf{c}_q(\varepsilon_r) \right)^2}{\mathbf{c}_q^H(\varepsilon_r) (\Phi_{-q}^m)^{-1} \Phi_{-q}^m (\Phi_{-q}^m)^{-1} \mathbf{c}_q(\varepsilon_r)} = \frac{A_r |H_{r,q}^m \mathbf{w}_{r,q}^H \mathbf{c}_q(\varepsilon_r)|^2}{\mathbf{w}_{r,q}^H \Phi_{-q}^m \mathbf{w}_{r,q}}, \end{aligned} \quad (4.20)$$

where

$$\mathbf{w}_{r,q} = (\mathbf{\Phi}_{-q}^m)^{-1} \mathbf{c}_q(\varepsilon_r) = (\mathbf{C}_{-q} \mathbf{D}_{-q}^m \mathbf{C}_{-q}^H + \sigma_V^2 \mathbf{I}_{N_{\text{fft}}})^{-1} \mathbf{c}_q(\varepsilon_r) \quad (4.21)$$

ICI-W requires estimating  $\mathbf{\Phi}_{-q}^m$ , which depends on  $H_{n,k}^m$ 's for  $k \in \mathcal{B} \setminus \Omega_{n,q}$ . Recall from Subsection 1.4.3 that the channel estimation on all subcarriers may not be available in our uRLLC downlink scenario, but by (4.19), the structure of  $\mathbf{\Phi}_{-q}^m$  can still be known from the estimate of CFOs. From the numerical analysis using (4.12),  $|\mathbf{c}_k^H(\varepsilon_n) \mathbf{c}_q(\varepsilon_r)|$  is less than 0.15 for  $k \in \mathcal{B} \setminus \Omega_{n,q}$  with  $\min\{\langle \pm(k-q) \rangle_{N_{\text{fft}}}\} > 2$ . That is, most of far ICI terms are nearly orthogonal to  $\mathbf{c}_q(\varepsilon_r)$ , yielding a conjecture that the post-processing SINR will not be significantly degraded even if the whitening operation is modified by replacing  $A_n |H_{n,k}^m|^2$ 's in (4.19) with positive real numbers  $G_n$ 's, whose values are chosen based on some more easily obtainable information and discussed later.

Construct a pseudo ICI-plus-noise covariance matrix as

$$\mathbf{\Psi}_{-q} = \mathbf{C}_{-q} \bar{\mathbf{D}}_{-q} \mathbf{C}_{-q}^H + \sigma_V^2 \mathbf{I}_{N_{\text{fft}}}, \quad (4.22)$$

where  $\bar{\mathbf{D}}_{-q}$  is the matrix obtained from  $\mathbf{D}_{-q}^m$  with the diagonal entries  $A_n |H_{n,k}^m|^2$ 's replaced by  $G_n$ 's. We propose Pseudo-ICI-W (P-ICI-W) to pre-multiplying  $\mathbf{y}_{z,\text{F}}^m$  by  $(\mathbf{\Psi}_{-q})^{-\frac{1}{2}}$ . Let  $\bar{\mathbf{c}}_q(\varepsilon_n) = (\mathbf{\Psi}_{-q})^{-\frac{1}{2}} \mathbf{c}_q(\varepsilon_n)$  denote the pseudo-whitened signature waveform. Next we analyze the difference between ICI-W and P-ICI-W in terms of post-processing SINR to observe how closely P-ICI-W can approach ICI-W. Likewise, we have

$$\begin{aligned} \text{SINR}_{\text{PW},r,q} &= \frac{A_r |H_{r,q}^m|^2 \|\bar{\mathbf{c}}_q(\varepsilon_r)\|_2^2}{\mathbb{E} \left[ \left| \frac{\bar{\mathbf{c}}_q^H(\varepsilon_r)}{\|\bar{\mathbf{c}}_q(\varepsilon_r)\|_2} (\mathbf{\Psi}_{-q}^m)^{-\frac{1}{2}} \mathbf{v}_{-q}^m \right|^2 \right]} = \frac{A_r |H_{r,q}^m|^2 \|\bar{\mathbf{c}}_q(\varepsilon_r)\|_2^4}{\bar{\mathbf{c}}_q^H(\varepsilon_r) (\mathbf{\Psi}_{-q}^m)^{-\frac{1}{2}} \mathbf{\Phi}_{-q}^m (\mathbf{\Psi}_{-q}^m)^{-\frac{1}{2}} \bar{\mathbf{c}}_q(\varepsilon_r)} \\ &= \frac{A_r |H_{r,q}^m|^2 \left( \mathbf{c}_q^H(\varepsilon_r) (\mathbf{\Psi}_{-q}^m)^{-1} \mathbf{c}_q(\varepsilon_r) \right)^2}{\mathbf{c}_q^H(\varepsilon_r) (\mathbf{\Psi}_{-q}^m)^{-1} \mathbf{\Phi}_{-q}^m (\mathbf{\Psi}_{-q}^m)^{-1} \mathbf{c}_q(\varepsilon_r)} = \frac{A_r |H_{r,q}^m \bar{\mathbf{w}}_{r,q}^H \mathbf{c}_q(\varepsilon_r)|^2}{\bar{\mathbf{w}}_{r,q}^H \mathbf{\Phi}_{-q}^m \bar{\mathbf{w}}_{r,q}}, \quad (4.23) \end{aligned}$$

$$\bar{\mathbf{w}}_{r,q} = \mathbf{\Psi}_{-q}^{-1} \mathbf{c}_q(\varepsilon_r) = (\mathbf{C}_{-q} \bar{\mathbf{D}}_{-q} \mathbf{C}_{-q}^H + \sigma_V^2 \mathbf{I}_{N_{\text{fft}}})^{-1} \mathbf{c}_q(\varepsilon_r), \quad (4.24)$$

where  $\text{SINR}_{\text{PW},r,q}$  is the SINR after P-ICI-W. From (4.20) and (4.23),  $\text{SINR}_{\text{PW},r,q} \approx$



$\text{SINR}_{\text{W},r,q}$  if  $\bar{\mathbf{w}}_{r,q} \approx \mathbf{w}_{r,q}$ . By (4.21) and (4.24),

$$\begin{aligned}
 \mathbf{w}_{r,q} - \bar{\mathbf{w}}_{r,q} &= \left[ (\mathbf{\Phi}_{-q}^m)^{-1} - \mathbf{\Psi}_{-q}^{-1} \right] \mathbf{c}_q(\varepsilon_r) \\
 &= \left\{ (\mathbf{C}_{-q} \mathbf{D}_{-q}^m \mathbf{C}_{-q}^H + \sigma_V^2 \mathbf{I}_{N_{\text{fft}}})^{-1} - (\mathbf{C}_{-q} \bar{\mathbf{D}}_{-q} \mathbf{C}_{-q}^H + \sigma_V^2 \mathbf{I}_{N_{\text{fft}}})^{-1} \right\} \mathbf{c}_q(\varepsilon_r) \\
 &= \frac{1}{\sigma_V^2} \left\{ \left[ \mathbf{I}_{N_{\text{fft}}} - \mathbf{C}_{-q} \left( \mathbf{C}_{-q}^H \mathbf{C}_{-q} + \sigma_V^2 (\mathbf{D}_{-q}^m)^{-1} \right)^{-1} \mathbf{C}_{-q}^H \right] \right. \\
 &\quad \left. - \left[ \mathbf{I}_{N_{\text{fft}}} - \mathbf{C}_{-q} \left( \mathbf{C}_{-q}^H \mathbf{C}_{-q} + \sigma_V^2 \bar{\mathbf{D}}_{-q}^{-1} \right)^{-1} \mathbf{C}_{-q}^H \right] \right\} \mathbf{c}_q(\varepsilon_r) \\
 &= \mathbf{C}_{-q} \mathbf{\Pi}_q \mathbf{C}_{-q}^H \frac{\mathbf{c}_q(\varepsilon_r)}{\sigma_V^2}, \tag{4.25}
 \end{aligned}$$

$$\mathbf{\Pi}_q = \left( \mathbf{C}_{-q}^H \mathbf{C}_{-q} + \sigma_V^2 \bar{\mathbf{D}}_{-q}^{-1} \right)^{-1} - \left( \mathbf{C}_{-q}^H \mathbf{C}_{-q} + \sigma_V^2 (\mathbf{D}_{-q}^m)^{-1} \right)^{-1}. \tag{4.26}$$

The third equality of (4.25) follows from the matrix inversion lemma [28]. Thus we have

$$\frac{\|\mathbf{w}_{r,q} - \bar{\mathbf{w}}_{r,q}\|_2}{\|\mathbf{w}_{r,q}\|_2} \leq \frac{\|\mathbf{C}_{-q}\|_F \|\mathbf{\Pi}_q\|_F \|\mathbf{C}_{-q}^H \mathbf{c}_q(\varepsilon_r)\|_2}{\sigma_V^2 \|\mathbf{w}_{r,q}\|_2}, \tag{4.27}$$

where  $\|\cdot\|_F$  stands for Frobenius norm, and the entries of  $\mathbf{C}_{-q}^H \mathbf{c}_q(\varepsilon_r)$  are the inner products between  $\mathbf{c}_q(\varepsilon_r)$  and  $\mathbf{c}_k(\varepsilon_n)$ 's for  $k \in \mathcal{B} \setminus \Omega_{n,q}$ . The upper bound in (4.27) is dominated by  $\|\mathbf{C}_{-q}^H \mathbf{c}_q(\varepsilon_r)\|_2$ , which decreases as  $\beta$  increases (see Property 3). Therefore,  $\|\mathbf{w}_{r,q} - \bar{\mathbf{w}}_{r,q}\|_2 / \|\mathbf{w}_{r,q}\|_2$  can be made small such that  $\text{SINR}_{\text{PW},r,q} \approx \text{SINR}_{\text{W},r,q}$  via adjusting  $\beta$  that determines the number of dominant ICI terms remaining after P-ICI-W.

When the synchronization is ideal (i.e. there are no CFOs), at the  $m$ th receiving antenna, the SINR of signal conveyed on the  $q$ th subcarrier of AP- $r$  is  $\text{SINR}_{\text{ideal},r,q} = A_r |H_{r,q}^m|^2 / \sigma_V^2$ , against which the average SINR loss from ICI-W and P-ICI-W can be stated as the ratios:

$$L_{\text{W},r,q} = \text{E} \left[ 10 \log_{10} \left( \frac{\text{SINR}_{\text{ideal},r,q}}{\text{SINR}_{\text{W},r,q}} \right) \right]. \tag{4.28}$$

$$L_{\text{PW},r,q} = \text{E} \left[ 10 \log_{10} \left( \frac{\text{SINR}_{\text{ideal},r,q}}{\text{SINR}_{\text{PW},r,q}} \right) \right], \tag{4.29}$$

where the expectation is taken w.r.t fading gains  $H_{n,k}^m$ . We simulate 2-AP case to observe the average SINR loss on the  $q$ th subcarrier of AP-2 (i.e  $L_{\text{W},2,q}$  and  $L_{\text{PW},2,q}$ ).



In addition to the parameters given in Table 4.1, we set that  $\varepsilon_2 = 0$  and the CFO difference  $\Delta\varepsilon = \varepsilon_1 - \varepsilon_2$  ranges from 0 to 0.5.

Table 4.1: Parameters/Notations

Parameter	Value
FFT size	$N_{\text{fft}} = 64$
CP length	$N_{\text{fft}}/4$
Channel Length	$N_{\text{ch}} = 11$
Indices of used subcarriers	$\mathcal{B} = \{1, \dots, 26, 38, \dots, 63\}$
Index of observed subcarrier	$q = 20$
Number of associated APs	$N$
Number of receiving antennas	$N_{\text{rx}}$

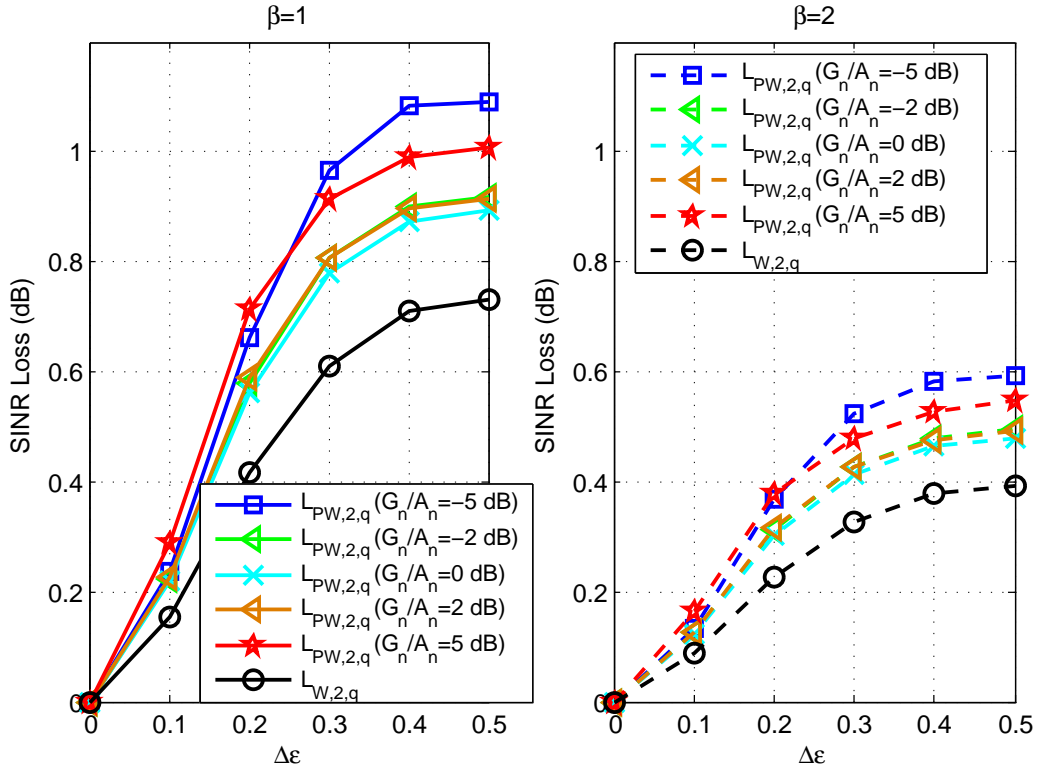


Figure 4.2: (Left)  $\beta = 1$ . (Right)  $\beta = 2$ . The average SINR loss of ICI-W and P-ICI-W versus CFO difference  $\Delta\varepsilon$  is plotted. The parameters are set as  $\frac{A_2}{\sigma_v^2} = \frac{A_1}{\sigma_v^2} = 10$  dB, and  $\frac{G_n}{A_n} = 0, \pm 2, \pm 5$  dB for  $n = 1, 2$ .

The results for different values of  $G_n$  are plotted in Fig. 4.2, where  $\frac{A_2}{\sigma_v^2} = \frac{A_1}{\sigma_v^2} = 10$  dB. In the left part of Fig. 4.2,  $\beta = 1$ ,  $L_{W,2,q}$  and  $L_{PW,2,q}$  increase as  $\Delta\varepsilon$  increases. For

$\Delta\varepsilon = 0.5$ , the difference between  $L_{W,2,q}$  and  $L_{PW,2,q}$  with  $\frac{G_n}{A_n} = 0$  dB is less than 0.2 dB. Even though  $\frac{G_n}{A_n} = \pm 5$  dB,  $L_{PW,2,q} - L_{W,2,q}$  is no more than 0.4 dB. When  $\beta = 2$ ,  $L_{W,2,q}$ ,  $L_{PW,2,q}$ , and  $L_{PW,2,q} - L_{W,2,q}$  shrink, as shown in the right part of Fig. 4.2, where we note that the difference between  $L_{W,2,q}$  and  $L_{PW,2,q}$  for  $\frac{G_n}{A_n} = \pm 5$  dB is only around 0.2 dB for  $\Delta\varepsilon = 0.5$ . Without actually estimating  $\Phi_{-q}^m$ , the SINR degradation from using  $\Psi_{-q}$  can be made little if we set  $\frac{G_n}{A_n} = 0$  dB. However, the closeness of  $L_{PW,2,q}$  to  $L_{W,2,q}$  for different  $\frac{G_n}{A_n}$ 's reveals that P-ICI-W is insensitive to  $G_n$ 's. The above observation tells that it may not be worth performing ICI-W or estimating the true ICI covariance matrix, the gain from which is very limited.

Before collecting the pseudo-whitened signals from different antennas for detection or further processing,  $(\Psi_{-q})^{-\frac{1}{2}} \mathbf{y}_{z,F}^m$  is projected to the subspace spanned by  $\bar{\mathbf{c}}_k(\varepsilon_r)$ 's for  $k \in \Omega_{r,q}$  (the pseudo-whitened signature waveforms of AP $-r$ ), whereby the signal's length can be shortened and is in favor of later operation. Let  $\mathbf{C}_\Omega$  express the matrix with columns  $\mathbf{c}_k(\varepsilon_r)$ 's for  $k \in \Omega_{r,q}$ , that is,  $\mathbf{C}_\Omega = [\mathbf{c}_{\langle q-\beta \rangle_{N_{\text{fft}}}}(\varepsilon_r) \cdots \mathbf{c}_{\langle q+\beta \rangle_{N_{\text{fft}}}}(\varepsilon_r)]$ , and denote the reduced QR-decomposition of  $(\Psi_{-q})^{-\frac{1}{2}} \mathbf{C}_\Omega$  by

$$(\Psi_{-q})^{-\frac{1}{2}} \mathbf{C}_\Omega = \mathbf{Q}_{F,q} \mathbf{R}_{F,q}, \quad (4.30)$$

where the sizes of  $\mathbf{Q}_{F,q}$  and  $\mathbf{R}_{F,q}$  are  $N_{\text{fft}} \times (2\beta + 1)$  and  $(2\beta + 1) \times (2\beta + 1)$ , respectively. The processing including P-ICI-W and the aforementioned projection is equivalent to

$$\bar{\mathbf{y}}_{z,F}^m \triangleq \mathbf{Q}_{F,q}^H (\Psi_{-q})^{-\frac{1}{2}} \mathbf{y}_{z,F}^m = \sum_{n=1}^N \sum_{k \in \Omega_{n,q}} \sqrt{A_n} H_{n,k}^m \mathbf{f}_k(\varepsilon_n) e^{j(z-1)\phi_n} X_{n,k}^z + \bar{\mathbf{v}}_{z,-q}^m, \quad (4.31)$$

$$\mathbf{f}_k(\varepsilon_n) = \mathbf{Q}_{F,q}^H (\Psi_{-q})^{-\frac{1}{2}} \mathbf{c}_k(\varepsilon_n), \quad (4.32)$$

$$\bar{\mathbf{v}}_{z,-q}^m = \mathbf{Q}_{F,q}^H (\Psi_{-q})^{-\frac{1}{2}} \mathbf{v}_{z,-q}^m. \quad (4.33)$$

The above frequency-domain processing is identical for the signals received from different antennas and does not depend on fading gains, and thus updating  $\mathbf{Q}_{F,q}$ ,  $\Psi_{-q}$ , and  $\mathbf{f}_k(\varepsilon_n)$  once every period of channel coherence time is not necessary.

$\Psi_{-q}$  is a  $N_{\text{fft}} \times N_{\text{fft}}$  matrix, calculating  $(\Psi_{-q})^{-\frac{1}{2}}$  costs a great amount of computation for large  $N_{\text{fft}}$ . To avoid this, Pseudo-Truncate ICI-W (PT-ICI-W) is proposed. For any  $N_{\text{fft}} \times 1$  column vector  $\mathbf{b} = [B_0 \cdots B_{N_{\text{fft}}-1}]^T$  and integer  $\alpha$  satisfying  $0 \leq \alpha \leq \lfloor \frac{N_{\text{fft}}-1}{2} \rfloor$ , let  $\Gamma_q^\alpha(\cdot)$  be an operation to truncate  $\mathbf{b}$  such that only its  $\langle q - \alpha \rangle_{N_{\text{fft}}}$ th,  $\dots$ ,  $\langle q + \alpha \rangle_{N_{\text{fft}}}$ th entries are retained, i.e.,  $\Gamma_q^\alpha(\mathbf{b}) = [B_{\langle q - \alpha \rangle_{N_{\text{fft}}}} \cdots B_{\langle q + \alpha \rangle_{N_{\text{fft}}}}]^T$ . Taking the truncation,  $\mathbf{y}_{z,\text{tF}}^m \triangleq \Gamma_q^\alpha(\mathbf{y}_{z,\text{F}}^m)$ ,  $\mathbf{c}_{t,k}(\varepsilon_n) \triangleq \Gamma_q^\alpha(\mathbf{c}_k(\varepsilon_n))$ , the column-truncated version of  $\mathbf{C}_{-q}$  is denoted by  $\mathbf{C}_{t,-q}$ , and the pseudo-truncate covariance matrix  $\Psi_{t,-q}$  is obtained from substituting  $\mathbf{C}_{t,-q}$  and  $\mathbf{I}_{2\alpha+1}$  respectively for  $\mathbf{C}_{-q}$  and  $\mathbf{I}_{N_{\text{fft}}}$  in (4.22). Following the same procedure from (4.30) to (4.33), the signal processing is modified as

$$\bar{\mathbf{y}}_{z,\text{tF}}^m \triangleq \mathbf{Q}_{\text{tF},q}^H (\Psi_{t,-q})^{-\frac{1}{2}} \mathbf{y}_{z,\text{tF}}^m, \quad (4.34)$$

$$\mathbf{f}_{t,k}(\varepsilon_n) = \mathbf{Q}_{\text{tF},q}^H (\Psi_{t,-q})^{-\frac{1}{2}} \mathbf{c}_{t,k}(\varepsilon_n), \quad (4.35)$$

$$(\Psi_{t,-q})^{-\frac{1}{2}} [\mathbf{c}_{t,\langle q - \beta \rangle_{N_{\text{fft}}}}(\varepsilon_r) \cdots \mathbf{c}_{t,\langle q + \beta \rangle_{N_{\text{fft}}}}(\varepsilon_r)] = \mathbf{Q}_{\text{tF},q} \mathbf{R}_{\text{tF},q}, \quad (4.36)$$

$$\bar{\mathbf{v}}_{z,t,-q}^m = \mathbf{Q}_{\text{tF},q}^H (\Psi_{t,-q})^{-\frac{1}{2}} \Gamma_q^\alpha(\mathbf{v}_{z,-q}^m). \quad (4.37)$$

From (4.12), the inner product of  $\mathbf{c}_{t,k}(\varepsilon_n)$  and  $\mathbf{c}_{t,q}(\varepsilon_r)$  is

$$\begin{aligned} & \mathbf{c}_{t,k}^H(\varepsilon_n) \mathbf{c}_{t,q}(\varepsilon_r) \\ &= \sum_{l \in \mathcal{N}_q^\alpha} (\mathbf{C}(\varepsilon_n))_{lk}^H (\mathbf{C}(\varepsilon_r))_{lq} \\ &= \sum_{l \in \mathcal{N}_q^\alpha} e^{\frac{j\pi(N_{\text{fft}}-1)(q-l+\varepsilon_r)}{N_{\text{fft}}}} \frac{(-1)^{q-l} \sin(\pi\varepsilon_r)}{N_{\text{fft}} \sin\left(\frac{\pi(q-l+\varepsilon_r)}{N_{\text{fft}}}\right)} e^{\frac{j\pi(N_{\text{fft}}-1)(-k+l-\varepsilon_n)}{N_{\text{fft}}}} \frac{(-1)^{k-l} \sin(\pi\varepsilon_n)}{N_{\text{fft}} \sin\left(\frac{\pi(k-l+\varepsilon_n)}{N_{\text{fft}}}\right)} \\ &= e^{\frac{j\pi(N_{\text{fft}}-1)(q-k+\varepsilon_r-\varepsilon_n)}{N_{\text{fft}}}} \frac{(-1)^{q+k} \sin(\pi\varepsilon_n) \sin(\pi\varepsilon_r)}{N_{\text{fft}}^2} \\ & \quad \sum_{l=-\alpha}^{\alpha} \left[ \sin\left(\frac{\pi(l+\varepsilon_r)}{N_{\text{fft}}}\right) \sin\left(\frac{\pi(k-q+l+\varepsilon_n)}{N_{\text{fft}}}\right) \right]^{-1}, \end{aligned} \quad (4.38)$$

where  $\mathcal{N}_q^\alpha = \{\langle q - \alpha \rangle_{N_{\text{fft}}}, \dots, \langle q + \alpha \rangle_{N_{\text{fft}}}\}$ . Exploiting (4.38), we observe that the numerical value of  $|\mathbf{c}_{t,k}^H(\varepsilon_n) \mathbf{c}_{t,q}(\varepsilon_r)|$  is also able to be made small through controlling  $\beta$ . Hence, by the same argument, the post-processing SINR of PT-ICI-W can be close to that of Truncate-ICI-W (T-ICI-W), which is similar to PT-ICI-W, the only

difference between them is that T-ICI-W exploits the covariance matrix of truncated far ICI plus noise.

The parameter  $\alpha$  that determines the lengths of truncated frequency-domain signals/signature waveforms can be selected according to how much energy loss from truncation is tolerated. By Property 4.13 and (4.38), the energy loss of AP- $n$ 's  $k$ th subcarrier due to truncation can be calculated as

$$\frac{\|\mathbf{c}_k(\varepsilon_n)\|_2^2}{\|\mathbf{c}_{t,k}(\varepsilon_n)\|_2^2} = \frac{1}{\mathbf{c}_{t,k}^H(\varepsilon_n) \mathbf{c}_{t,k}(\varepsilon_n)} = \frac{N_{\text{fft}}^2}{\sin^2(\pi\varepsilon_n) \sum_{l=-\alpha}^{\alpha} \left[ \sin^2\left(\frac{\pi(l+\varepsilon_n)}{N_{\text{fft}}}\right) \right]^{-1}}. \quad (4.39)$$

Once the maximum tolerated energy loss is set,  $\alpha$  is decided by (4.39).

## 4.2.2 Joint Detection

After performing (4.31),  $\bar{\mathbf{y}}_{z,F}^m$ 's from different receiving antennas are arranged as a vector  $\bar{\mathbf{y}}_{z,S}$  that can be expressed as

$$\bar{\mathbf{y}}_{z,S} = \sum_{(n,k) \in \Omega} \mathbf{s}_k(\varepsilon_n) e^{j(z-1)\phi_n} X_{n,k}^z + \bar{\mathbf{v}}_{z,S}, \quad (4.40)$$

where

$$\Omega = \bigcup_{n=1}^N \left\{ \{n\} \times \Omega_{n,q} \right\}, \quad (4.41)$$

$$\mathbf{s}_k(\varepsilon_n) = \sqrt{A_n} \mathbf{h}_{n,k} \otimes \mathbf{f}_k(\varepsilon_n), \quad (4.42)$$

$$\mathbf{h}_{n,k} = [H_{n,k}^1 \cdots H_{n,k}^{N_{\text{rx}}}]^T, \quad (4.43)$$

$$\bar{\mathbf{v}}_{z,S}^T = \left[ (\bar{\mathbf{v}}_{z,-q}^1)^T \cdots (\bar{\mathbf{v}}_{z,-q}^{N_{\text{rx}}})^T \right]. \quad (4.44)$$

Here  $\{n\}$  denotes the set with only one element “ $n$ ”, and  $\otimes$  stands for Kronecker product. Let  $\mathcal{M}_{n,k}$  be the signal constellation used on the  $k$ th subcarrier of AP- $n$ . The desired signal, CCI, and dominant ICI terms are jointly decoded by

$$\left( \hat{\mathbf{x}}_{1,q}^z, \dots, \hat{\mathbf{x}}_{N,q}^z \right) = \underset{(\mathbf{x}_{1,q}^z, \dots, \mathbf{x}_{N,q}^z) \in \prod_{(n,k) \in \Omega} \mathcal{M}_{n,k}}}{\arg \min} \left\| \bar{\mathbf{y}}_{z,S} - \sum_{(n,k) \in \Omega} \mathbf{s}_k(\varepsilon_n) e^{j(z-1)\phi_n} X_{n,k}^z \right\|_2, \quad (4.45)$$



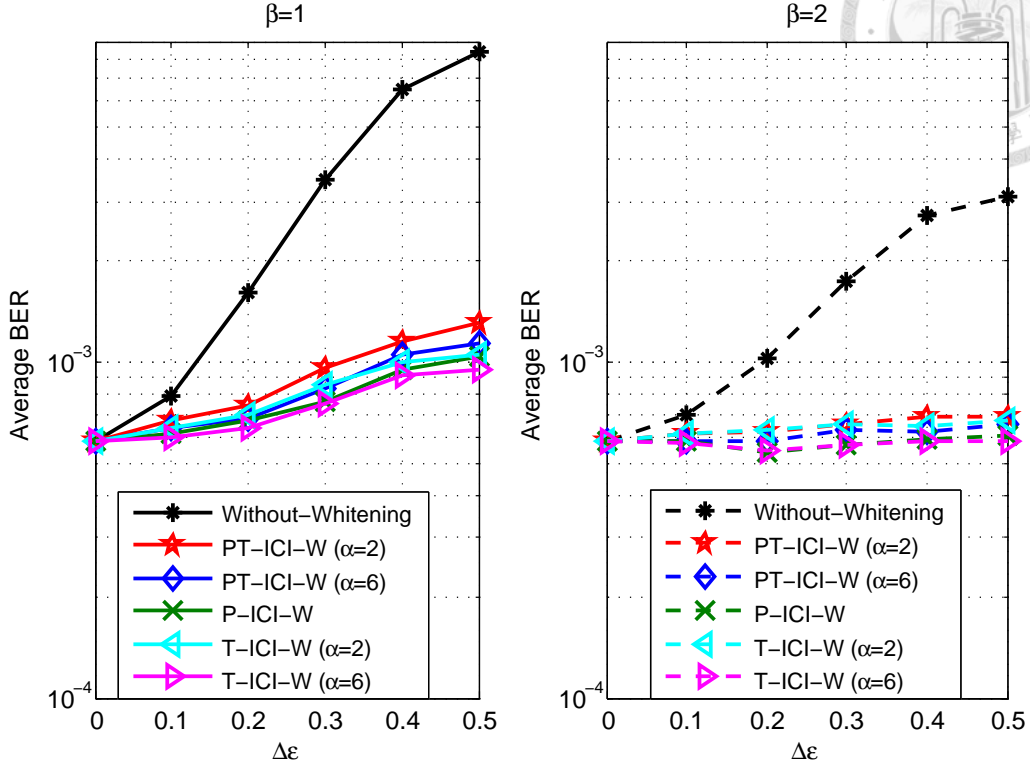


Figure 4.3: (Left)  $\beta = 1$ . (Right)  $\beta = 2$ . In 2-AP case, the average BERs of the  $q$ th subcarrier of AP-2 are plotted w.r.t  $\Delta\varepsilon$ . The parameters are set as  $\varepsilon_2 = 0$ ,  $\Delta\varepsilon = \varepsilon_1 - \varepsilon_2$ ,  $q = 20$ ,  $N_{\text{rx}} = 2$ ,  $\frac{A_2}{\sigma_v^2} = \frac{A_1}{\sigma_v^2} = 13$  dB, and  $\frac{G_n}{A_n} = 0$  dB for  $n = 1, 2$ .

where  $\mathbf{x}_{n,q}^z = \left( X_{n,(q_n-\beta)N_{\text{fft}}}^z, \dots, X_{n,(q_n+\beta)N_{\text{fft}}}^z \right)$ , and  $\hat{\mathbf{x}}_{n,q}^z$  is its estimate. If the frequency-domain processing is based on PT-ICI-W, the operation of (4.45) is revised by substituting  $\bar{\mathbf{y}}_{z,\text{tS}}$  for  $\bar{\mathbf{y}}_{z,\text{S}}$ , and  $\mathbf{s}_{t,k}(\varepsilon_n)$  for  $\mathbf{s}_k(\varepsilon_n)$ , where

$$\bar{\mathbf{y}}_{z,\text{tS}} = \sum_{(n,k) \in \Omega} \mathbf{s}_{t,k}(\varepsilon_n) e^{j(z-1)\phi_n} X_{n,k}^z + \bar{\mathbf{v}}_{z,\text{tS}}, \quad (4.46)$$

$$\mathbf{s}_{t,k}(\varepsilon_n) = \sqrt{A_n} \mathbf{h}_{n,k} \otimes \mathbf{f}_{t,k}(\varepsilon_n), \quad (4.47)$$

$$\bar{\mathbf{v}}_{z,\text{tS}}^T = \left[ (\bar{\mathbf{v}}_{z,t,-q}^1)^T \cdots (\bar{\mathbf{v}}_{z,t,-q}^{N_{\text{rx}}})^T \right]. \quad (4.48)$$

We compare different schemes, Without-Whitening, P-ICI-W, PT-ICI-W, and T-ICI-W. Without-Whitening means that the truncated frequency-domain signals, with the truncation parameter  $\alpha = \beta$ , are directly collected from the receiving antennas without whitening or pseudo-whitening. Assuming ideal estimates of CFOs, BPSK on all the used subcarriers, and the parameters in Table 4.1, we conduct simulations

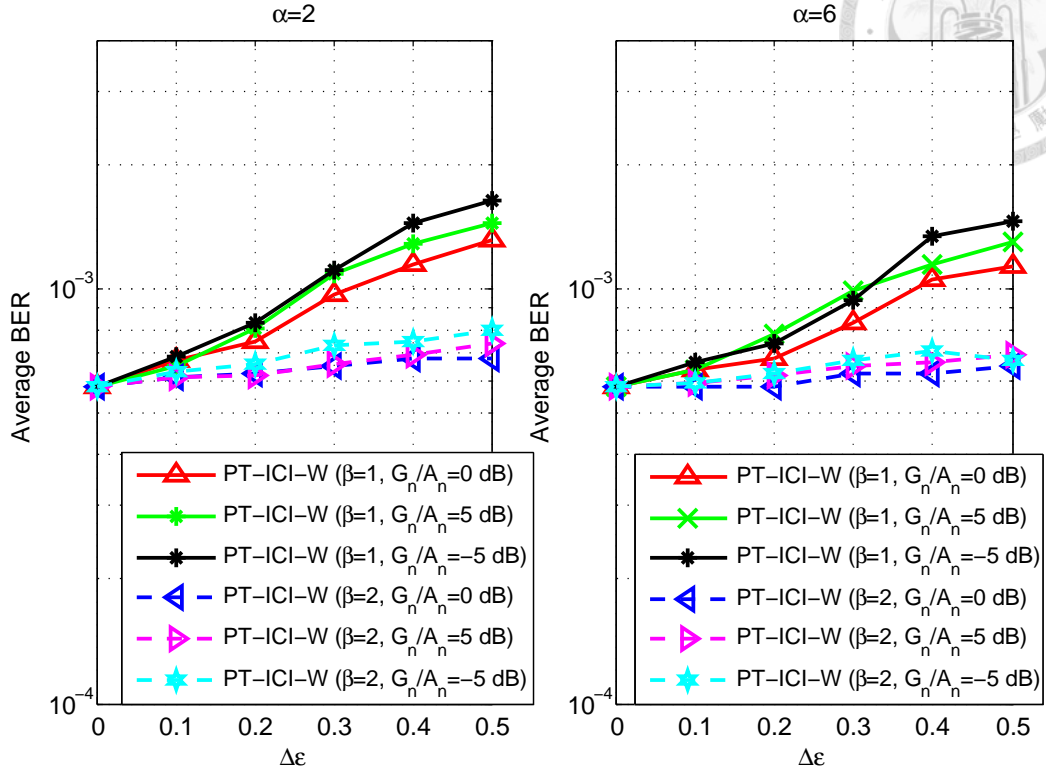


Figure 4.4: (Left)  $\alpha = 2$ . (Right)  $\alpha = 6$ . In 2-AP case, the average BERs of the  $q$ th subcarrier of AP-2 are plotted w.r.t  $\Delta\varepsilon$ . The parameters are set as  $\varepsilon_2 = 0$ ,  $\Delta\varepsilon = \varepsilon_1 - \varepsilon_2$ ,  $q = 20$ ,  $N_{\text{rx}} = 2$ ,  $\frac{A_2}{\sigma_v^2} = \frac{A_1}{\sigma_v^2} = 13$  dB, and  $\frac{G_n}{A_n} = 0, \pm 5$  dB for  $n = 1, 2$ .

to observe the average (uncoded) BERs of (4.45) as well as its counterparts based on different frequency-domain processing.

Fig. 4.3 shows the average BER on AP-2's  $q$ th subcarrier in 2-AP case with  $N_{\text{rx}} = 2$ ,  $\frac{A_2}{\sigma_v^2} = \frac{A_1}{\sigma_v^2} = 13$  dB, and  $\frac{G_n}{A_n} = 0$  dB. Without-Whitening is evidently worse than all the schemes. For  $\beta = 1$  (the left part of Fig. 4.3), the average BERs of PT-ICI-W/P-ICI-W are higher for larger CFO difference  $\Delta = \varepsilon_1 - \varepsilon_2$ , and T-ICI-W is slightly better than P-ICI-W and PT-ICI-W with  $\alpha = 6$ . However, when  $\beta = 2$  (the right part of Fig. 4.3), the performance gap between T-ICI-W and PT-ICI-W (P-ICI-W) reduces, furthermore, the average BERs of different whitening schemes does not become obviously worse as  $\Delta\varepsilon$  increases, the values are roughly between  $5.4 \times 10^{-4}$  and  $6.84 \times 10^{-4}$  for  $\Delta\varepsilon \in [0, 0.5]$ . With  $\frac{G_n}{A_n} = 0, \pm 5$  dB and  $\beta = 1, 2$ , the

results of PT-ICI-W for  $\alpha = 2$  and  $\alpha = 6$  are respectively plotted in the left and right parts of Fig. 4.4, from which it is suggested to set  $G_n = A_n$  to achieve lowest average BER. Nonetheless, the performance of  $\frac{G_n}{A_n} = \pm 5$  dB can be close to that of  $\frac{G_n}{A_n} = 0$  dB, especially for  $\beta = 2$ .

### 4.3 Second-Stage Processing

MUD is an effective countermeasure against MAI [28,29,38], however, the complexity of computing (4.45) may be too high if the number of jointly detected data symbols  $N_{\text{jd}} = (2\beta + 1)N$  is large. To reduce the complexity of joint detection, some of CCI and dominant ICI terms can be further suppressed. That is, the signal processing is facilitated by two stages: (i) P-ICI-W or PT-ICI-W in frequency domain (ii) interference suppression in space-frequency domain derived from (4.40) or (4.46).

#### 4.3.1 ICI Suppression by Projection Method

We formulate the second-stage processing based on PT-ICI-W in the first-stage processing, which outputs  $\bar{\mathbf{y}}_{z,\text{tS}}$  that has been expressed in (4.46). Let  $\Lambda_{n,q}$  represent the set of indices of AP- $n$ 's subcarriers, the signals from which are retained after the second-stage processing, and the sum of signals from the subcarriers with indices belonging to  $\Omega_{n,q} \setminus \Lambda_{n,q}$  is suppressed and denoted by  $\bar{\mathbf{v}}_{z,\text{NI}}$ . Then (4.46) is rewritten as

$$\bar{\mathbf{y}}_{z,\text{tS}} = \sum_{(n,k) \in \Lambda} \mathbf{s}_{t,k}(\varepsilon_n) e^{j(z-1)\phi_n} X_{n,k}^z + \bar{\mathbf{v}}_{z,\text{NI}} + \bar{\mathbf{v}}_{z,\text{tS}}, \quad (4.49)$$

where

$$\Lambda = \bigcup_{n=1}^N \{ \{n\} \times \Lambda_{n,q} \}, \quad (4.50)$$

$$\bar{\mathbf{v}}_{z,\text{NI}} = \sum_{(n,k) \in \Omega \setminus \Lambda} \mathbf{s}_{t,k}(\varepsilon_n) e^{j(z-1)\phi_n} X_{n,k}^z. \quad (4.51)$$

The receiver may use the conventional PR [35, 36] projecting  $\bar{\mathbf{y}}_{z,\text{tS}}$  towards the orthogonal complement of subspace spanned by the vectors  $\mathbf{s}_{t,k}(\varepsilon_n)$ 's in (4.51), then

performs detection, that is, to implement the following.

$$(\hat{\mathbf{x}}_{1,\Lambda}^z, \dots, \hat{\mathbf{x}}_{N,\Lambda}^z) = \arg \min_{(\mathbf{x}_{1,\Lambda}^z, \dots, \mathbf{x}_{N,\Lambda}^z) \in \prod_{(n,k) \in \Lambda} \mathcal{M}_{n,k}} \left\| \mathbf{P}_C \left( \bar{\mathbf{y}}_{z,\text{tS}} - \sum_{(n,k) \in \Lambda} \mathbf{s}_{t,k}(\varepsilon_n) e^{j(z-1)\phi_n} X_{n,k}^z \right) \right\|_2, \quad (4.52)$$

$$\mathbf{P}_C = \mathbf{I}_{N_{\text{rx}}(2\beta+1)} - \mathbf{S}_I (\mathbf{S}_I^H \mathbf{S}_I)^{-1} \mathbf{S}_I^H, \quad (4.53)$$

where  $\mathbf{S}_I$  is the matrix whose columns are composed of  $\mathbf{s}_{t,k}(\varepsilon_n)$ 's (appearing in (4.51)) for  $(n, k) \in \Omega \setminus \Lambda$ ,  $\mathbf{x}_{n,\Lambda}^z = \{X_{n,k}^z\}$  ( $\hat{\mathbf{x}}_{n,\Lambda}^z = \{\hat{X}_{n,k}^z\}$ ) with  $k$  running over the index set  $\Lambda_{n,q}$ . If  $\Lambda_{n,q}$  is an empty set, so are  $\mathbf{x}_{n,\Lambda}^z = \{X_{n,k}^z\}$  and  $\hat{\mathbf{x}}_{n,\Lambda}^z = \{\hat{X}_{n,k}^z\}$ , and they are not present in (4.52).

Alternatively, the second-stage processing can be developed based on GLMMSE [38]. The covariance matrix of  $\bar{\mathbf{v}}_{z,\text{NI}} + \bar{\mathbf{v}}_{z,\text{tS}}$  is  $\mathbf{S}_I \mathbf{S}_I^H + \text{E}[\bar{\mathbf{v}}_{z,\text{tS}} \bar{\mathbf{v}}_{z,\text{tS}}^H]$ . Applying GLMMSE to this context,  $\bar{\mathbf{y}}_{z,\text{tS}}$  is projected to the column space of  $(\mathbf{S}_I \mathbf{S}_I^H + \text{E}[\bar{\mathbf{v}}_{z,\text{tS}} \bar{\mathbf{v}}_{z,\text{tS}}^H])^{-1} \mathbf{S}_d$ , where  $\mathbf{S}_d$  is the matrix whose columns are constituted by  $\mathbf{s}_{t,k}(\varepsilon_n)$ 's for  $(n, k) \in \Lambda$  (appearing in the summation of (4.49)). Since the covariance of far ICI plus noise is not estimated,  $\text{E}[\bar{\mathbf{v}}_{z,\text{tS}} \bar{\mathbf{v}}_{z,\text{tS}}^H]$  is actually unknown to the receiver, so it is replaced by  $\mathbf{I}_{N_{\text{rx}}(2\beta+1)}$ . In other words, the pseudo-truncate whitened far ICI plus noise is treated as white noise. The above-mentioned projection is equivalent to pre-multiplying  $\bar{\mathbf{y}}_{z,\text{tS}}$  by the matrix  $\mathbf{P}_G = \mathbf{Q}_\Lambda^H$ , which is obtained from the QR-decomposition below.

$$(\mathbf{S}_I \mathbf{S}_I^H + \mathbf{I}_{N_{\text{rx}}(2\beta+1)})^{-1} \mathbf{S}_d = \mathbf{Q}_\Lambda \mathbf{R}_\Lambda. \quad (4.54)$$

Then the joint detection (4.52) is amended by replacing  $\mathbf{P}_C$  with  $\mathbf{P}_G$  accordingly.

### 4.3.2 Compare Different ICI-Suppression Alternatives by Simulations

In this subsection, we conduct simulations of 3-AP and 4-AP cases, where the performance AP- $r$ 's  $q$ th subcarrier ( $r = 2, q = 20$ ) is observed. In addition to the parameters in Table 4.1, BPSK is assumed. To facilitate the illustration of simulation results, the following are defined/recalled:

- *Self-adjacent ICI*: The ICI from the  $k$ th subcarrier of AP $-r$  for  $k = q \pm 1$ .
- *Near-adjacent ICI*: The ICI from AP $-n$ 's ( $n \neq r$ ) subcarrier with the index  $q_n - \text{sgn}(\tilde{\varepsilon}_n)$  (see (4.17) for the definition of  $\tilde{\varepsilon}_n$ ). For  $\tilde{\varepsilon}_n < 0$  or  $\tilde{\varepsilon}_n > 0$ , the ICI from the  $(q_n + 1)$ th or  $(q_n - 1)$ th of AP $-n$  is closest to AP $-r$ 's  $q$ th subcarrier in frequency domain.
- *Far-adjacent ICI*: The ICI from AP $-n$ 's subcarrier with the index  $q_n + \text{sgn}(\tilde{\varepsilon}_n)$  for  $n \neq r$ .
- *Adjacent ICI*: Self-, near-, and far-adjacent ICI terms are collectively termed adjacent ICI.
- *Far ICI*: The ICI from the  $k$ th subcarrier of any AP for  $k \in \mathcal{B} \setminus \Omega_{n,q}$ , which is suppressed in the first-stage processing.
- *Neighboring ICI*: The ICI terms from the  $k$ th subcarrier of any AP for  $k \in \Omega_{n,q} \setminus \{q_n, q_n \pm 1\}$ , which are the ICI remaining after the first-stage processing and not adjacent to the desired signal. This term is defined only when  $\beta > 1$ .
- *CCI*: The interference from  $q_n$ th subcarrier of AP $-n$  with  $n \neq r$ .

In 3-AP case, one-stage and two-stage ICI suppression schemes based on PT-ICI-W/T-ICI-W are compared. The CFO difference  $\Delta\varepsilon = \varepsilon_1 - \varepsilon_2 = \varepsilon_2 - \varepsilon_3$  ranges from 0 to 0.5,  $\varepsilon_2 = 0$ ,  $N_{\text{rx}} = 3$ ,  $\frac{A_n}{\sigma_V^2} = 10$  dB,  $\frac{G_n}{A_n} = 0$  dB for  $n = 1, 2, 3$ . The parameter  $\beta$  determines the number of remaining ICI terms after PT-ICI-W/T-ICI-W, CCI terms, and the desired signal, which totals  $(2\beta + 1)N$ . In the one-stage processing,  $\beta = 1$ , i.e.  $\Omega_{n,q} = \{q_n, q_n \pm 1\}$ ; in the two-stage processing,  $\beta = 2, 3$ ,  $\Lambda_{n,q} = \{q_n, q_n \pm 1\}$  (i.e.  $\Omega_{n,q} \setminus \Lambda_{n,q} = \{q_n \pm 2\}$  for  $\beta = 2$  and  $\Omega_{n,q} \setminus \Lambda_{n,q} = \{q_n \pm 2, q_n \pm 3\}$  for  $\beta = 3$ ), which means that neighboring ICI terms are suppressed in the second-stage processing. As shown in Fig. 4.5, the two-stage processing is better than the one-stage processing,

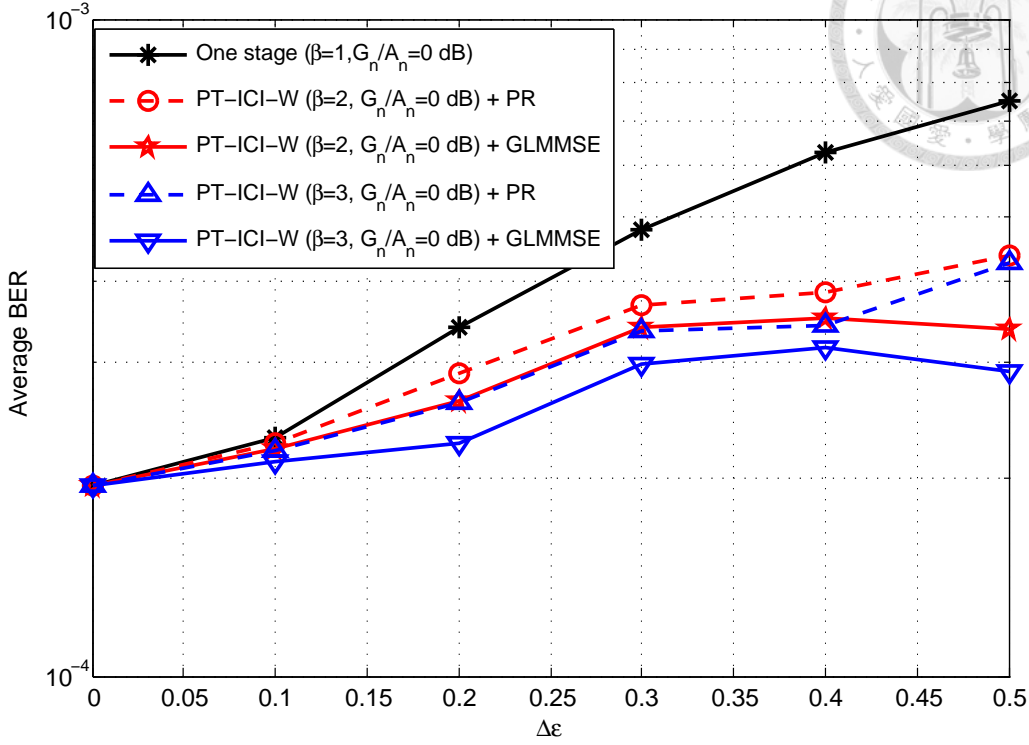


Figure 4.5: In 3-AP case, the average BERs of the  $q$ th subcarrier of AP-2 are plotted w.r.t  $\Delta\varepsilon$ . The parameters are set as  $\alpha = 10$ ,  $N_{\text{rx}} = 3$ ,  $\varepsilon_2 = 0$ ,  $\Delta\varepsilon = \varepsilon_1 - \varepsilon_2 = \varepsilon_2 - \varepsilon_3$ ,  $\frac{A_n}{\sigma_v^2} = 10$  dB, and  $\frac{G_n}{A_n} = 0$  dB for  $n = 1, 2, 3$ . The two-stage processing is implemented as PT-ICI-W + GLMMSE/PR.

and its performance is improved by increasing  $\beta$ . Additionally, the second-stage ICI suppression by GLMMSE behaves better than that by PR.

Fig. 4.6 shows the results of two-stage processing for different  $\frac{G_n}{A_n}$ 's. In the upper part of Fig. 4.6 with  $\beta = 2$ , the behaviors of PT-ICI-W plus GLMMSE for  $\frac{G_n}{A_n} = 0, \pm 5$  dB do not have prominent difference, the average BERs are between  $3.4 \times 10^{-4}$  and  $4.3 \times 10^{-4}$  when  $\Delta\varepsilon \geq 0.3$ , while in the lower part of Fig. 4.6 with  $\beta = 3$ , the average BERs for different ratios  $\frac{G_n}{A_n}$  fall within the interval  $(2.9 \times 10^{-4}, 3.7 \times 10^{-4})$  as  $\Delta\varepsilon \geq 0.3$ , revealing the insensitivity of PT-ICI-W to the value of  $G_n$ . In Fig. 4.6, we also observe that the performance of PT-ICI-W plus GLMMSE is slightly inferior to T-ICI-W plus GLMMSE, but please recall that T-ICI-W needs far ICI covariance estimation that may not be feasible in downlink.

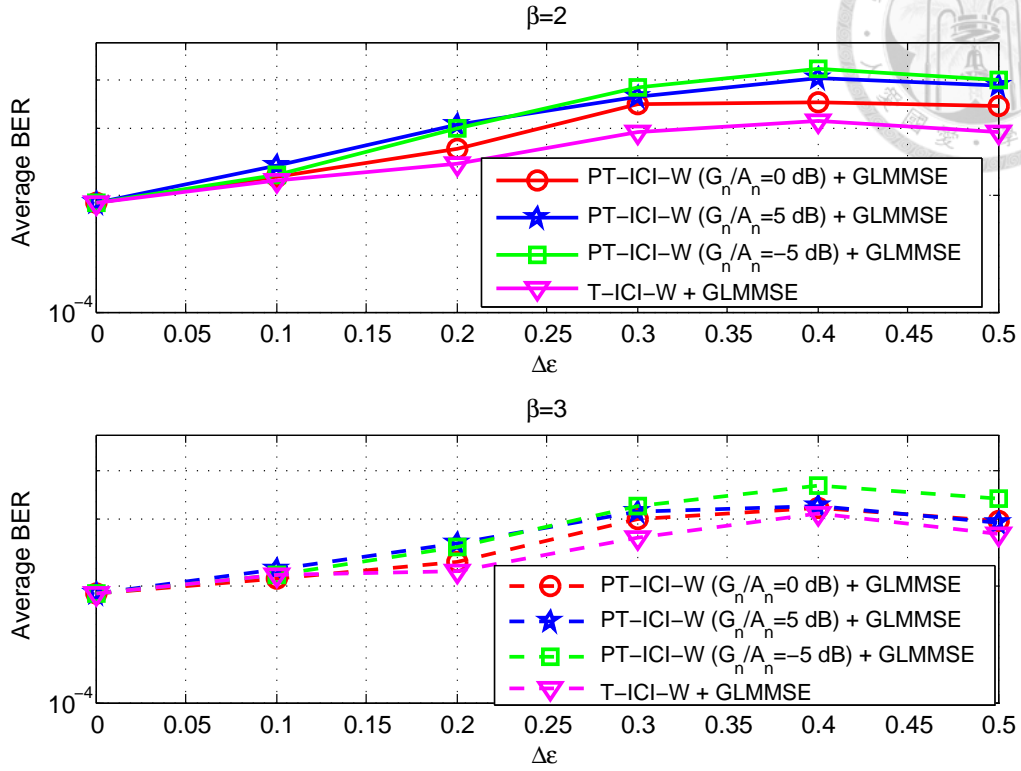
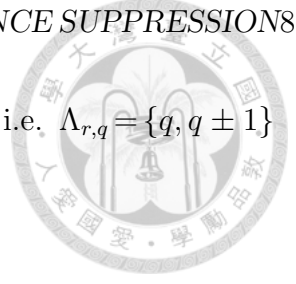


Figure 4.6: (Upper)  $\beta = 2$ . (Lower)  $\beta = 3$ . In 3-AP case, the average BERs of the  $q$ th subcarrier of AP-2 are plotted w.r.t  $\Delta\varepsilon$ . The parameters are set as  $\alpha = 10$ ,  $N_{\text{rx}} = 3$ ,  $\varepsilon_2 = 0$ ,  $\Delta\varepsilon = \varepsilon_1 - \varepsilon_2 = \varepsilon_2 - \varepsilon_3$ ,  $\frac{A_n}{\sigma_v^2} = 10$  dB, and  $\frac{G_n}{A_n} = 0, \pm 5$  dB for  $n = 1, 2, 3$ . One stage-processing is based on PT-ICI-W, and two-stage processing is implemented as PT-ICI-W + GLMMSE.

In addition to neighboring ICI, one may want to include more ICI/CCI terms to suppress by GLMMSE or PR. Different alternatives for second-stage processing are considered:

- Alternative-1: Cancel neighboring ICI, i.e. jointly detect the desired signal, CCI, and adjacent ICI terms ( $\Lambda_{n,q} = \{q_n, q_n \pm 1\}$  for  $n = 1, \dots, N$ ).
- Alternative-2: Cancel neighboring and far-adjacent ICI, i.e. jointly detect the desired signal, CCI, and near-adjacent ICI terms ( $\Lambda_{r,q} = \{q, q \pm 1\}$  and  $\Lambda_{n,q} = \{q_n, q_n - \text{sgn}(\tilde{\varepsilon}_n)\}$  for  $n \neq r$ ).
- Alternative-3: Cancel neighboring and self-adjacent ICI, i.e.  $\Lambda_{r,q} = \{q\}$  and  $\Lambda_{n,q} = \{q_n, q_n \pm 1\}$  for  $n \neq r$ .



- Alternative-4: Cancel neighboring and near-adjacent ICI, i.e.  $\Lambda_{r,q} = \{q, q \pm 1\}$  and  $\Lambda_{n,q} = \{q_n, q_n + \text{sgn}(\tilde{\varepsilon}_n)\}$  for  $n \neq r$ .

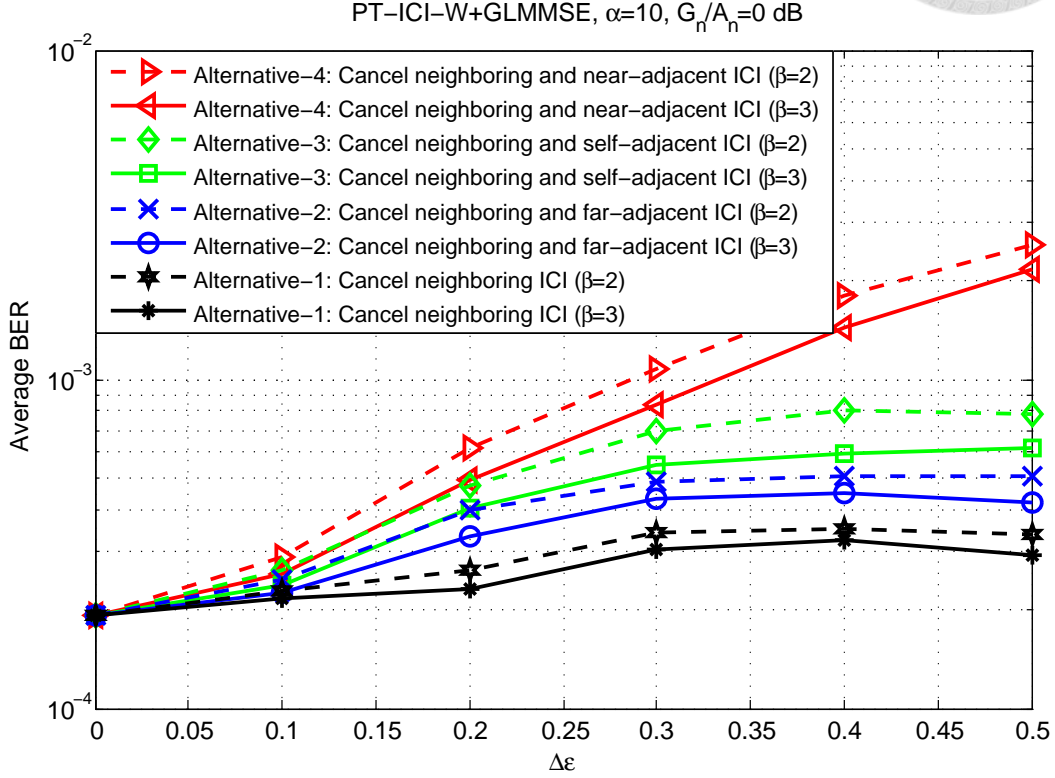


Figure 4.7: In 3-AP case, the average BERs of the  $q$ th subcarrier of AP-2 are plotted w.r.t  $\Delta\varepsilon$ . The parameters are set as  $\alpha = 10$ ,  $N_{\text{rx}} = 3$ ,  $\varepsilon_2 = 0$ ,  $\Delta\varepsilon = \varepsilon_1 - \varepsilon_2 = \varepsilon_2 - \varepsilon_3$ ,  $\frac{A_n}{\sigma_v^2} = 10$  dB, and  $\frac{G_n}{A_n} = 0$  dB for  $n = 1, 2, 3$ . The two-stage processing is implemented as PT-ICI-W + GLMMSE.

Applying the two-stage processing “PT-ICI-W + GLMMSE” to the 3-AP case of Fig. 4.5, the average BERs of cancelling neighboring ICI plus two more ICI terms according to different alternatives are plotted in Fig. 4.7, where we notice that suppressing near-adjacent ICI degrades the BER most and the far-adjacent ICI is least harmful to cancel among all adjacent ICI terms. For “PT-ICI-W + PR”, the average BERs of different alternatives are reported in Fig. 4.8, which also shows the serious BER degradation of suppressing near-adjacent ICI, moreover, increasing  $\beta$  does not yield obvious improvement. Comparing Fig. 4.7 with Fig. 4.8, we see that GLMMSE works better than PR, particularly for Alternatives-2~3 and  $\Delta\varepsilon > 0.3$ .



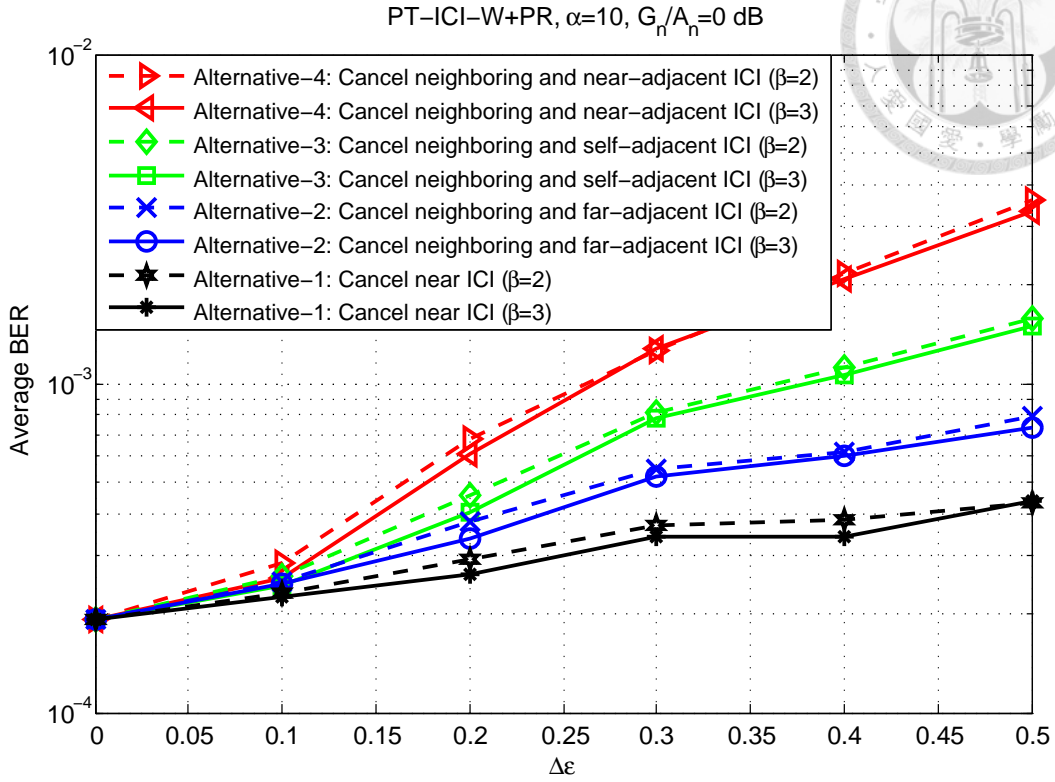


Figure 4.8: In 3-AP case, the average BERs of the  $q$ th subcarrier of AP-2 are plotted w.r.t  $\Delta\varepsilon$ . The parameters are set as  $\alpha = 10$ ,  $N_{\text{rx}} = 3$ ,  $\varepsilon_2 = 0$ ,  $\Delta\varepsilon = \varepsilon_1 - \varepsilon_2 = \varepsilon_2 - \varepsilon_3$ ,  $\frac{A_n}{\sigma_v^2} = 10$  dB, and  $\frac{G_n}{A_n} = 0$  dB for  $n = 1, 2, 3$ . The two-stage processing is implemented as PT-ICI-W + PR.

The performance of PT-ICI-W + GLMMSE with Alternative-2 for  $\frac{G_n}{A_n} = 0, \pm 5$  dB is reported in Fig. 4.9, in which the average BERs for  $\beta = 2$  and  $\beta = 3$  respectively fall within the intervals  $(4.1 \times 10^{-4}, 6.3 \times 10^{-4})$  and  $(3.4 \times 10^{-4}, 5.2 \times 10^{-4})$  as  $\Delta\varepsilon > 0.2$ . From the results in Fig. 4.2, Fig. 4.4, Fig. 4.6, and Fig. 4.9, it is better to set  $G_n = A_n$ , implying the need to estimate  $A_n$  (AP- $n$ 's mean signal power), however, those results also reveal that poor estimation of  $A_n$  (e.g.  $\frac{G_n}{A_n} = \pm 5$  dB) does not deteriorate the performance seriously, demonstrating the robustness of our method.

In Fig. 4.10, we report the performance of PT-ICI-W + GLMMSE ( $\alpha = 10$ ,  $\beta = 2, 3$ , and  $\frac{G_n}{A_n} = 0$  dB) of 4-AP case, where  $N_{\text{rx}} = 4$ ,  $\varepsilon_2 = 0.35$ ,  $\varepsilon_1 = 0.45$ ,  $\varepsilon_3 = \varepsilon_2 - \Delta\varepsilon$ ,  $\varepsilon_4 = \varepsilon_2 - \Delta\varepsilon - 0.02$ ,  $\frac{A_2}{\sigma_v^2} = 7$  dB,  $\frac{A_1}{A_2} = 3$  dB,  $\frac{A_3}{A_2} = -3$  dB,  $\frac{A_4}{A_2} = -5$  dB. In this case, Alternative-2 and Alternative-3 leads to almost identical BERs,

and the consequence of taking Alternative-4 is still terrible, even worse than that of suppressing neighboring, far- and self-adjacent ICI (Alternative-5).

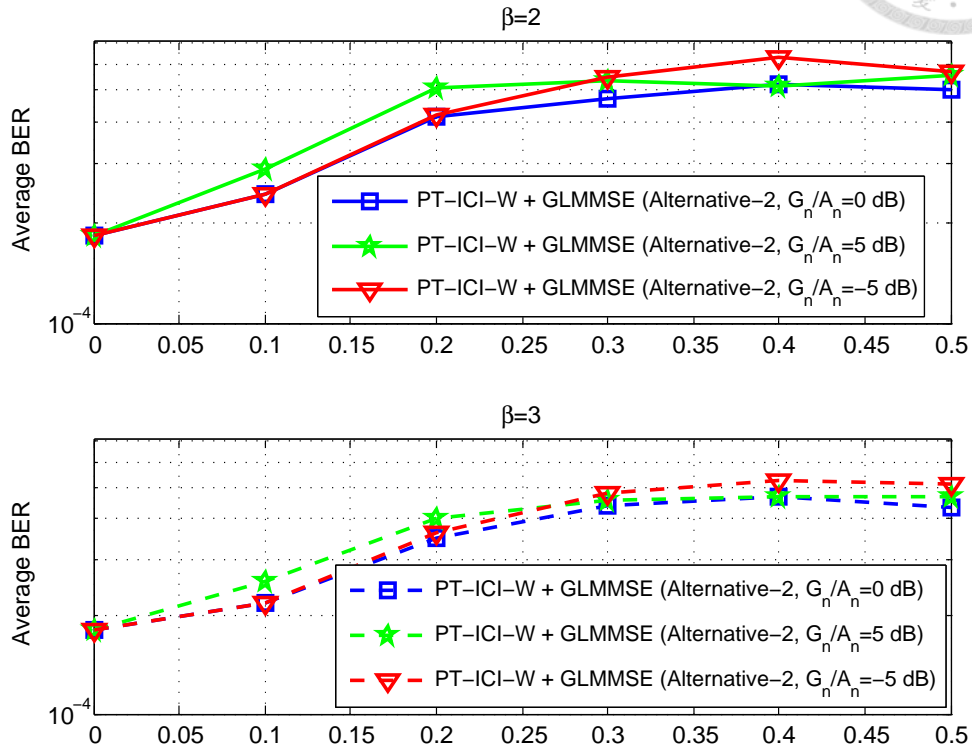


Figure 4.9: (Upper)  $\beta = 2$ . (Lower)  $\beta = 3$ . In 3-AP case, the average BERs of the  $q$ th subcarrier of AP-2 are plotted w.r.t  $\Delta\varepsilon$ . The parameters are set as  $\alpha = 10$ ,  $N_{\text{rx}} = 3$ ,  $\varepsilon_2 = 0$ ,  $\Delta\varepsilon = \varepsilon_1 - \varepsilon_2 = \varepsilon_2 - \varepsilon_3$ ,  $\frac{A_n}{\sigma_v^2} = 10$  dB, and  $\frac{G_n}{A_n} = 0, \pm 5$  dB for  $n = 1, 2, 3$ . The two-stage processing is implemented as PT-ICI-W + GLMMSE with Alternative-2.

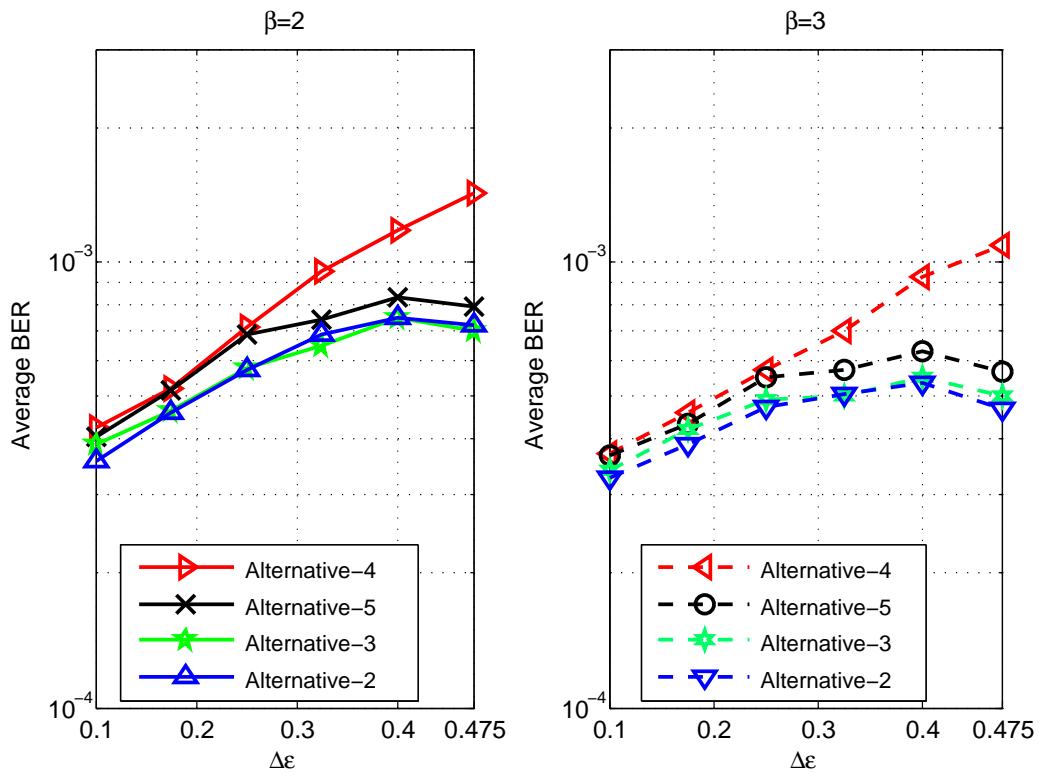


Figure 4.10: (Left)  $\beta = 2$ . (Right)  $\beta = 3$ . In 4-AP case, the average BERs of the  $q$ th subcarrier of AP-2 are plotted w.r.t  $\Delta\epsilon$ . The two-stage processing is implemented as PT-ICI-W + GLMMSE with  $\alpha = 10$  and  $\frac{G_n}{A_n} = 0$  dB for  $n = 1, 2, 3, 4$ . The parameters are set as  $N_{\text{rx}} = 4$ ,  $\epsilon_2 = 0.35$ ,  $\epsilon_1 = 0.45$ ,  $\epsilon_3 = \epsilon_2 - \Delta\epsilon$ ,  $\epsilon_4 = \epsilon_2 - \Delta\epsilon - 0.02$ ,  $\frac{A_2}{\sigma_v^2} = 7$  dB,  $\frac{A_1}{A_2} = 3$  dB,  $\frac{A_3}{A_2} = -3$  dB,  $\frac{A_4}{A_2} = -5$  dB. Alternative-5 means suppressing neighboring, far- and self-adjacent ICI.

## 4.4 Generalization to the Case with STBC

Our formulation of PT-ICI-W and GLMMSE can be generalized to the scenario, in which each AP has  $N_{\text{tx}}$  antennas. The first-stage processed signal is obtained by modifying (4.46) as

$$\bar{\mathbf{y}}_{z,\text{tS}} = \sum_{(n,k) \in \Omega} \sum_{b=1}^{N_{\text{tx}}} \frac{1}{\sqrt{N_{\text{tx}}}} \mathbf{s}_{t,b,k}(\varepsilon_n) e^{j(z-1)\phi_n} X_{n,k,b}^z + \bar{\mathbf{v}}_{z,\text{tS}}, \quad (4.55)$$

$$\mathbf{s}_{t,b,k}(\varepsilon_n) = \sqrt{A_n} \mathbf{h}_{n,k,b} \otimes \mathbf{f}_{t,k}(\varepsilon_n), \quad (4.56)$$

$$\mathbf{h}_{n,k,b} = [H_{n,k,b}^1, \dots, H_{n,b,k}^{N_{\text{rx}}}] . \quad (4.57)$$

Here  $X_{n,k,b}^z$  is the data symbol sent from AP- $n$ 's  $b$ th antenna on the  $k$ th subcarrier of  $z$ th OFDM symbol, and  $H_{n,k,b}^m$  is the  $k$ th subcarrier's fading gain from the  $b$ th antenna of AP- $n$  to the  $m$ th antenna of vehicle. For more reliable uRLLC transmissions, we assume that APs employ STBCs, considering Complex Interleaved Orthogonal Design (CIOD) [69] and Alamouti scheme [68].

### 4.4.1 Complex Interleaved Orthogonal Design

Let's first review CIOD for  $N_{\text{tx}} = 2$  [69]. Suppose that  $\bar{X}_{n,k,1}$  and  $\bar{X}_{n,k,2}$  are the transmitted QAM-symbols from AP- $n$ 's  $k$ th subcarrier over two OFDM symbol periods. Rotating the constellation counterclockwise by an angle  $\theta$  yields  $U_{n,k,1} = e^{j\theta} \bar{X}_{n,k,1}$  and  $U_{n,k,2} = e^{j\theta} \bar{X}_{n,k,2}$ , whose imaginary parts are swapped to obtain

$$\begin{aligned} \bar{U}_{n,k}^z &= \text{Re}(U_{n,k,1}) + j\text{Im}(U_{n,k,2}) \\ &= (\text{Re}(\bar{X}_{n,k,1}) \cos \theta - \text{Im}(\bar{X}_{n,k,1}) \sin \theta) + j (\text{Re}(\bar{X}_{n,k,2}) \sin \theta + \text{Im}(\bar{X}_{n,k,2}) \cos \theta), \end{aligned} \quad (4.58)$$

$$\begin{aligned} \bar{U}_{n,k}^{z+1} &= \text{Re}(U_{n,k,2}) + j\text{Im}(U_{n,k,1}) \\ &= (\text{Re}(\bar{X}_{n,k,2}) \cos \theta - \text{Im}(\bar{X}_{n,k,2}) \sin \theta) + j (\text{Re}(\bar{X}_{n,k,1}) \sin \theta + \text{Im}(\bar{X}_{n,k,1}) \cos \theta). \end{aligned} \quad (4.59)$$

The notations  $\text{Re}(\cdot)$  and  $\text{Im}(\cdot)$  express the real and imaginary parts. In the  $z$ th OFDM symbol duration  $\bar{U}_{n,k}^z$  is sent via the first antenna and the second antenna is inactive;

in the  $(z + 1)$ th OFDM symbol duration  $\bar{U}_{n,k}^{z+1}$  is sent via the second antenna and the first antenna is inactive. The angle of rotation is set as  $\theta = \frac{\arctan(2)}{2}$  to achieve the maximum coding gain [74].

Amending (4.55), the first-stage processed signals over two OFDM symbol periods are

$$\bar{\mathbf{y}}_{z,\text{tS}} = \sum_{(n,k) \in \Omega} \mathbf{s}_{t,1,k}(\varepsilon_n) e^{j(z-1)\phi_n} \bar{U}_{n,k}^z + \bar{\mathbf{v}}_{z,\text{tS}} \quad (4.60)$$

$$\bar{\mathbf{y}}_{z+1,\text{tS}} = \sum_{(n,k) \in \Omega} \mathbf{s}_{t,2,k}(\varepsilon_n) e^{jz\phi_n} \bar{U}_{n,k}^{z+1} + \bar{\mathbf{v}}_{z+1,\text{tS}}, \quad (4.61)$$

which are combined into a vector  $\tilde{\mathbf{y}}_{z,\text{CI}}$  written as

$$\tilde{\mathbf{y}}_{z,\text{CI}} = \sum_{(n,k) \in \Omega} e^{j(z-1)\phi_n} \left( \mathbf{s}_{\text{CI},1,k}(\varepsilon_n) \bar{U}_{n,k}^z + \mathbf{s}_{\text{CI},2,k}(\varepsilon_n) \bar{U}_{n,k}^{z+1} \right) + \tilde{\mathbf{v}}_{z,\text{CI}}, \quad (4.62)$$

$$\mathbf{s}_{\text{CI},1,k}^T(\varepsilon_n) = \left[ \mathbf{s}_{t,1,k}^T(\varepsilon_n) \quad \mathbf{0}_{1 \times N_{\text{rx}}(2\beta+1)} \right], \quad (4.63)$$

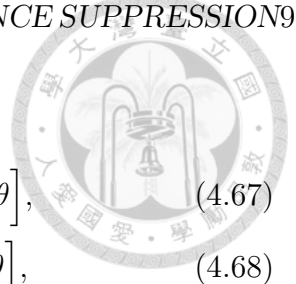
$$\mathbf{s}_{\text{CI},2,k}^T(\varepsilon_n) = \left[ \mathbf{0}_{1 \times N_{\text{rx}}(2\beta+1)} \quad e^{j\phi_n} \mathbf{s}_{t,2,k}^T(\varepsilon_n) \right], \quad (4.64)$$

$$\tilde{\mathbf{v}}_{z,\text{CI}}^T = \left[ \bar{\mathbf{v}}_{z,\text{tS}}^T \quad \bar{\mathbf{v}}_{z+1,\text{tS}}^T \right]. \quad (4.65)$$

$\mathbf{0}_{1 \times N_{\text{rx}}(2\beta+1)}$  is a  $1 \times N_{\text{rx}}(2\beta + 1)$  zero vector. Exploiting (4.62), we are now capable of deriving the operation of second-stage processing. From (4.58), (4.59), and (4.62),  $\mathbf{s}_{\text{CI},1,k}(\varepsilon_n)$  and  $\mathbf{s}_{\text{CI},2,k}(\varepsilon_n)$  carry the same information of two symbols  $\bar{X}_{n,k,1}$  and  $\bar{X}_{n,k,2}$ . Therefore,  $N_{\text{jd}}$  (the number of data symbols taken into joint detection) is only decreased by cancelling both of  $\mathbf{s}_{\text{CI},1,k}(\varepsilon_n)$  and  $\mathbf{s}_{\text{CI},2,k}(\varepsilon_n)$  (not by cancelling just either of them) for any index pair  $(n, k)$ .

An equivalent expression of  $\tilde{\mathbf{y}}_{z,\text{CI}}$  is given in (4.66), which we prove in Appendix C.

$$\tilde{\mathbf{y}}_{z,\text{CI}} = \sum_{(n,k,b) \in \tilde{\Omega}} \tilde{\mathbf{s}}_{\text{CI},b,k}(\varepsilon_n) e^{j(z-1)\phi_n} \tilde{X}_{n,k,b} + \tilde{\mathbf{v}}_{z,\text{CI}}, \quad (4.66)$$



where

$$\tilde{\mathbf{s}}_{\text{CI},1,k}^T(\varepsilon_n) = \begin{bmatrix} \mathbf{s}_{t,1,k}^T(\varepsilon_n) \cos \theta & j e^{j\phi_n} \mathbf{s}_{t,2,k}^T(\varepsilon_n) \sin \theta \end{bmatrix}, \quad (4.67)$$

$$\tilde{\mathbf{s}}_{\text{CI},2,k}^T(\varepsilon_n) = \begin{bmatrix} j \mathbf{s}_{t,1,k}^T(\varepsilon_n) \sin \theta & e^{j\phi_n} \mathbf{s}_{t,2,k}^T(\varepsilon_n) \cos \theta \end{bmatrix}, \quad (4.68)$$

$$\tilde{X}_{n,k,1} = \text{Re}(\bar{X}_{n,k,1}) + j \text{Im}(\bar{X}_{n,k,2}), \quad (4.69)$$

$$\tilde{X}_{n,k,2} = \text{Re}(\bar{X}_{n,k,2}) + j \text{Im}(\bar{X}_{n,k,1}), \quad (4.70)$$

$$\tilde{\Omega} = \Omega \times \{1, 2\}. \quad (4.71)$$

$\tilde{X}_{n,k,1}$  and  $\tilde{X}_{n,k,2}$  are also QAM-symbols from the same constellation of  $\bar{X}_{n,k,1}$  and  $\bar{X}_{n,k,2}$ , so using (4.66) does not bring any significant change in decoding operation. The estimate of  $\bar{X}_{n,k,1}$  and  $\bar{X}_{n,k,2}$  are easily obtained by swapping the imaginary parts of the estimates of  $\tilde{X}_{n,k,1}$  and  $\tilde{X}_{n,k,2}$ . Furthermore,  $\tilde{\mathbf{s}}_{\text{CI},1,k}(\varepsilon_n)$  and  $\tilde{\mathbf{s}}_{\text{CI},2,k}(\varepsilon_n)$ , called “streams” thereafter, carry different information, thus  $N_{\text{jd}}$  is able to be reduced by suppressing either or both of them, leading to more flexible alternatives for ICI suppression.

Let  $\tilde{\Lambda}$  be the set of triplets to index the symbols taken into joint detection, then (4.66) is rewritten as (4.72) (that is similar to (4.49)).

$$\tilde{\mathbf{y}}_{z,\text{CI}} = \sum_{(n,k,b) \in \tilde{\Lambda}} \tilde{\mathbf{s}}_{\text{CI},b,k}(\varepsilon_n) e^{j(z-1)\phi_n} \tilde{X}_{n,k,b} + \sum_{(n,k,b) \in \tilde{\Omega} \setminus \tilde{\Lambda}} \tilde{\mathbf{s}}_{\text{CI},b,k}(\varepsilon_n) e^{j(z-1)\phi_n} \tilde{X}_{n,k,b} + \tilde{\mathbf{v}}_{z,\text{CI}}. \quad (4.72)$$

Following the same procedure introduced in Subsection 4.3.1, GLMMSE is derived from (4.72). The projection matrix is obtained by revising (4.54) as

$$\left( \tilde{\mathbf{S}}_{\text{I}} \tilde{\mathbf{S}}_{\text{I}}^H + \mathbf{I}_{2N_{\text{rx}}(2\beta+1)} \right)^{-1} \tilde{\mathbf{S}}_{\text{d}} = \mathbf{Q}_{\tilde{\Lambda}} \mathbf{R}_{\tilde{\Lambda}}, \quad (4.73)$$

where  $\tilde{\mathbf{S}}_{\text{d}}$  and  $\tilde{\mathbf{S}}_{\text{I}}$  are the matrices consisting of  $\tilde{\mathbf{s}}_{\text{CI},b,k}(\varepsilon_n)$ 's with the indices respectively from  $\tilde{\Lambda}$  and  $\tilde{\Omega} \setminus \tilde{\Lambda}$  as their columns.

#### 4.4.2 Alamouti Coding

Next, we look into Alamouti scheme in our asynchronous scenario. At the  $z$ th OFDM symbol duration,  $\bar{X}_{n,k,1}$  is sent from AP- $n$ 's first antenna and  $\bar{X}_{n,k,2}$  is sent from

the second antenna. During the next symbol time interval,  $-\bar{X}_{n,k,2}^*$  and  $\bar{X}_{n,k,1}^*$  are respectively transmitted from the first and second antennas of AP- $n$ . The received signals after the first-stage processing are

$$\bar{\mathbf{y}}_{z,\text{tS}} = \sum_{(n,k) \in \Omega} \frac{1}{\sqrt{2}} e^{j(z-1)\phi_n} \left( \mathbf{s}_{t,1,k}(\varepsilon_n) \bar{X}_{n,k,1} + \mathbf{s}_{t,2,k}(\varepsilon_n) \bar{X}_{n,k,2} \right) + \bar{\mathbf{v}}_{z,\text{tS}}, \quad (4.74)$$

$$\bar{\mathbf{y}}_{z+1,\text{tS}} = \sum_{(n,k) \in \Omega} \frac{1}{\sqrt{2}} e^{jz\phi_n} \left( \mathbf{s}_{t,1,k}(\varepsilon_n) (-\bar{X}_{n,k,2}^*) + \mathbf{s}_{t,2,k}(\varepsilon_n) \bar{X}_{n,k,1}^* \right) + \bar{\mathbf{v}}_{z+1,\text{tS}}. \quad (4.75)$$

Likewise  $\bar{\mathbf{y}}_{z,\text{tS}}$  and  $\bar{\mathbf{y}}_{z+1,\text{tS}}^*$  are arranged as a vector  $\mathbf{y}_{z,\text{AL}}$ ,

$$\mathbf{y}_{z,\text{AL}} = \begin{bmatrix} \bar{\mathbf{y}}_{z,\text{tS}} \\ \bar{\mathbf{y}}_{z+1,\text{tS}}^* \end{bmatrix} = \sum_{(n,k,b) \in \tilde{\Lambda}} \mathbf{s}_{\text{AL},b,k}(\varepsilon_n) \bar{X}_{n,k,b} + \sum_{(n,k,b) \in \tilde{\Omega} \setminus \tilde{\Lambda}} \mathbf{s}_{\text{AL},b,k}(\varepsilon_n) \bar{X}_{n,k,b} + \mathbf{v}_{z,\text{AL}}, \quad (4.76)$$

where

$$\mathbf{s}_{\text{AL},1,k}^T(\varepsilon_n) = \frac{1}{\sqrt{2}} \begin{bmatrix} e^{j(z-1)\phi_n} \mathbf{s}_{t,1,k}^T(\varepsilon_n) & e^{-jz\phi_n} \mathbf{s}_{t,2,k}^H(\varepsilon_n) \end{bmatrix}, \quad (4.77)$$

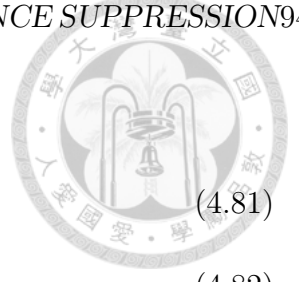
$$\mathbf{s}_{\text{AL},2,k}^T(\varepsilon_n) = \frac{1}{\sqrt{2}} \begin{bmatrix} e^{j(z-1)\phi_n} \mathbf{s}_{t,2,k}^T(\varepsilon_n) & -e^{-jz\phi_n} \mathbf{s}_{t,1,k}^H(\varepsilon_n) \end{bmatrix}, \quad (4.78)$$

$$\mathbf{v}_{z,\text{AL}}^T = \begin{bmatrix} \bar{\mathbf{v}}_{z,\text{tS}}^T & \bar{\mathbf{v}}_{z+1,\text{tS}}^H \end{bmatrix}. \quad (4.79)$$

From (4.76), GLMMSE is ready to be executed, and the projection matrix is yielded in the same way similar as (4.73). Nevertheless, due to CFO-induced phase rotation  $\pm z\phi_n$ ,  $\mathbf{s}_{\text{AL},1,k}(\varepsilon_n)$  and  $\mathbf{s}_{\text{AL},2,k}(\varepsilon_n)$  vary with the OFDM symbol index  $z$  (refer to (4.77) and (4.78)), so does the covariance matrix of ICI terms that are chosen to be suppressed by GLMMSE. It entails re-calculating the projection matrix very frequently (once every two OFDM symbol periods). This nature of Alamouti-coded interference causes similar trouble to PR and general zero-forcing/LMMSE filtering methods.

To eliminate the CFO-related trouble, we separate the real and imaginary parts of  $\bar{X}_{n,k,b}$ , and combine (4.74) and (4.75) to obtain

$$\tilde{\mathbf{y}}_{z,\text{AL}} = \sum_{(n,k,b) \in \tilde{\Omega}} e^{j(z-1)\phi_n} \left( \tilde{\mathbf{s}}_{\text{AR},b,k}(\varepsilon_n) \text{Re}(\bar{X}_{n,k,b}) + \tilde{\mathbf{s}}_{\text{AI},b,k}(\varepsilon_n) \text{Im}(\bar{X}_{n,k,b}) \right) + \tilde{\mathbf{v}}_{z,\text{AL}}, \quad (4.80)$$



where

$$\tilde{\mathbf{s}}_{\text{AR},1,k}^T(\varepsilon_n) = \frac{1}{\sqrt{2}} \begin{bmatrix} \mathbf{s}_{t,1,k}^T(\varepsilon_n) & e^{j\phi_n} \mathbf{s}_{t,2,k}^T(\varepsilon_n) \end{bmatrix}, \quad (4.81)$$

$$\tilde{\mathbf{s}}_{\text{AI},1,k}^T(\varepsilon_n) = \frac{1}{\sqrt{2}} \begin{bmatrix} j\mathbf{s}_{t,1,k}^T(\varepsilon_n) & -je^{j\phi_n} \mathbf{s}_{t,2,k}^T(\varepsilon_n) \end{bmatrix}, \quad (4.82)$$

$$\tilde{\mathbf{s}}_{\text{AR},2,k}^T(\varepsilon_n) = \frac{1}{\sqrt{2}} \begin{bmatrix} \mathbf{s}_{t,2,k}^T(\varepsilon_n) & -e^{j\phi_n} \mathbf{s}_{t,1,k}^T(\varepsilon_n) \end{bmatrix}, \quad (4.83)$$

$$\tilde{\mathbf{s}}_{\text{AI},2,k}^T(\varepsilon_n) = \frac{1}{\sqrt{2}} \begin{bmatrix} j\mathbf{s}_{t,2,k}^T(\varepsilon_n) & je^{j\phi_n} \mathbf{s}_{t,1,k}^T(\varepsilon_n) \end{bmatrix}, \quad (4.84)$$

$$\tilde{\mathbf{v}}_{z,\text{AL}}^T = \begin{bmatrix} \tilde{\mathbf{v}}_{z,\text{tS}}^T & \tilde{\mathbf{v}}_{z+1,\text{tS}}^T \end{bmatrix}. \quad (4.85)$$

The expressions of streams  $\tilde{\mathbf{s}}_{\text{AR},b,k}(\varepsilon_n)$  and  $\tilde{\mathbf{s}}_{\text{AI},b,k}(\varepsilon_n)$  do not involve the term  $\pm z\phi_n$ , thus frequent update of projection matrix is not needed if GLMMSE is derived from (4.80).

### 4.4.3 Performance Comparison

In 2-AP case with  $N_{\text{rx}} = 2$  and QPSK on all used subcarriers, we compare CIOD and Alamouti coding when applying PT-ICI-W + GLMMSE, in which  $\alpha = 8$ ,  $\beta = 2$ , and  $\frac{G_n}{A_n} = 0$  dB. The performance of interest is the BERs of data symbols conveyed by the streams of AP-2's  $q$ th subcarrier. Two ICI suppression alternatives for GLMMSE are taken in simulations:

- Alternative-5:  $\tilde{\Lambda} = \bigcup_{n=1}^2 \bigcup_{b=1}^2 \{(n, q_n, b)\} = \tilde{\Lambda}_{\text{AL5}}$ , which implies cancellation of interfering streams from all ICI terms and joint decoding of desired signal and CCI.
- Alternative-6: Joint detection of desired signal, CCI, near-adjacent ICI, and the stream(s) with  $b = 1$  from self-adjacent ICI, i.e.  $\tilde{\Lambda} = \bigcup_{b=1}^2 \{(1, q_1 - \text{sgn}(\tilde{\varepsilon}_1), b)\} \cup \tilde{\Lambda}_{\text{AL5}} \cup \{(2, q - 1, 1)\}$ .

The ICI suppression processes for Alamouti-coded signals based on (4.76) and (4.80) are labelled by “Alamouti-GL1” and “Alamouti-GL2”, respectively. In Alamouti-GL2 (using (4.80)), the projection matrix is obtained by (4.73) with some modification



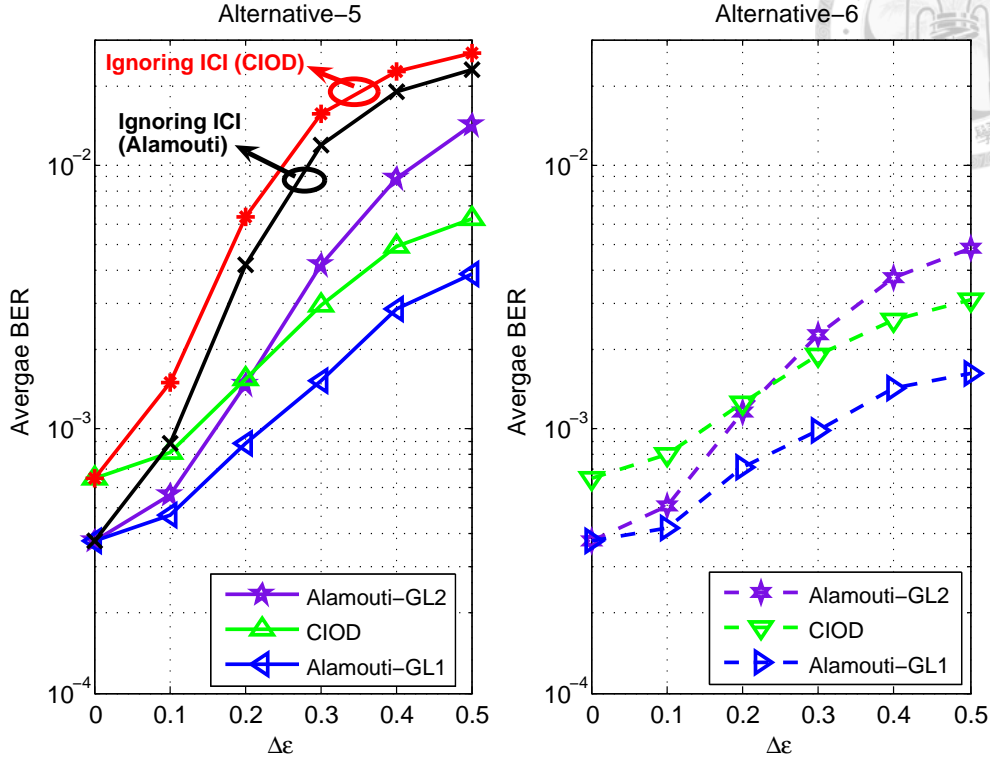


Figure 4.11: (Left) Alternative-5. (Right) Alternative-6. In 2-AP case, the average BERs of the  $q$ th subcarrier of AP-2 are plotted w.r.t  $\Delta\varepsilon$ . The two-stage processing is implemented as PT-ICI-W ( $\alpha = 8$ ,  $\beta = 2$ , and  $\frac{G_n}{A_n} = 0$  dB for  $n = 1, 2$ ) + GLMMSE. Other parameters are  $\varepsilon_2 = 0$ ,  $\Delta\varepsilon = \varepsilon_1 - \varepsilon_2 \in [0, 0.5]$ ,  $N_{\text{rx}} = 2$ ,  $\frac{A_2}{\sigma_v^2} = 13$  dB, and  $\frac{A_1}{A_2} = -3$  dB.

where the columns of  $\tilde{\mathbf{S}}_1$  are  $\tilde{\mathbf{s}}_{\text{AR},b,k}(\varepsilon_n)$ 's and  $\tilde{\mathbf{s}}_{\text{AI},b,k}(\varepsilon_n)$ 's for  $(n, k, b) \in \tilde{\Omega} \setminus \tilde{\Lambda}$ . To avoid retaining too much power of interfering streams after projection, we limit the dimension of subspace, towards which  $\tilde{\mathbf{y}}_{z,\text{AL}}$  is projected, setting  $\tilde{\mathbf{S}}_d = \tilde{\mathbf{S}}_{d,\text{AL}5}$  for Alternative-5 and  $\tilde{\mathbf{S}}_d = \tilde{\mathbf{S}}_{d,\text{AL}6}$  for Alternative-6, where

$$\tilde{\mathbf{S}}_{d,\text{AL}5} = \begin{bmatrix} \tilde{\mathbf{s}}_{\text{AR},1,q}(\varepsilon_2) & \tilde{\mathbf{s}}_{\text{AI},1,q}(\varepsilon_2) & \tilde{\mathbf{s}}_{\text{AR},2,q}(\varepsilon_2) & \tilde{\mathbf{s}}_{\text{AI},2,q}(\varepsilon_2) \end{bmatrix}, \quad (4.86)$$

$$\tilde{\mathbf{S}}_{d,\text{AL}6} = \begin{bmatrix} \tilde{\mathbf{S}}_{d,\text{AL}5} & \tilde{\mathbf{s}}_{\text{AR},1,q-1}(\varepsilon_2) & \tilde{\mathbf{s}}_{\text{AI},1,q-1}(\varepsilon_2) \end{bmatrix}. \quad (4.87)$$

The simulation results of the above alternatives as well as Without-Whitening with  $\alpha = \beta = 0$  (i.e. jointly decoding the desired signal and CCI while ignoring ICI) are given in Fig. 4.11, where  $\varepsilon_2 = 0$ ,  $\Delta\varepsilon = \varepsilon_1 - \varepsilon_2 \in [0, 0.5]$ ,  $N_{\text{rx}} = 2$ ,  $\frac{A_2}{\sigma_v^2} = 13$  dB, and  $\frac{A_1}{A_2} = -3$  dB. Clearly, ‘‘Ignoring ICI’’ works very poorly. Compared to CIOD,

Alamouti-GL1 achieves lower BER but is accompanied with highly dynamic ICI covariance to bring the aforementioned trouble, which can be avoided by Alamouti-GL2, however, at the expense of performance deterioration, as seen from the blue and purple curves in Fig. 4.11. We also notice that the average BERs of Alamouti-GL2 ascend more steeply than CIOD as the CFO difference,  $\Delta\varepsilon$ , increases.

The results of Alternative-6 versus signal-to-noise ratio (SNR)  $\frac{A_2}{\sigma_V^2}$  are plotted in Fig. 4.12. At identical average BER (say  $10^{-3}$  or less), the difference of  $\frac{A_2}{\sigma_V^2}$  between CIOD and Alamouti-GL1 is roughly 1 dB for different  $\Delta\varepsilon$ . When  $\Delta\varepsilon = 0.2$ , there is no clear distinction between the performance of CIOD and Alamouti-GL2 over the observed SNR range. However, at  $\Delta\varepsilon = 0.3, 0.5$  (see the lower parts of Fig. 4.12), in order to achieve the same BER of Alamouti-GL1, e. g.  $10^{-3}$ , Alamouti-GL2 requires additional 2 dB of SNR or more.

Alamouti-coded interference creates the dilemma between intensive re-calculation of projection matrix and serious BER degradation, especially for highly asynchronous situations. In spite of having lower coding gain than Alamouti scheme, CIOD with  $N_{\text{tx}} = 2$  serves a compromise to prevent such dilemma, hence is preferable to Alamouti coding and recommended for asynchronous transmissions to facilitate receiver design.

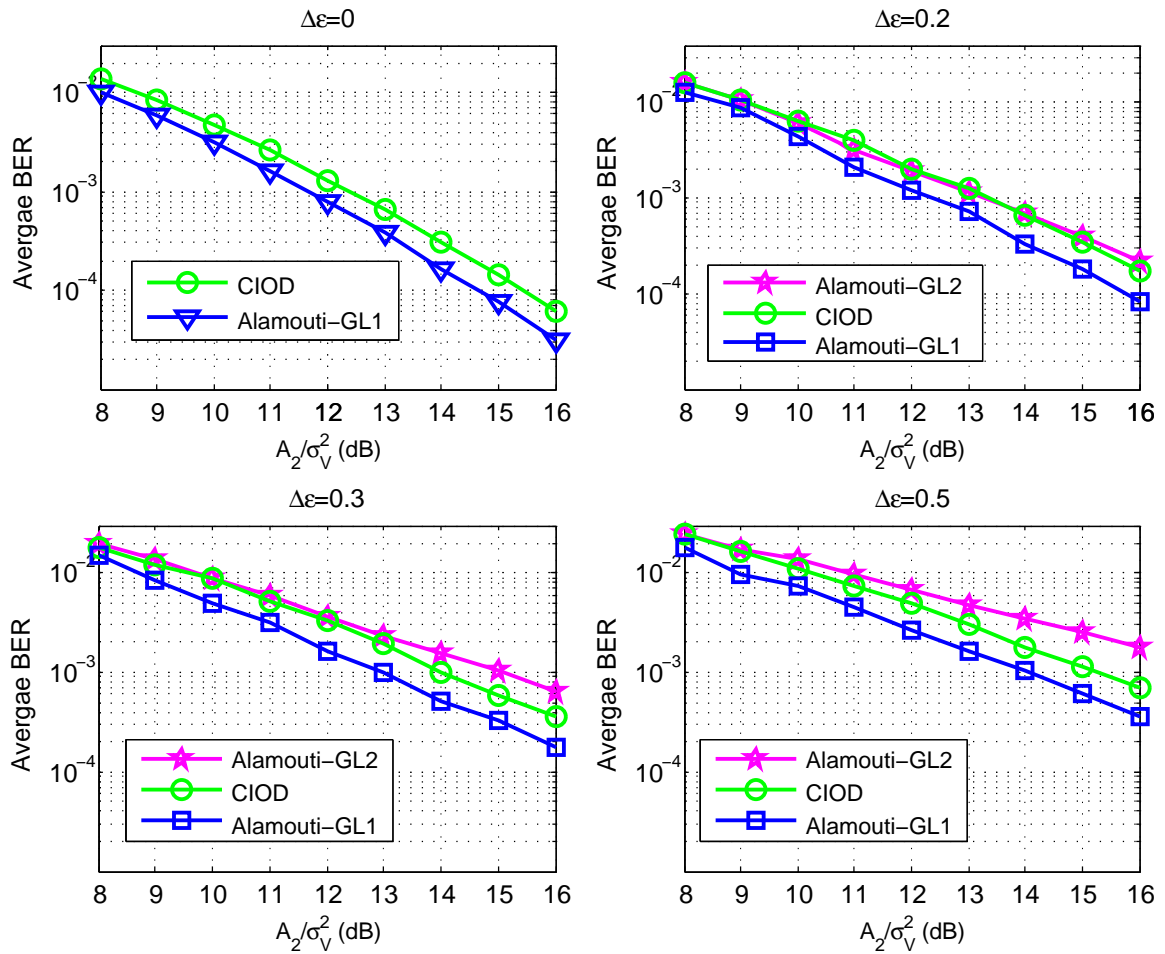


Figure 4.12: (Upper-Left)  $\Delta\varepsilon = 0$ . (Upper-Right)  $\Delta\varepsilon = 0.2$ . (Lower-Left)  $\Delta\varepsilon = 0.3$ . (Lower-Right)  $\Delta\varepsilon = 0.5$ . In 2-AP case, the average BERs of Alternative-6 versus SNR  $\frac{A_2}{\sigma_v^2}$  are plotted. The two-stage processing is implemented as PT-ICI-W ( $\alpha = 8$ ,  $\beta = 2$ , and  $\frac{G_n}{A_n} = 0$  dB for  $n = 1, 2$ ) + GLMMSE. Other parameters are  $\varepsilon_2 = 0$ ,  $\Delta\varepsilon = \varepsilon_1 - \varepsilon_2$ ,  $N_{\text{rx}} = 2$ , and  $\frac{A_1}{A_2} = -3$  dB.

## 4.5 Summary

Multi-CFO issue makes downlink MAI more serious, where the receiver faces both CCI and ICI. Whitening ICI prior to MUD can yield good performance, but such scheme does not fit downlink transmissions. Analyzing the inner products of signature waveforms, we discover that the estimation of far ICI covariance is not necessary, consequently proposing P-ICI-W and PT-ICI-W as the first-stage processing, which can approach traditional whitening scheme. For the second-stage processing, GLMMSE achieves better performance than PR, and the simulation studies also point out the serious BER aggravation of cancelling near-adjacent ICI. We also show how to decode received signals by our two-stage processing when APs use Alamouti coding or CIOD. Although CIOD has smaller coding gain, its projection matrix does not require frequent update, which practically is more suitable for proactive open-loop downlink uRLLC multiple access.



## Chapter 5

# Cooperative Coding in Frequency Domain

In the previous chapters, we focus on the receiver design in the worst case that the serving APs of the virtual randomly allocate the RRUs without using any PHY cooperative transmission schemes. In this chapter, we assume that, under the coordination of anchor node (AN), the APs allocate the same RRUs for the vehicle in service and are able to cooperatively encode the data symbols to gain the transmit diversity, as shown Fig. 5.1. With the multi-CFO issue still being included, we develop an easy principle for the AN to index the serving APs of virtual cell to achieve better performance. On the other hand, allowing the AN to index APs randomly, a robust cooperative encoding scheme is also proposed to counter against CFO problem. The signal model of this chapter is the same with that of Chapter 4, and the simulation parameters in Table 4.1 with  $q = 15$  are adopted.

The encoding can be performed over either or both of time and frequency domains. For simplicity, we adopt the coding scheme in just one domain. Due to CFOs, some of adjacent ICI terms should be included into MUD to achieve better performance, as indicated from Chapter 4. If time-domain encoding is taken, the receiver will need to jointly decode the data symbols across both time and frequency domains. Considering the practical detection complexity, this coding strategy is not favored in general  $N$ -AP case. Hence, we adopt cooperative coding in frequency domain.

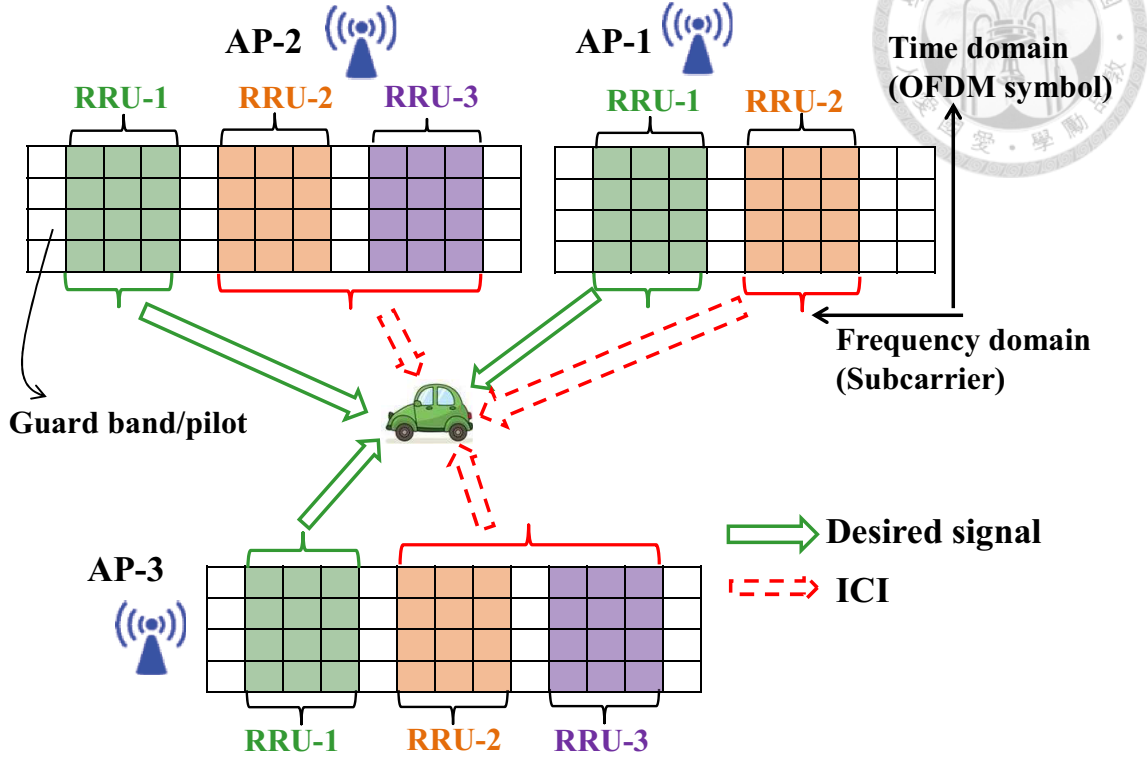


Figure 5.1: The serving APs in virtual cell are coordinated by the AN to allocate the same RRU for the green car and enforce cooperative transmissions. The blanks between different RRUs are intended for guard bands or pilots. Due to CFO issue, the ICI from other RRUs will interfere with green car's data receiving from RRU-1.

## 5.1 Cooperative Encoding and MRC

In OFDMA, we consider a virtual cell of  $N$  APs, which are coordinated by the AN to allocate the same  $\eta$  subcarriers for the vehicle, where  $\eta \geq N$  and the set of subcarriers indices is  $\mathcal{B}_{q,\eta} = \{q, \dots, q + \eta - 1\}$ . Recall that  $X_{n,k}^z$  represents the data symbol from AP- $n$ 's  $k$ th subcarrier of  $z$ th OFDM symbol. Using the coding scheme introduced in [75], AP- $n$ 's transmitted data sequence over the allocated subcarriers is as follows.

$$\mathbf{x}_{n,q}^z = [X_{n,q}^z \cdots X_{n,q+\eta-1}^z]^T = \mathbf{M}_\eta^{n-1} [\bar{X}_q^z \cdots \bar{X}_{q+\eta-1}^z]^T, \quad (5.1)$$

where

$$\mathbf{M}_\eta = \begin{bmatrix} \mathbf{0}_{1 \times (\eta-1)} & \gamma \\ \mathbf{I}_{(\eta-1)} & \mathbf{0}_{(\eta-1) \times 1} \end{bmatrix}. \quad (5.2)$$

Two examples are given in Fig. 5.2, where AP- $(n+1)$ 's transmitted sequence is obtained via circularly shifting  $\mathbf{x}_{n,q}^z$  as well as multiplying the first component

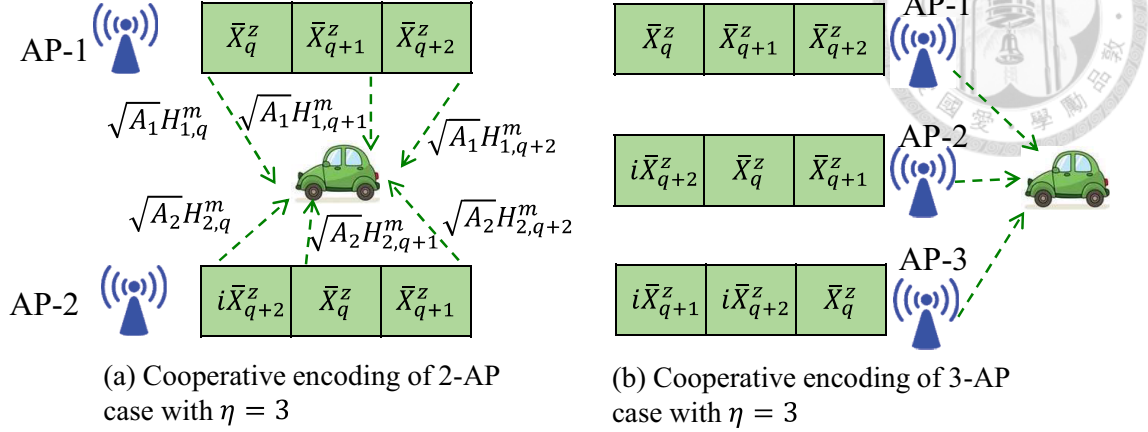


Figure 5.2: Illustration of frequency domain cooperative encoding.

of shifted sequence by  $\gamma$ . The number  $\gamma$  is the coding design parameter, and in this research we adopt  $\gamma = i$  as the special case of [75]. This encoding is straightforward for the AN to instruct the serving APs the placement of data symbols over the allocated subcarriers. But, the question is “how to index APs?”, that is, to the AN, “which AP is AP-1?”, “which AP is AP-2?”, and so on, so forth. This question will be analyzed later, and in the rest of this section, we give a comparison of this encoding and MRC that makes our analysis in Section 5.2 more understandable.

For simplicity, we take 2-AP case with  $\eta = 3$  and BPSK for illustration (refer to Fig. 5.2(a)), and assume no CFOs between the vehicle and the APs. Please note the assumption of perfect synchronization is just for facilitating our explanation, and will be removed in the following sections. At the  $m$ th antenna of receiver, the signals at the  $\eta$  FFT outputs with indices belonging to  $\mathcal{B}_{q,\eta}$  can be expressed as a  $\eta \times 1$  vector,

$$\mathbf{y}_{z,\text{coding}}^m = \sum_{k=q}^{q+2} \mathbf{h}_{\text{eff},k}^m \bar{X}_k^z + \mathbf{v}_{z,\eta}^m, \quad (5.3)$$

$$\mathbf{h}_{\text{eff},q}^m = \left[ \sqrt{A_1}H_{1,q}^m \quad \sqrt{A_2}H_{2,q+1}^m \quad 0 \right]^T, \quad (5.4)$$

$$\mathbf{h}_{\text{eff},q+1}^m = \left[ 0 \quad \sqrt{A_1}H_{1,q+1}^m \quad \sqrt{A_2}H_{2,q+2}^m \right]^T, \quad (5.5)$$

$$\mathbf{h}_{\text{eff},q+2}^m = \left[ i\sqrt{A_2}H_{2,q+1}^m \quad 0 \quad \sqrt{A_1}H_{1,q+2}^m \right]^T, \quad (5.6)$$

where  $A_n$  and  $H_{n,k}^m$  have been defined in Subsection 4.1.2, and  $\mathbf{v}_{z,\eta}^m$  is the noise term



with  $\mathbf{v}_{z,\eta}^m \sim CN(0, \sigma_V^2 \mathbf{I}_\eta)$ . Arranging  $\mathbf{y}_{z,\text{coding}}^m$ 's from different antennas as a vector, we have

$$\mathbf{y}_{z,\text{coding}} = \sum_{k=q}^{q+2} \mathbf{h}_{\text{eff},k} \bar{X}_k^z + \mathbf{v}_{z,\eta}, \quad (5.7)$$

$$\mathbf{y}_{z,\text{coding}}^T = \left[ (\mathbf{y}_{z,\text{coding}}^1)^T \cdots (\mathbf{y}_{z,\text{coding}}^{N_{\text{rx}}})^T \right], \quad (5.8)$$

$$\mathbf{h}_{\text{eff},k}^T = \left[ (\mathbf{h}_{\text{eff},k}^1)^T \cdots (\mathbf{h}_{\text{eff},k}^{N_{\text{rx}}})^T \right], \quad (5.9)$$

$$\mathbf{v}_{z,\eta}^T = \left[ (\mathbf{v}_{z,\eta}^1)^T \cdots (\mathbf{v}_{z,\eta}^{N_{\text{rx}}})^T \right]. \quad (5.10)$$

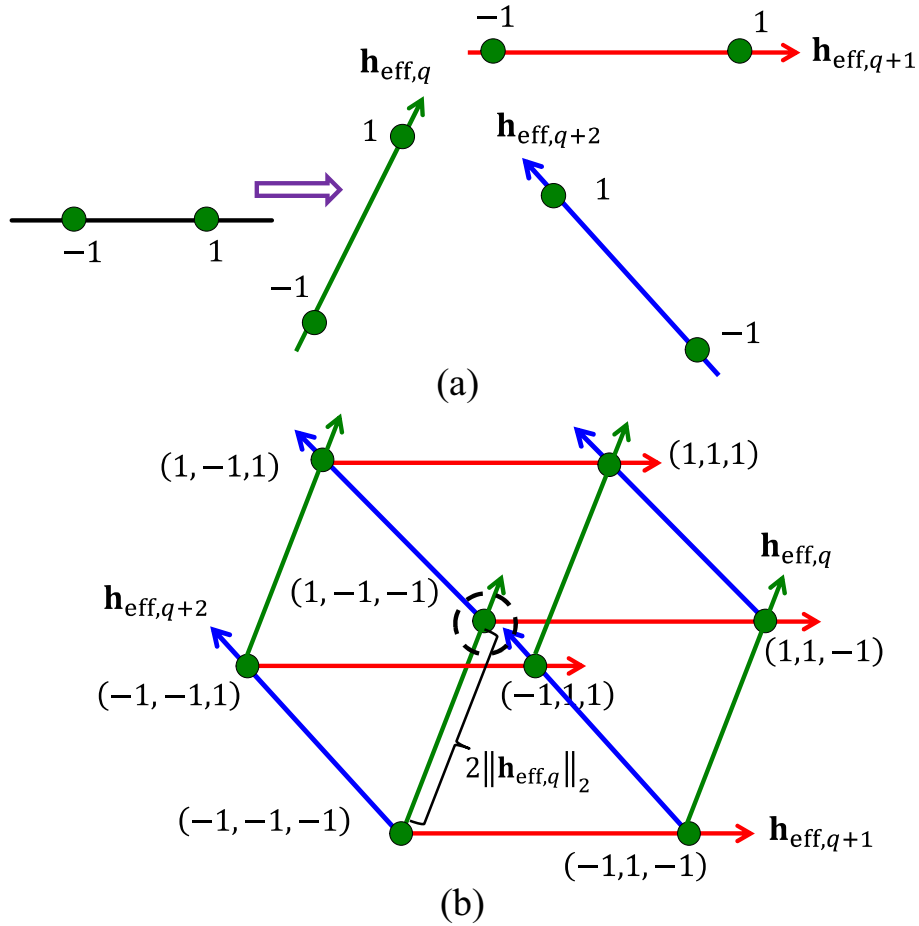
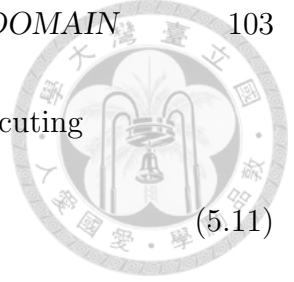


Figure 5.3: (a) The constellations  $\mathcal{M}_k$ 's are rotated and scaled by  $\mathbf{h}_{\text{eff},k}$ 's.  $\mathcal{M}_k = \{\pm 1\}$  for  $k = q, q+1, q+2$ . The green, red, and blue arrows point the directions of  $\mathbf{h}_{\text{eff},q}$ ,  $\mathbf{h}_{\text{eff},q+1}$ , and  $\mathbf{h}_{\text{eff},q+2}$ . (b) The receiver searches the ML solution from the composite constellation  $\mathcal{M}_{q,\eta}$ .





The receiver jointly decodes the desired data symbols by executing

$$\hat{\mathbf{x}}_{q,\eta}^z = \arg \min_{\substack{\mathbf{x}_{q,\eta}^z \in \prod_{k=q}^{q+2} \mathcal{M}_k}} \left\| \mathbf{y}_{z,\text{coding}} - \sum_{k=q}^{q+2} \mathbf{h}_{\text{eff},k} \bar{X}_k^z \right\|_2^2 \quad (5.11)$$

where  $\mathcal{M}_k$  is the constellation of  $\bar{X}_k^z$ ,  $\bar{\mathbf{x}}_{q,\eta}^z = (\bar{X}_q^z, \bar{X}_{q+1}^z, \bar{X}_{q+2}^z)$ , and  $\hat{\mathbf{x}}_{q,\eta}^z$  is defined similarly. As shown in Fig. 5.3,  $\mathcal{M}_k$ 's are rotated and scaled by the effective channel vectors  $\mathbf{h}_{\text{eff},k}$ 's, and form a composite constellation

$$\mathcal{M}_{q,\eta} = \left\{ \sum_{k=q}^{q+2} \mathbf{h}_{\text{eff},k} \bar{X}_k^z \mid (\bar{X}_q^z, \bar{X}_{q+1}^z, \bar{X}_{q+2}^z) \in \prod_{k=q}^{q+2} \mathcal{M}_k \right\}, \quad (5.12)$$

from which the receiver searches the ML solution.

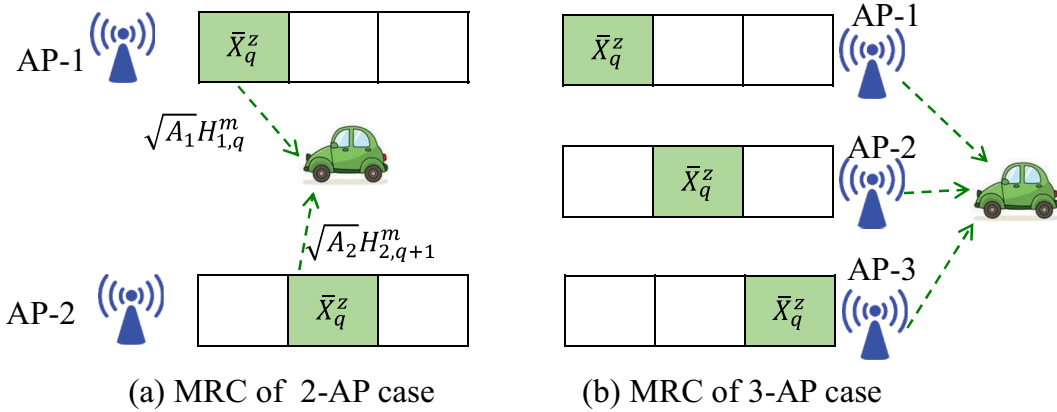


Figure 5.4: APs-1  $\sim$   $N$  respectively use only the  $q$ th  $\sim$   $(q + N - 1)$ th subcarriers to transmit  $\bar{X}_q^z$ . At the receiver, MRC is performed.

As a benchmark, we consider a spectrum-inefficient scheme, in which APs-1  $\sim$   $N$  respectively use only the  $q$ th  $\sim$   $(q + N - 1)$ th subcarriers to transmit  $\bar{X}_q^z$ , as illustrated in Fig. 5.4. Likewise, the received signals from different antennas and FFT outputs can be arranged as a vector, which for the 2-AP case is given in (5.13).

$$\mathbf{y}_{z,\text{mrc}} = \mathbf{h}_{\text{eff},q} \bar{X}_q^z + \mathbf{v}_{z,\eta}. \quad (5.13)$$

Applying MRC, we obtain

$$\frac{\mathbf{h}_{\text{eff},q}^H}{\|\mathbf{h}_{\text{eff},q}\|_2} \mathbf{y}_{z,\text{mrc}} = \|\mathbf{h}_{\text{eff},q}\|_2 \bar{X}_q^z + \frac{\mathbf{h}_{\text{eff},q}^H}{\|\mathbf{h}_{\text{eff},q}\|_2} \mathbf{v}_{z,\eta}. \quad (5.14)$$

Assuming perfect synchronization and disregarding spectrum efficiency, the operation of (5.14) is named as ideal MRC that achieves the best BER performance in open-loop communications. From (5.14), the BER is determined by  $\|\mathbf{h}_{\text{eff},q}\|_2$ , and

$$\text{BER}_{\text{ideal,mrc}} = Q \left( \sqrt{\frac{2 \|\mathbf{h}_{\text{eff},q}\|_2^2}{\sigma_V^2}} \right). \quad (5.15)$$

Return to the discussion of encoding scheme, and refer to Fig. 5.3(b). Suppose that the transmitted sequence is  $(\bar{X}_q^z, \bar{X}_{q+1}^z, \bar{X}_{q+2}^z) = (1, -1, -1)$ , the point enclosed by the dashed black circle in Fig. 5.3(b). Without loss of generality, we look at the detection error of  $\bar{X}_q^z$  that occurs when  $\hat{\mathbf{x}}_{q,\eta}^z$  is one of the sequences  $(-1, -1, 1)$ ,  $(-1, -1, -1)$ ,  $(-1, 1, 1)$ ,  $(-1, 1, -1)$ , among which,  $(-1, -1, -1)$  is closest to the transmitted sequence if  $\mathbf{h}_{\text{eff},q}$  is nearly orthogonal to  $\mathbf{h}_{\text{eff},q+1}$  and  $\mathbf{h}_{\text{eff},q+2}$ . Thus, the most likely error event for  $\bar{X}_q^z$  is that  $(1, -1, -1)$  is decoded as  $(-1, -1, -1)$ , and the distance between the two sequence is  $2 \|\mathbf{h}_{\text{eff},q}\|_2$ , which dominates the receiving performance of  $\bar{X}_q^z$ . Hence (5.15) serves as a BER lower bound. Recall that  $\mathbf{h}_{n,k} = [H_{n,k}^1 \cdots H_{n,k}^{N_{\text{rx}}}]^T$ , the correlation between  $\mathbf{h}_{\text{eff},q}$  and  $\mathbf{h}_{\text{eff},q+1}$  is

$$\begin{aligned} \frac{|\mathbf{h}_{\text{eff},q}^H \mathbf{h}_{\text{eff},q+1}|}{\|\mathbf{h}_{\text{eff},q}\|_2 \|\mathbf{h}_{\text{eff},q+1}\|_2} &= \frac{\sqrt{A_1 A_2} |\mathbf{h}_{2,q+1}^H \mathbf{h}_{1,q+1}|}{\sqrt{(A_1 \|\mathbf{h}_{1,q}\|_2^2 + A_2 \|\mathbf{h}_{2,q+1}\|_2^2) (A_1 \|\mathbf{h}_{1,q+1}\|_2^2 + A_2 \|\mathbf{h}_{2,q+2}\|_2^2)}} \\ &= \frac{\sqrt{A_1 A_2} \frac{|\mathbf{h}_{2,q+1}^H \mathbf{h}_{1,q+1}|}{\|\mathbf{h}_{2,q+1}\|_2}}{\sqrt{\left( A_1 \frac{\|\mathbf{h}_{1,q}\|_2^2}{\|\mathbf{h}_{2,q+1}\|_2^2} + A_2 \right) (A_1 \|\mathbf{h}_{1,q+1}\|_2^2 + A_2 \|\mathbf{h}_{2,q+2}\|_2^2)}}. \end{aligned} \quad (5.16)$$

Since  $\|\mathbf{h}_{n,k}\|_2^2 \sim \text{Gamma}(N_{\text{rx}}, 1)$  and  $\frac{\mathbf{h}_{2,q+1}^H \mathbf{h}_{1,q+1}}{\|\mathbf{h}_{2,q+1}\|_2} \sim \text{CN}(0, 1)$ , the correlation has smaller value with higher probability as  $N_{\text{rx}}$  increases. This is the same case with the correlation between any other pair of effective channel vectors, implying that the average BER of encoding scheme gets closer to that of ideal MRC.

For  $N_{\text{rx}} = 1$ , the simulated BER of BPSK in our 2-AP case is reported in the left part of Fig. 5.5, where the cooperative encoding approaches ideal MRC, showing that the encoding introduced in [75] is well-designed. In the right part of Fig. 5.5,  $N_{\text{rx}} = 2$ ,

and the gap between the encoding and ideal MRC almost vanishes, as consistent with the above analysis. The simulated BERs of QPSK are plotted in Fig. 5.6, where the similar behavior can also be observed.

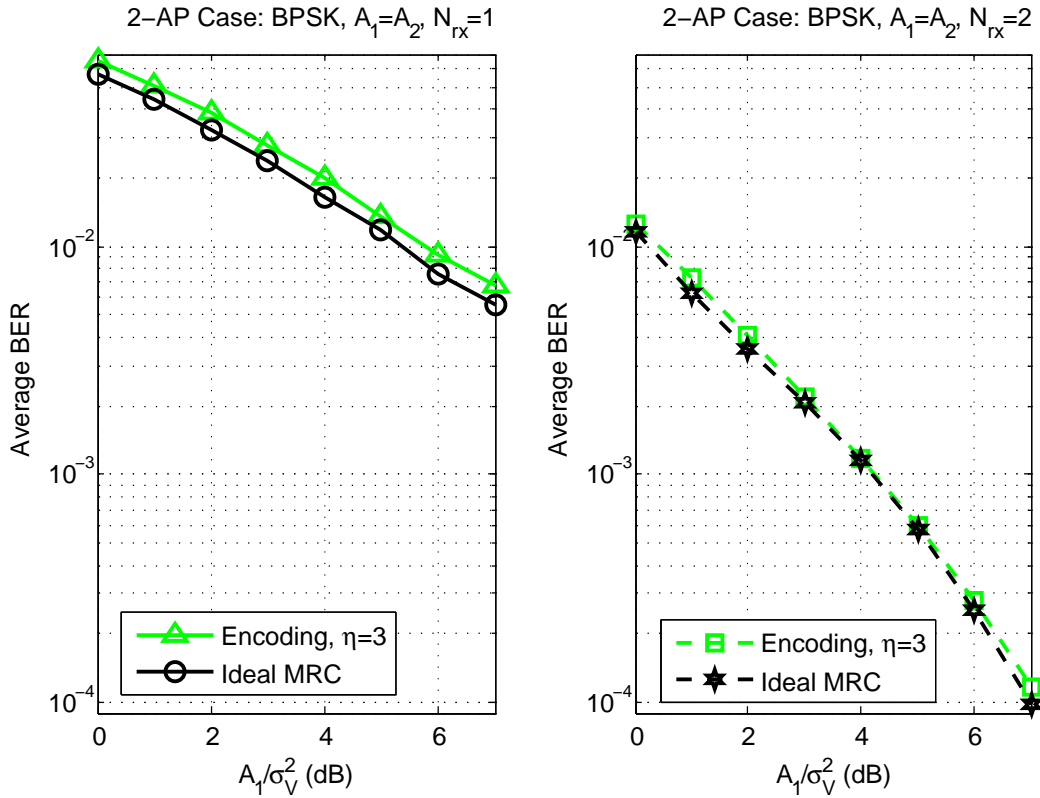


Figure 5.5: (Left)  $N_{rx} = 1$ . (Right)  $N_{rx} = 2$ . The average BER of ideal MRC and encoding scheme are plotted.  $A_1 = A_2$ ,  $\eta = 3$ , and BPSK is adopted.

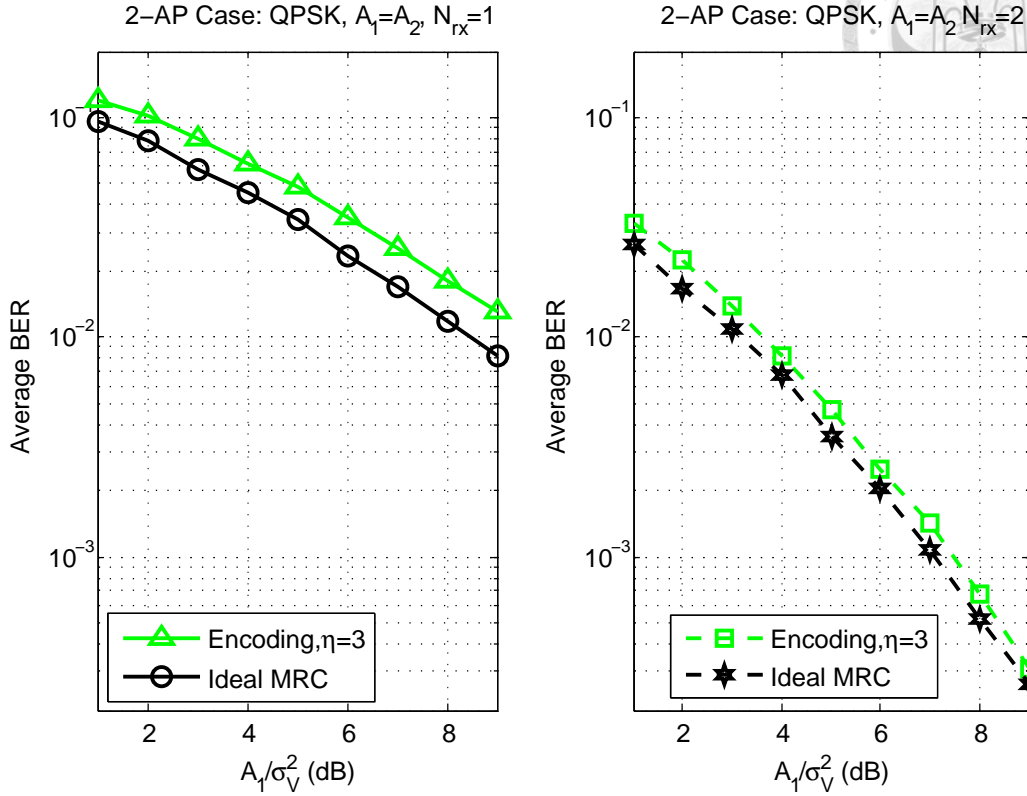


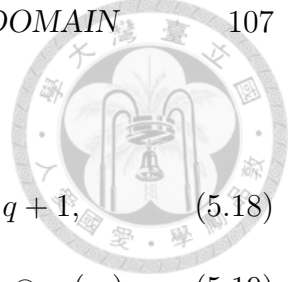
Figure 5.6: (Left)  $N_{rx} = 1$ . (Right)  $N_{rx} = 2$ . The average BER of ideal MRC and encoding scheme are plotted.  $A_1 = A_2$ ,  $\eta = 3$ , and QPSK is adopted.

## 5.2 Benchmark Analysis: Asynchronous MRC

Now we take the multi-CFO issue into account and exploit the signal model in Section 4.1.2. Suppose that  $|\varepsilon_n| \leq 0.5$ , thus  $|\varepsilon_n - \varepsilon_l| \leq 1$  for any pair of AP indices  $n$  and  $l$ . In the cooperative encoding of  $N$ -AP case, the frequency-domain received signal across all receiving antennas is

$$\mathbf{y}_{z,S,\text{coding}} = \sum_{k \in \mathcal{B}_{q,\eta}} \tilde{\mathbf{h}}_{\text{eff},z,k} \bar{X}_k^z + \sum_{n=1}^N \sum_{k \in \mathcal{B} \setminus \mathcal{B}_{q,\eta}} \sqrt{A_n} e^{j(z-1)\phi_n} \mathbf{h}_{n,k} \otimes \mathbf{c}_k(\varepsilon_n) X_{n,k}^z + \mathbf{v}_{z,S}, \quad (5.17)$$

where the terms of first summation notation are desired signals,  $\mathbf{v}_{z,S}$  is the noise term defined as  $\mathbf{v}_{z,S}^T = [(\mathbf{v}_{z,F}^1)^T \cdots (\mathbf{v}_{z,F}^{N_{rx}})^T]$ , and the other terms are ICI. For the definitions of  $\mathbf{c}_k(\varepsilon_n)$  and  $\mathbf{v}_{z,F}^m$ , please refer to Section 4.1.2. In addition,  $\tilde{\mathbf{h}}_{\text{eff},k}$ 's are the effective channel vectors carrying the data symbols  $\bar{X}_k^z$ 's. Specifically, for the 2-AP



case with  $\eta = 3$  (Fig. 5.2(a)),

$$\tilde{\mathbf{h}}_{\text{eff},z,k} = \sum_{n=1}^2 \sqrt{A_n} e^{j(z-1)\phi_n} \mathbf{h}_{n,k+n-1} \otimes \mathbf{c}_{k+n-1}(\varepsilon_n) \quad \text{for } k = q, q+1, \quad (5.18)$$

$$\tilde{\mathbf{h}}_{\text{eff},z,q+2} = \sqrt{A_1} e^{j(z-1)\phi_1} \mathbf{h}_{1,q+2} \otimes \mathbf{c}_{q+2}(\varepsilon_1) + i\sqrt{A_2} e^{j(z-1)\phi_2} \mathbf{h}_{2,q} \otimes \mathbf{c}_q(\varepsilon_2). \quad (5.19)$$

The subcarriers adjacent to the allocated RRUs are pilot tones or left unused to alleviate ICI. Thus, in (5.17),  $X_{n,k}^z$ 's for  $k = q-1, q+\eta$  are zeros or some values known to the receiver. However, there is another CFO-related factor that greatly impacts on BER, as stated below.

Evaluating the BER directly from (5.17) is difficult. Instead, we analyze the benchmark performance. Consider the spectrum-inefficient scheme in Fig. 5.4(a) again, the received signal is

$$\mathbf{y}_{z,S,\text{mrc}} = \tilde{\mathbf{h}}_{\text{eff},z,q} \bar{X}_q^z + \mathbf{v}_{z,S}, \quad (5.20)$$

which becomes (5.21) after MRC.

$$\frac{\tilde{\mathbf{h}}_{\text{eff},z,q}^H}{\|\tilde{\mathbf{h}}_{\text{eff},z,q}\|_2} \mathbf{y}_{z,S,\text{mrc}} = \|\tilde{\mathbf{h}}_{\text{eff},z,q}\|_2 \bar{X}_q^z + \frac{\tilde{\mathbf{h}}_{\text{eff},z,q}^H}{\|\tilde{\mathbf{h}}_{\text{eff},z,q}\|_2} \mathbf{v}_{z,S}. \quad (5.21)$$

The operation of (5.21) is called asynchronous MRC, whose performance serves as an indicator of how the encoding scheme behaves, its BER of BPSK is

$$\text{BER}_{\text{asyn,mrc}} = Q\left(\sqrt{\frac{2\|\tilde{\mathbf{h}}_{\text{eff},z,q}\|_2^2}{\sigma_V^2}}\right) \approx \sum_{t=1}^3 b_t \exp\left(\frac{-a_t \|\tilde{\mathbf{h}}_{\text{eff},z,q}\|_2^2}{\sigma_V^2}\right), \quad (5.22)$$

with

$$a_1 = 1.752, \quad a_2 = 0.15, \quad a_3 = 14.5,$$

$$b_1 = 0.208, \quad b_2 = 0.13, \quad b_3 = 0.14.$$

The approximation of (5.22) follows from  $Q(x) \approx 0.208e^{-0.876x^2} + 0.13e^{-0.525x^2} + 0.14e^{-7.25x^2}$  [76], and  $\|\tilde{\mathbf{h}}_{\text{eff},z,q}\|_2^2$  can be also be written as

$$\|\tilde{\mathbf{h}}_{\text{eff},z,q}\|_2^2 = \sum_{m=1}^{N_{\text{rx}}} \|\tilde{\mathbf{h}}_{\text{eff},z,q}^m\|_2^2, \quad (5.23)$$



where

$$\begin{aligned} \left\| \tilde{\mathbf{h}}_{\text{eff},z,q}^m \right\|_2^2 &= \left\| \sum_{n=1}^2 \sqrt{A_n} H_{n,q+n-1}^m e^{j(z-1)\phi_n} \mathbf{c}_{q+n-1}(\varepsilon_n) \right\|_2^2 \\ &= \sum_{n=1}^2 A_n |H_{n,q+n-1}^m|^2 + 2\sqrt{A_1 A_2} \text{Re} \left( (H_{1,q}^m)^* H_{2,q+1}^m e^{j(z-1)(\phi_2 - \phi_1)} \rho_{q,q+1}(\varepsilon_1, \varepsilon_2) \right), \end{aligned} \quad (5.24)$$

$$\rho_{q,k}(\varepsilon_n, \varepsilon_l) \triangleq \frac{\mathbf{c}_q^H(\varepsilon_n) \mathbf{c}_k(\varepsilon_l)}{\|\mathbf{c}_q(\varepsilon_n)\|_2 \|\mathbf{c}_k(\varepsilon_l)\|_2}. \quad (5.25)$$

The second term of (5.24) can be either negative or positive, and it being negative will possibly worsen the BER prominently. Taking the expectation of  $\text{BER}_{\text{asyn},\text{mrc}}$  w.r.t the fading gains  $H_{n,k}^m$ 's, we obtain

$$\text{E}[\text{BER}_{\text{asyn},\text{mrc}}] \approx \sum_{t=1}^3 b_t \left[ \left( 1 + a_t \frac{A_1}{\sigma_V^2} \right) \left( 1 + a_t \frac{A_2}{\sigma_V^2} \right) - a_t^2 \frac{A_1 A_2}{\sigma_V^4} |\rho_{q,q+1}(\varepsilon_1, \varepsilon_2)|^2 \right]^{-N_{\text{rx}}}. \quad (5.26)$$

The derivation of (5.26) is provided in Appendix D, and demonstrated via simulations, as shown in the upper part of Fig. 5.7, where  $\frac{A_1}{\sigma_V^2} = \frac{A_2}{\sigma_V^2} = 5$  dB,  $N_{\text{rx}} = 2$ , and  $\Delta\varepsilon = \varepsilon_2 - \varepsilon_1 \in [-1, 1]$ . The analytical and simulated results reveal that multi-CFO problem can still cause serious performance loss, even if ICI does not exist.

Let  $\Delta f_{k,nl}$  denote the normalized frequency difference (w.r.t the subcarrier spacing) between AP- $n$ 's and AP- $l$ 's subcarriers that convey  $\tilde{X}_k^z$ . In our currently considered 2-AP case,

$$\Delta f_{q,12} = |(q+1+\varepsilon_2) - (q+\varepsilon_1)| = 1 + \Delta\varepsilon. \quad (5.27)$$

The correlation between  $\mathbf{c}_q(\varepsilon_1)$  and  $\mathbf{c}_{q+1}(\varepsilon_2)$ ,  $|\rho_{q,q+1}(\varepsilon_1, \varepsilon_2)|$ , is plotted in the lower part of Fig. 5.7, from which we note that the average BER does not obviously increase as  $\Delta f_{q,12} > 1$ , corresponding to small values of  $|\rho_{q,q+1}(\varepsilon_1, \varepsilon_2)|$ .

For asynchronous MRC of 3-AP case (Fig. 5.4(b)),

$$\left\| \tilde{\mathbf{h}}_{\text{eff},z,q}^m \right\|_2^2 = \left\| \sum_{n=1}^3 \sqrt{A_n} H_{n,q+n-1}^m e^{j(z-1)\phi_n} \mathbf{c}_{q+n-1}(\varepsilon_n) \right\|_2^2 \quad (5.28)$$

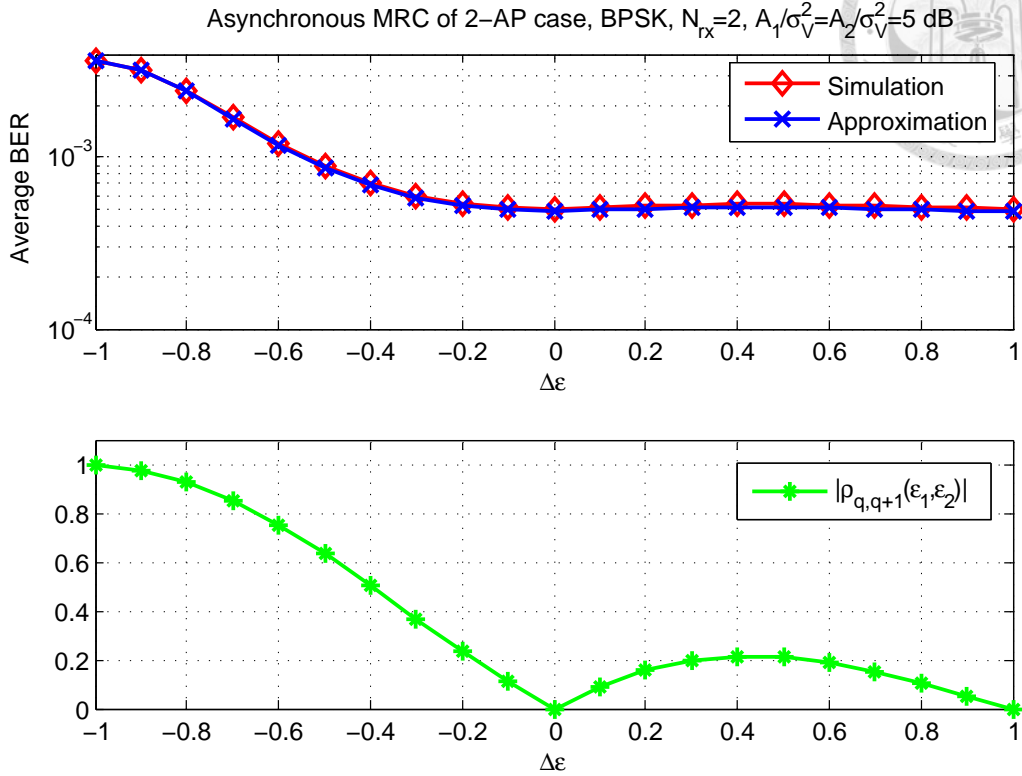


Figure 5.7: (Upper) For asynchronous MRC of 2-AP case, the approximated and simulated values of average BERs are plotted w.r.t  $\Delta\varepsilon = \varepsilon_2 - \varepsilon_1$ . The parameters are  $\frac{A_1}{\sigma_V^2} = \frac{A_2}{\sigma_V^2} = 5$  dB,  $N_{rx} = 2$ . (Lower) The correlation between  $\mathbf{c}_q(\varepsilon_1)$  and  $\mathbf{c}_{q+1}(\varepsilon_2)$  is plotted w.r.t  $\Delta\varepsilon$ .

The average BER of BPSK can be approximated as

$$\begin{aligned}
 & \mathbb{E}[\text{BER}_{\text{asyn, mrc}}] \\
 & \approx \sum_{t=1}^3 b_t \left[ \prod_{n=1}^3 \left( 1 + a_t \frac{A_n}{\sigma_V^2} \right) - a_t^2 \sum_{n < l} \frac{A_n A_l |\rho_{nl}|^2}{\sigma_V^4} - a_t^3 \frac{A_1 A_2 A_3}{\sigma_V^6} \sum_{n < l} |\rho_{nl}|^2 \right]^{-N_{rx}}, \quad (5.29)
 \end{aligned}$$

where

$$\rho_{12} = \rho_{q,q+1}(\varepsilon_1, \varepsilon_2), \quad (5.30)$$

$$\rho_{23} = \rho_{q+1,q+2}(\varepsilon_2, \varepsilon_3), \quad (5.31)$$

$$\rho_{13} = \rho_{q,q+2}(\varepsilon_1, \varepsilon_3). \quad (5.32)$$

In Appendix E, we derive (5.29), which again shows that the BER is greatly affected by the correlations between signature waveforms ( $|\rho_{12}|$ ,  $|\rho_{23}|$ , and  $|\rho_{13}|$ ). The approx-

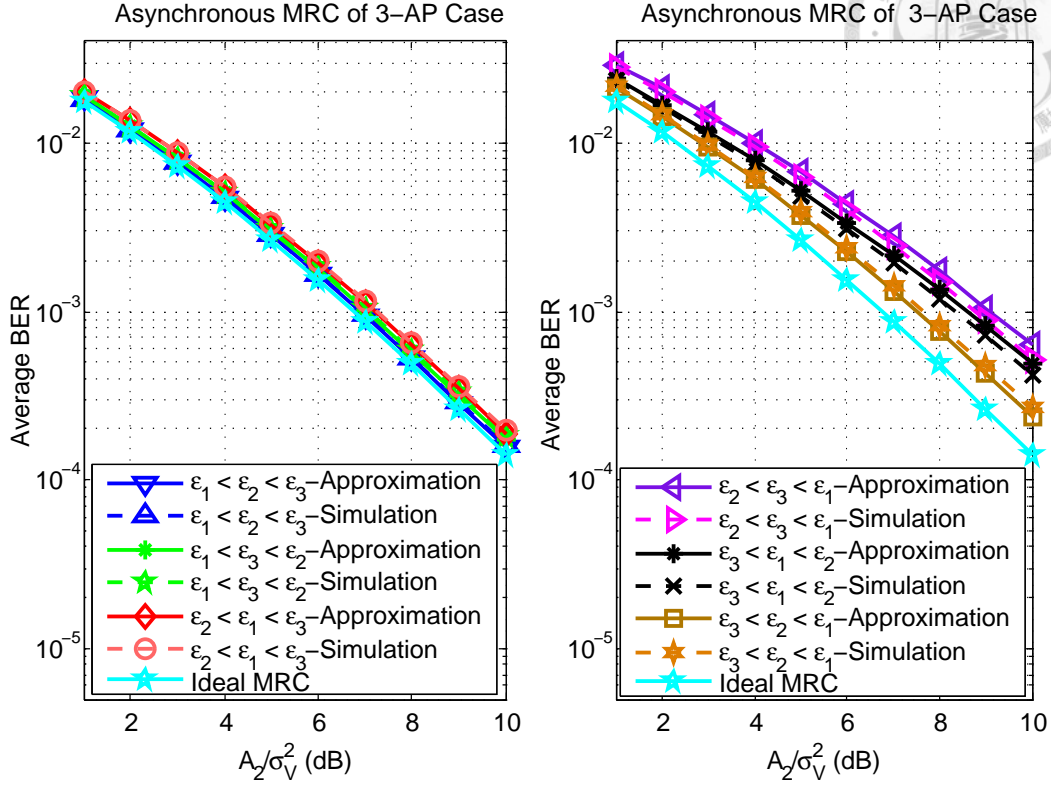


Figure 5.8: The approximated and simulated values of average BERs are plotted for different CFO orders. The values of CFOs are all different, and  $\varepsilon_1, \varepsilon_2, \varepsilon_3 \in \{-0.3, 0.1, 0.45\}$ , and other parameters are  $N_{\text{rx}} = 1$ ,  $\frac{A_1}{A_2} = 2$  dB,  $\frac{A_3}{A_2} = -3$  dB.

imated and simulated values of results are plotted in Fig. 5.8, where the values of CFOs are all different with  $\varepsilon_1, \varepsilon_2, \varepsilon_3 \in \{-0.3, 0.1, 0.45\}$ . It is clear that the order of CFOs make great difference to BER. In this case, the normalized frequency differences between the pairs of subcarriers conveying  $\bar{X}_q^z$  are

$$\Delta f_{q,12} = |(q + 1 + \varepsilon_2) - (q + \varepsilon_1)| = 1 + \varepsilon_2 - \varepsilon_1, \quad (5.33)$$

$$\Delta f_{q,23} = |(q + 1 + \varepsilon_3) - (q + 1 + \varepsilon_2)| = 1 + \varepsilon_3 - \varepsilon_2, \quad (5.34)$$

$$\Delta f_{q,13} = |(q + 2 + \varepsilon_3) - (q + \varepsilon_1)| = 2 + \varepsilon_3 - \varepsilon_1. \quad (5.35)$$

The best average BER is achieved as  $\varepsilon_1 < \varepsilon_2 < \varepsilon_3$  corresponding to  $\Delta f_{q,12} > 1$ ,  $\Delta f_{q,23} > 1$ , and  $\Delta f_{q,13} > 1$ , while at least one of  $\Delta f_{q,12}$ ,  $\Delta f_{q,23}$ , and  $\Delta f_{q,13}$  are smaller than one for other CFO orders.



### 5.3 AP Indexing Principle

Now we go back to the cooperative encoding of 2-AP case of Fig. 5.2(a), and assume that the subcarriers with indices  $k \in \mathcal{B} \setminus \mathcal{B}_{q,\eta}$  are not used to avoid any ICI. The simulated BERs of  $\bar{X}_q^z$ ,  $\bar{X}_{q+1}^z$ ,  $\bar{X}_{q+2}^z$  are reported in Fig. 5.9, where the correlations respectively between  $\mathbf{c}_q(\varepsilon_1)$  and  $\mathbf{c}_{q+1}(\varepsilon_2)$ ,  $\mathbf{c}_{q+1}(\varepsilon_1)$  and  $\mathbf{c}_{q+2}(\varepsilon_2)$ ,  $\mathbf{c}_{q+2}(\varepsilon_1)$  and  $\mathbf{c}_q(\varepsilon_2)$  are also plotted. The performance of  $\bar{X}_{q+2}^z$  is robust against CFO because the normalized frequency difference between the subcarriers carrying  $\bar{X}_{q+2}^z$  is always greater than one, i.e.,

$$\Delta f_{q+2,12} = |(q + \varepsilon_2) - (q + 2 + \varepsilon_1)| > 1. \quad (5.36)$$

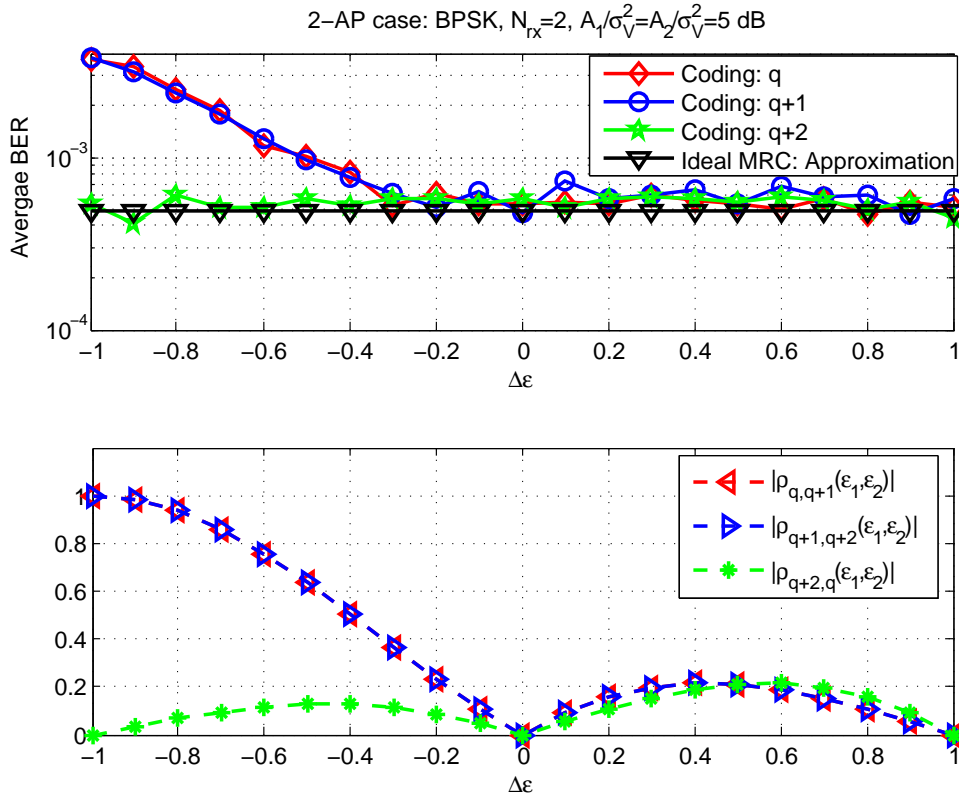


Figure 5.9: (Upper) For the cooperative encoding of 2-AP case with  $\eta = 3$ , the simulated values of average BERs are plotted w.r.t  $\Delta\varepsilon = \varepsilon_2 - \varepsilon_1$ . BPSK is adopted, and the parameters are  $\frac{A_1}{\sigma_V^2} = \frac{A_2}{\sigma_V^2} = 5$  dB,  $N_{rx} = 2$ . (Lower) The correlations respectively between  $\mathbf{c}_q(\varepsilon_1)$  and  $\mathbf{c}_{q+1}(\varepsilon_2)$ ,  $\mathbf{c}_{q+1}(\varepsilon_1)$  and  $\mathbf{c}_{q+2}(\varepsilon_2)$ ,  $\mathbf{c}_{q+2}(\varepsilon_1)$  and  $\mathbf{c}_q(\varepsilon_2)$  are plotted w.r.t  $\Delta\varepsilon$

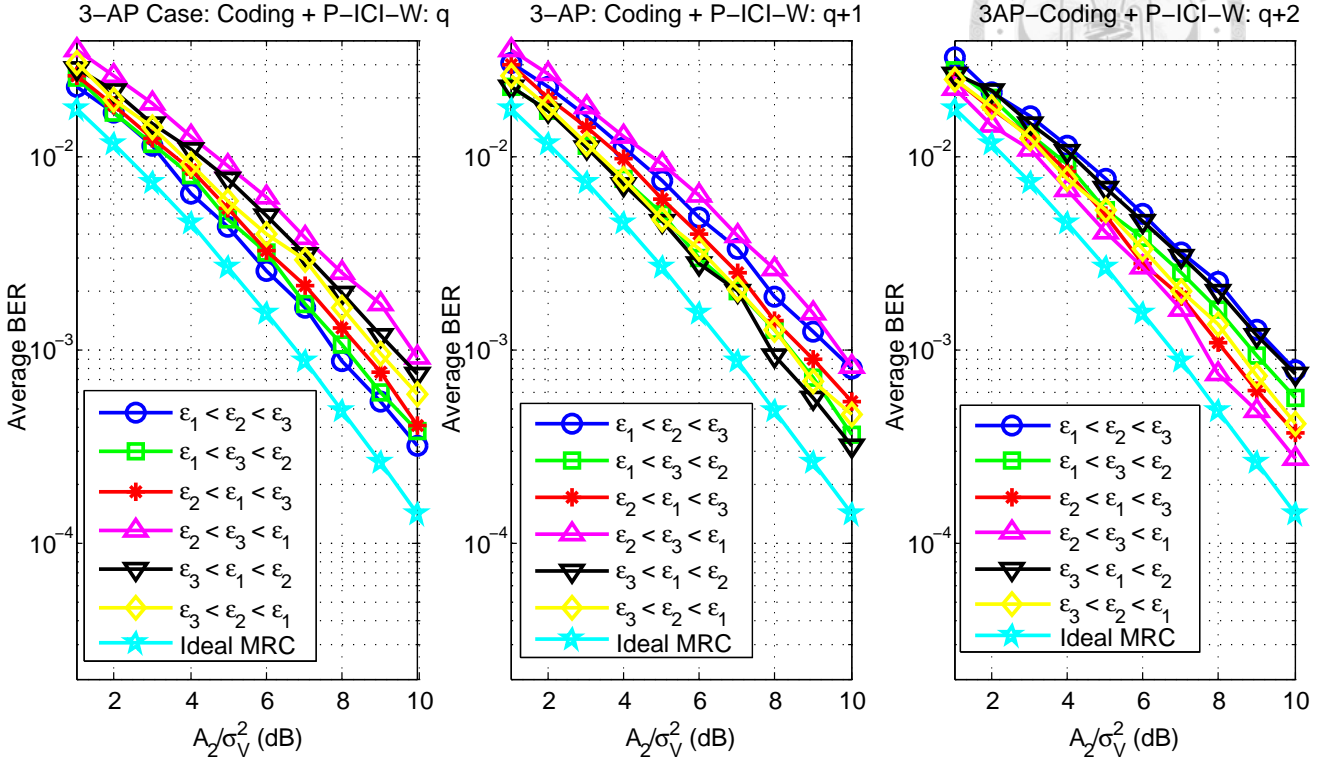


Figure 5.10: (Left)  $\bar{X}_q^z$ . (Middle)  $\bar{X}_{q+1}^z$ . (Right)  $\bar{X}_{q+2}^z$ . For the cooperative encoding of 3-AP case with  $\eta = 3$ , the simulated values of average BERs are plotted. The values of CFOs are all different, and  $\varepsilon_1, \varepsilon_2, \varepsilon_3 \in \{-0.3, 0.1, 0.45\}$ . BPSK is adopted, and the parameters are  $\frac{A_1}{A_2} = 2$  dB,  $\frac{A_3}{A_2} = -3$  dB,  $N_{\text{rx}} = 1$ .

But, it is not the same case for  $\bar{X}_q^z$  and  $\bar{X}_{q+1}^z$ , whose average BERs ascends as  $\Delta\varepsilon < 0$ , being consistent with the observation of Fig. 5.7. Therefore, the AN should index APs according to CFO order such  $\varepsilon_1 < \varepsilon_2$ .

Next we study the 3-AP case of Fig. 5.2(b) and take ICI into account. The received signal  $\mathbf{y}_{z,S,\text{coding}}$  given in (5.17) with  $\tilde{\mathbf{h}}_{\text{eff},k}$ 's expressed as

$$\tilde{\mathbf{h}}_{\text{eff},q} = \sum_{n=1}^3 \sqrt{A_n} e^{j(z-1)\phi_n} \mathbf{h}_{n,q+n-1} \otimes \mathbf{c}_{q+n-1}(\varepsilon_n), \quad (5.37)$$

$$\tilde{\mathbf{h}}_{\text{eff},q+1} = \sum_{n=1}^2 \sqrt{A_n} e^{j(z-1)\phi_n} \mathbf{h}_{n,q+n} \otimes \mathbf{c}_{q+n}(\varepsilon_n) + i\sqrt{A_3} e^{j(z-1)\phi_3} \mathbf{h}_{3,q} \otimes \mathbf{c}_q(\varepsilon_3), \quad (5.38)$$

$$\tilde{\mathbf{h}}_{\text{eff},q+2} = \sqrt{A_1} e^{j(z-1)\phi_1} \mathbf{h}_{1,q+2} \otimes \mathbf{c}_{q+2}(\varepsilon_1) + \sum_{n=2}^3 i\sqrt{A_n} e^{j(z-1)\phi_n} \mathbf{h}_{n,q+n-2} \otimes \mathbf{c}_{q+n-2}(\varepsilon_n). \quad (5.39)$$

Applying pseudo whitening in advance, the signature waveforms  $\mathbf{c}_k(\varepsilon_n)$ 's in (5.17),

(5.37)~(5.39) are replaced with the corresponding pseudo-whitened signature waveforms, then the desired data symbols are jointly detected. The simulated BERs of  $\bar{X}_q^z$ ,  $\bar{X}_{q+1}^z$ , and  $\bar{X}_{q+2}^z$  are plotted in Fig. 5.10, where the parameters  $\varepsilon_1, \varepsilon_2, \varepsilon_3, \frac{A_1}{A_2}, \frac{A_3}{A_2}, N_{rx}$  are the same those used in Fig. 5.8. The average BER of  $\bar{X}_q^z$  is best when  $\varepsilon_1 < \varepsilon_2 < \varepsilon_3$ , being consistent with the results of Fig. 5.8. But, for the same CFO order, the detection performance of  $\bar{X}_{q+1}^z$  and  $\bar{X}_{q+2}^z$  is much worse, and

$$\Delta f_{q+1,13} = |(q + \varepsilon_3) - (q + 1 + \varepsilon_1)| = 1 + \varepsilon_1 - \varepsilon_3 < 1, \quad (5.40)$$

$$\Delta f_{q+2,13} = |(q + 1 + \varepsilon_3) - (q + 2 + \varepsilon_1)| = 1 + \varepsilon_1 - \varepsilon_3 < 1. \quad (5.41)$$

In this case, no CFO order can make  $\Delta_{k,nl} > 1$  hold for all  $n \neq l$  and  $k = q, q + 1, q + 2$ . Therefore, none of the CFO orders is universally good to the detection of  $\bar{X}_q^z, \bar{X}_{q+1}^z, \bar{X}_{q+2}^z$ .

With proper AP indexing such that  $\varepsilon_1 < \varepsilon_2 < \varepsilon_3$ , the aforementioned issue can be easily avoided by setting  $\eta = 4$ , as depicted in Fig. 5.11(a), where  $\Delta f_{k,nl} > 1$  holds for all  $\bar{X}_k^z$ 's. The simulation results of this setting are shown in Fig. 5.12. Compared to Fig. 5.10, the BERs of  $\bar{X}_{q+1}^z$  and  $\bar{X}_{q+2}^z$  are much better as  $\varepsilon_1 < \varepsilon_2 < \varepsilon_3$ , furthermore, there is no significant difference between the detection of performance of different data symbols.

From the above analysis and simulations, we summarize our cooperative open-loop downlink transmissions design in the following.

- For each vehicle, the serving APs allocate the same RRUs that contain  $\eta$  subcarriers.
- The AN indexes APs in ascending order of CFOs such that the CFO of AP- $n$  is  $\varepsilon_n$ , and  $\varepsilon_s \leq \varepsilon_l$  for  $s < l$ .
- AP- $n$ 's transmitted data sequence over the allocated subcarriers is  $\bar{\mathbf{x}}_{n,q}^z$ , as given in (5.1).

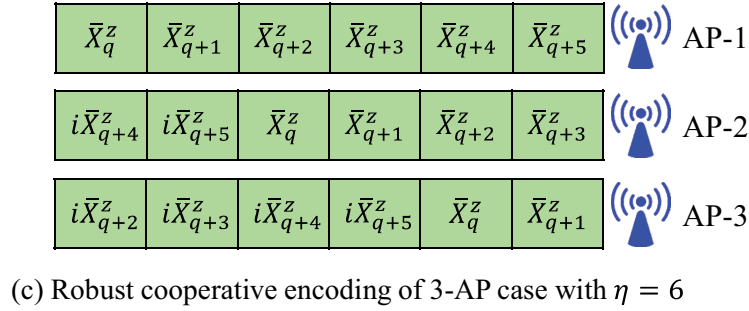
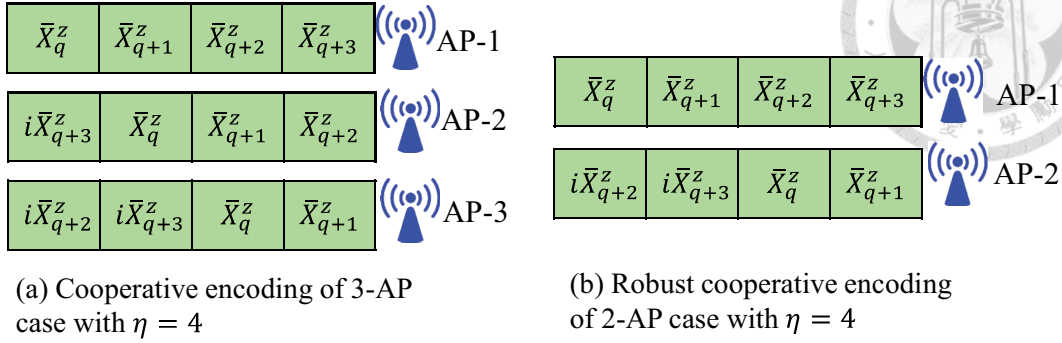


Figure 5.11: Illustration of frequency domain cooperative encoding. The scheme in (a) requires proper AP indexing such that  $\varepsilon_1 < \varepsilon_2 < \varepsilon_3$ . The coding schemes in (b) and (c) are robust in the sense that the AN can index APs randomly.

- Set  $\eta \geq N + 1$  such that  $\Delta f_{k,nl} > 0$  can hold for all  $\bar{X}_k^z$ 's and  $n \neq l$ .
- To enable the AP indexing principle, CFO feedback from the vehicle is required, but only initially and when the CFO order changes.

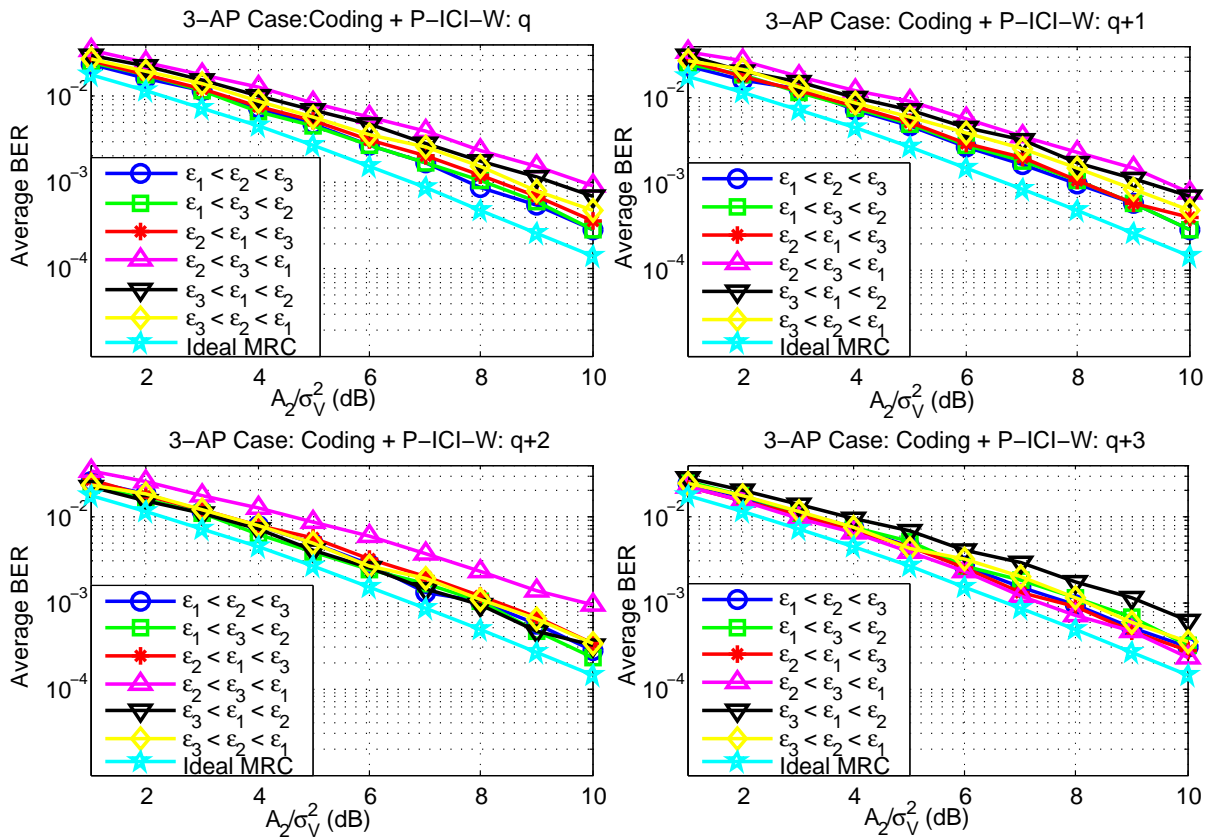
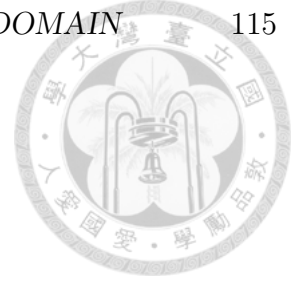


Figure 5.12: (Upper-Left)  $\bar{X}_q^z$ . (Upper-Right)  $\bar{X}_{q+1}^z$ . (Lower-Left)  $\bar{X}_{q+2}^z$ . (Lower-Right)  $\bar{X}_{q+3}^z$ . For the cooperative encoding of 3-AP case with  $\eta = 4$ , the simulated values of average BERs are plotted. The values of CFOs are all different, and  $\varepsilon_1, \varepsilon_2, \varepsilon_3 \in \{-0.3, 0.1, 0.45\}$ . BPSK is adopted, and the parameters are  $\frac{A_1}{A_2} = 2$  dB,  $\frac{A_3}{A_2} = -3$  dB,  $N_{rx} = 1$ .

## 5.4 Robust Cooperative Encoding Against CFO

Modifying the encoding, we propose a robust cooperative encoding, where AP- $n$ 's transmitted data sequence is

$$\mathbf{x}_{n,q}^z = \mathbf{M}_\eta^{2(n-1)} [\bar{X}_q^z \cdots \bar{X}_{q+\eta-1}^z]^T. \quad (5.42)$$

By set  $\eta \geq 2N$ , for any  $\bar{X}_k^z$ , it is put on the different APs' subcarriers with index differences at least two, and the correlations between the associated signature waveforms will be smaller, The examples of 2-AP and 3-AP cases are respectively illustrated in Fig. 5.11(b) and Fig. 5.11(c).

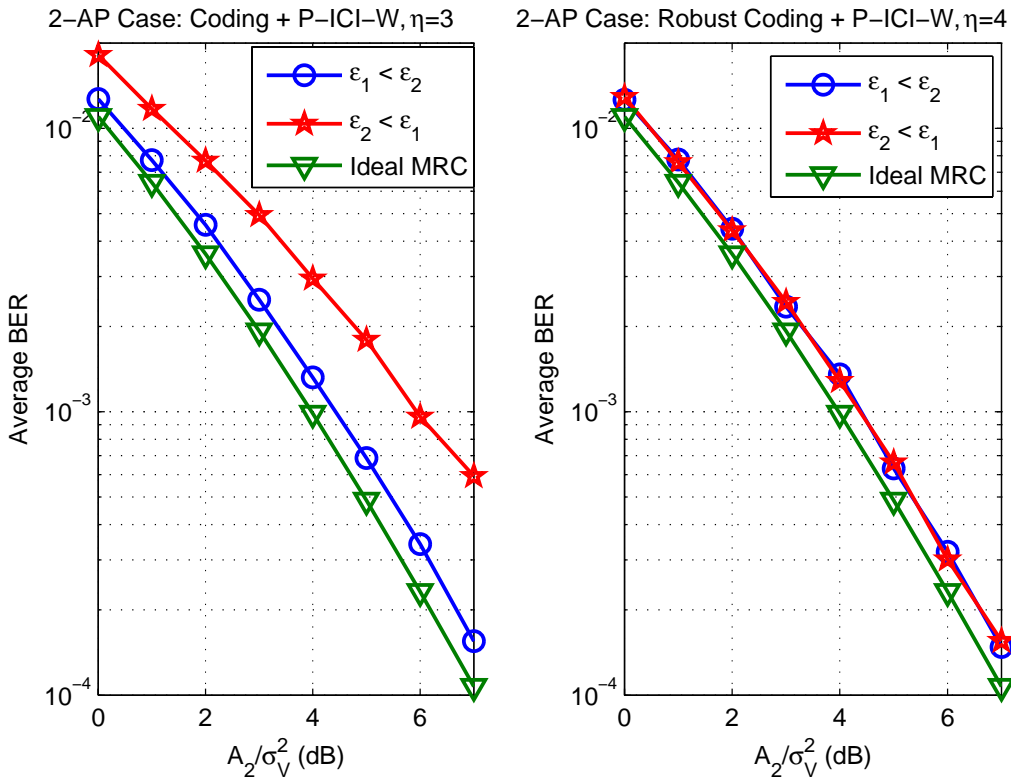


Figure 5.13: (Left) 2-AP case cooperative encoding with  $\eta = 3$ . (Right) 2-AP case robust encoding with  $\eta = 4$ . the average BERs of different  $\bar{X}_k^z$ 's are collectively evaluated. the CFOs are different with  $\varepsilon_1, \varepsilon_2 \in \{\pm 0.35\}$ . BPSK is adopted, and the parameters are  $A_1 = A_2$ ,  $N_{rx} = 2$ .

The 2-AP case encoding schemes in Fig. 5.2(a) and Fig. 5.11(b) are compared through simulations, where the CFOs are different with  $\varepsilon_1, \varepsilon_2 \in \{\pm 0.35\}$ , and the

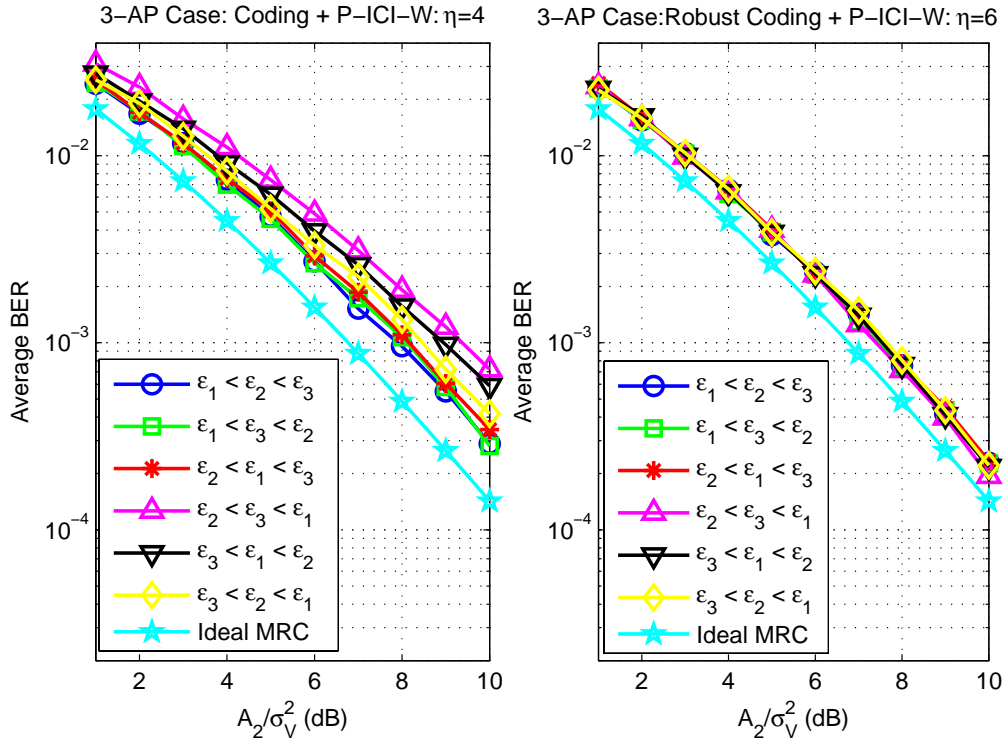


Figure 5.14: (Left) 3-AP case cooperative encoding with  $\eta = 4$ . (Right) 2-AP case robust encoding with  $\eta = 6$ . the average BERs of different  $\bar{X}_k^z$ 's are collectively evaluated. The values of CFOs are all different, and  $\varepsilon_1, \varepsilon_2, \varepsilon_3 \in \{-0.3, 0.1, 0.45\}$ . BPSK is adopted, and the parameters are  $\frac{A_1}{A_2} = 2$  dB,  $\frac{A_3}{A_2} = -3$  dB,  $N_{\text{rx}} = 1$ .

average BERs of different  $\bar{X}_k^z$ 's are collectively evaluated. As shown in Fig. 5.13, the scheme of Fig. 5.11(b) is insensitive to CFO order, so it is possible that the AN can index APs randomly without hurting the performance. In other words, CFO feedback can be avoided.

For 3-AP case, the simulation results of encodings in Fig. 5.11(a) and Fig. 5.11(c) are compared in Fig. 5.14, which again demonstrates the robustness of our modified encoding against CFO orders.

## 5.5 Summary

Coordinated by the AN, the serving APs are able to perform cooperative encoding to serve the vehicle. In addition to ICI, the correlations between signature waveforms, which conveying the same data symbols, also cause serious performance loss. An easy AP indexing according CFO order is provided to resolve this problem. Furthermore, by trading the complexity of joint detection with robustness, a modified encoding method is also proposed to allow AN to randomly index APs.





# Chapter 6

## Conclusion

### 6.1 Dissertation Summary

This dissertation focuses on downlink receiving/transmission design in OFDMA-based virtual cell networks. We develop two new detection schemes, and construct a procedure to suppress ICI at receivers. Moreover, an easy AP indexing principle and robust frequency-domain encoding are proposed to facilitate cooperative open-loop transmissions.

Our research begins with the scenario that synchronization is ideally achieved but each of the serving APs allocates RRUs non-cooperatively and randomly, thus the receiver decodes the packets from different APs individually. Chapter 2 describes the fundamental properties of ML-MUD, particularly “modulation sensitivity” which is deemed as a big concern about reliability under the coexistence of uRLLC and eMBB (or some other services that often use high-order modulation).

Without precise power control and allocation in open-loop communications, the strengths of received signals from different APs may be significantly different. Chapter 3 invents two methods R-ML-MUD and GLMMSE to address interference weaker than the desired signal. Utilizing the weakness of interfering signal and the characteristic of downlink transmissions, R-ML-MUD treats the interference with high-order modulation as being lower-order modulated such that the complexity of joint detection can be greatly decreased. On the other hand, compared with conventional PR,

GLMMSE can avoid losing too much of the desired signal's power when cancelling weak signals from multiple interfering APs, hence a notable SNR gain is earned. Although the proposed schemes are developed under the assumption of perfect synchronization, our proposed methods can be applied to asynchronous scenarios with proper signal model formulation.

Starting from Chapter 4, we take CFO issue into account to look at the scenario that is more challenging than the considered situation in Chapter 2 and Chapter 3. Analyzing the signature waveforms of subcarriers, we propose P-ICI-W/PT-ICI-W that is able to approach tradition whitening scheme in terms of BER and SINR. With pseudo whitening and GLMMSE, we develop a two-stage ICI suppression strategy suitable for downlink receiver implementation. Furthermore, Alamouti coding [68] and CIOD [69] are taken into the two-stage processing, being evaluated and compared via simulations for a comprehensive study.

In Chapter 5, APs' cooperative transmissions enabled by the coordination of AN is assumed. A very straightforward cooperative encoding scheme [75] is implemented over frequency domain. Despite that ICI can be pseudo-whitened, the multiple CFOs still significantly degrade BER due to the increasing correlations between signature waveforms that convey the same data symbols. By indexing APs according to CFO order, this performance loss can be alleviated. Finally, a robust encoding scheme is proposed such that indexing APs in a random manner without hurting performance is made possible.

## 6.2 Future Work

R-ML-MUD and sphere decoding are two very different complexity reduction methods, however, such difference does not prevent them from being executed together. Actually, their integration is straightforward and will be one of the extended works. Besides, R-ML-MUD shares similar concept of interference-ignorant SUD and power-

domain NOMA to utilize differences in received signal strengths, as mentioned in Section 3.5. Applying R-ML-MUD in NOMA scenario, the stringent signal power ratio condition can be relaxed at the expense of higher detection complexity. This application of R-ML-MUD increases the flexibility in implementing power-domain NOMA, and is worth further investigation.

Also mentioned at the end of Section 3.5, R-ML-MUD can not be used to address strong interference, and GLMMSE may not be better than PR in this case. Generalizing the idea of LMMSE-SIC, we can use GLMMSE-SIC to deal with stronger interfering signals. The details of this new detection scheme as well as its resultant performance is also one of our interests.

In Chapter 5, our research is based on the assumption that  $|\varepsilon_n| \leq 0.5$ . When  $|\varepsilon_n| > 0.5$ , from the vehicle's angle, it is like that APs randomly allocate RRUs, the receiver may just decodes the desired signals from serving APs separately using the schemes introduced in Chapter 3 and Chapter 4. Nevertheless, for non-cooperative transmissions, we only look at the detection performance of desired data from one single path (AP), the overall reliability of multi-path transmissions is not evaluated and shall be analyzed in the future work. We are also interested in how to combine received signals from different paths for imperfect (non-cooperative) RRUs allocation or  $|\varepsilon_n| > 0.5$  as well as the question "Which transmission scheme is better in terms of overall system design, cooperative or non-cooperative?".

In our dissertation, the channel gains and CFO values from different APs are assumed perfectly known to the receiver. In the next step of this research, we shall start to consider channel/CFO estimation that may be facilitated by proper preamble/pilot arrangement.

Another fundamental question we have not yet answered is "How to decide the size of virtual cell?" or specifically, "What is the minimum number of APs/paths to ensure the predetermined reliability?". Due to the path loss to attenuate signal


strength, we ignore the interference from any AP not belonging to the virtual cell in this dissertation. However, when it comes to the virtual cell size design, we are supposed to consider the accumulated interference from the nearby APs outside the virtual cell that might not be ignorable and have great impact on overall reliability if the virtual cell size is small. AP density and CP length should also be included in consideration because a big virtual size may result in TDOA-related ISI/ICI if AP deployment is not so dense in some areas or CP length is not long enough.

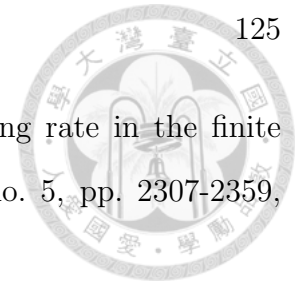
In open-loop communications, it not feasible for APs and AN to exactly know the channel conditions, making the determination of virtual cell size very challenging. Leveraging machine learning techniques [77], it is possible to learn the path loss law, shadowing effect, interference map in surrounding area, etc. to help the AN form the virtual cells for vehicles in service, which will be our principal research in the future towards the development of virtual cell networking.



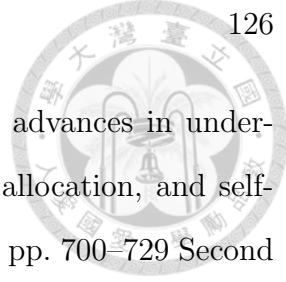
## Bibliography

- [1] 3GPP, "Study on scenarios and requirements for next generation access technologies," 3GPP, Sophia Antipolis, France, Tech. Rep. 38.913, v14.2, 2017.
- [2] H. Shariatmadari, S. Iraji, R. Jantti, P. Popovski, Z. Li, and M. A. Uusitalo, "Fifth-generation control channel design: Achieving ultrareliable low-latency communications," *IEEE Veh. Technol. Mag.*, vol. 13, no. 2, pp. 84–93, Jun. 2018.
- [3] G. Pocovi, H. Shariatmadari, G. Berardinelli, K. Pedersen, J. Steiner, and Z. Li, "Achieving ultra-reliable low-latency communications: Challenges and envisioned system enhancements," *IEEE Netw.*, vol. 32, no. 2, pp. 8–15, Mar./Apr. 2018.
- [4] M. A. Lema, A. Laya, T. Mahmoodi, M. Cuevas, J. Sachs, J. Markendahl, and M. Dohler, "Business case and technology analysis for 5G low latency applications," *IEEE Access*, vol. 5, pp. 5917–5935, May 2017.
- [5] H. Chen, R. Abbas, P. Cheng, M. Shirvanimoghaddam, W. Hardjawana, W. Bao, Y. Li, and B. Vucetic, "Ultra-reliable low latency cellular networks: Use cases, challenges and approaches," *IEEE Commun. Mag.*, vol. 56, no. 12, pp. 119–125, Dec. 2018.
- [6] G. P. Fettweis, "The tactile Internet: applications and challenges," *IEEE Veh. Technol. Mag.*, vol. 9, no. 1, pp. 64–70, Mar. 2014.

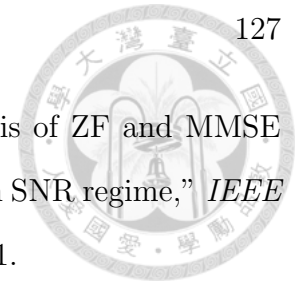
- 
- [7] D.-J. Deng, S.-Y. Lien, C.-C. Lin, S.-C. Hung, and W.-B. Chen, "Latency control in software-defined mobile-edge vehicular networking," *IEEE Commun. Mag.*, vol. 55, no. 8, pp. 87–93, Aug. 2017.
- [8] S.-Y. Lien, S.-C. Hung, K.-C. Chen, and Y.-C. Liang, "Ultra-low latency ubiquitous connections in heterogeneous cloud radio access networks," *IEEE Wireless Commun.*, vol. 22, no. 3, pp. 22–31, Jun. 2015.
- [9] S.-C. Hung, H. Hsu, S.-M. Cheng, Q. Cui, and K.-C. Chen, "Delay guaranteed network association for mobile machines in heterogeneous cloud radio access networks," *IEEE Trans. Mobile Comput.*, vol. 17, no. 12, pp. 2744–2760, Dec. 2018.
- [10] K.-C. Chen, T. Zhang, R. D. Gitlin, and G. Fettweis, "Ultra-low latency mobile networking," *IEEE Netw.*, vol. 33, no. 2, Mar./Apr. 2019.
- [11] G. Berardinelli, N. H. Mahmood, R. Abreu, T. Jacobsen, K. Pedersen, I. Z. Kovács, and P. Mogensen, "Reliability analysis of uplink grant-free transmission over shared resources," *IEEE Access*, vol. 6, pp. 23602–23611, May 2018.
- [12] Y. Du, B. Dong, W. Zhu, P. Gao, Z. Chen, X. Wang, and J. Fang, "Joint channel estimation and multiuser detection for uplink grant-free NOMA," *IEEE Wireless Commun. Lett.*, vol. 7, no. 4, pp. 682–685, Aug. 2018.
- [13] C.-Y. Lin, K.-C. Chen, D. Wickramasuriya, S.-Y. Lien, and R. D. Gitlin, "Anticipatory mobility management by big data analytics for ultra-low latency mobile networking," in *Proc. IEEE Int. Conf. Commun.*, Kansas City, MO., USA, 2018, pp. 1–7.
- [14] H. Ji, S. Park, J. Yeo, Y. Kim, J. Lee, and B. Shim, "Ultra-reliable and low-latency communications in 5G downlink: Physical layer aspects," *IEEE Wireless Commun.*, vol. 25, no. 3, pp. 124–130, Jun. 2018.



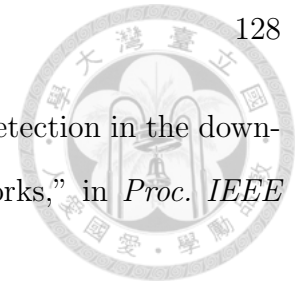
- [15] Y. Polyanskiy, H. V. Poor, and S. Verdù, “Channel coding rate in the finite blocklength regime,” *IEEE Trans. Inf. Theory*, vol. 56, no. 5, pp. 2307-2359, May 2010.
- [16] G. Durisi, T. Koch, and P. Popovski, “Toward massive, ultrareliable, and low-latency wireless communication with short packets,” in *Proc. IEEE*, vol. 104, no. 9, pp. 1711-1726, Sep. 2016.
- [17] C. Pan, H. Ren, Y. Deng, M. ElKashlan, and A. Nallanathan, “Joint blocklength and location optimization for URLLC-enabled UAV relay systems,” *IEEE Commun. Lett.*, vol. 23, no. 3, pp. 498–501, March, 2019.
- [18] M. Shirvanimoghaddam *et al.*, “Short block-length codes for ultra-reliable low latency communications,” *IEEE Commun. Mag.*, vol. 57, no. 2, Feb. 2019.
- [19] M. Sybis, K. Wesolowski, K. Jayasinghe, V. Venkatasubramanian, and V. Vukadinovic, “Channel coding for ultra-reliable low-latency communication in 5G systems,” in *Proc. IEEE VTC Fall*, Montreal, QC., Canada, 2016, pp. 1–5.
- [20] M. Richart, J. Baliosian, J. Serrat, and J.-L. Gorricho, “Resource slicing in virtual wireless networks: A survey,” *IEEE Trans. Netw. Service Manage.*, vol. 13, no. 3, pp. 462–476, Sep. 2016.
- [21] P. Popovski, K. F. Trillingsgaard, O. Simeone, and G. Durisi, “5G wireless network slicing for eMBB, URLLC, and mMTC: A communication-theoretic view,” *IEEE Access*, vol. 6, pp. 55765–55779, Oct. 2018.
- [22] C. She, C. Yang, and T. Q. S. Quek, “Radio resource management for ultra-reliable and low-latency communications,” *IEEE Commun. Mag.*, vol. 55, no. 6, pp. 72-78, Jun. 2017.

- 
- [23] M. Peng, C. Wang, J. Li, H. Xiang, and V. Lau, “Recent advances in underlay heterogeneous networks: Interference control, resource allocation, and self-organization,” *IEEE Commun. Surveys Tuts.*, vol. 17, no. 2, pp. 700–729 Second Quarter 2015.
- [24] K. Wang, H. Li, F. R. Yu, W. Wei, and L. Suo, “Interference alignment in virtualized heterogeneous cellular networks with imperfect channel state information,” *IEEE Trans. Veh. Technol.*, vol. 66, no. 2, pp. 1519–1532, Feb. 2017.
- [25] J. Kim, H.-W. Lee, and S. Chong, “Virtual cell beamforming in cooperative networks,” *IEEE J. Sel. Areas Commun.*, vol. 32, no. 6, pp. 1126–1138, Jun. 2014.
- [26] J. Wang and L. Dai, “Downlink rate analysis for virtual-cell based large-scale distributed antenna systems,” *IEEE Trans. Wireless Commun.*, vol. 15, no. 3, pp. 1998–2011, Mar. 2016.
- [27] X. Jiang, B. Zheng, W.-P. Zhu, L. Wang, and Y. Zou, “Large system analysis of heterogeneous cellular networks with interference alignment,” *IEEE Access*, vol. 6, pp. 8148–8160, Mar. 2018.
- [28] S. Verdù, *Multiuser Detection*, Cambridge, U.K.: Cambridge University Press, 1998.
- [29] J. Lee, D. Toumpakaris, and W. Yu, “Interference mitigation via joint detection,” *IEEE J. Sel. Areas Commun.*, vol. 29, no. 6, pp. 1172–1184, Jun. 2011.
- [30] H. Schulze and C. Lueders *Theory and Applications of OFDM and CDMA Wideband Wireless Communications*, England: John Wiley & Sons, 2005.

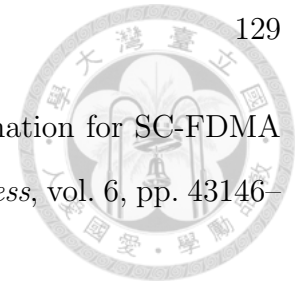




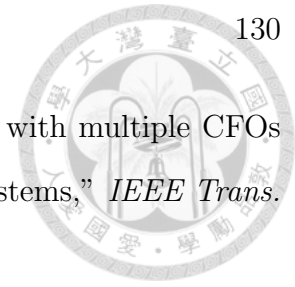
- [31] Y. Jiang, M. K. Varanasi, and J. Li, “Performance analysis of ZF and MMSE equalizers for MIMO systems: An in-depth study of the high SNR regime,” *IEEE Trans. Inf. Theory*, vol. 57, no. 4, pp. 2008–2026, Apr. 2011.
- [32] J. R. Hampton, *Introduction to MIMO Communications*, New York: Cambridge University Press, 2014.
- [33] Z. Bai, B. Badic, S. Iwelski, T. Scholand, R. Balraj, G. Bruck, and P. Jung, “On the equivalence of MMSE and IRC receiver in MU-MIMO systems,” *IEEE Commun. Lett.*, vol. 15, no. 12, pp. 1288–1290, Dec. 2011.
- [34] B. Flury, *A First Course in Multivariate Statistics*, New York: Springer Verlag, 1997.
- [35] C. Schlegel, S. Roy, P. D. Alexander, and Z.-J. Xiang, “Multiuser projection receivers,” *IEEE J. Sel. Areas Commun.*, vol. 14, no. 8, pp. 1610–1618, Oct. 1996.
- [36] S. Bahng, S. Shin, and Y.-O. Park, “ML approaching MIMO detection based on orthogonal projection,” *IEEE Commun. Lett.*, vol. 11, no. 6, pp. 474–476, June 2007.
- [37] S. Verdù, “Minimum probability of error for asynchronous Gaussian multiple-access channels,” *IEEE Trans. Inf. Theory*, vol. 32, no. 1, pp. 85–96, Jan. 1986.
- [38] C.-H. Zeng and K.-C. Cheng, “Downlink multiuser detection in the virtual cell-based ultra-low latency vehicular networks,” *IEEE Trans. Veh. Technol.*, vol. 68, no. 5, pp. 4651–4666, May 2019.
- [39] C.-H. Zeng and K.-C. Cheng, “Downlink multiuser detection of ultra-low latency virtual-cell vehicular networks,” in *Proc. IEEE Veh. Technol. Conf. Fall*, Chicago, IL, USA, 2018, pp. 1–5.




- [40] C.-H. Zeng and K.-C. Cheng, "Low complexity multiuser detection in the down-link of ultra-low latency virtual-cell based vehicular networks," in *Proc. IEEE Veh. Technol. Conf. Fall*, Chicago, IL, USA, 2018, pp. 1–5.
- [41] J. H. Winters, J. Salz, and R. D. Gitlin, "The impact of antenna diversity on the capacity of wireless communication systems," *IEEE Trans. Commun.*, vol. 42, no. 2/3/4, pp. 1740–1751, Feb/Mar./Apr. 1994.
- [42] Y. S. Cho, J. Kim, W. Y. Yang, and C. G. Kang, *MIMO-OFDM Wireless Communications with MATLAB*, Singapore: John Wiley & Sons (Asia) Pte Ltd, 2010.
- [43] T.-D. Chiueh, P.-Y. Tsai, and I.-W. Lai, *Baseband Receiver Design for Wireless MIMO-OFDM Communications*, Singapore: John Wiley & Sons (Asia) Pte Ltd, 2012.
- [44] J. Sachs, G. Wikström, T. Dudda, R. Baldemair, and K. Kittichokechai, "5G radio network design for ultra-reliable low-latency communication," *IEEE Netw.*, vol. 32, no. 2, pp. 24–31, Mar./Apr. 2018.
- [45] V. Kotsch, W. Rave, and G. Fettweis, "Interference cancellation and suppression in asynchronous cooperating base station systems," in *Proc. Int. ITG Workshop Smart Antenna*, Dresden, Germany, Mar. 2012, pp. 78–85.
- [46] M. Haenggi, *Stochastic Geometry for Wireless Networks*, New York: Cambridge University Press, 2013.
- [47] Y. Feng, W. Zhang, Y. Ge, and H. Lin, "Frequency synchronization in distributed antenna systems: Pairing based multi-CFO estimation, theoretical analysis, and optimal pairing scheme," *IEEE Trans. Commun.*, vol. 67, no. 4, Apr. 2019.

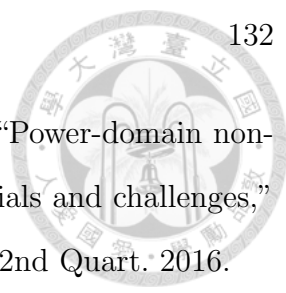


- [48] S. Kumar, S. Majhi, and C. Yuen., “Multi-user CFO estimation for SC-FDMA system over frequency selective fading channels,” *IEEE Access*, vol. 6, pp. 43146–43156, Aug. 2018.
- [49] Y.-R. Tsai *et al.*, “Simultaneous multiple carrier frequency offsets estimation for coordinated multi-point transmission in OFDM system,” *IEEE Trans. Wireless Commun.*, vol. 12, no. 9, pp. 4558–4568, Sep. 2013.
- [50] H. C. Nguyen, E. De Carvalho, and R. Prasad, “Multi-user interference cancellation schemes for carrier frequency offset compensation in uplink OFDMA,” *IEEE Trans. Wireless Commun.*, vol. 13, no. 3, pp. 1164–1171, Mar. 2014.
- [51] A. Santra and K. V. S. Hari, “A novel subspace based method for compensation of multiple CFOs in uplink MIMO OFDM systems,” *IEEE Commun. Lett.*, vol. 21, no. 9, pp. 1993–1996, Sep. 2017.
- [52] T. Wang and S. C. Liew, “Frequency-asynchronous multiuser joint channel-parameter estimation CFO compensation and channel decoding,” *IEEE Trans. Veh. Technol.*, vol. 65, no. 12, pp. 9732–9746, Dec. 2016.
- [53] A. Farhang, N. Marchetti, L. E. Doyle, and B. F.-Boroujeny, “Low complexity CFO compensation in uplink OFDMA systems with receiver windowing,” *IEEE Trans. Signal Process.*, vol. 63, no. 10, pp. 2546–2558, May 2015.
- [54] Y. Ge , W. Zhang , F. Gao , and G. Y. Li, “Frequency synchronization for uplink massive MIMO with adaptive MUI suppression in angle domain,” *IEEE Trans. Signal Process.*, vol. 67, no. 8, pp. 2143–2158, Apr. 2019.
- [55] Z. Cao, U. Tureli, Y.-D. Yao, and P. Honan, “Frequency synchronization for generalized OFDMA uplink,” in *Proc. IEEE Globecom*, vol. 2, Dallas, TX., USA, Nov. 2004, pp. 1071–1075.



- [56] Y.-S. Yang *et al.*, “A low-complexity transceiver structure with multiple CFOs compensation for OFDM-based coordinated multi-point systems,” *IEEE Trans. Commun.*, vol. 63, no. 7, pp. 2658–2670, Jul. 2015.
- [57] V. Kotzsch, J. Holfeld, and G. Fettweis, “Joint detection and CFO compensation in asynchronous multi-user MIMO OFDM systems,” in *Proc. IEEE Veh. Technol. Conf. Spring*, Barcelona, Spain, 2009, pp.1–5.
- [58] W. Zhang, F. Gao, Q. Yin, and H. M. Wang, “Alamouti coding scheme for AF relaying with Doppler shifts,” *IEEE Trans. Veh. Technol.*, vol. 62, no. 3, pp. 1241–1250, Mar. 2013.
- [59] Y. Yao, and X. Dong, “Multiple CFO mitigation in amplify-and-forward cooperative OFDM transmission,” *IEEE Trans. Commun.*, vol. 60, no. 12, pp. 3844–3854, Dec. 2012.
- [60] Q. Huang, M. Ghogho, D. Ma, and J. Wei, “Low-complexity data-detection algorithm in cooperative SFBC-OFDM systems with multiple frequency offsets,” *IEEE Trans. Veh. Technol.*, vol. 59, no. 9, pp. 4614–4620, Nov. 2010.
- [61] F. Tian, X.-G. Xia, and P. C. Ching, “Signal detection in a space-frequency coded cooperative communication system with multiple carrier frequency offsets by exploiting specific properties of the code structure,” *IEEE Trans. Veh. Technol.*, vol. 58, no. 7, pp. 3396–3409, Sep. 2009.
- [62] Y. Zhao *et al.*, Efficient detection of spatial modulation OFDM systems with multiple carrier frequency offsets, *IEEE Commun. Lett.*, vol. 21, no. 2, pp. 426–429, Feb. 2017.
- [63] Y. Zhao *et al.*, “MMSE-based detector for spatial modulation OFDM systems with multiple CFOs,” in *Proc. 10th Int. Conf. Wireless Commun. Signal Process.*, Hangzhou, China, Dec. 2018, pp. 1-6.

- 
- [64] H. -W. Wang, D. W. Lin, and T.-H. Sang, "OFDM signal detection in doubly selective channels with blockwise whitening of residual intercarrier interference and noise," *IEEE J. Sel. Areas Commun.*, vol. 30, no. 4, pp. 684–694, May 2012.
- [65] H. Jang, S. Nooshabadi, K. Kim, and H.-N. Lee "Circular sphere decoding: A low complexity detection for MIMO systems with general two-dimensional signal constellations," *IEEE Trans. Veh. Technol.*, vol. 66, no. 3, pp. 2085–2098, Mar. 2017.
- [66] E. Viterbo and J. Boutros, "A universal lattice code decoder for fading channels," *IEEE Trans. Inf. Theory*, vol. 45, no. 5, pp. 1639-1642, Jul. 1999.
- [67] C.-H. Zeng and K.-C. Chen, "Pseudo whitening of intercarrier interference in the asynchronous URLLC downlink," in *Proc. IEEE Int. Conf. Commun.*, Shanghai, China, May, 2019, pp. 1–6.
- [68] S. M. Alamouti, "A simple transmit diversity technique for wireless communications," *IEEE J. Sel. Areas Commun.*, vol. 16, no. 8, pp. 1451–1458, Oct. 1998.
- [69] R. Rajashekar and K. V. S. Hari, "Modulation diversity for spatial modulation using complex interleaved orthogonal design," in *Proc. IEEE Region 10 Conf. TENCN*, Cebu, Philippines, Nov. 2012, pp. 1–6.
- [70] A. M. Tulino and S. Verdu, *Random Matrix Theory and Wireless Communications*, Now Publisher, 2004.
- [71] B. Hassibi, "A fast square-root implementation for BLAST," in *Proc. 34th Asilomar Conf. Signals, Syst. Comput.*, Pacific Grove, CA., USA, Nov. 2000, pp. 1255-1259.

- 
- [72] S. M. R. Islam, N. Avazov, O. A. Dobre, and K.-S. Kwak, “Power-domain non-orthogonal multiple access (NOMA) in 5G systems: Potentials and challenges,” *IEEE Commun. Surveys Tuts.*, vol. 19, no. 2, pp. 721–742, 2nd Quart. 2016.
- [73] J. Jalden and B. Ottersten, “On the complexity of sphere decoding in digital communications,” *IEEE Trans. Signal Process.*, vol. 53, no. 4, pp. 1474–1484, 2005.
- [74] M. Z. A. Khan and B. S. Rajan, “Single-symbol maximum likelihood decodable linear STBCs,” *IEEE Trans. Inf. Theory*, vol. 52, no. 5, pp. 2062–2091, May 2006.
- [75] F. Oggier and B. Hassibi, “An algebraic coding scheme for wireless relay networks with multiple-antenna nodes,” *IEEE Trans. Signal Process.*, vol. 56, no. 7, July 2008.
- [76] P. C. Sofotasios and S. Freear, “Novel expressions for the one and two dimensional Gaussian Q-functions,” in *Proc. IEEE ICWITS*, Aug./Sep. 2010, Hawaii, USA.
- [77] C. Jiang, H. Zhang, Y. Ren, Z. Han, K.-C. Chen, and L. Hanzo, “Machine learning paradigms for next-generation wireless networks,” *IEEE Wireless Commun.*, vol. 24, no. 2, pp. 98–105, Apr. 2017.



# Appendix A

## Proof of (2.23)

Let  $\widehat{\mathbf{h}}_N$  stand for the orthogonal projection of  $\mathbf{h}_N$  on  $\text{span}(\mathbf{h}_1, \dots, \mathbf{h}_{N-1})$ , then we have the following.

$$\mathbf{q}_N = \frac{1}{R_{NN}} (\mathbf{h}_N - \widehat{\mathbf{h}}_N), \quad (\text{A.1})$$

$$D_{\text{ML}}^2 = D_{\text{ZF}}^2 + \min_{\tilde{\mathbf{x}}_{-N} \in \prod_{n=1}^{N-1} \mathcal{M}_n} \left\| \sqrt{A_N} (X_N - \tilde{X}_N) \widehat{\mathbf{h}}_N - \sum_{n=1}^{N-1} \sqrt{A_n} (\tilde{X}_n - X_n) \mathbf{h}_n \right\|_2^2. \quad (\text{A.2})$$

Since  $\mathbf{Q} = \mathbf{H}\mathbf{R}^{-1}$ ,

$$\mathbf{q}_N = \sum_{n=1}^{N-1} (\mathbf{R}^{-1})_{nN} \mathbf{h}_n + R_{NN}^{-1} \mathbf{h}_N. \quad (\text{A.3})$$

Express  $\mathbf{R}$  as

$$\mathbf{R} = \begin{bmatrix} \mathbf{R}_{IS} & \mathbf{r}_{NS} \\ \mathbf{0}_{1 \times (N-1)} & R_{NN} \end{bmatrix}. \quad (\text{A.4})$$

By the block-wise matrix inversion formula [34], we have

$$\mathbf{R}^{-1} = \begin{bmatrix} \mathbf{R}_{IS}^{-1} & \mathbf{r}_{NS}^- \\ \mathbf{0}_{1 \times (N-1)} & R_{NN}^{-1} \end{bmatrix}, \quad (\text{A.5})$$

$$\mathbf{r}_{NS}^- = -\mathbf{R}_{IS}^{-1} \mathbf{r}_{NS} R_{NN}^{-1}. \quad (\text{A.6})$$



From (A.1), (A.3), (A.5), and (A.6),

$$\begin{aligned}
 \widehat{\mathbf{h}}_N &= -R_{NN}\mathbf{q}_N + \mathbf{h}_N \\
 &= -R_{NN} \sum_{n=1}^{N-1} (\mathbf{r}_{NS}^-)_n \mathbf{h}_n \\
 &= -R_{NN} \sum_{n=1}^{N-1} (-\mathbf{R}_{IS}^{-1} \mathbf{r}_{NS} R_{NN}^{-1})_n \mathbf{h}_n \\
 &= \sum_{n=1}^{N-1} \sum_{m=n}^{N-1} (\mathbf{R}_{IS}^{-1})_{nm} R_{mN} \mathbf{h}_n \\
 &= \sum_{n=1}^{N-1} \sum_{m=n}^{N-1} \left[ \frac{\text{cof}(\mathbf{R}_{IS})_{mn} R_{mN}}{\prod_{i=1}^{N-1} R_{ii}} \right] \left( \sum_{k=1}^n |R_{kn}|^2 \right)^{\frac{1}{2}} \frac{\mathbf{h}_n}{\|\mathbf{h}_n\|_2} \\
 &= \sum_{n=1}^{N-1} \sum_{m=n}^{N-1} \left[ \frac{\text{cof}(\mathbf{R}_{IS})_{mn} R_{mN}}{\prod_{i \neq n} R_{ii}} \right] \left( \sum_{k=1}^n \frac{|R_{kn}|^2}{R_{nn}^2} \right)^{\frac{1}{2}} \frac{\mathbf{h}_n}{\|\mathbf{h}_n\|_2} \\
 &= \sum_{n=1}^{N-1} \left( R_{nN} + \frac{\sum_{m=n+1}^{N-1} \text{cof}(\mathbf{R}_{IS})_{mn} R_{mN}}{\prod_{i \neq n} R_{ii}} \right) \left( \sum_{k=1}^n \frac{|R_{kn}|^2}{R_{nn}^2} \right)^{\frac{1}{2}} \frac{\mathbf{h}_n}{\|\mathbf{h}_n\|_2} \\
 &= \sum_{n=1}^{N-1} \frac{R'_{nN} \mathbf{h}_n}{\|\mathbf{h}_n\|_2}. \tag{A.7}
 \end{aligned}$$

By (A.2), (A.7), and  $\Delta_n = 2\sqrt{A_n} \|\mathbf{h}_n\|_2 d_n$ , (2.23) is obtained.





# Appendix B

## Proof of (2.32)

Express  $\tilde{\mathbf{R}}$  as

$$\tilde{\mathbf{R}} = \begin{bmatrix} \tilde{\mathbf{R}}_{IS} & \tilde{\mathbf{r}}_{NS} \\ \mathbf{0}_{1 \times (N-1)} & \tilde{R}_{NN} \end{bmatrix} = \begin{bmatrix} \tilde{\mathbf{R}}_I & \tilde{\mathbf{r}}_N \end{bmatrix}. \quad (\text{B.1})$$

From Lemma 2 and Lemma 3,

$$\begin{aligned} \eta_{\text{SNR}} &= \frac{A_N}{\sigma_V^2} \tilde{R}_{NN}^2 - 1 - \frac{A_N}{\sigma_V^2} R_{NN}^2 \\ &= \frac{A_N}{\sigma_V^2} \left( \sum_{n=1}^N |\tilde{R}_{nN}|^2 - \sum_{n=1}^{N-1} |R_{nN}|^2 \right) - 1 - \frac{A_N}{\sigma_V^2} R_{NN}^2 \\ &= \frac{A_N}{\sigma_V^2} \left( \|\mathbf{h}_N\|_2^2 + \frac{\sigma_V^2}{A_N} - \sum_{n=1}^{N-1} |R_{nN}|^2 \right) - 1 - \frac{A_N}{\sigma_V^2} R_{NN}^2 \\ &= \frac{A_N}{\sigma_V^2} \sum_{n=1}^{N-1} \left( |R_{nN}|^2 - |\tilde{R}_{nN}|^2 \right) \\ &= \frac{A_N}{\sigma_V^2} \left( \mathbf{r}_{NS}^H \mathbf{r}_{NS} - \tilde{\mathbf{r}}_{NS}^H \tilde{\mathbf{r}}_{NS} \right) \\ &= \frac{A_N}{\sigma_V^2} \left[ \mathbf{r}_{NS}^H \mathbf{r}_{NS} - \tilde{\mathbf{r}}_{NS}^H \tilde{\mathbf{R}}_{IS} \left( \tilde{\mathbf{R}}_{IS}^H \tilde{\mathbf{R}}_{IS} \right)^{-1} \tilde{\mathbf{R}}_{IS}^H \tilde{\mathbf{r}}_{NS} \right] \\ &= \frac{A_N}{\sigma_V^2} \left[ \mathbf{r}_{NS}^H \mathbf{r}_{NS} - \tilde{\mathbf{r}}_N^H \tilde{\mathbf{R}}_I \left( \tilde{\mathbf{R}}_I^H \tilde{\mathbf{R}}_I \right)^{-1} \tilde{\mathbf{R}}_I^H \tilde{\mathbf{r}}_N \right] \end{aligned} \quad (\text{B.2})$$

In (B.2), the last equality follows from  $\tilde{\mathbf{r}}_{NS}^H \tilde{\mathbf{R}}_{IS} = \tilde{\mathbf{r}}_N^H \tilde{\mathbf{R}}_I$  and  $\tilde{\mathbf{R}}_{IS}^H \tilde{\mathbf{R}}_{IS} = \tilde{\mathbf{R}}_I^H \tilde{\mathbf{R}}_I$ , as easily seen from (B.1). In (2.10), if  $\mathbf{R}$  is substituted for  $\mathbf{H}$ , then

$$\begin{bmatrix} \mathbf{R}_{IS} & \mathbf{r}_{NS} \\ \mathbf{0}_{1 \times (N-1)} & R_{NN} \\ \tilde{\mathbf{D}}_I & \sqrt{\frac{\sigma^2}{A_N}} \mathbf{e}_N \end{bmatrix} = \bar{\mathbf{Q}} \begin{bmatrix} \tilde{\mathbf{R}}_I & \tilde{\mathbf{r}}_N \end{bmatrix}, \quad (\text{B.3})$$

where  $\bar{\mathbf{Q}}$  is some unitary matrix different from  $\tilde{\mathbf{Q}}$ ,  $\mathbf{e}_N$  is the  $N \times 1$  zero vector with the  $N$ th entry replaced by 1,

$$\tilde{\mathbf{D}}_I = [ \mathbf{D}_I \quad \mathbf{0}_{(N-1) \times 1} ]^T, \quad (\text{B.4})$$

$$\mathbf{D}_I = \text{diag} \left( \sqrt{\frac{\sigma_V^2}{A_1}}, \dots, \sqrt{\frac{\sigma_V^2}{A_{N-1}}} \right). \quad (\text{B.5})$$

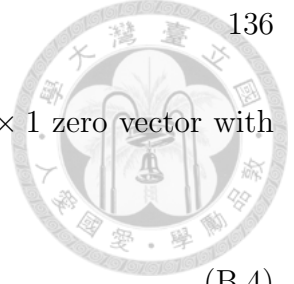
(B.3) holds because the entries of  $\tilde{\mathbf{R}}$  depends only on the norms of the columns of matrix to be QR-factorized and the inner products between them. From (B.2) and (B.3), we have

$$\begin{aligned} \eta_{\text{SNR}} &= \frac{A_N}{\sigma_V^2} \mathbf{r}_{NS}^H \left[ \mathbf{I}_{N-1} - \mathbf{R}_{IS} (\mathbf{R}_{IS}^H \mathbf{R}_{IS} + \mathbf{D}_I^2)^{-1} \mathbf{R}_{IS}^H \right] \mathbf{r}_{NS} \\ &= \mathbf{r}_{NS}^H \left( \frac{\sigma_V^2}{A_N} \mathbf{I}_{N-1} + \mathbf{R}_{IS} \mathbf{\Gamma}_N^{-1} \mathbf{\Gamma}_N^{-1} \mathbf{R}_{IS}^H \right)^{-1} \mathbf{r}_{NS}. \end{aligned} \quad (\text{B.6})$$

In (B.6), the second equality follows from the matrix inversion lemma [28], and  $\mathbf{\Gamma}_N$  is defined in (2.33). Hence,

$$\begin{aligned} \lim_{\substack{A_N \rightarrow \infty \\ \sigma_V^2}} \eta_{\text{SNR}} &= \mathbf{r}_{NS}^H (\mathbf{R}_{IS} \mathbf{\Gamma}_N^{-1} \mathbf{\Gamma}_N^{-1} \mathbf{R}_{IS}^H)^{-1} \mathbf{r}_{NS} \\ &= \|\mathbf{\Gamma}_N \mathbf{R}_{IS}^{-1} \mathbf{r}_{NS}\|_2^2 \\ &= \|R_{NN} \mathbf{\Gamma}_N (-\mathbf{R}_{IS}^{-1} \mathbf{r}_{NS} R_{NN}^{-1})\|_2^2 \\ &= \|R_{NN} \mathbf{\Gamma}_N \mathbf{r}_{NS}^-\|_2^2, \end{aligned} \quad (\text{B.7})$$

where the last equality follows from (A.6).





# Appendix C

## Proof of (4.66)

By (4.58), (4.59), (4.67), and (4.68), we have

$$\begin{aligned}
& \mathbf{s}_{\text{CI},1,k}(\varepsilon_n) \bar{U}_{n,k}^z + \mathbf{s}_{\text{CI},2,k}(\varepsilon_n) \bar{U}_{n,k}^{z+1} \\
&= \begin{bmatrix} \mathbf{s}_{t,1,k}(\varepsilon_n) \\ \mathbf{0}_{N_{\text{rx}}(2\beta+1)\times 1} \end{bmatrix} \{(\text{Re}(\bar{X}_{n,k,1}) \cos \theta - \text{Im}(\bar{X}_{n,k,1}) \sin \theta) + j (\text{Re}(\bar{X}_{n,k,2}) \sin \theta + \text{Im}(\bar{X}_{n,k,2}) \cos \theta)\} \\
&+ \begin{bmatrix} \mathbf{0}_{N_{\text{rx}}(2\beta+1)\times 1} \\ e^{j\phi_n} \mathbf{s}_{t,2,k}(\varepsilon_n) \end{bmatrix} \{(\text{Re}(\bar{X}_{n,k,2}) \cos \theta - \text{Im}(\bar{X}_{n,k,2}) \sin \theta) + j (\text{Re}(\bar{X}_{n,k,1}) \sin \theta + \text{Im}(\bar{X}_{n,k,1}) \cos \theta)\} \\
&= \left\{ \begin{bmatrix} \mathbf{s}_{t,1,k}(\varepsilon_n) \cos \theta \\ \mathbf{0}_{N_{\text{rx}}(2\beta+1)\times 1} \end{bmatrix} + \begin{bmatrix} \mathbf{0}_{N_{\text{rx}}(2\beta+1)\times 1} \\ j e^{j\phi_n} \mathbf{s}_{t,2,k}(\varepsilon_n) \sin \theta \end{bmatrix} \right\} (\text{Re}(\bar{X}_{n,k,1}) + j \text{Im}(\bar{X}_{n,k,2})) \\
&+ \left\{ \begin{bmatrix} j \mathbf{s}_{t,1,k}(\varepsilon_n) \sin \theta \\ \mathbf{0}_{N_{\text{rx}}(2\beta+1)\times 1} \end{bmatrix} + \begin{bmatrix} \mathbf{0}_{N_{\text{rx}}(2\beta+1)\times 1} \\ e^{j\phi_n} \mathbf{s}_{t,2,k}(\varepsilon_n) \cos \theta \end{bmatrix} \right\} (\text{Re}(\bar{X}_{n,k,2}) + j \text{Im}(\bar{X}_{n,k,1})) \\
&= \tilde{\mathbf{s}}_{\text{CI},1,k}(\varepsilon_n) \tilde{X}_{n,k,1} + \tilde{\mathbf{s}}_{\text{CI},2,k}(\varepsilon_n) \tilde{X}_{n,k,2}. \tag{C.1}
\end{aligned}$$

Hence, (4.66) is proved.





# Appendix D

## Proof of (5.26)

The following lemma is useful in our proof.

**Lemma 4.** Let  $a, b$  be any two real numbers, and  $X$  be a Gaussian random variable with variance  $\frac{1}{2}$ , i.e.  $X \sim CN(0, \frac{1}{2})$ , then

$$\mathbb{E} \left\{ e^{-aX^2 - 2bX} \right\} = (1 + a)^{-\frac{1}{2}} \exp\left(\frac{b^2}{1 + a}\right). \quad (\text{D.1})$$

From (5.22) and (5.23), we have

$$\begin{aligned} \mathbb{E} [\text{BER}_{\text{asyn, mrc}}] &\approx \sum_{t=1}^3 b_t \mathbb{E} \left[ \exp\left(\frac{-a_t \|\tilde{\mathbf{h}}_{\text{eff},q}\|_2^2}{\sigma_V^2}\right) \right] \\ &= \sum_{t=1}^3 b_t \left( \prod_{m=1}^{N_{\text{rx}}} \mathbb{E} \left[ \exp\left(\frac{-a_t \|\tilde{\mathbf{h}}_{\text{eff},q}^m\|_2^2}{\sigma_V^2}\right) \right] \right). \end{aligned} \quad (\text{D.2})$$

The equality of (D.2) follows from that  $H_{n,k}^m$ 's are independent across different indices  $n$  and  $m$ . Let  $w = \frac{a_t}{\sigma_V^2}$ ,  $\rho_{12} = \rho_{q,q+1}(\varepsilon_1, \varepsilon_2)$ , and

$$\bar{H}_{1,q}^m = (H_{1,q}^m)^* e^{j\arg(\rho_{12} H_{2,q+1}^m)}. \quad (\text{D.3})$$



By (5.24),

$$\begin{aligned}
 & \mathbb{E} \left[ \exp \left( \frac{-a_t \|\tilde{\mathbf{h}}_{\text{eff},q}^m\|_2^2}{\sigma_V^2} \right) \right] \\
 &= \mathbb{E} \left[ \exp \left( -wA_1 |\bar{H}_{1,q}^m|^2 - 2w\sqrt{A_1A_2} |\rho_{12}H_{2,q+1}^m| \operatorname{Re}(\bar{H}_{1,q}^m) - wA_2 |H_{2,q+1}^m|^2 \right) \right] \\
 &= (1 + wA_1)^{-1} \mathbb{E} \left[ \exp \left( \frac{w^2A_1A_2|\rho_{12}|^2}{1 + wA_1} |H_{2,q+1}^m|^2 - wA_2 |H_{2,q+1}^m|^2 \right) \right] \quad (\text{D.4})
 \end{aligned}$$

$$= (1 + wA_1)^{-1} \left( 1 - \frac{w^2A_1A_2|\rho_{12}|^2 - wA_2 - w^2A_1A_2}{1 + wA_1} \right)^{-1} \quad (\text{D.5})$$

$$= ((1 + wA_1)(1 + wA_2) - w^2A_1A_2|\rho_{12}|^2)^{-1}. \quad (\text{D.6})$$

In the above equations, (D.4) and (D.5) follow from taking expectation w.r.t  $\bar{H}_{1,q}^m$  and  $H_{2,q+1}^m$  using Lemma 4. From (D.2) and (D.6), we obtain (5.26).



## Appendix E

### Proof of (5.29)

$$\begin{aligned}
& \mathbb{E} \left[ \exp \left( \frac{-a_t \left\| \tilde{\mathbf{h}}_{\text{eff},q}^m \right\|_2^2}{\sigma_V^2} \right) \right] \\
&= \mathbb{E} \left[ \exp \left( -w \left\| \sum_{n=1}^3 \sqrt{A_n} H_{n,q+n-1}^m \mathbf{c}_{q+n-1}(\varepsilon_n) \right\|_2^2 \right) \right] \\
&= \mathbb{E} \left[ \exp \left( -w A_1 |H_{1,q}^m|^2 - 2w \sqrt{A_1} \operatorname{Re} \left\{ \sum_{n=2}^3 \sqrt{A_n} (H_{1,q}^m)^* H_{n,q+n-1}^m \rho_{1n} \right\} \right) \right. \\
&\quad \left. \exp \left( -w \left\| \sum_{n=2}^3 \sqrt{A_n} H_{n,q+n-1}^m \mathbf{c}_{q+n-1}(\varepsilon_n) \right\|_2^2 \right) \right] \\
&= (1 + w A_1)^{-1} \mathbb{E} \left[ \exp \left( \frac{w^2 A_1 \left| \sum_{n=2}^3 \sqrt{A_n} H_{n,q+n-1}^m \rho_{1n} \right|^2}{1 + w A_1} \right) \right. \\
&\quad \left. \exp \left( -w \left\| \sum_{n=2}^3 \sqrt{A_n} H_{n,q+n-1}^m \mathbf{c}_{q+n-1}(\varepsilon_n) \right\|_2^2 \right) \right] \tag{E.1}
\end{aligned}$$

$$\begin{aligned}
&= (1 + w A_1)^{-1} \mathbb{E} \left[ \exp \left( - \sum_{n=2}^3 \left( w A_n - \frac{w^2 A_1 A_n |\rho_{1n}|^2}{1 + w A_1} \right) |H_{n,q+n-1}^m|^2 \right) \right. \\
&\quad \left. \exp \left( 2 \operatorname{Re} \left\{ (H_{2,q+1}^m)^* \left( w \sqrt{A_2 A_3} \rho_{23} - \rho_{12}^* \rho_{13} \frac{w^2 A_1 \sqrt{A_2 A_3}}{1 + w A_1} \right) H_{3,q+2}^m \right\} \right) \right] \\
&= (1 + w A_1)^{-1} \left( 1 + w A_2 - \frac{w^2 A_1 A_2 |\rho_{12}|^2}{1 + w A_1} \right)^{-1} \\
&\quad \mathbb{E} \left[ \exp \left( \frac{|H_{3,l}^m|^2 \left| w \sqrt{A_2 A_3} \rho_{23} - \rho_{12}^* \rho_{13} \frac{w^2 A_1 \sqrt{A_2 A_3}}{1 + w A_1} \right|^2}{1 + w A_2 - \frac{w^2 A_1 A_2 |\rho_{12}|^2}{1 + w A_1}} - \left( w A_3 - \frac{w^2 A_1 A_3 |\rho_{13}|^2}{1 + w A_1} \right) |H_{3,q+2}^m|^2 \right) \right]. \tag{E.2}
\end{aligned}$$

In the above equations,  $w = \frac{a_t}{\sigma_V^2}$ , (E.1) and (E.2) are obtained by taking expectation w.r.t  $H_{1,q}^m$  and  $H_{2,q+1}^m$ . Ignoring the term  $\rho_{12}^* \rho_{13} \frac{w^2 A_1 \sqrt{A_2 A_3}}{1+wA_1}$  in (E.2) and performing the expectation lead to

$$\begin{aligned} & \mathbb{E} \left[ \exp \left( \frac{-a_t \|\tilde{\mathbf{h}}_{\text{eff},q}^m\|_2^2}{\sigma_V^2} \right) \right] \\ & \approx \left( (1+wA_1)(1+wA_2) - w^2 A_1 A_2 |\rho_{12}|^2 \right)^{-1} \\ & \quad \left( 1 - \frac{(1+wA_1)w^2 A_2 A_3 |\rho_{23}|^2}{(1+wA_1)(1+wA_2) - w^2 A_1 A_2 |\rho_{12}|^2} + wA_3 - \frac{w^2 A_1 A_3 |\rho_{13}|^2}{1+wA_1} \right)^{-1} \\ & \approx \left[ (1+wA_1)(1+wA_2) - w^2 A_1 A_2 |\rho_{12}|^2 - (1+wA_1)w^2 A_2 A_3 |\rho_{23}|^2 \right. \\ & \quad \left. + wA_3(1+wA_1)(1+wA_2) - w^3 A_1 A_2 A_3 |\rho_{12}|^2 - (1+wA_2)w^2 A_1 A_3 |\rho_{13}|^2 \right]^{-1}, \end{aligned} \quad (\text{E.3})$$

$$= \left[ \prod_{n=1}^3 (1+wA_n) - w^2 \sum_{n<l} A_n A_l |\rho_{nl}|^2 - w^3 A_1 A_2 A_3 \sum_{n<l} |\rho_{nl}|^2 \right]^{-1}. \quad (\text{E.4})$$

The approximation of (E.3) comes from ignoring  $w^2 A_1 A_2 |\rho_{12}|^2 \frac{w^2 A_1 A_3 |\rho_{13}|^2}{1+wA_1}$ . Substituting (E.4) into (D.2), (5.29) is yielded.